

Novel Electrolyte Systems for High-Performance Magnesium Batteries

Von der Fakultät Chemie der Universität Stuttgart zur Erlangung der Würde eines
Doktors der Naturwissenschaften (Dr. rer. nat.) genehmigte Abhandlung

vorgelegt von

Peiwen Wang

aus Shanghai, China

Hauptberichter: Herr Prof. Dr. Michael R. Buchmeiser

Mitberichter: Herr Prof. Dr. Oliver Clemens

Mitprüfer: Herr Prof. Dr. Rainer Niewa

Tag der mündlichen Prüfung: 19.07.2022

Institut für Polymerchemie der Universität Stuttgart

2022

Erklärung über die Eigenständigkeit der Dissertation

Ich versichere, dass ich die vorliegende Arbeit mit dem Titel Neue Elektrolyte für Magnesium Hochleistungsbatterien selbständig verfasst und keine anderen als die angegebenen Quellen und Hilfsmittel benutzt habe; aus fremden Quellen entnommene Passagen und Gedanken sind als solche kenntlich gemacht.

Declaration of Authorship

I hereby certify that the dissertation entitled

Novel Electrolyte Systems for High-Performance Magnesium Batteries

is entirely my own work except where otherwise indicated. Passages and ideas from other sources have been clearly indicated.

Name/Name: Peiwen Wang

Unterschrift/Signed: _____

Datum/Date: _____

Dedicated to My Family

Life is all about experiences.

Acknowledgements

It has been a long way to accomplish this PhD thesis and put it in front of you. Twenty-four year's education, it is like a dream. I feel yesterday I was a little girl, standing in front of the school, trying to open a brand new world. All the way until now, I would like to thank a lot of people.

First and foremost, I wish to express my deepest appreciation to my supervisor *Prof. Dr. Michael R. Buchmeiser* for this dissertation. It has been my privilege to be his student and work in his research group. I appreciate all his encouragements, superfast e-mail replying, superfast manuscripts correction, 7:30 am's appointments in his office and acceptance of buying chemicals that I needed, to make my research productive and fruitful.

I also want to acknowledge *Prof. Dr. Oliver Clemens*, as my second examiner, for his superfast agreement as my second examiner and his time and interest for my PhD work. In addition, I would like to thank *Prof. Dr. Rainer Niewa* for his willingness to chair the examination committee.

Furthermore, my thanks are also due to *Miss. Parastatidou, Dr. Wang, Mr. Wendel, Mrs. Kalizan* and *Mrs. Keller* for their supports and help during the working time. I also want to thank *Miss. Förtch* (Inorganic Department) for elemental analysis; *Mr. Hageroth* (DITF) for handling the SEM/EDX samples; *Dr. Küster* (Max Planck Institute) for the XPS measurement and training of the peaks fitting; *Joachim Häcker* (DLR), *Dr. Schlosser* (Customcell) from the MagSiMal project for their support during my PhD.

I would also like to express my acknowledgement to the battery group, *Janina*, who also fought with me against the Mg batteries, and *Stefan, Julian, Alina, Kumar, Qian* and *Tim*, for the fruitful discussions, efficient cooperation and the effort of producing a pleasant and productive lab environment. My thanks are also due to the entire working group of the IPOC: particularly *Yavus, Janis, Hande, Patrick, Philipp*, for the small talks during the work time, which are always helpful to refresh the mind.

Outside of the lab, I would like to thank my friends: *Chen*, also a PhD student (Inorganic department), who always listens to my complaints and stress and at the same time encourages me to learn other skills apart from chemistry; *Hong*, also a PhD student (Materials department), who always says yes when I ask her to eat something nice even when she is very busy. I also want to thank *Liu* (Dr. Yang), *Caiyun* (Dr. Xu in the near future), *Hang* (Dr. Liu in the near future), *Ruojun* (Master Tian), *Jie* (Dr. Chen in the near future), *Ke* (Dr. Wang in the near future), *Zheng* (Dr. Li in the near future), who have had a really great time with me in Stuttgart. I really hope that they achieve much success and happiness in their future life.

I would also love to send my deepest acknowledgements to my perfect family, *my parents, my husband and my grandma*. My parents and grandparents, have put so much efforts on my education and personal development: teaching me English from 3 years old; developing my hobbies, such as Chinese painting, when I was a little kid; sending me to the best schools, providing me with almost everything I need...I remember clearly, when I was at the airport ready to fly to England for the one-year exchange, my parents told me “We are happy only if you are happy.” I feel I am always being loved. They have also inspired me in the daily life. For example, my grandma was an English professor at Fudan University (Top 2 in Shanghai). She spoke English, Russian and Chinese fluently. In her generation, it was not easy and I am so proud of her! She compiled and edited English dictionaries until she was almost 70 years old. My mom is a doctor. She compromised her chance of promoting because of the birth of me. Nonetheless, she did not stop studying and used the time when I went to bed every night for learning. My husband, who I met ten years ago in the German class, is a really smart and positive person. What he always tells me is “Don’t worry~ Take it easy~”, using his funny and somehow stupid tone. Without his love and supports, it would have been impossible for me to overcome so much difficulties and loneliness in a foreign country.

Last but not least, I would like to thank myself. 5 years’ elementary school, 7 years’ high school, 12 years’ University, from China to England and then to Germany, ambition, stress, depression, happiness of achievements, loneliness, ..., I have all experienced and all of these were not easy. I always believe that life is all about experiences. The people who I have met and all the experiences have shaped who I am. Now, educations are completed,

but learning will never stop. With all these experiences, I am not in fear of the challenges and difficulties in my future life.

I do not have huge dreams. I only hope, when I am old, I still have a young heart and loads of sweet memories. If I can also make some positive changes to the society or to the human beings, my whole life has been worth living.

Peiwen Wang

2022.3.19 Stuttgart

Content

1. Introduction.....	1
2. Theory and State of the Art.....	5
2.1 Basics of Electrochemistry	5
2.2 Before Li-Ion Batteries.....	8
2.3 Li-Ion Batteries	10
2.3.1 An Overview	10
2.3.2 Principles of Lithium-Ion Batteries.....	11
2.3.3 Cathode and Anode Materials	12
2.3.4 Electrolyte Systems	16
2.4 Lithium-Sulfur Batteries	21
2.4.1 Principles of Lithium-Sulfur Batteries	22
2.4.2 Electrolyte Systems	24
2.4.3 Cathode Materials	26
2.5 Magnesium-Sulfur Batteries	30
2.5.1 Principle of Magnesium-Sulfur Batteries.....	31
2.5.2 Comparison of Mg-S and Li-S Systems.....	34
2.5.3 Cathode and Anode Materials	38
2.5.4 Electrolyte Systems	43
3. Research Objectives	59
4. Magnesium-Sulfur Batteries Based on SPAN Cathodes	61

4.1 Motivation	61
4.2 Publication: “Characteristics of Magnesium-Sulfur Batteries Based on a Sulfurized Poly(acrylonitrile) Composite and a Fluorinated Electrolyte”	63
4.3 Supporting Information to “Characteristics of Magnesium-Sulfur Batteries Based on a Sulfurized Poly(acrylonitrile) Composite and a Fluorinated Electrolyte”	73
5. Use of a Dual-Salt-Electrolyte in Mg-SPAN Batteries.....	87
5.1 Motivation	87
5.2 Publication: “High-Performance Magnesium-Sulfur Batteries Based on a Sulfurated Poly(acrylonitrile) Cathode, a Borohydride Electrolyte, and a High-Surface Area Magnesium Anode”	89
5.3 Supporting Information to: “High-Performance Magnesium-Sulfur Batteries Based on a Sulfurated Poly(acrylonitrile) Cathode, a Borohydride Electrolyte, and a High-Surface Area Magnesium Anode”	100
6. Understanding the Role of a Lithium Salt in Mg-SPAN Batteries.....	107
6.1 Motivation	107
6.2 Publication: “Performance Enhancement of Rechargeable Magnesium-Sulfur Batteries Based on a Sulfurized Poly(acrylonitrile) Composite and a Lithium Salt”	109
6.3 Supporting Information to: “Performance Enhancement of Rechargeable Magnesium-Sulfur Batteries Based on a Sulfurized Poly(acrylonitrile) Composite and a Lithium Salt”	122
7. Design of a Gel Polymer Electrolyte for Magnesium-Sulfur/Ion Batteries	139
7.1 Motivation	139
7.2 Publication: “A Design Concept for Halogen-Free Mg^{2+}/Li^{+} -Dual Salt-Containing Gel-Polymer-Electrolytes for Rechargeable Magnesium Batteries”	140
7.3 Supporting Information to: “A Design Concept for Halogen-Free Mg^{2+}/Li^{+} - Dual Salt-Containing Gel-Polymer-Electrolytes for Rechargeable Magnesium Batteries”	151
8. Conclusions	173
9. Future work	175
10. References	177

11. Curriculum Vitae	193
12. Review Publication.....	197

List of Figures

Figure 2.1: The main components of a cell: cathode, anode, separator and electrolyte. This scheme shows a discharge process. ^[2]	5
Figure 2.2: A brief history of the battery development. ^[1, 9]	8
Figure 2.3: Illustration of a typical lithium-ion battery (discharge process).....	11
Figure 2.4: a) Three typical crystal structures of cathodes for LIBs; b) typical discharge profiles of some intercalation cathodes. ^[18, 38] Reproduced with permission from ref. ^[18] . Copyright (2015). Elsevier.....	14
Figure 2.5: Chemical structures of the used electrolyte systems: conductive salts, solvents and selected additives in current LIBs. ^[62]	17
Figure 2.6: Schematic illustration of a lithium-sulfur cell based on elemental sulfur.	22
Figure 2.7: Typical voltage profile of a Li-S ₈ battery in an ether-based liquid electrolyte during discharge and charge processes. ^[97] Reprinted with permission from Ref. ^[97] . Copyright 2012 Macmillan Publishers Ltd.	23
Figure 2.8: Hierarchical designs of sulfur-carbon composites: a) microporous carbon; b) spherical ordered mesoporous carbon nanoparticles; c) porous hollow carbon; d) graphene oxide sheets; e) porous carbon nanofibers; f) hollow carbon nanofibers to encapsulate the sulfur. ^[96] Reprinted with permission from Ref. ^[96] . Copyright 2012 American Chemical Society.....	26
Figure 2.9: Two types of binder-free cathodes: a) sulfur impregnated carbon fiber cloth; b) self-weaving sulfur-CNT composites. ^[96] Reprinted with permission from Ref. ^[96] . Copyright 2012 American Chemical Society.....	27

Figure 2.10: Schematic illustration of a magnesium-sulfur cell using elemental sulfur-based cathodes.	32
Figure 2.11: a) A typical voltage profile of a Mg-S cell based on S ₈ during discharge. ^[144] Reproduced with permission from ref. ^[144] . Copyright (2015). WILEY-VCH Verlag GmbH & Co. KGaA, Weinheim; b) Voltage profile of a Mg-S cell based on S ₈ during discharge. ^[165] Reproduced with permission from ref. ^[165] . Copyright (2019). American Chemical Society.....	33
Figure 2.12: Comparison between Li-S batteries (LSB, blue) and Mg-S batteries (MSB, red) in the aspect of anode reversibility, number of publications, sulfur utilization, cycle life, current rate, electrolyte-to-sulfur (E:S) ratio, voltage efficiency and deposition morphology. ^[146] Reproduced with permission from ref. ^[146] . Copyright (2021). Springer Nature.	37
Figure 2.13: a) Illustration of S ₈ (yellow) imbedded in CMK-3 (gray); b) synthetic procedure of S/CMK-3 composites. ^[120] Reprinted by permission from ref ^[120] . Copyright (2009). Springer Nature: Nature Materials.....	38
Figure 2.14: Illustration of a sulfur graphdiyne (SGDY) cathode. ^[185] Reproduced from the permission of ref ^[185] Copyright (2017). WILEY-VCH Verlag GmbH & Co. KGaA, Weinheim.....	40
Figure 2.15: a) Preparation of an S ₈ -mixed cathode material; b) Mg-S ₈ cell using the MXene as the interlayer. ^[161] Reproduced from the permission of ref ^[161] . Copyright (2021). WILEY-VCH Verlag GmbH & Co. KGaA, Weinheim.	42
Figure 2.16: a) Structure (ORTEP plot) of the [Mg ₂ (μ-Cl) ₃ 6THF][HMDSAICl ₃], hydrogen atoms and THF molecules are omitted for clarity; b) voltage profile of a Mg-S cell with the [Mg ₂ (μ-Cl) ₃ 6THF][HMDSAICl ₃] electrolyte. ^[89] Reproduced with permission from ref ^[89] . Copyright (2011). Nature Publishing Group.	47
Figure 2.17: a) Chemical reaction for the synthesis of [Mg(THF) ₆][AlCl ₄] ₂ ; b) chemical structure of [Mg(THF) ₆][AlCl ₄] ₂ . ^[151] Reproduced with permission from ref ^[151] . Copyright (2016). WILEY-VCH Verlag GmbH & Co. KGaA, Weinheim.	49

Figure 2.18: a) Chemical reaction for the synthesis of a fluorinated magnesium alkoxyborate-based electrolyte; b) chemical structure of $\text{Mg}[\text{B}(\text{hfip})_4]_2 \cdot 3\text{DME}$. ^[184] Reproduced with permission from ref. ^[184] . Copyright (2017). Royal Society of Chemistry.....	51
Figure 2.19: a) Overview of the potentials and restrictions of conductive salts for magnesium-sulfur batteries; b) anion of the as-prepared BCM electrolyte ($[\text{FTHB}]^-$); c) cation of the BCM electrolyte; d) effective anion species of the cycled BCM electrolyte. ^[217] Reproduced from the ref. ^[217] . Copyright (2017). WILEY-VCH Verlag GmbH & Co. KGaA, Weinheim.....	53
Figure 2.20: Chemical structures of the cation: $[\text{Mg}_4\text{Cl}_6(\text{DME})_6]^{2+}$ (right) and anion: $[\text{B}(\text{hfip})_4]_2^-$ (left). ^[180] Reproduced from the ref. ^[180] . Copyright (2017). Royal Society of Chemistry.	54
Figure 2.21: a) XPS analysis of the Mg anode cycled from a Mg-HMDS electrolyte; b) XPS analysis of the Mg anode cycled from a Mg-HMDS electrolyte with LiTFSI as additive; c) proposed charging and discharging voltage profile of a Mg-ACC/S cell using a Li-containing electrolyte. ^[154] Reproduced with permission from ref. ^[154] . Copyright (2015). American Chemical Society.	56
Figure 2.22: Illustration of a) a Mg anode cycled in a Mg electrolyte with polysulfide additive; b) a Mg anode cycled in a Mg electrolyte with polysulfide and I_2 additive. ^[220] Reproduced from the ref. ^[220] . Copyright (2017). Royal Society of Chemistry.....	57
Figure 4.1: a) CV scans of Mg-Pt cell using the 0.6 M $\text{Mg}[\text{B}(\text{hfip})_4]_2/\text{DME}$ electrolyte at 25 mV s^{-1} ; b) LSV analysis of the 0.6 M $\text{Mg}[\text{B}(\text{hfip})_4]_2/\text{DME}$ against various current collectors. ^[184] Reproduced with permission from ref. ^[184] . Copyright (2017). Royal Society of Chemistry.	61
Figure 4.2: a) Voltage profile; b) cycle stability test of the Mg/S-CMK-3 cell using a $\text{Mg}[\text{B}(\text{hfip})_4]_2/\text{diglyme-tetraglyme}$ (1-1, v-v) electrolyte at 0.1 C; ^[184] Reproduced with permission from ref. ^[184] . Copyright (2017). Royal Society of Chemistry. c) Voltage profile; d) cycle stability test of the Mg-ACC/S cell using 0.4 M	

Mg[B(hfip)]₄/DME at 0.1 C.^[194] Reproduced with permission from ref.^[194].
Copyright (2018). American Chemical Society. 62

Figure 4.3: Graphical abstract of the publication “Characteristics of magnesium-sulfur batteries based on a sulfurized poly(acrylonitrile) composite and a fluorinated electrolyte”. 63

Figure 5.1: a) Comparison of the cell performance of Mg-ACC/S cells using a pure magnesium electrolyte (black) and a Mg-HMDS electrolyte with the LiTFSI additive (red); b) SEM image of the surface of the Mg anode using the Mg-HMDS electrolyte with the LiTFSI additive; c) SEM image of the cross-section of the cycled Mg anode from the Mg-ACC/S cell using the Mg-HMDS electrolyte with the LiTFSI additive.^[154] Reproduced with permission from ref.^[154]. Copyright (2015) American Chemical Society. 88

Figure 6.1: a) Proposed formation of the electroactive species; b) simulated molecular structure of the electroactive species $[\text{Mg}_2(\mu_2\text{-Cl})_2(\text{DME})_4]^{2+}$; c) cell stability test of a Mg-S cell with a $\text{Mg}(\text{CF}_3\text{SO}_3)_2$, MgCl_2 and AlCl_3 -based electrolyte at 0.3 C.^[192] Reproduced with permission from ref.^[192]. Copyright (2020) American Chemical Society. 108

Figure 7.1: Graphical abstract of the publication “A design concept for halogen-free $\text{Mg}^{2+}/\text{Li}^+$ -dual salt-containing gel-polymer-electrolytes for rechargeable magnesium batteries”. 141

List of Tables

Table 2.1: A summary and a comparison of the history and the state-of-the-art battery chemistries. ^[1, 9, 10, 12-14]	9
Table 2.2: Summary of typical cathode materials for LIBs and their features. ^[38]	13
Table 2.3: Major differences between Mg-S and Li-S battery systems.	35

List of Abbreviations

Full name	Abbreviation
1,2-dimethoxyethane	DME
1,2-dioxolane	DOL
ampere	A
all phenyl complex	APC
Brunauer-Emmett-Teller	BET
carbon nanofiber	CNF
cyclic voltammetry	CV
composite polymer electrolyte	CPE
Coulombic efficiency	CE
diethyl carbonate	DEC
diethylene glycol dimethyl ether	diglyme
dimethyl carbonate	DMC
electric vehicle	EV
energy dispersive X-ray analysis	EDX
ethylene carbonate	EC
ethyl-methyl carbonate	EMC
fluoro-tris(2H-hexafluoroisopropyl) borate	FTHB
gel-polymer electrolyte	GPE
galvanostatic intermittent titrations technique	GITT
glass transition temperature	T _g
guar gum	GG
hexafluoro-2-propanol	hfip
hexamethyldisilazide magnesium chloride	HMDSMgCl
hybrid electrical vehicle	HEV
inorganic solid electrolyte	ISE

Full name**Abbreviation**

ionic liquid	IL
LiFePO ₄	LFP
lithium bis-trifluoromethanesulfonimide	LiTFSI
lithium cobalt oxide	LCO; LiCoO ₂
lithium super ionic conductor	LISICON
lithium titanate	LTO, Li ₄ Ti ₅ O ₁₂
lithium-ion battery	LIB
magnesium bis(diisopropylamide)	MBA
magnesium tetrakis(hexafluoroisopropoxy) borate	Mg[B(hfip) ₄] ₂
metal organic framework	MOF
microporous carbon	MC
multiwall carbon nanotube	MWCNT
<i>n</i> -methyl-(<i>n</i> -butyl) pyrrolidinium	PYR14TFSI
bis(trifluoromethanesulfonyl)imide	
N-methyl-2-pyrrolidone	NMP
<i>N</i> -methyl- <i>N</i> -butyl-piperidinium	PP14TFSI
bis(trifluoromethanesulfonyl)imide	
open circuit voltage	OCV
poly(ethylene oxide)	PEO
poly(tetrahydrofuran)	PTHF
poly(vinylidene fluoride)	PVDF
scanning electron microscopy	SEM
sodium polyacrylate	PAAS
sodium super ionic conductor	NSICON
solid electrolyte interface	SEI
solid polymer electrolyte	SPE
solid-state electrolyte	SSE
standard hydrogen electrode	SHE
state of charge	SOC
sulfur @ activated carbon cloth	ACCS
sulfur graphdiyne	SGDY

Full name

sulfur poly(acrylonitrile)
tetraethylene glycol dimethyl ether
tetrahydrofuran
triethyl phosphate
trimethyl phosphate
tris(2H-hexafluoroisopropyl) borate
US Advanced Battery Consortium
weakly coordinating anion
X-ray diffraction
X-ray photoelectron spectroscopy

Abbreviation

SPAN
tetraglyme
THF
TEP
TMP
THFPB
USABC
WCA
XRD
XPS

Abstract

Due to the increasing demand for energy storage materials, nowadays dominated by lithium-ion batteries (LIBs), battery technology has shown great potential, *e.g.* in the field of portable electrical power applications. Nonetheless, considering the safety issues and the high costs of lithium batteries, rechargeable magnesium batteries have obtained increased attention as an alternative due to their improved safety, high theoretical volumetric energy density (3832 mAh cm^{-3}), as well as high earth-abundancy and low costs of the anode materials. At the same time, sulfur, which possesses a high theoretical capacity (1672 mAh g^{-1}), non-toxicity and also earth abundance, is attractive as the cathode material to be coupled with the magnesium anodes. However, research on magnesium-sulfur (Mg-S) batteries is still very limited, compared to the developments in lithium batteries, mainly due to the lack of efficient electrolyte systems and compatible cathodes.

The main objectives of this work are the fulfillments of stable-cycling Mg-S cells with high specific capacities, with a profound understanding of the cell mechanisms. In this work, four electrolyte systems have been developed for Mg-S batteries.

The first Mg-S battery system based on a sulfur poly(acrylonitrile) (SPAN) composite as the cathode, a magnesium tetrakis(hexafluoroisopropoxy) borate ($\text{Mg}[\text{B}(\text{hfip})_4]_2$) as the conductive salt in the electrolyte and a Mg foil as the anode, is presented. Despite an average cell performance (*ca.* 300 mAh g_s^{-1} at C/30), the possibility of the reversible cycling of cells containing an SPAN cathode and a Mg anode has been demonstrated.

In order to further improve cell performance, a second Mg-SPAN battery system containing a $\text{Mg}^{2+}/\text{Li}^+$ hybrid electrolyte ($\text{Li}[\text{BH}_4]$ and $\text{Mg}[\text{BH}_4]_2$ in diglyme) has been developed. Strikingly, this cell system stably delivers *ca.* 800 mAh g_s^{-1} at C/10 with $> 99\%$ Coulombic efficiency for 100 cycles, suggesting that the use of a dual salt electrolyte shows distinct benefits in Mg-SPAN batteries.

In order to further understand the role of a lithium salt in a Mg-SPAN battery, a third battery system has been developed, mainly because of the low solubility of $\text{Mg}[\text{BH}_4]_2$ in the previous electrolyte system. An electrolyte, which can dissolve both magnesium and lithium salts, has been found. A Mg-SPAN cell with a $\text{Mg}^{2+}/\text{Li}^+$ hybrid electrolyte ($\text{Mg}[\text{CF}_3\text{SO}_3]_2$, $\text{Li}[\text{CF}_3\text{SO}_3]$, MgCl_2 and AlCl_3 in 1,2-dimethoxyethane (DME)) delivers *ca.* 1100 mAh g_s^{-1} at 1 C with > 99.9% Coulombic efficiency for 100 cycles; whereas the Mg-SPAN cell with a pure Mg^{2+} electrolyte ($\text{Mg}[\text{CF}_3\text{SO}_3]_2$, MgCl_2 and AlCl_3 in DME) delivers much lower capacities. Electrochemical measurements as well as *post-mortem* analysis reveal that the addition of a lithium salt in the electrolyte is crucial for the suppression of the polysulfide shuttle. It also dramatically reduces the cell resistance and the overpotential *via* the possible formation of MgLiS_x species. At the same time, according to cyclic voltammetry results, *post-mortem* X-ray photoelectron spectroscopy (XPS) and scanning electron microscopy (SEM) analysis, the whole redox chemistry in the cell with the $\text{Mg}^{2+}/\text{Li}^+$ hybrid electrolyte is solely based on magnesium. Hence, the addition of a lithium salt does not compromise the safety of Mg-SPAN cells.

Furthermore, a novel design concept comprising a gel-polymer electrolyte (GPE) has been developed for Mg-S/ion batteries, which can be achieved by *in-situ* crosslinking $\text{Li}[\text{BH}_4]$ and $\text{Mg}[\text{BH}_4]_2$ with poly(tetrahydrofuran) (PTHF). This GPE displays outstanding ionic conductivities in a wide temperature range and superior polarization behavior. Also, due to the successful suppression of the polysulfide shuttle by the gel, the GPE not only shows good cycle performance with SPAN cathodes, but also with conventional S_8 -based cathodes. In addition, this GPE shows wide compatibility, which can not only be used with sulfur-based cathodes, but also with intercalation-based cathodes. Remarkably, Mg-SPAN cells containing the GPE feature low self-discharge, excellent flexibility and safety characteristics, which all together significantly improve the possibility for future technical use.

Zusammenfassung

Aufgrund der steigenden Nachfrage nach Energiespeichermaterialien, die heutzutage von Lithium-Ionen-Batterien (LIBs) dominiert werden, hat die Batterietechnologie ein großes Potenzial gezeigt. Aufgrund der verbesserten Sicherheit, der hohen theoretischen volumetrischen Energiedichte (3832 mAh cm^{-3}) sowie der hohen Erdreichum und der günstigen Rohstoffe sind Magnesium-Schwefel-Batterien eine vielversprechende Technologie für zukünftige Energiespeicher.

Im ersten Teil dieser Arbeit wird das Mg-S-Batteriesystem auf der Basis von SPAN-Kompositen als Kathode, Magnesiumtetrakis(hexafluorisopropoxy)borat ($\text{Mg}[\text{B}(\text{hfp})_4]_2$) als Leitsalz im Elektrolyten und einer Mg-Folie als Anode gefertigt, analysiert und elektrochemisch getestet. Trotz einer durchschnittlichen Zelleistung (ca. 300 mAh g_s^{-1} bei C/30) wurde die Möglichkeit des reversiblen Zyklus von Zellen mit einer SPAN-Kathode und einer Mg-Anode nachgewiesen.

Im zweiten Teil wurde ein SPAN-basiertes Mg-S-Batteriesystem mit einem $\text{Mg}^{2+}/\text{Li}^+$ -Hybridelektrolyten ($\text{Li}[\text{BH}_4]$ und $\text{Mg}[\text{BH}_4]_2$ in Diglyme) entwickelt, um die Leistung der Zelle weiter zu verbessern. Bemerkenswerterweise liefert dieses Zellsystem ca. 800 mAh g_s^{-1} bei C/10 mit $>99\%$ Coulomb-Effizienz für 100 Zyklen, was darauf hindeutet, dass die Verwendung eines Dualsalzelektrolyten deutliche Vorteile in Mg-S-Batterien aufweist.

Im dritten Teil wurde ein anderes Batteriesystem mit einem neuen Elektrolyten entwickelt, der sowohl Magnesium- als auch Lithiumsalze lösen kann, um die Rolle eines Lithiumsalzes in einer Mg-S-Batterie besser zu verstehen. Diese neue Mg-S-Zelle unter Verwendung von einer $\text{Mg}^{2+}/\text{Li}^+$ Hybridelektrolyten ($\text{Mg}[\text{CF}_3\text{SO}_3]_2$, $\text{Li}[\text{CF}_3\text{SO}_3]$, MgCl_2 und AlCl_3 in 1,2-Dimethoxyethan (DME)) liefert ca. $1100 \text{ mAh g}_s^{-1}$ bei 1 C mit $>99.9\%$ Coulomb-Effizienz für 100 Zyklen, während die Mg-S-Zelle mit einem reinen Mg^{2+} -Elektrolyten ($\text{Mg}[\text{CF}_3\text{SO}_3]_2$, MgCl_2 und AlCl_3 in DME) wesentlich geringere Kapazitäten liefert. Elektrochemische Untersuchung und die *post mortem* Messungen zeigen, dass die Zugabe eines Lithiumsalzes zum Elektrolyten entscheidend für die Unterdrückung des

Polysulfid-Shuttlings, die Reduzierung des Zellwiderstands und der Überspannung durch die mögliche Bildung von MgLiS_x -Spezies ist. Außerdem zeigen die Ergebnisse der analytischen Untersuchungen wie z. B. zyklischen Voltammetrie (CV), post-mortem-Röntgenphotoelektronenspektroskopie (XPS) und Rasterelektronenmikroskopie (REM), dass die gesamte Redoxchemie in der Zelle mit dem $\text{Mg}^{2+}/\text{Li}^+$ -Hybridelektrolyten ausschließlich auf Magnesium basiert. Daher beeinträchtigt die Zugabe eines Lithiumsalzes die Sicherheit der SPAN-basierten Mg-S-Zellen nicht.

Im vierte Teil wurde ein neuartiges Konzept mit einem Gel-Polymerelektrolyten (GPE) für Mg-S/Ionen-Batterien im vierten Forschungsjahr entwickelt, der durch In-situ-Vernetzung von $\text{Li}[\text{BH}_4]$ und $\text{Mg}[\text{BH}_4]_2$ mit Poly(tetrahydrofuran) (PTHF) hergestellt werden kann. Dieses GPE zeigt hervorragende Ionenleitfähigkeiten in einem breiten Temperaturbereich und ein hervorragendes Polarisationsverhalten. Aufgrund der erfolgreichen Unterdrückung des Polysulfid-Shuttles durch das Gel zeigt das GPE nicht nur eine gute Zyklusperformance mit SPAN-Kathoden, sondern auch mit herkömmlichen Kathoden auf S_8 -Basis. Die Mg-S-Zellen schafften 140 Zyklen mit ca. 600 mAh g_s^{-1} bei fast 100 % Coulomb-Effizienz. Des Weiteren zeigt dieses GPE eine breite Kompatibilität, die nicht nur mit schwefelbasierten Kathoden, sondern auch mit interkalationsbasierten Kathoden verwendet werden kann.

Chapter 1

Introduction

Energy storage technologies, such as batteries, hydrogen storage and fuel cells, have shown great potential to replace conventional energy supply methods, such as combustion reactions, to reduce the emission of carbon dioxide (CO₂), and consequently protect the environment.^[1] Batteries, nowadays dominated by LIBs, have already shown the tendency to partially replace gasoline for portable power applications. Due to better safety, high theoretical volumetric energy density (3832 mAh cm⁻³), high earth-abundancy and low costs of magnesium metal, magnesium batteries have attracted substantial attention in the recent years as an alternative to lithium batteries. Meanwhile, sulfur, which possesses a high theoretical capacity (1672 mAh g⁻¹), non-toxicity and also earth abundancy, has intensively been applied in the field of lithium-sulfur (Li-S) batteries. The coupling of a magnesium anode with a sulfur cathode has also shown great potential due to the attractive features of both electrodes; however, Mg-S systems with good electrochemical performance have been rarely reported, mainly due to the incompatible electrolyte systems that allow reversible cycling, passivation of the anode, slow kinetics and polysulfide shuttle.

In order to improve the performance of Mg-S batteries, in this work, four novel Mg-S battery systems have been developed. This dissertation is organized as follows:

Chapter 1 gives a brief introduction on batteries and the structure of the dissertation.

Chapter 2 contains the basic theory of batteries, the state-of-the-art of the three relevant battery systems: LIBs, Li-S batteries and Mg-S batteries.

Chapter 3 introduces the main research objectives of this work.

Chapter 4 conceptualizes and presents the Mg-S batteries based on an SPAN cathode.

Chapter 5 presents a high-performance Mg-SPAN battery by utilizing a Mg²⁺/Li⁺ hybrid electrolyte system.

Chapter 6 investigates the role of a lithium salt inside of Mg-SPAN batteries in detail.

Chapter 7 conceptualizes and presents a novel gel polymer electrolyte for Mg-S and magnesium-ion batteries.

In Chapter 8 and 9, a summary of the work and an outlook for future Mg batteries are presented, respectively.

The cited references and the curriculum vitae of the author are shown in Chapter 10 and 11, respectively.

In Chapter 12, a review article by the author in the field of Mg-S batteries is attached.

The work presented in this dissertation has been partly published and presented. The following articles and patents are published within the PhD period:

Publications (including conference papers):

1. A Design Concept for Halogen-Free Mg²⁺/Li⁺ - Dual Salt-Containing Gel-Polymer-Electrolytes for Rechargeable Magnesium Batteries
P. Wang, J. Trück, J. Häcker, A. Schlosser, K. Küster, U. Starke, L. Reinders, M. R. Buchmeiser, *Energy Storage Mater.* **2022**, *49*, 509-517.
2. Lithium Titanate as Mg-Ion Insertion Anode for Mg-Ion/Sulfur Batteries Based on Sulfurated Poly(acrylonitrile)
J. Trück, P. Wang, E. Buch, J. Groos, S. Niesen, M. R. Buchmeiser, *J. Electrochem. Soc.* **2022**, *169*, 010505.
3. Performance Enhancement of Rechargeable Magnesium-Sulfur Batteries Based on a Sulfur Poly(acrylonitrile) Composite and a Lithium Salt
P. Wang, K. Küster, U. Starke, C. Liang, R. Niewa, M. R. Buchmeiser, *J. Power Sources* **2021**, *515*, 230604.
4. A Novel Modelling Approach for Metal-SPAN Batteries
S. Kezia, T. Danner, P. Wang, M. R. Buchmeiser, International Conference on Lithium-Sulfur Batteries, **2021**.

5. High-Performance Magnesium-Sulfur Batteries Based on a Sulfurated Poly(acrylonitrile) Cathode, a Borohydride Electrolyte and a High-Surface Area Magnesium Anode
P. Wang, J. Trück, S. Niesen, J. Kappler, K. Küster, U. Starke, F. Ziegler, A. Hintennach, M. R. Buchmeiser, *Batter. Supercaps* **2020**, *3*, 1239-1247.
6. Characteristics of Magnesium-Sulfur Batteries Based on a Sulfurized Poly(acrylonitrile) Composite and a Fluorinated Electrolyte
P. Wang, J. Kappler, B. Sievert, J. Häcker, K. Müller, M. R. Buchmeiser, *Electrochim. Acta.*, **2022**, *361*, 137024.
7. Rechargeable Magnesium-Sulfur Battery Technology: State of the Art and Key Challenges
P. Wang, M. R. Buchmeiser, *Adv. Funct. Mater.* **2019**, *29*, 1905248-1905275.

Patents:

1. Borate-based Gel-Polymer Electrolyte for Rechargeable Magnesium Batteries
M. R. Buchmeiser, P. Wang (University of Stuttgart), patent pending (2021)
2. Magnesium Sulfur Battery with High Discharge Capacity
P. Wang, M. R. Buchmeiser (University of Stuttgart), EP3826095A1

Chapter 2

Theory and State of the Art

2.1 Basics of Electrochemistry

A battery is an electrochemical device that converts chemical energy directly into electric energy by electrochemical redox reactions.^[2] One battery cell is composed of two electrodes: an anode and a cathode, which possess different chemical potentials. These two electrodes are connected by an electrolyte, an ionically conductive material, which provides a medium for the charge transfer (**Figure 2.1**).^[1] The electrodes, at the same time, are physically separated by a separator to avoid an internal short-circuit. When an external electronic device is connected to the electrodes, ions are transported through the electrolyte; at the same time, electrons flow from the anode to the cathode by the external circuit to keep the charge balance and power the electronic device.^[1] In rechargeable batteries, the cell can be recharged in a reversible process, when the cell is connected to a charging circuit.^[1]

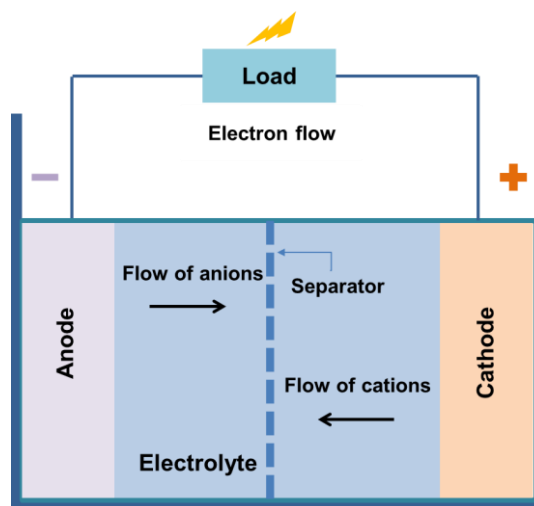


Figure 2.1: The main components of a cell: cathode, anode, separator and electrolyte. This scheme shows a discharge process.^[2]

Whenever a conversion of chemical energy into electric energy occurs, a decrease in the standard free energy of the system (ΔG^0) will spontaneously occur, which follows the *Faraday equation* (Equation 2.1):^[2]

$$\Delta G^0 = -nFE^0 \quad (2.1)$$

where n is the number of electrons; F is the Faraday constant (26.8 Ah); E^0 is the standard potential of the system (V).

If the conditions are not the standard state, the voltage E is expressed by the *Nernst equation* (Equation 2.2).

$$E = E^0 - \frac{RT}{nF} \ln \frac{a_{Ox.}}{a_{Red.}} \quad (2.2)$$

where R is the gas constant ($8.314 \text{ J}\cdot\text{mol}^{-1}\cdot\text{K}^{-1}$); a_i is the activity of the relevant species; T is the absolute temperature (K).

When discussing a battery system, some terminologies need to be identified. The energy output (**energy density**) of a battery system is commonly described based on the weight (**specific energy**, Wh/kg) or volume (Wh/L). The energy density is a function of the theoretical voltage and the capacity of a cell.^[1, 3] The **theoretical voltage** of the cell is commonly calculated by the difference between the potential of the cathode and anode. It depends on the types of the active materials in the electrodes. The **theoretical capacity** describes the total quantity of electricity involved in the electrochemical reaction. It is based on the amounts of the active materials that are applied. However, in practice, the theoretical energy density cannot be realized due to the inactive components in the cell (separators, cell body *etc.*) and other practical factors (voltage level, polarization of the electrodes, current rate *etc.*) that influence the cell performance, which are discussed below.^[4-6]

When a cell is discharged, the working voltage is lower than the **open circuit voltage** (OCV, unconditioned state of a cell, approximately the theoretical voltage) due to the IR losses caused by the cell resistance and the polarization of the electrodes.^[2, 5] Ideally, the voltage of the cell retains at the theoretical voltage during discharge until the active materials are totally consumed and the capacity is fully finished. This is accompanied by the sudden drop of the voltage. In reality, the voltage of a cell is lower than the theoretical

voltage and the voltage profile shows a sloping behavior. With a higher discharge current or a higher cell resistance, the discharge curve shows a more sloped profile. In addition, the **cut-off voltage** (end of discharge) is usually at which most of the capacity is delivered, resulting in a lowered capacity.

The cell performance is related to the applied currents. Charge and discharge rates of a cell are governed by the **C-rate**, which can be expressed by Equation 2.3.

$$C - rate = \frac{I}{C_N} \quad (2.3)$$

Where I is the charge/discharge current (A); C_N is the capacity of the battery (Ah). For example, a C-rate of 1 C means a fully charged cell should deliver 1 A for 1 hour. If the same cell discharges at 0.5 C, it should provide 500 mA for 2 hours.^[2, 7] Further on, the temperature of battery during discharge/charge, the types of discharge, as well as the cell design *etc.* all have great impact on the cell performance.^[2]

Coulombic efficiency (CE) is used to estimate the cycling life of a cell since it quantifies the reversibility of batteries.^[8] In practice, the energy output is always less than the energy put in, leading to a loss of reversibility. CE interprets the charge efficiency of the transfer of the electrons in a cell, which can be expressed by Equation 2.4.

$$Coulombic\ efficiency = \frac{total\ charge\ extracted\ from\ the\ battery}{total\ charge\ put\ into\ the\ battery} \times 100\% \quad (2.4)$$

An ideal cell reaches a CE of 100%; however, because of heating, self-discharge and parasitic reactions, the CE is always <100%.^[7]

2.2 Before Li-Ion Batteries

Since Volta's invention, the development in the battery technology is boosting due to the ever-increasing demands in electric applications. Several cell-prototypes have already been proposed and commercialized.^[9] **Figure 2.2** and **Table 2.1** summarize a brief history of the major milestones and the detailed corresponding battery chemistries during the battery development.

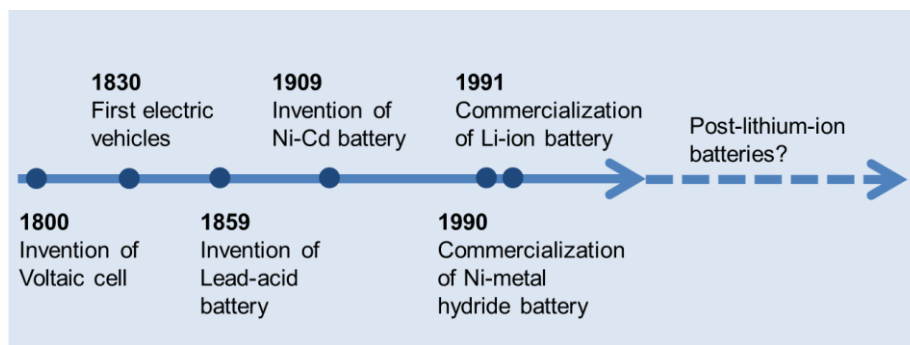


Figure 2.2: A brief history of the battery development.^[1, 9]

In 1800, Alessandro Volta invented the voltaic pile, the first electrical battery, which is composed of two plates of different metals (for example, zinc and copper) immersed in a salt solution with a closed circuit. This simple equipment was able to generate an electric current, which started a brand new research field, electrochemistry.^[1, 9]

Cell types with various electrochemical couples were then proposed, including primary cells (also known as Voltaic or Galvanic cells): Zn-MnO₂ cells; and secondary cells (also known as rechargeable cells): lead-acid cells and nickel-cadmium (Ni-Cd) cells. In 1859, lead-acid batteries were the first commercialized rechargeable batteries and are nowadays still widely used, due to the advantages of low costs on a cost-per-watt base and moderate service life without deep discharge.^[7] However, lead-acid batteries are heavy and less durable when they are deep cycled. After a deep charging/discharging, a strain and a permanent loss of capacity occurs. The ageing problem will be even severe at a higher operating temperature. Moreover, the toxicity of electrodes (lead) and the corrosion issues of the electrolytes are extremely harmful to the environment and health, which lead to the development of other types of cell systems to minimize the contamination of the environment.

Nickel-based batteries, such as Ni-Cd batteries, were then invented, showing the advantages of better safety, low-costs and long service life.^[10] The low and degrading capacity, the ‘memory effect’ and toxicity issues of Ni-Cd batteries promoted the further development of the nickel-metal hydride batteries.^[10] In the 1990s, Ni-metal hydride batteries were invented and gradually replaced Ni-Cd batteries.^[10] The positive electrode of Ni-metal hydride batteries was similar to that of Ni-Cd batteries; whereas hydrogen in the form of a metal hydride was applied on the negative side. Ni-metal hydride batteries showed much higher energy density than Ni-Cd batteries.^[10, 11] Nevertheless, the use of toxic and hazardous chemicals during the production of Ni-metal hydride batteries hindered its further development in battery technology, which encouraged the further investigation of the battery systems with the features of environmental-friendliness and higher energy density. As a consequence, LIBs then entered the battery market and are still attracting great research attentions.

Table 2.1: A summary and a comparison of the history and the state-of-the-art battery chemistries.^[1, 9, 10, 12-14]

Battery type	Cell voltage (V)	Energy density (cycle durability)	Features ^[1, 9, 10, 12-14]	Applications
Lead-acid	2.1	30-50 Wh/kg (<350 cycles)	Low cost, moderate service life ^[12] , heavy, electrolyte corrosion, environment-unfriendly	Automobile, cell phone tower,
Ni-Cd	1.2	40-60 Wh/kg (~2000 cycles)	Broad temperature range, toxic (Cd), severe self-discharge, memory effect	Aircraft, emergency medical equipment, power tools
Ni-metal hydride	1.2	60-120 Wh/kg (~180-2000 cycles)	Considered non-toxic, self-discharge issues	Hybrid cars, consumer electronics
Lithium-ion batteries	3.8	100-265 Wh/kg (~400-1200 cycles)	Fire hazard, voltage limits, environmental impacts	Portable electronics, electric vehicles

2.3 Li-Ion Batteries

2.3.1 An Overview

The research on LIBs started in 1980 by *Goodenough et al.*^[15] They reported a new type of cathode material, Li_xCoO_2 , prepared by electrochemical extraction of lithium from lithium cobalt oxide (LCO; LiCoO_2).^[15] The use of the cathode material together with a lithium metal as the anode allowed a high OCV and a high energy density^[15], which opened an avenue for a new area of electrochemistry. Two years later, *Yazami et al.*^[16] developed a type of anode material using lithium electrochemically intercalated into graphite instead of lithium metal, to avoid the dendritic electrodeposition. At the same time, the intercalation of lithium into graphite allowed a relatively high current density. This research provided the scientific basis of the application of graphite as the anode material, which is still one of the standard anodes in today's LIBs. A prototype of the early-stage LIBs was then formed using LCO as cathode and lithium intercalated in graphite as anode.

In 1991, LIBs were commercialized by *SONY*.^[13, 15, 17, 18] The commercialized LIB was composed of “soft carbon” as the anode, LCO as the cathode and a carbonate ester-based solution as the electrolyte.^[19] The commercialization of LIBs significantly promoted battery applications in portable devices due to their doubled energy density compared to Ni-Cd and Ni-metal hydride batteries. The further commercialization and academic progress on LIBs did not stop afterwards. Researchers put great effort into the investigation of better LIBs with reduced weight and size, increased cycle durability, lowered costs and better safety.^[19]

Nowadays, LIBs are not only applied in the small portable electronics, such as cell phones, computers, but also in electric vehicles (EVs).^[20] One of the main current challenges that the electric vehicles are facing, is the relatively long charging time.^[21] Refueling a combustion engine-powered car (500-800 km) in a gas station takes 5 minutes, which is reasonable to let the customers expect a fast recharging of EVs.^[22] To date, the Tesla Model 3 (with a 76 kWh battery) needs about 30 minutes to reach the 80% state of charge (SOC) with a charging power of 250 kW; the Porsche Taycan (with a 93.4 kWh battery) takes 23 mins to charge to 80% SOC with a charging power of 270 kW. The charging speed for refueling a car is still much slower than the traditional routine.^[22] The US Advanced

Battery Consortium (USABC) therefore listed a target for electric vehicles: charging 80% SOC in 15 minutes. The current state-of-the-art electric vehicles apparently still do not meet these requirements.^[22]

Another major challenge for LIBs is the limited safety performance.^[23-26] Several fire accidents and explosions have been reported due to the burning of the LIBs, which are not desired and will greatly reduce the reputations and potential markets.^[26-28] The reasons causing a fire accident in batteries are predominantly the internal battery chemistry (such as the flammable electrolytes in the LIBs) and the working environment. In addition, fire accidents are always accompanied by a continuous heat and gas generation, which further lead to the combustion of combustible materials, resulting in more severe accidents.^[29-31] Therefore, understanding the cell chemistry of LIBs is crucial to further improve the cell chemistry and prevent undesirable accidents. In the following chapters, principles, applied electrodes and electrolytes for LIBs are discussed.

2.3.2 Principles of Lithium-Ion Batteries

Similar to standard battery system, LIBs are composed of a cathode, an anode, an electrolyte and a separator.^[20] **Figure 2.3** shows a scheme of the discharging process of a typical LIB. In this example, the LiCoO_2 and graphite were used as cathode and anode material, respectively, for the illustration.

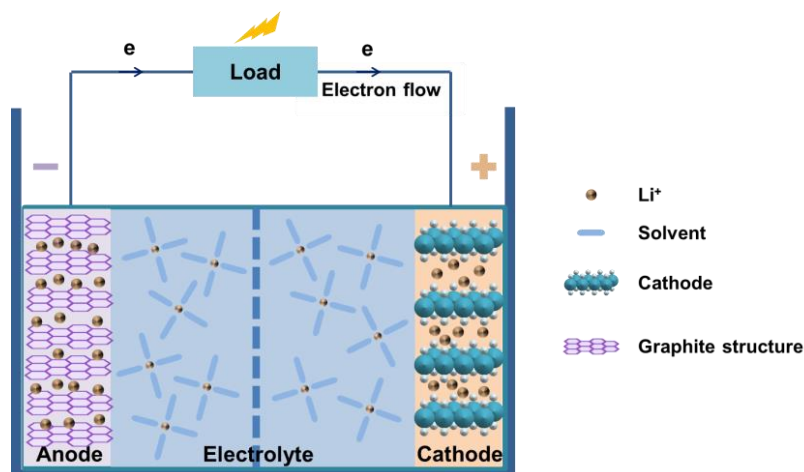
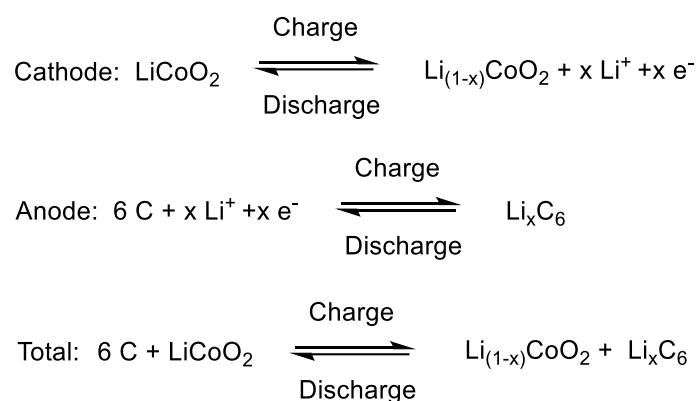


Figure 2.3: Illustration of a typical lithium-ion battery (discharge process).

During discharge, Li^+ ions de-intercalate from the graphite anode and diffuse through the electrolyte and intercalate into the cathode. At the same time, the electrons move in the opposite direction in the external circuit to generate electricity. During charging, Li^+ ions move in a different direction: de-intercalate from the cathode, move through the electrolyte and intercalate into the graphite. The individual reactions are summarized as follows:



2.3.3 Cathode and Anode Materials

According to Argonne National Laboratory Battery Performance and Cost Model, in a typical battery system (including cathode, anode, current collector, separator, *etc.*), the costs for the electrode materials are *ca.* 44%, of which *ca.* 30% are for the cathode materials and *ca.* 14% are for the anode materials.^[32] The price of the electrodes is almost half of the total cell costs, which underlines the dominant impact of the electrode materials in the cells. Therefore, it is crucial to understand and discuss the development of electrodes in the current LIBs.

Cathode Materials

The successful commercialization of LCO-based cathodes did not stop further developments and investigations of novel and promising cathodes for LIBs due to some limitations of the LCO cathodes. The drawbacks of the commercialized layered LCO cathodes, such as the low energy density (up to 274 mAh g^{-1}), degradation over cycling and the low availability of cobalt, result in the unsuitability of LIBs for stationary energy storage applications and transportation, which lead to an evolution of novel cathode materials for LIBs.^[33-35]

Several categories of cathode materials have been developed: i) olivine LiMPO_4 ($M = \text{Fe, Co, Ni, Mn, etc.}$); ii) spinel LiM_2O_4 ($M = \text{Ni, Mn, etc., LMO}$); iii) layered lithiated transition metal oxide LiMO_2 ($M = \text{Ni, Co, Mn, etc.}$) and iv) layered Li-rich oxides $x\text{Li}_2\text{MnO}_3 \cdot (1-x)\text{LiMO}_2$ ($M = \text{Ni, Co, Mn, etc.}$).^[32, 36, 37] **Table 2.2** summarizes the most typical cathode materials for LIBs. For a clearer observation, the crystal structures of the cathodes of each category are illustrated in **Figure 2.4a**. Since voltage profiles are an important parameter to characterize a cathode material, **Figure 2.4b** shows the voltage profiles of typical cathode materials.^[18]

Table 2.2: Summary of typical cathode materials for LIBs and their features.^[38]

Structure; category	Cathodes	Approx. working potential vs. Li/Li^+ (V) ^[38]	Specific capacity, (mAh g^{-1}) ^[38]
Layered	LiCoO_2 (LCO)	3.7	274
Olivine; i	LiFePO_4 (LFP)	3.5	140
Olivine; i	LiMnPO_4	4.1	170
Olivine; i	LiCoPO_4	4.8	167
Olivine; i	LiNiPO_4	5.2	170
Spinel; ii	LiMn_2O_4	4.0	148
Layered; iii	LiMnO_2	4.0	285
Layered; iii	$\text{LiNi}_{1-x-y}\text{Co}_x\text{Mn}_y\text{O}_2$, (NMC)	4.5	200

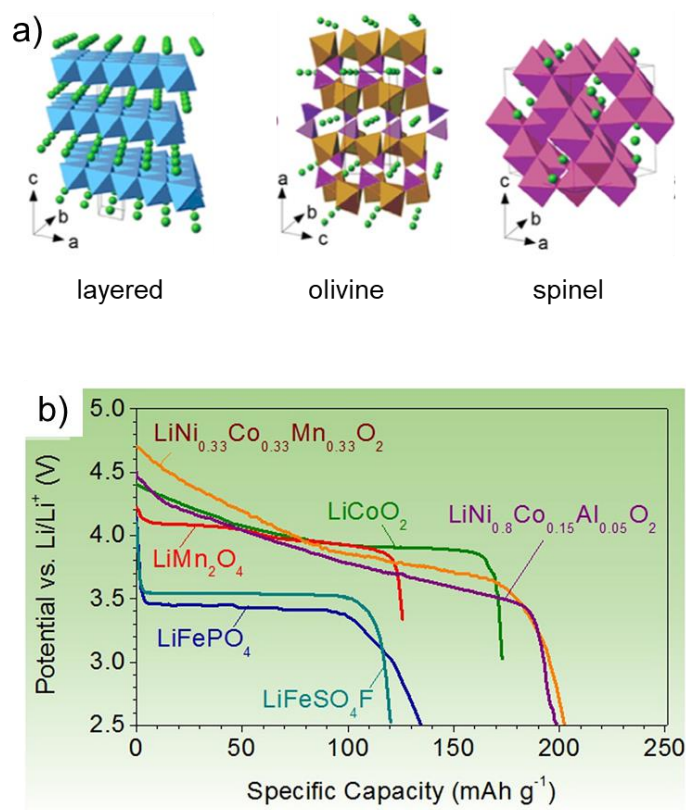


Figure 2.4: a) Three typical crystal structures of cathodes for LIBs; b) typical discharge profiles of some intercalation cathodes.^[18, 38] Reproduced with permission from ref.^[18]. Copyright (2015). Elsevier.

Olivine LiFePO_4 (LFP), one typical cathode material in the LiMPO_4 compounds group, has been commercialized due to its low cost and excellent cycling performance. The LFP cathodes typically show a long and clear plateau at *ca.* 3.5 V (*vs.* Li/Li^+) and a specific capacity of *ca.* 140 mAh g^{-1} (**Figure 2.4b**). However, due to the extremely low electric conductivity of LFP ($10^{-10} \sim 10^{-5} \text{ S cm}^{-1}$ at room temperature), additional processes are necessary in the preparation of LFP, such as the reduction of the particle size and mixing with conductive carbon. One of the main desired features of the cathode materials are the higher operating potential and, consequently, a higher energy density. In the same category, LiMPO_4 ($M = \text{Co}, \text{Ni}, \text{Mn}$) cathodes show higher working potentials (for example, 5.2 V *vs.* Li/Li^+ for LiNiPO_4) than the LFP-based cathodes (3.5 V *vs.* Li/Li^+), leading to a higher theoretical energy density.^[38, 39] Nonetheless, the high working voltages, on the other hand, reduce their compatibility with established electrolyte systems, resulting in a less stable cell system.^[40] Take spinel LiMn_2O_4 as another example, which possesses a working potential of around 4.1 V. This material has also been intensively researched for EVs due to low costs, earth abundance, high safety and environmental-friendliness.^[41-43] However, LIBs based on

these cathodes suffer from severe capacity decay at relatively high temperatures ($> 60\text{ }^{\circ}\text{C}$) due to the dissolution of manganese from LiMn_2O_4 into the liquid electrolyte.^[41] Various attempts, such as coating with inorganic materials (Al_2O_3 , SiO_2) as protective layer on LiMn_2O_4 have been made to avoid a direct contact of the cathode with the electrolyte.^[44, 45] However, it is very important to control the thickness of the coating in order to balance the protective effect and the electrical conductivity.^[46] These extra procedures certainly cause some additional efforts and costs in the processing routines.

Due to the toxicity and the high costs of Co metal in LCO, researchers also tried to partially/fully substitute Co by more environmental-friendly metals, like Ni and Mn. Consequently, the Li-Co-Ni-Mn-O layered transition metal compounds ($\text{LiNi}_{1-x-y}\text{Co}_x\text{Mn}_y\text{O}_2$), so called NMC-type cathodes, have been intensively investigated in the last several decades.^[47-49] In general, NMC-type cathodes show higher working potentials than LFP cathodes, leading to higher specific capacities. At the same time, the voltage profiles are sloped instead of the long plateau of LFP cathodes (**Figure 2.4b**). The different stoichiometric compositions of NMC-type cathodes based on Co, Ni and Mn greatly influence the properties of the final NMC, such as structural and chemical stability and cell capacity. In NMC-type cathodes, Ni shows the features of high specific energy but poor stability; whereas Mn can lower the internal resistance but has a low specific energy. Researchers are trying to increase the Ni content rather than the Co content to achieve higher energy density, better stability and lower costs.^[13, 50]

Anode Materials

To fulfill the requirements of (hybrid) electrical vehicles (HEVs), a high-performance anode material that has high reversible capacity, long cycle life, low costs and high rate capability, is of great importance. Pure lithium metal is known to be the best candidate to reach the highest specific capacity in an HEV application due to the absence of any dead weight. However, lithium deposits in form of dendrites, which is very likely causing internal short circuits, greatly reducing the safety characteristics. As an alternative, carbon materials, such as graphite^[51], graphene^[52, 53], carbon nanotubes^[54] and carbon nanofibers^[55], have then been researched as anode materials to reversibility hold lithium ions for LIBs.

Graphite is nowadays the most widely applied anode material in commercial LIBs due to its low costs, low working voltages and good cycle stability.^[51] Nonetheless, the allowance of the intercalation of one lithium atom into six carbon atoms (LiC_6) limits the capacity of graphite (372 mAh g^{-1}). On the other hand, the slow diffusion rate of lithium into carbon materials ($10^{-12} \sim 10^{-6} \text{ cm}^2 \text{ s}^{-1}$) limits the power density.^[51] Due to these concerns, alternative new-generation anode materials, such as intercalation anodes $\text{Li}_4\text{Ti}_5\text{O}_{12}$ (LTO), alloy anodes (Si-based oxides), and conversion anodes (metal sulfides, nitrides) that possess high capacities and power densities have been intensively investigated in the past decades.

Among all the potential anodes, silicon (Si) is considered the most promising anode to replace graphite due to its high gravimetric capacity (4200 mAh g^{-1} , lithiated to $\text{Li}_{4.4}\text{Si}$), high volumetric capacity (9786 mAh cm^{-3}), acceptable discharge voltage (0.4 V), high earth-abundancy and low costs. The major issues regarding Si are its poor intrinsic electronic conductivity, the huge volume expansion and the generated stress upon lithiation and de-lithiation, which consequently leads to the deterioration of the electrode structure and the disconnection between electrode materials and current collectors. The anodes will finally collapse and the cell will become irreversible. To overcome these issues, strategies including structural modifications (Si nanoparticles, Si nanowire, *etc.*), compositional modifications (with different carbon species, metal oxides *etc.*) and hierarchical structure modifications (core-shell, yolk-shell *etc.*), have been intensively investigated.^[56]

2.3.4 Electrolyte Systems

The electrolyte is also one of the most crucial components inside of a battery cell, since it serves as a connection between anode and cathode materials, to allow free diffusion of ions during charging and discharging of the cell.^[57, 58] Important features regarding electrolytes to ensure a high performance lithium-ion cell include high stability in a wide electrochemical window, a wide temperature usability, high safety characteristics, and the same important, appropriate reaction with the electrodes to form a homogeneous and efficient solid electrolyte interface (SEI) layer.^[57, 58] The research on the electrolyte systems starts from a conventional liquid electrolyte soaked by ceramic or polymeric separators, which nowadays gradually changes direction to solid-state electrolytes, which allow for a higher energy density and also possess better safety characteristics.^[59-61]

Liquid electrolyte systems

Conventional liquid electrolytes for current commercialized LIBs are based on LiPF_6 dissolved in a mixture of alkyl carbonates, such as ethylene carbonate (EC), dimethyl carbonate (DMC), diethyl carbonate (DEC) and ethyl-methyl carbonate (EMC). The chemical structures of the widely used conductive salts, solvents and additives in the current state-of-the-art electrolytes for LIBs are summarized in **Figure 2.5**. Generally, the use of EC is considered necessary to ensure the formation of an SEI layer on the negative electrode.^[57] The conductive salt LiPF_6 outperforms other commercialized lithium conductive salts, such as LiClO_4 , LiBF_4 , LiSO_3CF_3 due to better safety characteristics, less passivation on the anodes and better conductivity, respectively. Nonetheless, commercialized LIBs are still limited in terms of cell performance at elevated temperatures, safety characteristics and consequently, stable long-term cycling. The use of various additives in the electrolyte is considered an efficient way to overcome these limitations in existing LIBs.^[62]

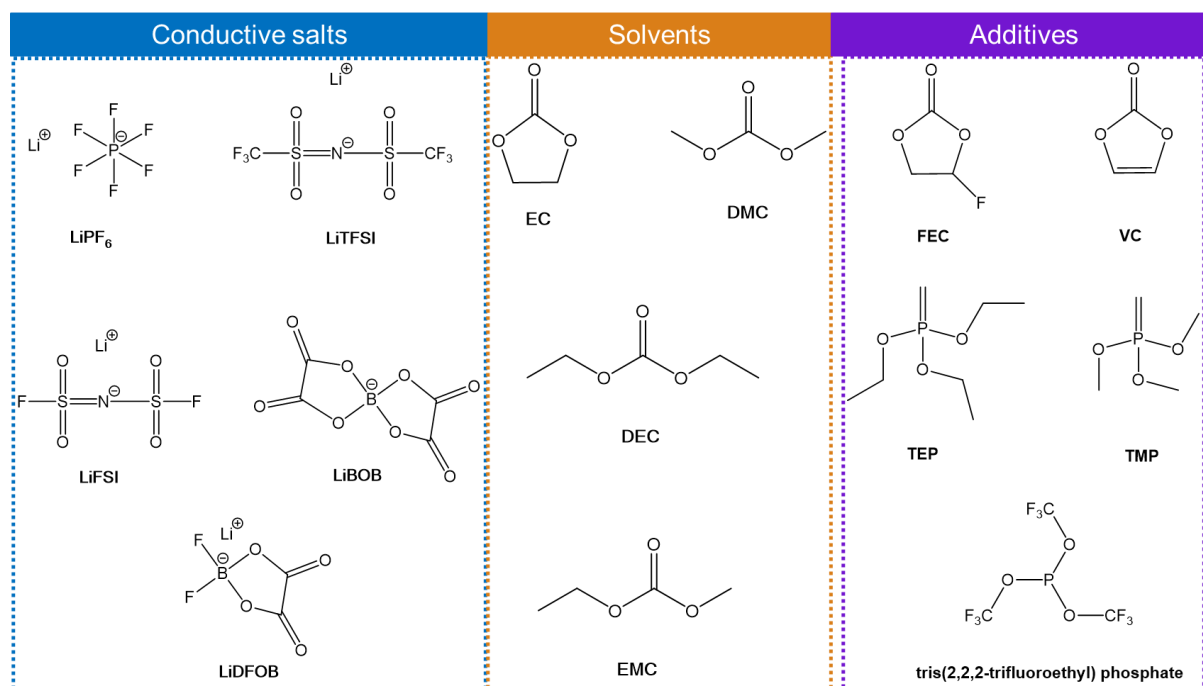


Figure 2.5: Chemical structures of the used electrolyte systems: conductive salts, solvents and selected additives in current LIBs.^[62]

One of the major issues in LIBs, especially in HEV applications, are safety concerns, because the applied solvents, as introduced above (such as DEC, DMC, EC), are volatile

and flammable organic solvents, which greatly reduce the safety characteristics of the entire battery systems.^[57]

Many attempts to suppress the flammability of the electrolytes have been made by adding various additives, such as phosphate-based flame-retardant additives, including trimethyl phosphate (TMP), triethyl phosphate (TEP), ionic liquids (ILs) and fluorinated solvents.^[58, 63] It was found that the flame-retardancy can be improved by using the above-mentioned phosphate-based flame retardants, however, on the expense of the reductive stability of the graphite anode.^[64] Further attempts, including the synthesis of a series of partially fluorinated alkyl phosphates, such as tris(2,2,2-trifluoroethyl) phosphate, can not only improve the flame-retardancy, but also increase the reductive stability on the anode side.^[65-67] In addition, strategies, such as increasing the alkyl chain length^[68], generating cyclic phosphate^[69] or partially replacing the alkyl group with the aryl(phenyl) group^[68, 70], are successful with regards to an improved flame retardancy and anode stability. Another method to improve the safety characteristic of a cell is replacing conventional flammable liquid electrolytes by solid-state electrolytes, which are discussed below.

Solid-state electrolyte systems

Nowadays, the application of a solid-state electrolyte (SSE) into a LIB is considered to lead to the most promising next generation batteries.^[59] The use of a solid electrolyte is expected to significantly improve energy density, electrode stability and safety of a cell system.^[63] With the application of a SSE, a bipolar stacking, with the anode of one cell and the cathode of the next cell using the same current collector, can be achieved. This will significantly improve the quantity of energy stored per mass/volume in an electrical device, *i.e.* energy density.

SSEs are generally composed of either a polymer electrolyte or an inorganic solid electrolyte (ISE).^[59, 71, 72] Polymer electrolytes can then be sub-categorized into solid polymer electrolytes (SPEs) and gel polymer electrolytes (GPEs).^[72] It needs to be mentioned that a small amount of organic liquid is immobilized inside the polymer network in GPEs, hence safety issues cannot be fundamentally solved by GPEs due to the existence of the remaining solvent inside of LIBs.^[73] Therefore, in a strict categorization method, the all-solid-state electrolytes only include ISEs and SPEs.

To date, two major groups of ISEs exist: oxide-based electrolytes (γ - Li_3PO_4 type oxysalts, $\text{LiTi}_2(\text{PO}_4)_3$, *etc.*) and sulfide-based electrolytes (sulfide oxide: $0.6\text{Li}_2\text{S}-0.4\text{SiS}_2$, $\text{Li}_{10}\text{GeP}_2\text{S}_{12}$, *etc.*).^[71, 74] Actually, back to 1994, *Panasonic* (called as *Matsushita Battery Industrial Co. Ltd.* before) first filed a patent on the applicability of sulfide-based all solid state batteries (ASSBs).^[75] One of the examples in this patent is an ISE based on Li_2S and SiS_2 , with a doping by lithium orthosilicate (Li_4SiO_4). After tuning the composition, the ionic conductivity of the $0.15\text{Li}_4\text{SiO}_4-0.5\text{Li}_2\text{S}-0.35\text{SiS}_2$ reached $10^{-3} \text{ S cm}^{-1}$ at room temperature.^[75]

Apart from a better safety and higher energy density, ISEs also allow the operation of batteries at low or high temperatures; for example, from -50 to $200 \text{ }^\circ\text{C}$, where traditional liquid electrolytes already freeze or decompose.^[71, 74] Although ISEs have been widely researched, they are still not commercialized due to several remaining challenges.^[76, 77] The low ionic conductivity of ISEs at room temperature is considered one of the most critical issues. The ionic conductivity of ISEs is in general lower than the use of organic liquid electrolytes.^[78] Another limitation is the possible dendrite growth of lithium into the ISEs, leading to internal short circuits.^[76, 79] *Porz et al.*^[76] tested four types of ISEs (amorphous 70/30 mol% $\text{Li}_2\text{S}-\text{P}_2\text{S}_5$, polycrystalline β - Li_3PS_4 , polycrystalline and single-crystalline $\text{Li}_6\text{La}_3\text{ZrTaO}_{12}$ garnet) by galvanostatic electrodeposition together with *in-situ* microscopies. They found that the plating of lithium will penetrate into the cracks on the current collector if the applied current density is above a critical value, which consequently lead to the short circuit.^[76] Another challenge is the formation of a resistive layer on the interface between ISE and electrodes, caused by the major differences of the interfacial composition and the structure between electrolytes and electrodes.^[71] Last but not least, the physical contact between the ISEs and the electrodes is poor, especially when the volume change of the electrodes happens, which highly influences the ionic diffusion.^[71, 77, 80]

In contrast, SPEs possess advantages over ISEs in the aspects of better flexibility, easier processability, better compatibility and contact between electrodes and electrolytes.^[73, 81, 82] The SPEs are usually prepared by mixing a polymer solution and conductive salt solution, followed by the removal of the organic liquid solvent.^[73, 83] To date, SPEs have been developed based on several polymeric matrixes, such as poly(ethylene oxide) (PEO), polycarbonate and polysiloxane.^[73] An ideal SPE should possess a low glass transition

temperature (T_g), to ensure the rubbery state of the polymer matrix at room temperature, and a similar ion conductivity as the liquid electrolytes. The most conventional PEO-LiX system shows a low ionic conductivity at room temperature ($\sim 10^{-7} \text{ S cm}^{-1}$). Meyer *et al.* [60] pointed out that the mobility of Li cations highly depends on the segmental motions of PEO. These segmental motions are believed to be significantly reduced with a decreasing temperature or an increasing crystallinity. On the other hand, the continuous movements of the amorphous chain segments above T_g is vital for the ion transport. Hence, increasing the amorphous region in PEO is considered important. Several strategies have been investigated, such as developing single-ion solid polymer electrolytes, copolymerization and crosslinking, to optimize the structure of the PEO polymer matrix. Polysiloxane has been well investigated due to the low T_g (such as, poly(dimethyl) siloxane: $-123 \text{ }^\circ\text{C}$), high conductivity ($\sim 10^{-4} - 10^{-5} \text{ S cm}^{-1}$) high flexibility, high chemical stability and high free volumes. The research on this polymer focuses on the improvement of the mechanical strength by crosslinking.[73]

Further on, the addition of inorganic fillers to SPEs, resulting in composite polymer electrolytes (CPEs), has been considered as a comprehensive strategy to improve the overall properties of the solid electrolytes.[73] The added fillers can be categorized into two groups: active and passive fillers, categorized by their ionic conductivities. Active fillers are in general the ISEs, such as NSICON (sodium super ionic conductor) and LISICON (lithium super ionic conductor). Passive fillers include oxide ceramics, such as Al_2O_3 , TiO_2 *etc.*, and natural clays.[59] The incorporation of nanofillers is expected to improve the electrochemical properties, mainly ionic conductivity, and also the mechanical strength of the solid electrolyte. For example, Wieczorek *et al.*[84] discovered that the addition of alumina powders (Al_2O_3) into PEO-based SPE can increase the ionic conductivity by at least one order of magnitude. However, up to now, the developed CPEs still show insufficient ionic conductivity ($\sim 10^{-4} \text{ S cm}^{-1}$) with respect to the requirements for any practical applications ($> 10^{-4} \text{ S cm}^{-1}$). The interactions between the SPEs and the inorganic fillers also need to be further understood.[59]

2.4 Lithium-Sulfur Batteries

Beyond the horizons of LIBs, the exploration of new materials for an increased energy density of a cell never stops. For example, sulfur-based cathode materials have been intensively investigated in the last three decades due to their potential high theoretical capacity compared to conventional cathodes for LIBs.^[59, 85, 86] Assuming full discharge cases, an elemental sulfur based-cathode is expected to deliver a specific discharge capacity of 1675 mAh g⁻¹ and an energy density of 2600 Wh kg⁻¹, which is 3-5 times higher than the current state-of-the-art LIBs.^[14, 85, 87] On the other hand, sulfur is non-toxic and earth-abundant. These attractive features have encouraged intensive investigations of rechargeable lithium-sulfur (Li-S) batteries, including the development of novel sulfur cathodes, efficient electrolyte systems and also novel cell designs.^[14] Li-S batteries are also believed to be one of the most promising next-generation high-energy density batteries.

Research on Li-S batteries over the decades resulted in significant progress in this technology. A deeper understanding of the Li-S chemistry and the fundamental mechanisms has also been achieved through several *in-situ* characterization methods.^[14, 85, 87] However, some tremendous challenges due to the nature of the sulfur materials slow down their further practical applications.^[88-93] For example, the reduction of the sulfur-based cathodes into the final discharge product, lithium sulfide (Li₂S), is accompanied by a *ca.* 80% volume change, which results in cracks in the electrodes.^[14] Another well-known challenge is the “polysulfide-shuttle”, especially in elemental sulfur-based cathodes.^[90, 94] The formed sulfur intermediates tend to dissolve in electrolytes and gradually migrate to the anode side, leading to a loss of active material and the corrosion of the anode. Consequently, the “polysulfide shuttle” results in a capacity decay and reduced cycle life. Further on, sulfur is an insulator, which indicates that a certain amount of conductive material, such as carbon black, needs to be incorporated into the cathode. This will on the other hand reduce the loading of the active materials.^[14, 85, 87, 95]

In this section, the basic electrochemical principles of Li-S cells and state-of-the-art cathode materials will be detailed discussed. In addition, a brief introduction of the nowadays applied electrolyte systems is given.

2.4.1 Principles of Lithium-Sulfur Batteries

A Li-S cell, an electrochemical energy storage system, is composed of a sulfur-based cathode, a lithium anode and an electrolyte soaked in a separator, as is illustrated in **Figure 2.6**.^[14, 85, 87, 95] In the case of all-solid-state Li-S batteries, the separator can be omitted, *i.e.* replaced solely by a solid electrolyte.

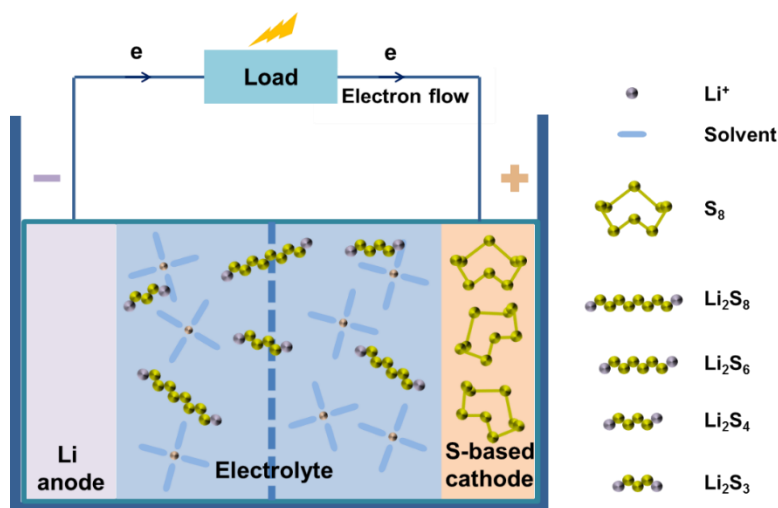


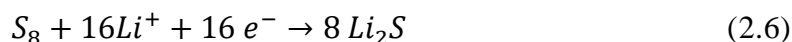
Figure 2.6: Schematic illustration of a lithium-sulfur cell based on elemental sulfur.

In a Li-S battery, the electrical energy is stored inside the sulfur cathode. Since sulfur is typically in the charged state, the operation of the cell begins with the discharge process.^[14] Upon discharging, the lithium anode is oxidized to produce lithium ions and electrons (**Equation 2.5**). The lithium ions migrate through the electrolyte to the cathode; whereas the electrons move through the external electrical circuit to generate electricity. At the same time, the sulfur cathode is reduced. It accepts the electrons and the lithium ions, to form Li_2S as the final product (**Equation 2.6**). The overall reaction during discharge is shown in **Equation 2.7**. The charge process is accompanied by the reversed reaction.^[14]

Reaction on the anode side during discharge (oxidation):



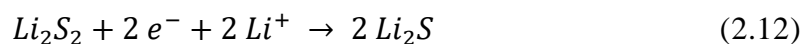
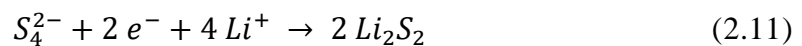
Reaction on the cathode side during discharge (reduction):



Overall reaction:



During the entire discharge process, several sulfur species are stepwise formed, although the final reduction product is Li_2S . Using an elemental sulfur-based cathode, the stepwise reduction reactions are listed from **Equation 2.8** to **Equation 2.12**. The discharge process starts from the ring-opening of cyclo- S_8 , resulting in the formation of a series of long-chain polysulfides, S_8^{2-} , S_6^{2-} and S_4^{2-} , which are generally considered to be soluble in the electrolyte. At the final steps of the reduction, the short-chain polysulfides, Li_2S_2 and Li_2S , which are insoluble in the electrolyte, are formed.^[14, 95, 96] Upon charging, the entire reactions reverse back.



Cell voltage is an important parameter to monitor the stages of the redox processes. **Figure 2.7** shows a typical voltage profile of the discharge and charge processes of a Li-S cell.

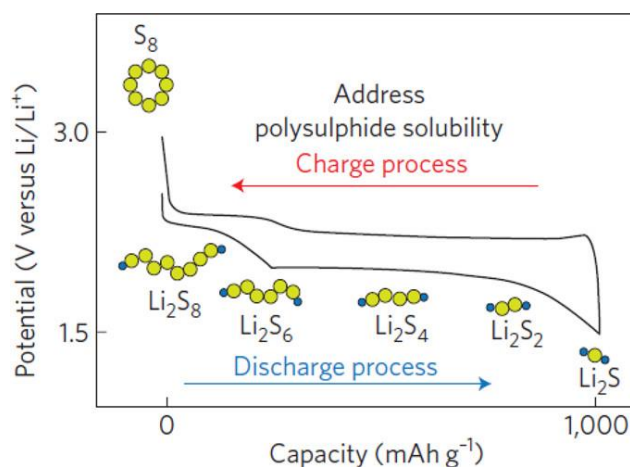


Figure 2.7: Typical voltage profile of a Li- S_8 battery in an ether-based liquid electrolyte during discharge and charge processes.^[97] Reprinted with permission from Ref.^[97]. Copyright 2012 Macmillan Publishers Ltd.

During the discharge process, after an initial sharp voltage drop, two distinct voltage plateaus at *ca.* 2.3 V and *ca.* 2.1 V can be detected. These two plateaus correspond to the reduction of S₈ to Li₂S₄, and the reduction of Li₂S₄ to short-order lithium sulfides (Li₂S), respectively. In the following recharge process, in an ideal case, the formed lithium sulfides stepwise re-oxidize back to the S₈, thereby generating a reversible cycle.^[14, 95, 96, 98]

2.4.2 Electrolyte Systems

The main challenge in the development of electrolytes for Li-S batteries is that the formed lithium polysulfides tend to react with common electrolyte solvents, such as esters and phosphates.^[85, 99] Therefore, the selection of the solvents for Li-S batteries is limited to ether-based and carbonate-based electrolytes, such as 1,2-dimethoxyethane (DME), 1,2-dioxolane (DOL), EC, DEC, *etc.*^[85, 100]

A typical ether-based electrolyte for Li-S batteries is composed of 1 M lithium bis-trifluoromethanesulfonimide (LiTFSI) in DME/DOL, with LiNO₃ as an additive.^[101, 102] The main advantages of ether-based electrolytes are their high stability towards polysulfide species, low viscosity and good contact between electrolytes and electrodes.^[85, 99, 103] The combination of DME and DOL, as a binary solvent, is considered to have synergistic effects that improve the cell performance. On the one hand, DOL is able to assist the formation of a stable SEI layer on the Li metal anode, for a better protection from the corrosive polysulfides.^[104] On the other hand, DME has a high solubility for polysulfides, which improves the reaction kinetics at the cathodes.^[104] Ether-based solvents are not limited to DME and DOL, other types of the ether solvents, such as tetraethylene glycol dimethyl ether (tetraglyme), diethylene glycol dimethyl ether (diglyme), tetrahydrofuran (THF), have also been investigated, with respect to their viscosities, polysulfides solubility, SEI layer formation, *etc.*^[105]

A small amount of additives is usually added to the electrolyte to protect the lithium anode. LiNO₃ is one of the most common additives for ether-based electrolytes. *Aurbach et al.*^[106] investigated the functions of LiNO₃. It was found that a surface film, which is composed of Li_xNO_y, is formed on the lithium anode, which protects the lithium anode from further corrosion by the polysulfides. Nonetheless, it has also been reported that the lower voltage

window cannot exceed 1.6 V in a LiNO₃-containing electrolyte, due to decomposition issues of LiNO₃.^[107]

Carbonate-based electrolytes have initially been considered unsuitable for Li-S batteries, due to the side reactions between polysulfide anions and carbonates.^[102] The irreversible degradation of carbonates in the first cycle and the loss of sulfur result in a sharp capacity decay.^[100] However, *Xin et al*^[108] have successfully addressed this issue by controlling the chain lengths of sulfur molecules to S₂₋₄, and at the same time, by confining S₂₋₄ in a conductive microporous carbon matrix. With this invention, Li-S cells were successfully cycled for 200 cycles with > 1000 mAh g_s⁻¹ in a carbonate-based electrolyte (1 M LiPF₆ in EC/DMC (1/1 wt%)).^[108]

It has also been found that cathodes with sulfur covalently bound to polymeric composites are compatible with carbonate-based electrolytes.^[109-114] One typical example is sulfur poly(acrylonitrile) composite (SPAN), in which the sulfur chain length is <8. During reduction, the Li-SPAN cells undergo a solid-to-solid single-phase reaction. The formed lithium (poly)sulfides (Li₂S₂ and Li₂S) are insoluble in carbonate-based electrolytes; hence they do not react with them. Consequently, these cathodes are compatible with carbonate electrolytes.^[109-114] Due to the attractive characteristics of SPAN, the corresponding structures and properties will be discussed in detail in **Chapter 2.4.3**. One limiting factor of either S₂₋₄ confined in microporous carbon or sulfur covalently bound to polymer matrix is the limited sulfur loading in the active material. Nevertheless, these materials are considered as one of the benchmarks in Li-S batteries, which not only widen the compatibility of commercialized carbonate-based electrolytes, but also significantly improve cell performance.

Despite the dominated usage of organic liquid electrolytes in Li-S batteries, research on alternatives, such as solid-state electrolytes, is considered necessary for solving remaining issues, including polysulfide shuttle.^[115, 116] Actually, the concepts for solid-state electrolytes for Li-S batteries are similar to those for LIBs. For example, in the field of polymer-based solid electrolytes, despite the intrinsic low conductivity, PEO-based electrolytes are intensively investigated. Various inorganic fillers have also been incorporated to improve the overall properties of the electrolytes.

2.4.3 Cathode Materials

In a Li-S cell, the development of cathode materials is challenging, but important, since the efficiency of a cathode material directly influences the performance of the cell. A Li-S cell is generally considered performing well when the following three aspects are fulfilled at the same time:

- i) the loading of the active cathode material is > 70 wt%;
- ii) the specific capacity is > 1200 mAh g_s⁻¹;
- iii) the capacity loss is $< 10\%$ over 100 cycles.^[96]

A series of cathode materials have been developed and characterized, which can be generally categorized into two groups, sulfur-carbon composite cathodes and sulfur-polymer hybrid cathodes.^[96, 98, 117-119] Research on sulfur-carbon composites has gained substantial attention since the breakthrough in highly ordered nanostructured carbon-sulfur cathodes, reported by *Ji et al* in 2009.^[120] Generally, the carbon matrix, which serves as a repository for sulfur, should possess high electrical conductivity, sufficient accessibility for the electrolyte to the active material, electrochemical affinity for sulfur and high stability to allow for volume changes during cycling.^[96] **Figure 2.8** summarizes a series of hierarchical designs of various carbon matrixes: microporous carbon^[121], porous carbon nanofibers^[122], spherical ordered mesoporous carbon nanoparticles^[96], porous hollow carbon^[96], graphene oxide sheets^[123] and hollow carbon nanofibers^[124].

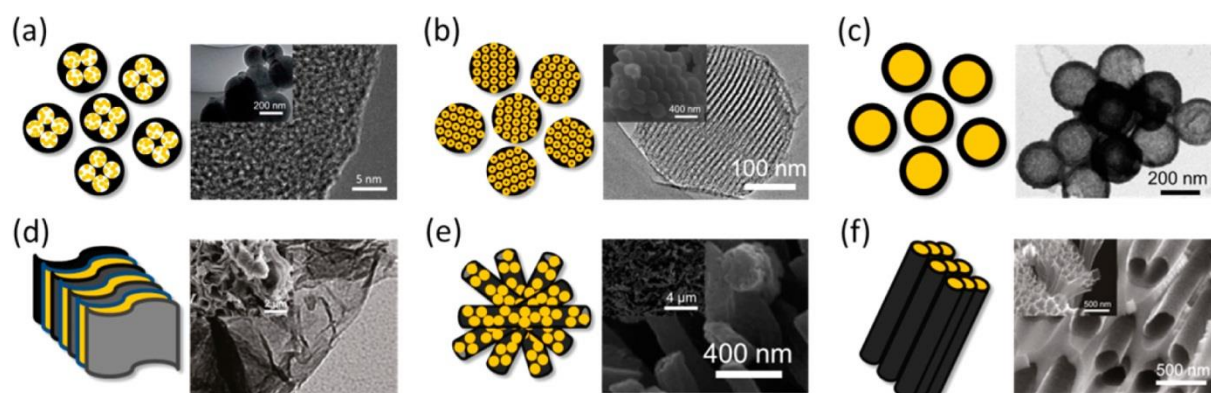


Figure 2.8: Hierarchical designs of sulfur-carbon composites: **a)** microporous carbon; **b)** spherical ordered mesoporous carbon nanoparticles; **c)** porous hollow carbon; **d)** graphene oxide sheets; **e)** porous carbon nanofibers; **f)** hollow carbon nanofibers to encapsulate the sulfur.^[96] Reprinted with permission from Ref.^[96]. Copyright 2012 American Chemical Society.

The basic concept behind these materials is that elemental sulfur physically embeds inside the porous carbon-based composites with various pore sizes. Substantial progress has been achieved in the development of these cathode materials; however, they still cannot fulfill all requirements of a high-performance Li-S cell at the same time.

Another attractive concept regarding cathode materials are binder-free composite electrodes, since it excludes the use of the toxic solvents such as N-methyl-2-pyrrolidone (NMP) during the preparation of the cathodes. At the same time, the cathode conductivity and the loading of active materials can be increased.^[125, 126] *Aurbach et al.*^[125] have developed a method to produce a binder-free composite, named as “sulfur @ activated carbon cloth” (“ACC/S”), in 2011 (**Figure 2.9a**). They employed commercially available activated carbon cloth as carbon matrix and impregnated elemental sulfur into the carbon matrix at elevated temperature (155 °C) and reduced pressure, resulting in a cathode with sulfur loading of up to 6.5 mg cm⁻².^[125] In addition, the deposition of elemental sulfur onto multiwall carbon nanotubes (MWCNTs), followed by a vacuum filtration, also leads to a free-standing binder-free cathode (**Figure 2.9b**).^[127, 128]

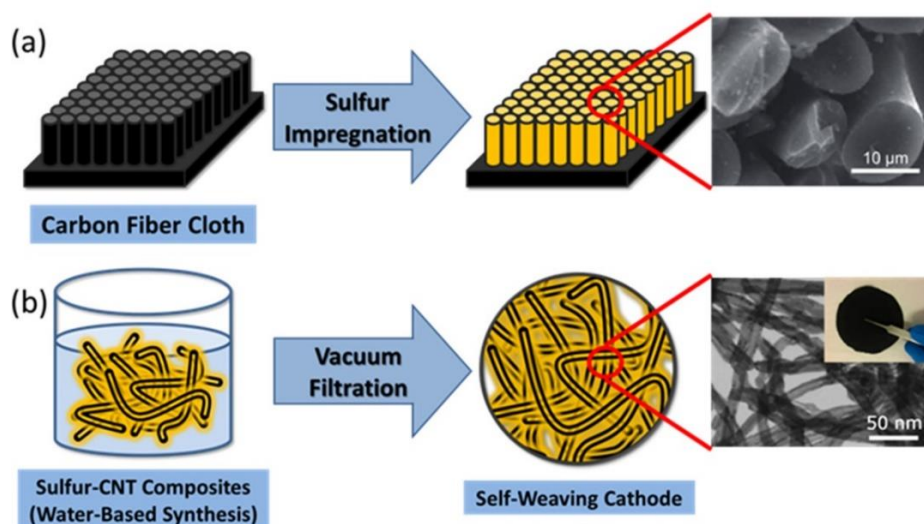
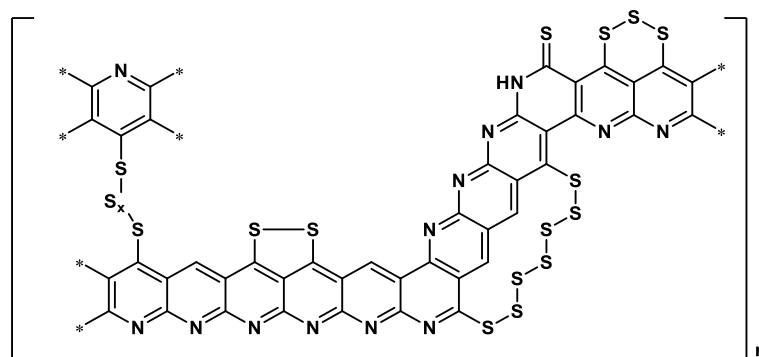


Figure 2.9: Two types of binder-free cathodes: **a)** sulfur impregnated carbon fiber cloth; **b)** self-weaving sulfur-CNT composites.^[96] Reprinted with permission from Ref.^[96]. Copyright 2012 American Chemical Society.

Apart from the sulfur-carbon composites, an alternative sulfur cathode can be achieved by covalently binding sulfur to a conductive carbon matrix, such as poly(acrylonitrile)^[110, 112-114, 129-132], polyethylene glycol^[133], polypyrrole^[134], polyaniline^[135] *etc.* These sulfurized

polymers are generally prepared by a vulcanization process, leading to a carbon matrix with covalently bound sulfur.^[136]

Among these reported sulfurized polymers, the sulfur poly(acrylonitrile) composite (SPAN) is considered a promising cathode material for Li-S batteries due to its superior cycle stability and higher specific capacity when comparing with other reported cathode materials.^[136, 137] Research on SPAN as cathode material for battery applications was started by *Wang et al.*^[110], which opened a new avenue for the research on this material. SPAN can be synthesized by the dehydrogenation of poly(acrylonitrile) (PAN), followed by cyclization through a vulcanization process, with the generation of H₂S as the side product.^[136] *Buchmeiser et al.*^[112-114, 129] identified the predominant structural features, shown in **Scheme 1**, where sulfur is covalently bound to the PAN polymer backbone, with short sulfur chains in the structure.



Scheme 1: Proposed chemical structure of the sulfur poly(acrylonitrile) (SPAN) composite ($x < 6$).^[112-114, 129]

Using SPAN as cathode material and a commercially available electrolyte, 1 M LiPF₆ in EC:DEC (1:1, v:v), Li-S cells delivered *ca.* 1200 and *ca.* 600 mAh g⁻¹ at C/4 and 4 C, respectively, in a rate capability test, as reported by *Buchmeiser et al.*^[138] The reasons behind the outstanding cycle stability of Li-S batteries are of great interest.^[139, 140] It is worldwide commonly accepted that no long-chain polysulfides form during the discharge process.^[112-114, 129] Therefore, the whole discharge mechanism is based on the “solid-solid redox mechanism”, which entails a direct reduction of sulfur in SPAN to the final reduction products, lithium sulfides.^[109, 141] Actually, this mechanism is in accordance with the unique voltage profile of SPAN-based cathode materials, in which only one sloped region

instead of two distinct plateaus can be detected.^[141] These explanations might be able to explain the successful suppression of the polysulfide shuttle.

However, some issues still remain unclear. For example, a much better cell performance has been observed in carbonate-based than in ether-based electrolytes. The reasons behind this phenomenon are still unclear due to the complex system. Also, the exact reaction mechanisms and the chemical structures are still subject of debate. At the same time, the low sulfur loading in SPAN is certainly a limitation for the future applications of this material, which requires the development of new materials with covalently bound sulfur but higher sulfur loadings.

2.5 Magnesium-Sulfur Batteries

Research on LIBs and Li-S batteries has definitely made significant progress during the past decades; nonetheless, lithium-based batteries still show safety issues due to the intrinsic chemical nature of lithium, such as the uncontrolled electrochemical deposition of lithium in a dendritic manner, which bears the potential to pierce the separators, causing short microcircuits.^[88-90] On the other hand, the formed lithium dendrites can detach from the lithium anodes, resulting in a de-lithiation and the formation of ‘dead’ lithium; which consequently leads to the ‘death’ of the cells.^[90-93]

As an alternative to lithium batteries, rechargeable magnesium batteries have gained increasing attention.^[142] Apart from the application of the intercalation cathodes in magnesium batteries, similar to Li-S batteries, sulfur cathodes have also been considered compatible with magnesium anodes. The first magnesium-sulfur (Mg-S) battery was reported by a research group from *Toyota Motor* in 2011.^[89] In this report, although the Mg-S cell was only successfully cycled for three cycles, it showed the possibility to couple a Mg anode with a sulfur cathode.^[89] At the same time, the advantages of a Mg anode together with a sulfur cathode have attracted increasing attention, leading to the acceleration of the research in this field over the last ten years.^[143]

The advantages of Mg-S batteries can be summarized as follows. First, magnesium usually plates in a non-dendritic manner, which hints towards better safety characteristics of Mg anodes compared to lithium or sodium anodes.^[144-146] Second, although Mg shows a higher reduction potential (-2.37 V *vs.* standard hydrogen electrode, SHE) than Li (-3.04 V *vs.* SHE), the divalent Mg²⁺ cation allows for the transfer of two electrons per Mg atom, which leads to a high theoretical specific capacity (2205 mAh g⁻¹).^[147] At the same time, Mg-S batteries possess a higher theoretical volumetric capacity than Li-S batteries (3832 *vs.* 2062 mAh·cm⁻³).^[144, 148] Last but not least, magnesium, the fifth-most abundant metal on earth, has substantial cost advantages over lithium.^[149] Actually, in Li-S batteries, the cost advantages of the sulfur cathode have been compromised by the limited and expensive Li metal (*ca.* 250 dollar/kg). In comparison, both electrodes in Mg-S batteries are earth-abundant and low-cost, with Mg metal only *ca.* 2.5 dollar/kg.^[146] In view of these merits, Mg-S batteries are an attractive alternative to LIBs or Li-S batteries.^[88, 150-153]

Despite these attractive advantages, substantial limitations or challenges have slowed down the development of Mg-S batteries. Apart from the common “polysulfide shuttle” issues remaining in the batteries with a sulfur-based cathode, additional problems emerged regarding the Mg anode and the electrolyte systems compared to Li batteries. These include a high overpotential during Mg plating/stripping, severe overcharge over cycling, a lack of compatible electrolyte systems and low sulfur utilization of the cathode. These all lead to poor electrochemical behavior and hinder future developments.^[144, 152, 154, 155] Also, these encountered obstacles deviate largely from those in Li-S batteries. Therefore, the development in Mg-S batteries is considered more challenging.

Substantial efforts have been made to understand the chemistry behind this type of battery and to improve the overall cell performance over the last decade.^[143, 154-156] Since there are no commercial electrolytes available for Mg-batteries, the development of efficient electrolyte systems that are compatible with Mg anodes and also sulfur-based cathodes is of great importance. The research community has also developed a strong preference for investigating novel electrolyte systems, such as various magnesium salts, additives *etc.*^[143, 154-158] At the same time, the modification of the separator, the development of novel cathodes and anodes, new binder systems for cathodes, as well as the investigation of the artificial SEI layer, have been reported.^[158-162]

In this chapter, the working mechanism of Mg-S batteries and the state-of-the-art electrolyte development will be discussed in detail. In addition, a brief introduction of the cathode, anode and separator design will be given.

2.5.1 Principle of Magnesium-Sulfur Batteries

A typical Mg-S half-cell is composed of a sulfur-based cathode, a magnesium metal anode and an organic electrolyte soaked in separators, as is illustrated in **Figure 2.10**.^[143, 163, 164] Similar to Li-S batteries, the majority of the energy is stored in the sulfur-based cathodes, so the entire electrochemical mechanism of Mg-S cells is based on the redox reactions of sulfur.

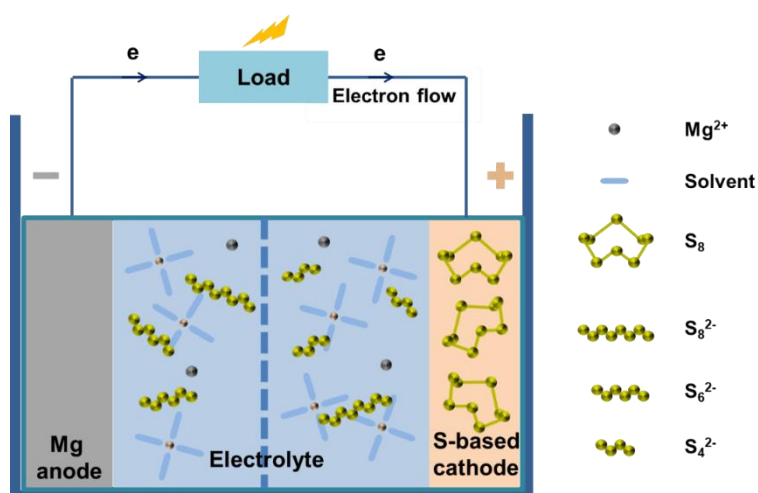


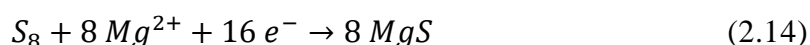
Figure 2.10: Schematic illustration of a magnesium-sulfur cell using elemental sulfur-based cathodes.

During the discharge process, the Mg anode is oxidized to Mg^{2+} , yielding two electrons (**Equation 2.13**). Upon the migration of Mg^{2+} to the sulfur cathode, these electrons also transfer from the Mg anode to the sulfur cathode using an external electrical circuit. This process is accompanied by the reduction of the sulfur cathodes and the formation of magnesium sulfides as the final reduction products (**Equation 2.14**). The overall reaction is shown in **Equation 2.15**.

Reaction on the anode side during discharge (oxidation):



Reaction on the cathode side during discharge (reduction):



Overall reaction:



Similar to Li-S batteries, in the discharging process, S_8 also stepwise converts to long-chain polysulfides, then short-chain polysulfides and finally magnesium sulfide. In the following charging process, the formed magnesium sulfides ideally successively reverse back to the original S_8 .

In detail, the whole discharge process can be divided into three steps, as proposed by *Zhao-Karger et al.* [144] **Figure 2.11a** shows the proposed typical discharging voltage profile of a Mg-S₈ cell using a magnesium conductive salt (magnesium tetrakis(hexafluoroisopropoxy) borate, Mg[B(hfip)₄]₂) dissolved in a mixture of diglyme and tetraglyme.

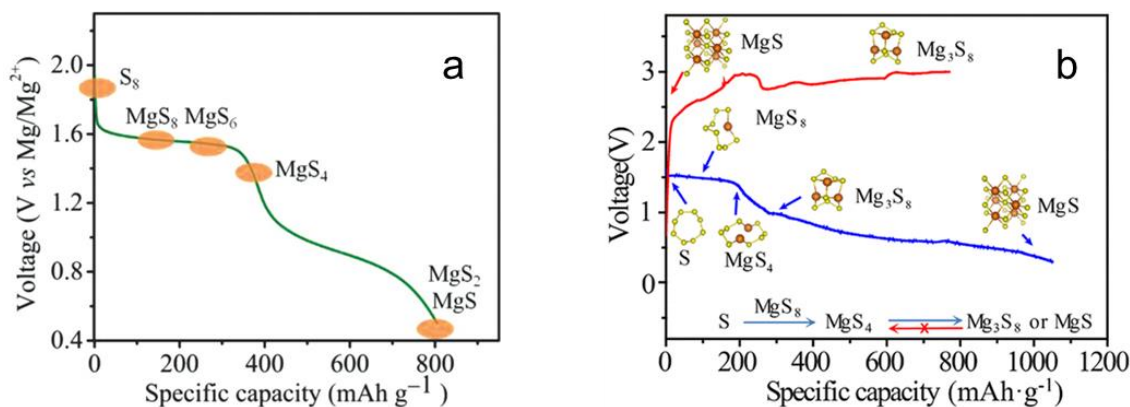
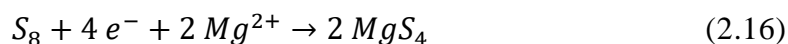
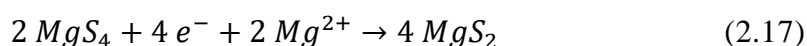


Figure 2.11: **a)** A typical voltage profile of a Mg-S cell based on S₈ during discharge.^[144] Reproduced with permission from ref.^[144]. Copyright (2015). WILEY-VCH Verlag GmbH & Co. KGaA, Weinheim; **b)** Voltage profile of a Mg-S cell based on S₈ during discharge.^[165] Reproduced with permission from ref.^[165]. Copyright (2019). American Chemical Society.

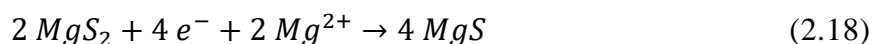
According to **Figure 2.11a**, the whole voltage profile is composed of two distinct voltage plateaus, which correspond to the two major reduction steps. The first step entails a solid-to-liquid two-phase reduction; *i.e.* the elemental sulfur in the cathode transforms to MgS₈ and MgS₆, which can be dissolved in the electrolyte. The formed MgS₈ and MgS₆ subsequently convert to the low-order polysulfide, MgS₄. After the first step of the reduction of S₈, the voltage profile reaches the first voltage plateau at *ca.* 1.5 V. The reaction in the first step is shown in **Equation 2.16**.^[144]



In the second step, a liquid-to-solid two-phase reduction happens; *i.e.* the reduction from MgS₄ (soluble in electrolyte) to MgS₂ (insoluble in electrolyte). The second reduction step corresponds to the second voltage plateau at *ca.* 1 V in **Figure 2.11a**. The reaction is described in **Equation 2.17**.^[144]



The final step is the further reduction from MgS_2 to MgS , which is shown in **Equation 2.18**.^[144]



However, there are some debates about the discharge mechanism of Mg-S₈ systems. For instance, *Xu et al.*^[165] pointed out a different reduction routine, shown in **Figure 2.11b**. They have proposed the formation of different magnesium polysulfide species *via in-situ* X-ray absorption spectroscopy (XAS) based on a Mg-S₈ cell using a $\text{Mg}(\text{HMDS})_2\text{-AlCl}_3$ electrolyte. Similar to the reduction routine proposed by *Zhao-Karger et al.*^[144], in the initial cycle, the initial voltage plateau appears at *ca.* 1.5 V, which is accompanied by the formation of MgS_8 and MgS_4 , resulting in a *ca.* 1080 $\text{mAh}\cdot\text{g}_s^{-1}$ discharge capacity. However, according to their observation, there are only two sloped regions, instead of distinguishable plateaus in the following discharging process. In detail, the sharp slope from 1.5 to 1.0 V and the long slope region from 1.0 to 0.3 V correspond to the formation of Mg_3S_8 and MgS , respectively. Interestingly, from the second cycle on, even the voltage plateau at *ca.* 1.5 V vanishes, which at the same time is accompanied by the drop of discharge capacity to only 400 and 200 $\text{mAh}\cdot\text{g}_s^{-1}$ in the second and third cycle, respectively. *Xu et al.*^[165] have also investigated the reasons for the severe capacity decay. It has been reported that the severe capacity decay in the initial two cycles in the Mg-S system is not due to the shuttle effect of the polysulfides.^[129, 166] Instead, they proposed that the main reason is an irreversible charging reaction; specifically, the irreversible formation of Mg_3S_8 . The electrochemically inert MgS species are hard to be re-oxidized to Mg_3S_8 ; consequently, the discharge capacity from the second cycle on solely originates from the redox reactions between low-order magnesium polysulfides: Mg_3S_8 and MgS . The missing redox processes of the transformation between short-order polysulfides and long-chain polysulfides cause the sharp capacity decay in the initial two cycles.^[165]

2.5.2 Comparison of Mg-S and Li-S Systems

The diagonal relationship between Mg and Li metal in the periodic table results in some similarities of the chemical properties, such as the formation of monoxides during combustion. However, when applied as metal anodes in the sulfur batteries, despite some superficial similarities between Mg-S and Li-S batteries such as the successive formation

of various polysulfides upon charging/discharging, the distinct differences between these two metals lead to the totally different cell chemistry and also different challenges.^[164, 167] In order to get a better overview and understanding of the two systems, a comparison between Mg-S and Li-S systems is provided in this chapter before the further discussion of the electrodes and electrolyte systems in Mg-S batteries. **Table 2.3** summarizes the major differences between Mg-S batteries and Li-S batteries, regarding their theoretical properties, metal anodes and the formed polysulfides.

Table 2.3: Major differences between Mg-S and Li-S battery systems.

	Li-S	Mg-S
Theoretical energy density ^[146]	2654 Wh kg ⁻¹ 2856 Wh L ⁻¹	1684 Wh kg ⁻¹ 3221 Wh L ⁻¹
Standard reduction potential (metal) ^[146]	-3.04 V (vs. SHE)	-2.36 V (vs. SHE)
Thermodynamic stability (metal) against liquid electrolyte ^[146]	Low (SEI formation, electrolyte decomposition)	High (only initial reaction with impurities)
Deposit morphology ^[146]	Dendrite-like, needle-like	Homogeneous, dendrite-free
Polysulfides species (in ether-based electrolytes) ^[146]	Li ₂ S ₈ , Li ₂ S ₄ , Li ₂ S ₂ , Li ₂ S	MgS ₈ , MgS ₂ , MgS
Solubility of polysulfides ^[154]	High	Low
Utilization of sulfur ^[168]	High	Low

One major difference is the different standard reduction potentials. The less negative standard reduction potential of magnesium metal leads to the high thermodynamic stability against liquid organic electrolytes. Therefore, in Li-S cells, a Li⁺-conductive solid electrolyte interphase (SEI) layer, which is formed by the decomposition of the electrolyte, is usually formed on the surface of the lithium metal to protect the lithium anode from further corrosion. This protective SEI layer is helpful to improve the cycle life.^[146] In contrast, in the case of Mg-S cells, due to the high stability of the magnesium metal against the electrolyte, a homogeneous SEI layer to protect the Mg anode is hard to form. Instead, a “conditioning process” has been observed in Mg batteries, as reported in several publications.^[146, 169-171] During the “conditioning process”, some irreversible capacities

and low Coulombic efficiency can be observed during the initial cycling of the cells. This is caused by the initial reaction between electrolyte/magnesium with the impurities, such as water.^[146, 169-171]

Also, the lower theoretical cell voltage of Mg-S cells (*ca.* 1.77 V) compared to Li-S cells (*ca.* 2.24 V) leads to lower voltage plateaus during discharge, which consequently lowers the gravimetric energy density of Mg-S systems (1684 Wh kg⁻¹) compared to Li-S cells (2654 Wh kg⁻¹).^[164, 167]

Another major difference which leads to the different cell performances, is related to the formed polysulfides. Since carbonate-based solvents are generally considered incompatible with the magnesium metal anode, only ether-based solvents such as THF, DME *etc.* are discussed here. In ether-based lithium electrolytes, the reduction of S₈ successively proceeds through Li₂S₄ and Li₂S₂ species *via* the disproportionation of Li₂S₈. Therefore, in the majority of reported Li-S batteries, two distinct voltage plateaus are described.^[100, 172] However, a tendency for a direct reduction of S₈ to MgS₂ species has been reported for certain Mg²⁺-based electrolytes.^[146] This corresponds to one distinct plateau in Mg-S cells, which is also accompanied by a fast decrease of the cell voltage until the lower voltage limit is reached.^[148, 156, 173]

Further on, Mg²⁺ cations show a strong electrostatic interaction with polysulfides. Consequently, the solubility of magnesium polysulfides in ether-based electrolytes is much lower than the one of lithium polysulfides. For example, the solubility of MgS₈ in tetraglyme is < 100 mM. In contrast, the solubility of Li₂S₈ in the same solvent is 6 M.^[100, 172] The huge solubility difference results in different conversion rates and reversibility, and consequently, cell performance.^[154]

Figure 2.12 provides a comparison between these two systems, with regards to the number of publications, sulfur utilization, cycle life, current rate, deposition morphology *etc.*^[146] It is clear that research on Mg-S batteries is still at an early stage compared to the intensive research on Li-S batteries. As shown in **Figure 2.12**, the number of publications, the sulfur utilization, cycle life, current rate and the efficiency of Mg-S systems are still far behind the one of Li-S systems.

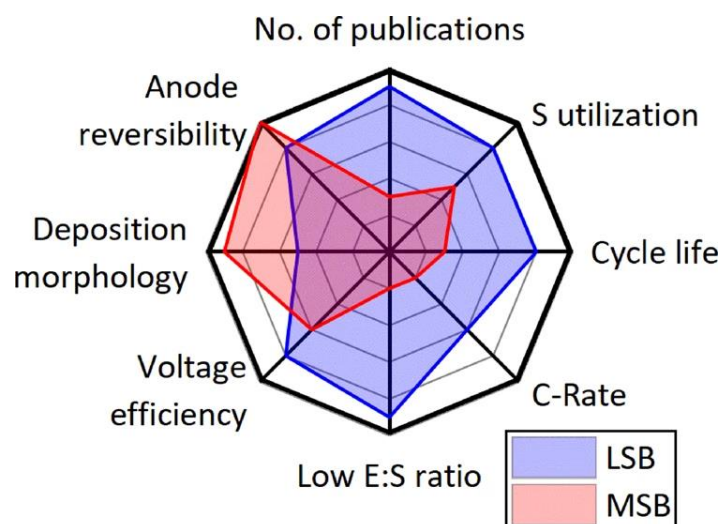


Figure 2.12: Comparison between Li-S batteries (LSB, blue) and Mg-S batteries (MSB, red) in the aspect of anode reversibility, number of publications, sulfur utilization, cycle life, current rate, electrolyte-to-sulfur (E:S) ratio, voltage efficiency and deposition morphology.^[146] Reproduced with permission from ref.^[146]. Copyright (2021). Springer Nature.

Compared to Li-S systems, the major obstacle in Mg-S systems is the lack of suitable electrolyte systems, which must be compatible with the electrophilic sulfur cathodes and allow for a reversible Mg plating/stripping. Most of the commercial available magnesium salts cannot meet these requirements; hence, extensive efforts have been put to the synthesis of novel electrolyte systems for Mg-S batteries. In addition, some common solvents for electrolytes, *i.e.* carbonate-based solvents, are not compatible with Mg anodes, which certainly increases the challenges in electrolyte developments. Additionally, the passivation of the Mg anodes due to minor impurities (such as water, oxygen) results in a poor cell performance, underlining the need for highly clean working conditions. Also, similar to Li-S cells, a high-performance sulfur cathode is necessary for high-performance Mg-S batteries. Similar issues regarding the sulfur cathodes in the Li-S cells, such as the low conductivity of sulfur, low sulfur loadings and polysulfide shuttle *etc.*, also slow down the development of Mg-S batteries. Overall, substantial modifications and developments in the cell components are definitely needed for a high-performance Mg-S battery.

2.5.3 Cathode and Anode Materials

Cathode Design

In a Mg-S cell, the discharge and charge processes are governed by the redox reactions of sulfur. The sulfur-based cathodes belong to the group of conversion cathodes, rather than to intercalation cathodes.^[174] In view of the attractive features of sulfur, such as earth abundancy, low-cost, non-toxicity and high theoretical energy density ($1675 \text{ mAh}\cdot\text{g}^{-1}$), a sulfur-based cathode is considered beneficial for use in rechargeable Mg batteries.^[149] In this section, the sulfur-based conversion cathodes applied in Mg batteries are discussed.

Indeed, the majority of the reported sulfur cathodes applied in Mg batteries originate from Li-S batteries, which mainly focus on the accommodation of elemental sulfur in carbonaceous materials.^[14, 175-180] Similar to S_8 -based cathodes in Li-S batteries, a porous, conductive and mechanically stable carbon matrix is required to embed the elemental sulfur, in order to increase the utilization of active material and reduce the polysulfide shuttle effect.^[143, 173] The reported carbon matrix used in Mg-S cells includes carbon black^[89, 181, 182], CMK-3^[120, 180, 183, 184], sulfur graphdiyne (SGDY)^[185], activated carbon clothes (ACC/S)^[154, 186], microporous carbon^[187], and metal organic frameworks (MOFs)^[188] *etc.*

One typical example is the elemental sulfur imbedded in CMK-3, which was invented by *Nazar et al.*^[120] for the use as cathode material in Li-S systems in 2009. Recently, the CMK-3/S composite materials were then utilized by *Ha et al.*^[183], *Zhao-Karger et al.*^[144] and *Gao et al.*^[189] as cathode material in Mg-S batteries. **Figure 2.13 a, b** show a schematic illustration of the S/CMK-3 composite and the synthetic procedures.^[120]

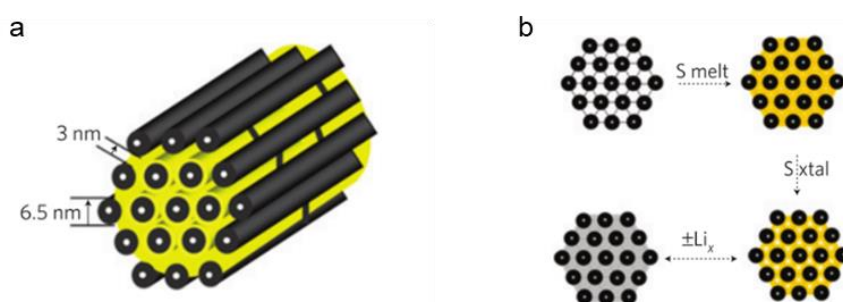


Figure 2.13: **a)** Illustration of S_8 (yellow) imbedded in CMK-3 (gray); **b)** synthetic procedure of S/CMK-3 composites.^[120] Reprinted by permission from ref^[120]. Copyright (2009). Springer Nature: Nature Materials.

In S/CMK-3, sulfur is filled into a highly ordered mesoporous carbon framework, which is composed of a series of carbon nanotubes with uniform pore diameters between 3-4 nm. Due to the excellent contact between carbon and the non-conductive sulfur, electrical conductivity of the composites is *ca.* 0.2 S cm^{-1} , which is similar to one of the CMK-3 carbon matrix (0.2 S cm^{-1}), indicating a homogeneous distribution of the insulating sulfur within the mesoporous carbon. In addition, the preparation of the composite follows a simple melt-diffusion method (**Figure 2.13b**).^[190] It is prepared by the impregnation of molten sulfur into the pores at $160 \text{ }^\circ\text{C}$ by capillary forces and the densification by crystallization. After the incorporation of sulfur, the Brunauer-Emmett-Teller (BET) surface area and the pore volume of the CMK-3 matrix drops from 1976 to $46 \text{ m}^2\cdot\text{g}^{-1}$, and from 2.1 to $0.028 \text{ cm}^3 \text{ g}^{-1}$, respectively,^[120] indicating the successful impregnation of the elemental sulfur in to the pores.

The stunning properties of S/CMK-3 composites encouraged the researchers to apply them in a Mg-S battery. *Zhao-Karger et al.*^[144] utilized this cathode together with a modified non-nucleophilic electrolyte, $(\text{HMDS})_2\text{Mg}-2\text{AlCl}_3\text{-MgCl}_2/\text{tetraglyme}$, in a Mg cell. The cell possessed a specific discharge capacity of *ca.* $250 \text{ mAh}\cdot\text{g}_s^{-1}$ for 20 cycles. The authors reported that a huge voltage hysteresis accounts for the quick capacity fading. In 2017, the same group combined the S/CMK-3 cathode with a new electrolyte system ($\text{Mg}[\text{B}(\text{hfp})_4]_2$ in diglyme-tetraglyme), resulting in improved cycle stability. The initial discharge capacity was *ca.* $500 \text{ mAh}\cdot\text{g}_s^{-1}$, which, however, dropped to *ca.* $200 \text{ mAh}\cdot\text{g}_s^{-1}$ in the 100th cycle at 0.1 C .^[184]

In 2017, *Du et al.*^[185] developed a sulfur graphdiyne (SGDY) cathode (**Figure 2.14**), which can be prepared by the incorporation of molten sulfur into the layered structure of GDY. One attractive feature of the SGDY cathode is its compatibility with the nucleophilic electrolytes in the presence of a lithium salt. The majority of the sulfur cathodes are only compatible with non-nucleophilic electrolytes, due to the reaction between sulfur and nucleophilic systems.^[185, 187, 191] However, the authors stated that the reduced electrophilicity of the SGDY cathode allows for its use with nucleophilic electrolytes. Another important feature is that only short-sulfide units (S_x , $1 < x < 5$, with dimension of $< 0.5 \text{ nm}$) are accommodated in the structure due to the limited size of the carbon skeleton GDY, which possesses uniformly distributed pores with a diameter of 5.42 \AA and large interlayer distances of 0.365 nm . The confining of short-chain sulfur species in the

nanopores reduces the dissolution of sulfur and consecutive shuttle effects.^[185] In addition, the butadiene groups serve as conjugated linkages and connect the individual benzene rings in the layered GDY, thereby providing a high electrical conductivity of the cathode material ($4.37 \times 10^{-4} \text{ S m}^{-1}$).^[185] However, the sulfur content of the SGDY composite is only 30.2 wt%, which is comparably low for practical use.

By using the SGDY cathode in a Mg battery, together with the all phenyl complex (APC, AlCl_3 and phenyl magnesium chloride in THF) electrolyte, and with LiCl as the additive, the cell delivered a discharge capacity of *ca.* $1125 \text{ mAh g}_s^{-1}$ in the initial cycle, which, however, dropped to only *ca.* 540 mAh g_s^{-1} at the 35th cycle at a charge/discharge rate of C/30. The authors observed severe overcharging of the system, be attributable to the reduction of the electrolytes or the corrosion of the cells.^[185]

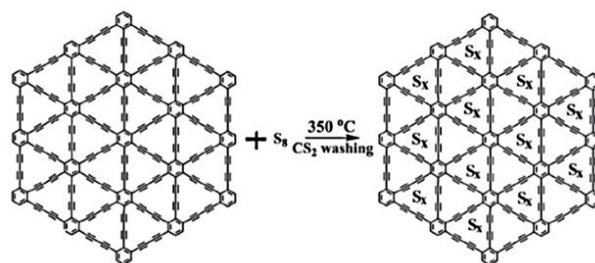


Figure 2.14: Illustration of a sulfur graphdiyne (SGDY) cathode.^[185] Reproduced from the permission of ref^[185] Copyright (2017). WILEY-VCH Verlag GmbH & Co. KGaA, Weinheim.

Using a similar concept, namely distributing of short chain sulfides in the pores of a microporous carbon (MC) matrix and elemental sulfur on the outside surface of the carbon matrix, Wang *et al.*^[187] developed a carbon-sulfur composite sulfur at microporous carbon composite (S@MC), again using a melt-diffusion method. In addition, they confirmed the compatibility of S@MC with a nucleophilic electrolyte (with the addition of lithium salts) using S@MC cathodes coated on a copper current collector, dried at 50 °C. Due to the formation of copper sulfides in course of the reaction between the elemental sulfur on the outside surface of carbon and the copper current collector, the interaction between sulfur and copper prevents the sulfur from further reacting with the nucleophilic electrolyte.^[187] On the other hand, the good adsorption of the polysulfides inside the microporous carbon increases cycle stability.^[187, 191] With this S@MC cathode, Mg-S cell with an APC-based electrolyte with LiCl as the additive delivered *ca.* 350 mAh g_s^{-1} at 0.1 C for 200 cycles. In

comparison, cells with an elemental sulfur cathode were only cyclable for 50 cycles with *ca.* 180 mAh g⁻¹ at 0.1 C.^[187] Similar concept of stabilizing elemental sulfur *via* the use of a copper current collector has also been applied by *Zeng et al.*^[191] and *Huang et al.*^[192] Based on these reports, *Robba et al.*^[193] investigated the functions of a copper current collector. The use of a copper current collector can improve cycle stability; however, they observed certain corrosion of the copper foil by means of scanning electron microscopy (SEM), which might be caused by its reaction with the formed sulfur species.^[193]

Sulfur at activated carbon clothes (ACC/S), a binder-free and current collector-free cathode, which has been intensively applied in Li-S systems (**Chapter 2.4.3, Figure 2.9a**), has also been reported for use in Mg-S batteries. *Zhao-Karger et al.*^[194] reported a type of Mg-ACC/S cell, together with the use of a Mg[B(hfip)₄]₂-based electrolyte. The cell delivered an initial discharge capacity of around *ca.* 950 mAh g⁻¹, whereas the discharge capacity quickly dropped to only *ca.* 200 mAh g⁻¹ at the 100th cycle at 0.1 C. They outlooked the future work by using novel methods to restrain the dissolution of magnesium polysulfides. *Gao et al.*^[154, 156] have also applied the ACC/S cathodes in a series of Mg-S cells, using a concentrated (1 M Mg(TFSI)₂/MgCl₂/DME) and a diluted electrolytes (0.25 M Mg(TFSI)₂/MgCl₂/DME). Discharge capacities were *ca.* 530 mAh g⁻¹ for 110 cycles at 100 mA g⁻¹ (C/15) in the concentrated electrolyte; whereas only *ca.* 400 mAh g⁻¹ for 20 cycles at 200 mA g⁻¹ (C/7) were found for the diluted electrolyte. The authors stated that the better cell performance in the concentrated electrolyte is mainly due to a reduced dissolution of magnesium polysulfides due to the highly concentrated electrolytes, leading to the suppression of the polysulfide shuttle and a reduced loss of active materials.^[156]

Similar to Li-S batteries, apart from S₈-based cathodes, sulfur covalently bound to a carbonaceous matrix as the cathode materials, such as SPAN cathodes (**Scheme 1, Chapter 2.4.3**), have also been utilized in the Mg batteries.^[157, 158, 162, 195, 196] Up to date, only the research groups of *Prof. Buchmeiser*^[157, 158, 195, 197] and *Prof. Wang*^[162] reported on Mg-SPAN batteries. In 2020, *Wang et al.*^[162] reported on the influence of different binder systems, such as poly(vinylidene fluoride) (PVDF), poly(ethylene oxide) (PEO), sodium polyacrylate (PAAS), guar gum (GG), on the Mg-SPAN cell performance. They observed certain improvements regarding cycle stability and rate capability with the water-soluble binder PAAS, compared to conventional PVDF and PEO binders. With an SPAN cathode coated on a Cu current collector using the PAAS binder, the corresponding Mg-S cell

delivered around 400 mAh g_s^{-1} for 50 cycles at 0.1 C. In contrast, cells with SPAN cathodes using PVDF and PEO binders delivered only *ca.* 180 and 150 mAh g_s^{-1} , respectively, under the same cycling conditions. They stated that the better cell performance with the PAAS binder is mainly due to a better adhesion and better stretchability of the PAAS binder.^[162]

Apart from the developments in cathodes, the design of an interlayer, which is normally placed between the cathode and the separator to restrain the movement of polysulfide species, has also been reported.^[161, 165, 198] For example, *Kaland et al.*^[161] reported a type of current collector- and binder-free Mg-S battery by the use of an interlayer placed between the cathode material and the separator, in order to improve sulfur utilization and at the same time capture the formed polysulfides. They prepared the interlayer, MXene-based composites, as the sulfur host material, by a low-temperature, wet-chemical procedure.^[161] They used an S_8 -based cathode, prepared by the mixing of S_8 nanoparticles with MXene-CNT dispersion, called S_8 -mixed cathode with a 50% sulfur content (**Figure 2.15a**).^[161]

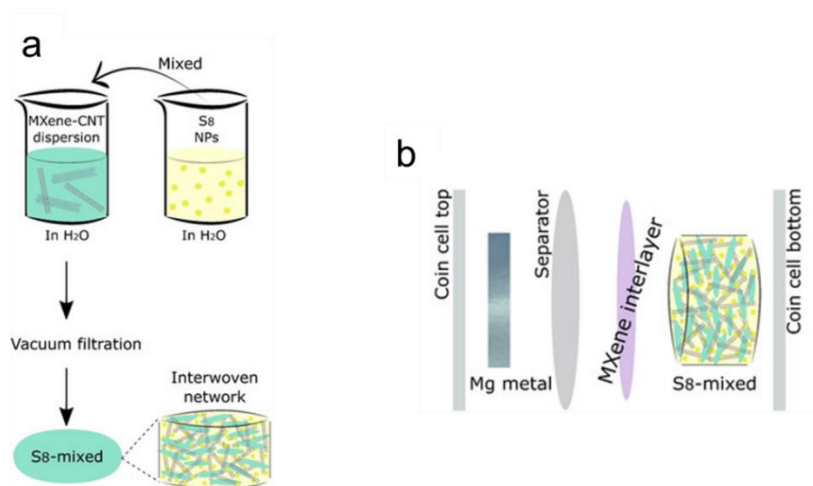


Figure 2.15: a) Preparation of an S_8 -mixed cathode material; b) Mg- S_8 cell using the MXene as the interlayer.^[161] Reproduced from the permission of ref^[161]. Copyright (2021). WILEY-VCH Verlag GmbH & Co. KGaA, Weinheim.

The Mg-S cell with the as-prepared S_8 -mixed cathode in a $\text{Mg}[\text{B}(\text{hfp})_4]_2$ -based electrolyte, together with an MXene interlayer (**Figure 2.15b**) delivered *ca.* 400 mAh g_s^{-1} at C/30 for 25 cycles. In comparison, a Mg-S cell without the MXene interlayer delivered only half of the capacity, indicating the synergistic effect of MXene and CNT. However, severe overcharging was observed in the Mg-S cell with the MXene interlayer, which might be

due to the collapse of the unstable SEI layer formed by the $[B(hfip)_4]^-$ anion; followed by the severe polysulfide shuttle.^[161] The authors proposed the addition of a lithium salt to improve the stability of the SEI layer and the cycle performance.^[161]

Anode Design

Research on Mg-S batteries focuses on the design of cathodes and electrolyte systems whereas the anode developments are very rare. The reported Mg metal anodes are generally used in form of discs or foils^[148, 154, 155, 180, 183, 184, 188, 194, 199, 200]. Unlike Li anodes, which tends to form dendrites over cycling, one drawback of these Mg anodes is their low surface area. While dendrites can cause short-circuits, their formation increases the surface area, consequently more active sites exist.^[143]

Friedrich et al.^[201] reported a type of pressed Mg pellets out of Mg powders in 2017 to increase the surface area of Mg anodes. They prepared and compared three different types of Mg anodes: Mg pellets pressed at high pressure, Mg pellets pressed at low pressure and conventional Mg foils. The Mg pellets were composed of commercialized Mg powder and graphite powder (weight ratio=4:1). The authors observed an improved cycling performance of Mg-S cells with the porous Mg electrodes comparing to conventional Mg foils due to a better electrolyte addressability. However, the discharge capacity still vanished to almost neglectable after 10 cycles, even with the pressed Mg anodes. Most likely, the incompatible sulfur cathodes and electrolytes can be well accountable for that. In addition, the commercial Mg powder might also be partially passivated before the cell assembling.

2.5.4 Electrolyte Systems

Great efforts have been put into the development of suitable electrolytes for rechargeable Mg-S batteries.^[202-206] Indeed, one of the main obstacles in the Mg-S systems is the lack of suitable electrolytes. Generally, a high-performance electrolyte should possess the following properties: high ionic conductivity, high chemical/electrochemical stability against the cathode and anode to allow a wide cell operation window, high thermal stability, no passivation towards electrodes, high electroactivity to allow for a reversible Mg plating and stripping, low toxicity and flammability.^[143, 144, 207] With Mg batteries, carbonate-based electrolytes are in general incompatible due to the reaction between magnesium and

carbonates. In addition, a group of conductive salts in the electrolytes that have been developed for Mg batteries are not suitable for sulfur-based cathodes, due to their nucleophilic properties.^[185, 187, 191] Hence, the design of fully compatible electrolytes for Mg-S batteries is challenging and of great importance. In this chapter, the current developments of various electrolyte systems for Mg-S batteries, such as the design of novel non-nucleophilic electrolytes and the modification of cell components to fit the nucleophilic electrolytes, are discussed.

Nucleophilic Electrolytes

The reported state-of-the-art nucleophilic electrolytes are rarely applied in Mg-S batteries, due to the nucleophilicity of the organo-magnesium compounds.^[88, 208] The use of a nucleophilic electrolyte in Mg-S batteries is always accompanied by the modification of the cathode, such as using different active material/carbon matrixes or different current collectors, to generally prevent the reaction of the sulfur (species) with the electrolyte. One example of a Grignard-based nucleophilic electrolyte, the so called “all-phenyl complex (APC)” electrolyte, $(\text{PhMgCl})_2\text{-AlCl}_3$ in THF, shows good compatibility with Mg anodes, including high oxidative stability (3.2 V) and allows for an efficient Mg plating and stripping.

Due to these attractive features, *Zeng et al.*^[191] have pointed out a strong dependency of the electrochemical performance of Mg-S cells containing a nucleophilic electrolyte, on the applied current collector. The authors replaced the conventional stainless steel or aluminum current collector by a copper foil. The authors confirmed the formation of copper sulfide during the drying process of the cathode (50 °C), due to the strong interaction between sulfur and copper.^[191] The protection of sulfur by the copper current collector was believed to increase the compatibility of sulfur with the nucleophilic electrolytes. In addition, they characterized cells based on a conventional S_8 -based cathode coated on Cu (70 wt% S_8 powder, 20 wt% Super-P carbon powder and 10 wt% PVDF in NMP) and an APC-based electrolyte, $(\text{PhMgCl})_2\text{-AlCl}_3$ in THF, and found a reversible cycling of the cell.^[191] The cell delivered *ca.* 650 $\text{mAh}\cdot\text{g}_s^{-1}$ in the initial cycle, which decreased to *ca.* 100 $\text{mAh}\cdot\text{g}_s^{-1}$ in the 20th cycle, with almost 100% Coulombic efficiency at 10 $\text{mA}\cdot\text{g}^{-1}$ (0.005 C). Despite the poor cycle performance, which might be due to the formation of irreversible magnesium polysulfides, the cells showed the possibility of combining an S_8 -based cathode coated on a Cu current collector with a nucleophilic APC electrolyte.^[191] In

order to further improve this system, the authors added some LiCl to the APC electrolyte but kept the other cell parameters. The cell performance substantially improved. These cells successfully delivered *ca.* 300 mAh g_s⁻¹ for 40 cycles with approximately 100% Coulombic efficiency at a discharge rate of 10 mA g⁻¹ (0.005 C).^[191]

The still unsatisfactory cell performance regarding the specific capacity and the life span encouraged the same research group to further modify the cathode material.^[187] Instead of using a conventional coating of a slurry of S₈, carbon black and binder on Cu, they used sulfur at microporous carbon composites (S@MC) coated on Cu as the cathode. As discussed in **Chapter 2.5.3**, the novelty of this S@MC was combining small-chain S₂₋₄ inside microporous carbon, and ring-like S₈ molecules outside the microporous carbon surface.^[187] Using this concept, the sulfur content was not greatly compromised (sulfur content of S@MC: 64.7 wt%); at the same time, the sulfur can be either immobilized inside of the micropores, or stabilized by the Cu current collector.^[187] The authors characterized the performance of Mg-S cells using the APC electrolyte (0.4 M (PhMgCl)₂-AlCl₃ in THF) and the S@MC coated on Cu. The discharge capacity stabilized at *ca.* 200 mAh g_s⁻¹ at 0.006 C at the 50th cycle, which was a substantial improvement, compared to conventional S₈-based cathodes at that time. However, the cell experienced overcharging in the initial 10 cycles, followed by a decrease in Coulombic efficiency and, consequently, loss of reversibility. To further improve the reversibility of the system, the authors added 1 M LiCl to the 0.4 M (PhMgCl)₂-AlCl₃ in THF. Cell performance was enhanced due to the reactivation of the short-chain magnesium polysulfides by the addition of the lithium salt. The corresponding cell successfully delivered *ca.* 360 mAh g_s⁻¹ at 200th cycle at 0.1 C.^[187] Using the similar LiCl-containing APC-based electrolyte, the Mg-S cell, composed of short-chain sulfides-containing SGDY coated on Cu cathode (**Chapter 2.5.3, Figure 2.14**) has also been reported.^[185] The cell delivered *ca.* 400 mAh g_s⁻¹ at 50 mA g⁻¹ (0.03 C) for 35 cycles.

In general, the reports on the use of nucleophilic electrolytes together with sulfur-based cathodes are scarce. All of them have applied a Cu current collector to form copper sulfide to stabilize the sulfur, which tended to reduce the reaction between sulfur and the electrolyte. At the same time, LiCl has been also added to improve the reversibility of the system. Nonetheless, the reported cells did not show superior cycling performance and

reversibility. Consequently, the focus in the electrolyte development for Mg-S batteries was placed on non-nucleophilic electrolytes.

Non-Nucleophilic Electrolytes

The reported non-nucleophilic electrolytes for Mg-S batteries can be mainly classified into two groups: i) the electroactive species $[\text{Mg}_2(\mu\text{-Cl})_3]^+$ -containing electrolytes; ii) magnesium conductive salts with a weakly-coordinating anion (WCA)-containing electrolytes. Similar to the reported nucleophilic electrolyte, the used solvents are generally ether-based solvents, such as DME, THF, diglyme, tetraglyme *etc.* Researchers have also utilized various additives, such as ionic liquids, lithium salts *etc.*, in the electrolytes to improve the cell reversibility and the formation of stable SEI layer on the Mg anode.

i) Electroactive species $[\text{Mg}_2(\mu\text{-Cl})_3]^+$ -containing electrolytes

Back to the year of 2011, *Muldoon et al. from Toyota research group* ^[89] demonstrated the first proof-of-concept Mg-S battery using a non-nucleophilic electrolyte synthesized by the reaction between hexamethyldisilazide magnesium chloride (HMDSMgCl) and aluminum trichloride (AlCl_3) in a ratio of 3 to 1 in THF as the solvent. The crystal structure of $[\text{Mg}_2(\mu\text{-Cl})_3 \cdot 6\text{THF}][\text{HMDSA}\text{AlCl}_3]$ was solved (**Figure 2.16a**). The cation is composed of two octahedrally coordinated Mg centers, each of which is bridged by three chlorides. The other empty sites are occupied by the three THF molecules bridged by the oxygen atoms. The electroactive species $[\text{Mg}_2(\mu\text{-Cl})_3 \cdot 6\text{THF}]^+$ was also confirmed.^[89] Although the whole synthetic procedure was conducted in an oxygen and water-free glovebox due to the sensitivity of the organo-magnesium chemistry to water and air, the author found the resulting products were not pure enough. This was attributed to an excess of unreacted HMDSMgCl, leading to low oxidative stability (2.5 V) and insufficient Coulombic efficiency (95%). After crystallization of the compounds, the electrochemical properties of the electrolytes substantially improved, the oxidative stability increased to 3.2 V and Coulombic efficiency reached 100%.^[89]

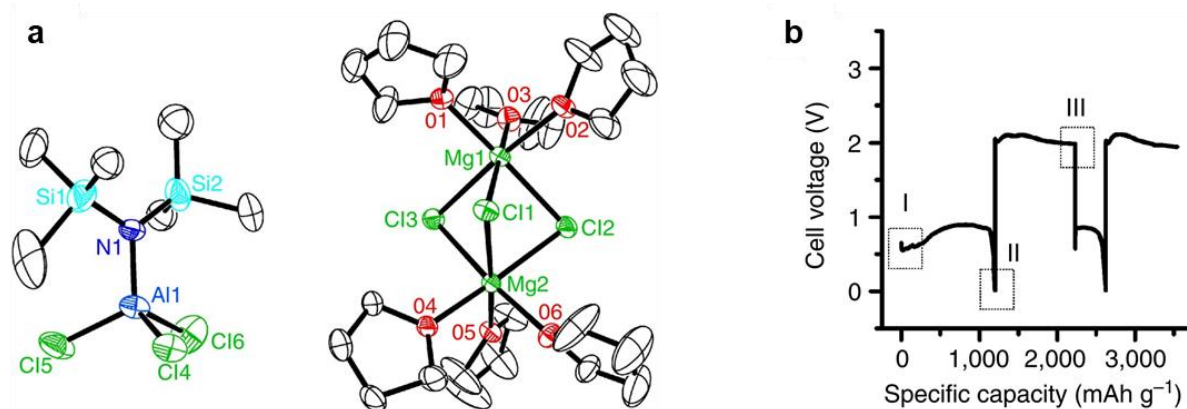


Figure 2.16: a) Structure (ORTEP plot) of the $[\text{Mg}_2(\mu\text{-Cl})_3 \cdot 6\text{THF}][\text{HMDSAICl}_3]$, hydrogen atoms and THF molecules are omitted for clarity; b) voltage profile of a Mg-S cell with the $[\text{Mg}_2(\mu\text{-Cl})_3 \cdot 6\text{THF}][\text{HMDSAICl}_3]$ electrolyte.^[89] Reproduced with permission from ref^[89]. Copyright (2011). Nature Publishing Group.

Muldoon et al.^[89] also cycled the first Mg-S cell using the above-synthesized electrolyte and an elemental sulfur-based cathode, to investigate the feasibility of the electrolyte. The corresponding voltage profile is shown in **Figure 2.16b**. Although the capacity faded from *ca.* 1200 mAh g_s^{-1} in the initial cycle to only *ca.* 394 mAh g_s^{-1} in the second cycle, the first Mg-S battery proved cyclable. Based on the X-ray photoelectron spectroscopy (XPS) data, the fast capacity fading and overcharging of the cells were mainly attributed to the dissolution of sulfur and magnesium polysulfides, which are the common problems in sulfur batteries.^[89]

Actually, a common approach to synthesize this type of organo-magnesium complex can be realized *via* the reaction between a Mg complex containing a non-nucleophilic base, such as $\text{Mg}[\text{HMDS}]_2$ ^[153, 209], HMDSMgCl ^[89, 210], bis(diisopropyl)amide^[211] and a boron- or aluminum-containing Lewis acid, such as AlCl_3 and boron chloride (BCl_3).^[151] The purpose of the addition of the Lewis acid was mainly to increase the current density for Mg deposition, as pointed out by *Muldoon et al.*^[89] Using this synthesis routine, the obtained electroactive species was $[\text{Mg}_2(\mu\text{-Cl})_3 \cdot 6\text{THF}]^+$.

Fichtner et al.^[144] modified the above-outlined synthesis route of *Muldoon et al.* to avoid the use of flammable and volatile THF. They reacted magnesium bis(hexamethyldisilazide), $[(\text{HMDS})_2\text{Mg}]$, with two equivalents of AlCl_3 in ether-based solvents, such as diglyme and tetraglyme, resulting in a similar electroactive species, $[\text{Mg}_2\text{Cl}_3][\text{HMDSAICl}_3]$ and a by-product, HMDSAICl_2 . The by-product can be converted to the desired electroactive species *via* the addition of MgCl_2 .^[144] They further modified the electrolyte by adding the ionic

liquid, *N*-methyl-*N*-butyl-piperidinium bis(trifluoromethanesulfonyl)imide (PP14TFSI) to increase the viscosity of the entire system, which should reduce the diffusion of polysulfides to the anode side. In addition, the ionic liquid was expected to improve the conductivity, increase the boiling point and the chemical, as well as the thermal stability of the electrolyte system. Using the electrolyte, $[\text{Mg}_2\text{Cl}_3][\text{HMDSA}(\text{AlCl}_3)]$ in diglyme/PP14TFSI or tetraglyme/PP14TFSI, Mg cells using a Pt disc as the working electrode in a cyclic voltammetry test showed successful Mg plating/stripping. Unfortunately, when applying the electrolyte to a sulfur-based magnesium cell (cathode: S/CMK), the cell experienced a sharp capacity decay within the initial 20 cycles, resulting in less than *ca.* 200 mAh g_s^{-1} discharge capacity in the 20th cycle. The authors stated the capacity fading could be due to the large hysteresis between charge and discharge voltage.^[144] Owing to the simplicity of the synthesis procedures, this type of electrolytes has also been used in combination with various separator designs, cathodes and anodes, as reported by *Vinayan et al.*^[173], *Yu et al.*^[155], *Friedrich et al.*^[201] and *Muthuraj et al.*^[212].

Similar to the synthesis routine of *Fichtner et al.*^[144], *Nuli et al.*^[211, 213] replaced $(\text{HMDS})_2\text{Mg}$ by magnesium bis(diisopropylamide) (MBA). They reacted MBA with AlCl_3 in a ratio of 1 to 2 in THF. The authors also found that an increase in the amount of the AlCl_3 could improve the cycle efficiency and oxidative stability of the Mg cells, due to the stabilization effect of the Lewis acid to the Mg-N bond in MBA.^[211] Using single-crystal X-ray analysis, the electroactive species was determined to be $[\text{Mg}_2(\mu\text{-Cl})_3(\text{THF})_6][\text{AlCl}_4]$, which is the same as that of the *Muldoon et al.*^[89] The prepared electrolyte, 0.25 M MBA and 0.5 M AlCl_3 in THF, allowed for a successful Mg plating and stripping. However, using this electrolyte, the discharge capacity of the Mg-S@microporous carbon (MC) cells dropped to only around 100 mAh $\cdot \text{g}^{-1}$ in the 3rd cycle at 0.04 C.

The electroactive species $[\text{Mg}_2(\mu\text{-Cl})_3\text{6THF}]^+$ -containing electrolytes allowed for a Mg plating and stripping; however, they did not show good compatibility with the elemental sulfur-based cathodes. Capacity faded quickly when using these electrolytes. At the same time, chloride-containing $[\text{Mg}_2(\mu\text{-Cl})_3\text{6THF}]^+$ was considered corrosive. In 2016, *Li et al.*^[151] developed a non-corrosive salt containing a chloride-free $[\text{Mg}(\text{THF})_6]^{2+}$ cation, with AlCl_4^- as the counter-anion. The preparation of the magnesium salt proceeded *via* the simple reaction between magnesium chloride (MgCl_2) and AlCl_3 in a molar ratio of 1 to 2, in a mixture of the ionic liquid *N*-methyl-(*N*-butyl) pyrrolidinium

bis(trifluoromethanesulfonyl)imide (PYR14TFSI) and THF at 95 °C (**Figure 2.17a**).^[151] The authors also characterized the molecular structure of the resulting magnesium salt, shown in **Figure 2.17b**, by means of single-crystal X-ray diffraction. The structure clearly shows replacement of the chlorides from MgCl₂ by solvent molecules, THF. The anion of the magnesium salt is [AlCl₄]⁻, which has also been proved by means of Raman spectroscopy.^[151]

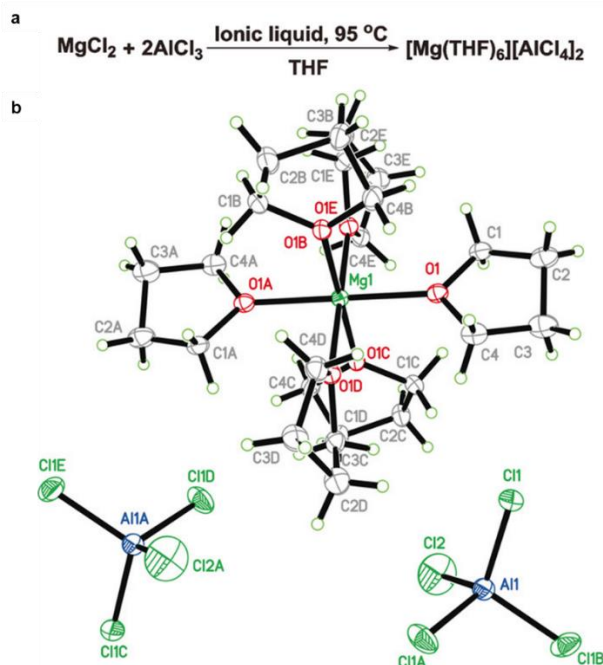


Figure 2.17: a) Chemical reaction for the synthesis of [Mg(THF)₆][AlCl₄]₂; b) chemical structure of [Mg(THF)₆][AlCl₄]₂.^[151] Reproduced with permission from ref^[151]. Copyright (2016). WILEY-VCH Verlag GmbH & Co. KGaA, Weinheim.

The as-prepared electrolyte, 0.3 M [Mg(THF)₆][AlCl₄]₂ in PYR14TFSI/THF (1/1 v/v), showed several promising features. First, the ionic conductivity was 8.5 mS cm⁻¹, which was comparably high among other Mg²⁺ electrolytes.^[151] In addition, this electrolyte showed acceptable oxidative stability, up to 2.3 V, 2.1 V, 2.5 V, 2.4 V and 2.4 V, against carbon coated on Al foil, Cu, nickel (Ni), stainless steel and platinum (Pt), respectively.^[151] Equally important, CV of a Mg cell with a Pt disc or Cu foil as working electrode containing this electrolyte showed excellent reversible Mg plating/stripping, indicating the electroactivity of this electrolyte against Mg.^[151] Also, a symmetric Mg-Mg cell showed relatively low overpotential (0.5 V) at a current density < 0.1 mA cm⁻². The Mg-S cell performance using this electrolyte and an elemental sulfur-based cathode (N-doped graphene-sulfur composite) has also been determined by charging and discharging the cell

at 0.02 C and 0.01 C, respectively. Unfortunately, the cell was only capable of cycling for 20 cycles, with a severe capacity dropping from the initial discharge capacity of *ca.* 700 mAh g⁻¹, to only *ca.* 70 mAh g⁻¹ from the 6th to 20th cycle.^[151] The authors also conducted *post-mortem* SEM/EDX study on the cathode and the anode after 20 cycles. Some obvious cracks were found on the cathode, which might be the reason for the poor electric conductivity and final capacity decay. On the anode side, although no dendrites were observed, some obvious sulfur signals were detected, indicating the loss of sulfur and a polysulfide shuttle, which was most likely the reason for the fast capacity fading.^[151]

ii) *Magnesium conductive salts containing a weakly-coordinating anion*

Another group of non-nucleophilic electrolytes in Mg-S batteries is based on weakly coordinating anion (WCA)-containing conductive salts dissolved in ether-based solvents. WCAs-containing conductive salts show favorable properties, such as their high solubility in low polarity solvents and low nucleophilicity.^[214] These attractive features have widened their applications in the field of electrolytes for battery technology. For example, in the field of LIBs or Li-S batteries, one typical conductive salt in the electrolyte is LiTFSI, which is a WCA-containing conductive salt. There are scarcely commercialized highly purified WCA-containing conductive salts for use in Mg batteries. Hence, the development of novel conductive salts with a WCA is of great interest.^[215, 216]

One typical example of a magnesium salt containing a WCA is magnesium tetrakis(hexafluoroisopropoxy) borate, Mg[B(hfip)₄]₂·3DME (hfip=OCH(CF₃)₂), synthesized by *Fichtner et al.*^[184, 194] for use in Mg-S batteries. Mg[B(hfip)₄]₂·3DME can be synthesized by the reaction between Mg[BH₄]₂ and excess hexafluoro-2-propanol (hfip) in DME, with an evolution of hydrogen (general chemical reaction see **Figure 2.18a**). After removing the solvent and excess hfip, the white conductive salt can be obtained. One attractive feature of Mg[B(hfip)₄]₂·3DME is the water- and air- insensitivity of the final product, though the educts should be handled under inert gas atmosphere.^[184, 194]

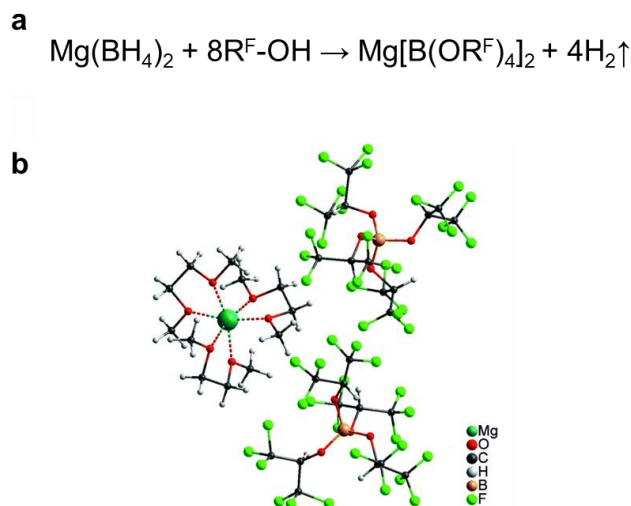


Figure 2.18: **a)** Chemical reaction for the synthesis of a fluorinated magnesium alkoxyborate-based electrolyte; **b)** chemical structure of $\text{Mg}[\text{B}(\text{hfip})_4]_2 \cdot 3\text{DME}$.^[184] Reproduced with permission from ref.^[184]. Copyright (2017). Royal Society of Chemistry.

The single crystal X-Ray structure of $\text{Mg}[\text{B}(\text{hfip})_4]_2 \cdot 3\text{DME}$ was determined by *Fichtner et al.*^[184, 194] (**Figure 2.18b**). The anion shows a boron-centered tetrahedral structure, with a boron coordinated by four hexafluoroisopropoxy groups. Mg^{2+} is solvated by three DME molecules. Successful Mg plating and stripping was observed by CV using 0.6 M $\text{Mg}[\text{B}(\text{hfip})_4]_2 \cdot 3\text{DME}$ dissolved in DME as electrolyte and Pt as the working electrode. *Post-mortem* XRD also proved the deposition of Mg metal.^[184] Furthermore, the authors characterized the oxidative stability of the electrolyte against various common current collectors, Cu (2.8 V), Al (3.6 V), Pt (3.6 V), stainless steel (4.3 V). The electrolyte showed promising stability against these current collectors.^[184] They also prepared the electrolyte using the solvents with relatively high boiling temperatures, such as a mixture of diglyme and tetraglyme (1:1, v:v) with 0.8 M $\text{Mg}[\text{B}(\text{hfip})_4]_2$.^[184] Furthermore, the Mg-S cell performance was characterized at a charge and discharge rate of 0.1 C, using the corresponding electrolyte, a S-CMK-3 cathode and a Mg metal anode. The discharge capacity of the Mg-S cell increased from *ca.* 400 to 500 $\text{mAh} \cdot \text{g}_s^{-1}$ in the initial two cycles, due to the activation of the Mg anode; however, the capacity dropped successively to *ca.* 200 $\text{mAh} \cdot \text{g}_s^{-1}$ in the 100th cycle. The cell experienced overcharging in the initial 10 cycles (Coulombic efficiency > 100%), but gradually stabilized in the following cycles, indicating a comparably good reversibility of the system.^[184]

In view of these results, $\text{Mg}[\text{B}(\text{hfip})_4]_2$ -based electrolytes are considered suitable for use in Mg-S batteries. In order to further investigate this electrolyte, *Fichtner et al.*^[194]

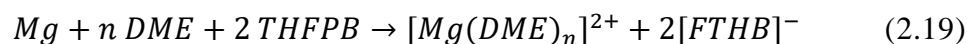
published a more detailed study about this electrolyte. They evaluated the ionic conductivity of $\text{Mg}[\text{B}(\text{hfip})_4]_2$ dissolved in DME at different concentrations.^[194] The electrolyte showed relatively high ionic conductivities (*ca.* $10.5 \text{ mS}\cdot\text{cm}^{-1}$ and $9.8 \text{ mS}\cdot\text{cm}^{-1}$, respectively) when the electrolyte concentration was 0.3 M and 0.4 M, respectively. Hence, they additionally characterized the overpotential of a 0.3 M and 0.4 M electrolyte, respectively, using Mg-Mg symmetric cells by charging and discharging the cells for 0.5 hours.^[194] The 0.3 M $\text{Mg}[\text{B}(\text{hfip})_4]_2/\text{DME}$ electrolyte showed a relatively constant and low overpotential of $<0.09 \text{ V}$ at 0.1 mA cm^{-2} for more than 1000 hours; whereas the 0.4 M electrolyte showed a gradually increased overpotential after 260 hours. In general, $\text{Mg}[\text{B}(\text{hfip})_4]_2$ showed high compatibility with the magnesium metal anode. To further evaluate its compatibility with a sulfur cathode, the authors assembled the cell with the ACC/S cathodes. They selected a more concentrated electrolyte, 0.4 M $\text{Mg}[\text{B}(\text{hfip})_4]_2/\text{DME}$, to suppress the solubility of the polysulfides.^[194] Similar to the above-discussed Mg-S/CMK-3 cell, the Mg-ACC/S cell delivered a high discharge capacity in the initial cycle (*ca.* $980 \text{ mAh}\cdot\text{g}_s^{-1}$), whereas the capacity sharply dropped to only *ca.* $500 \text{ mAh}\cdot\text{g}_s^{-1}$ in the 8th cycle, followed by the continuous dropping of the electrolyte to only *ca.* $200 \text{ mAh}\cdot\text{g}_s^{-1}$ in the 100th cycle.^[194] The authors attributed the capacity fading to the dissolution of polysulfides and loss of active material. Also, a carbon nanofiber (CNF)-coated separator was applied in the cell to trap the magnesium polysulfides. A slight improvement in cell performance was observed in the initial 20 cycles. However, the beneficial effect of the CNF-coated separator gradually vanished, because a large amount of the electrolyte was utilized to fully wet the CNF-coated separator and the formed polysulfides were likely flushed to the anode during cycling.^[194]

Apart from the above-discussed fluorinated alkoxyborate-based electrolytes, the authors also reported a fluorinated alkoxyaluminate-based electrolyte, $\text{Mg}[\text{Al}(\text{hfip})_4]_2\cdot 3\text{DME}$, which is also electroactive, although it has not been applied to Mg-S batteries yet.^[184]

Cui et al.^[217] summarized the most relevant conductive salts and their disadvantages (**Figure 2.19a**). In general, the potential conductive salts for Mg batteries are restricted to the group of anionic boron-based salts, mostly because of the passivation and corrosion issues with other elements with boron-centered anions. Commercial $\text{Mg}[\text{BF}_4]_2$ is incompatible with Mg metal and $\text{Mg}[\text{B}(\text{Bu})_4]_2$ has a limited voltage window. Hence, the invention of novel conductive-salts for Mg batteries is challenging.^[217] Nonetheless, apart

from the above-discussed alkoxyborate-based and alkoxyaluminate-based conductive salts, *Cui et al.*^[217] developed a boron-centered anion-based magnesium electrolyte (BCM electrolyte), showing a prolonged cycle life and good rate capability.

The BCM electrolyte can be easily synthesized *via* the mixing of tris(2H-hexafluoroisopropyl) borate (THFPB) and MgF₂ in DME (Equation 2.19).^[217]



The proposed mass spectroscopy derived structure of the salt in the as-prepared electrolyte is shown in **Figure 2.19 b and c**.^[217] Interestingly, the authors observed a gradually improved scan performance in the CV scans. In addition, after cycling, the effective anion species in the BCM electrolyte proved to be the tetra(hexafluoroisopropyl) borate anion (**Figure 2.19d**), which is the same as the above-discussed weakly coordinating [B(hfip)₄]⁻ anion.^[194]

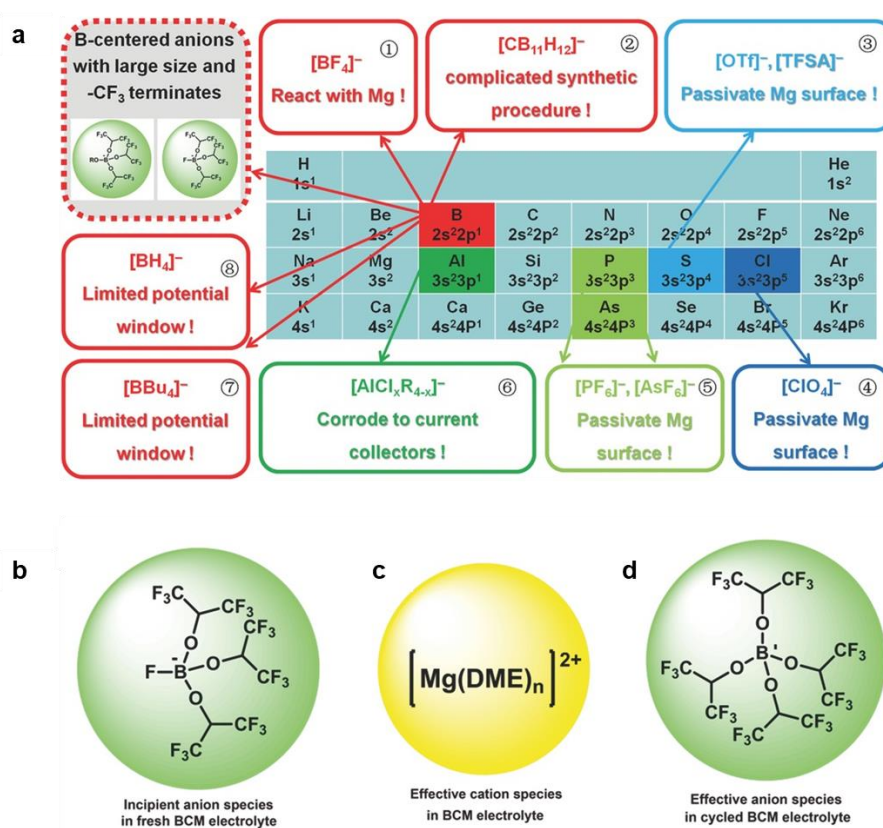


Figure 2.19: **a**) Overview of the potentials and restrictions of conductive salts for magnesium-sulfur batteries; **b**) anion of the as-prepared BCM electrolyte ([FTHB]⁻); **c**) cation of the BCM electrolyte; **d**) effective anion species of the cycled BCM electrolyte.^[217] Reproduced from the ref.^[217]. Copyright (2017). WILEY-VCH Verlag GmbH & Co. KGaA, Weinheim.

The authors further characterized the Mg-S cell performance with the BCM electrolyte and a sulfur@microporous carbon composite coated on a Cu current collector. The cell delivered a discharge capacity of *ca.* 1000 mAh g⁻¹ for 30 cycles at 0.05 A g⁻¹, with almost 100% Coulombic efficiency, which was stated as the best system until 2017.^[217]

The same working group, *Cui et al.*^[180] reported on another borate-based electrolyte for Mg-S batteries in the same year by a facile one-step reaction between tris(hexafluoroisopropyl) borate [B(hfip)₃], MgCl₂ and Mg powder in DME, named as organic magnesium borate-based (OMBB) electrolyte. The cation and anion in the electrolyte are the tetranuclear complex [Mg₄Cl₆(DME)₆]²⁺ and the tetrakis(hexafluoroisopropyl)borate ([B(hfip)₄]₂)⁻, respectively. Their chemical structures are shown in **Figure 2.20**. The reported anion is also a WCA, which is the same as the previous discussed anion reported by *Fichtner et al.*^[184, 194] and *Cui et al.*^[217]. However, the change of cation from the mononuclear complex [Mg(DME)₃]²⁺ to the larger tetranuclear complex [Mg₄Cl₆(DME)₆]²⁺ allows for an easier desolvation during magnesium deposition. The authors also stated that the preparation of the OMBB electrolyte was facile and *in-situ*; also, it does not need the rigorous synthetic routine, as demonstrated by *Fichtner et al.*^[184, 194].

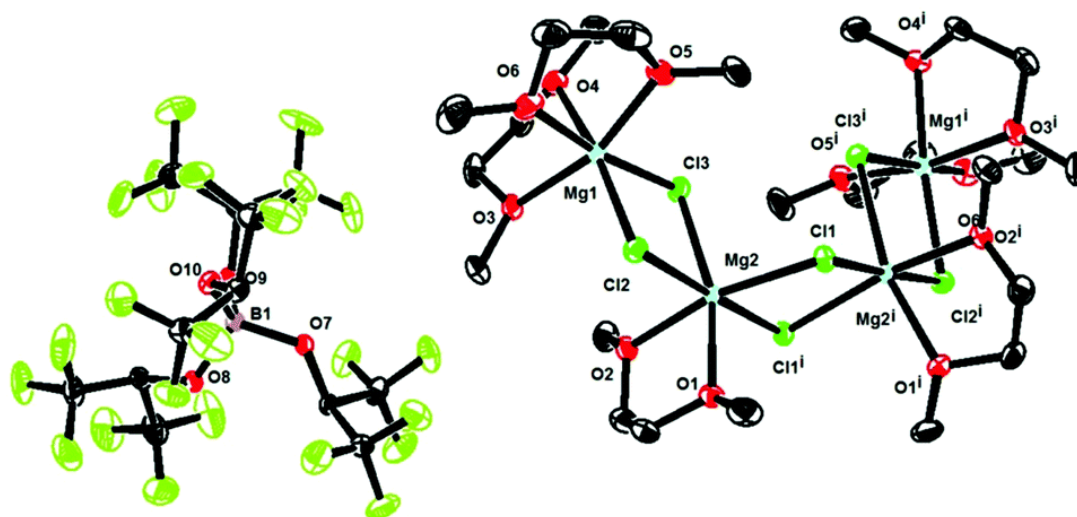


Figure 2.20: Chemical structures of the cation: [Mg₄Cl₆(DME)₆]²⁺ (right) and anion: [B(hfip)₄]₂⁻ (left).^[180] Reproduced from the ref.^[180]. Copyright (2017). Royal Society of Chemistry.

The authors prepared the OMBB electrolyte by dissolving 0.5 M B(HFP)₃ and 0.25 M MgCl₂ in DME, with the addition of an excess amount of Mg powder. They adjusted the

ratio between $B(HFP)_3$ and $MgCl_2$ to 2:1, because with this ratio the plating overpotential was the lowest (0.11 V) and the oxidation peak signal was the strongest in the CV test.^[180] Further on, the authors tested the compatibility of the OMBB electrolyte with a sulfur-carbon composite cathode, S-CNT composites. The Mg-S cell delivered a discharge capacity of *ca.* 1000, 800 and 400 mAh g_s^{-1} at current rates of 160 mA/g (0.1 C), 320 mA/g (0.2 C) and 500 mA/g (0.3 C), respectively, for 100 cycles with almost 100% Coulombic efficiency.^[180] Compared to the literature until 2017, the cell performance using this system was a significant improvement with regards to discharge capacity, rate capability and cycle stability.^[180]

Additives

Considering the unsatisfactory cell performance of Mg-S batteries using either nucleophilic or non-nucleophilic electrolytes, predominantly a result of a severe polysulfide shuttle, limited selections of the conductive salts, slow Mg^{2+} diffusion and passivation of the Mg anode *etc.*, great efforts have also been devoted to the use of various additives in the electrolyte, in order to suppress the polysulfide shuttle, construct a homogeneous SEI layer on the Mg anode or improve the general properties of the electrolyte.^[218] Several categories of additives have been reported. For example, lithium salts, such as LiTFSI^[154], $Li[BH_4]$ ^[158], $Li[CF_3SO_3]$ ^[157, 192], $LiCl$ ^[200], are considered efficient to improve the overall Mg-S cell reversibility. In addition, additives such as YCl_3 ^[219] and I_2 ^[220] have also been applied in the Mg-S batteries.

Back in 2015, Wang *et al.*^[154] introduced the concept of adding a lithium salt, 1 M LiTFSI, to a magnesium electrolyte, 0.1 M $Mg[HMDS]_2-2AlCl_3-MgCl_2$ (termed Mg-HMDS electrolyte). They observed a significant improvement in the reversibility of the Mg-ACCS cells by the addition of the lithium salt into the electrolyte. At the same time, no dendrites were detected on the cycled Mg anode even when a relatively large amount of the lithium salt was present. The Mg-S cell with the Li^+ -containing electrolyte delivered a discharge capacity of *ca.* 1000 mAh g_s^{-1} for 30 cycles; however, severe overcharging was observed. The authors attributed the high capacity to the improved reversibility of the magnesium (poly)sulfides. To further confirm this, they analyzed the surface of the Mg anode after cycling with a Mg-HMDS electrolyte and a LiTFSI-containing electrolyte, respectively, by means of XPS analysis (**Figure 2.21 a and b**). Distinct signals of MgS were observed on the Mg anode from the Mg-HMDS electrolyte. In comparison, no MgS species were

detected on the Mg anode from the LiTFSI-contained electrolyte. The authors stated that the presence of Li^+ successfully dissolved MgS through lithiation, and formed higher-order magnesium lithium polysulfides, which possessed a higher solubility.^[154]

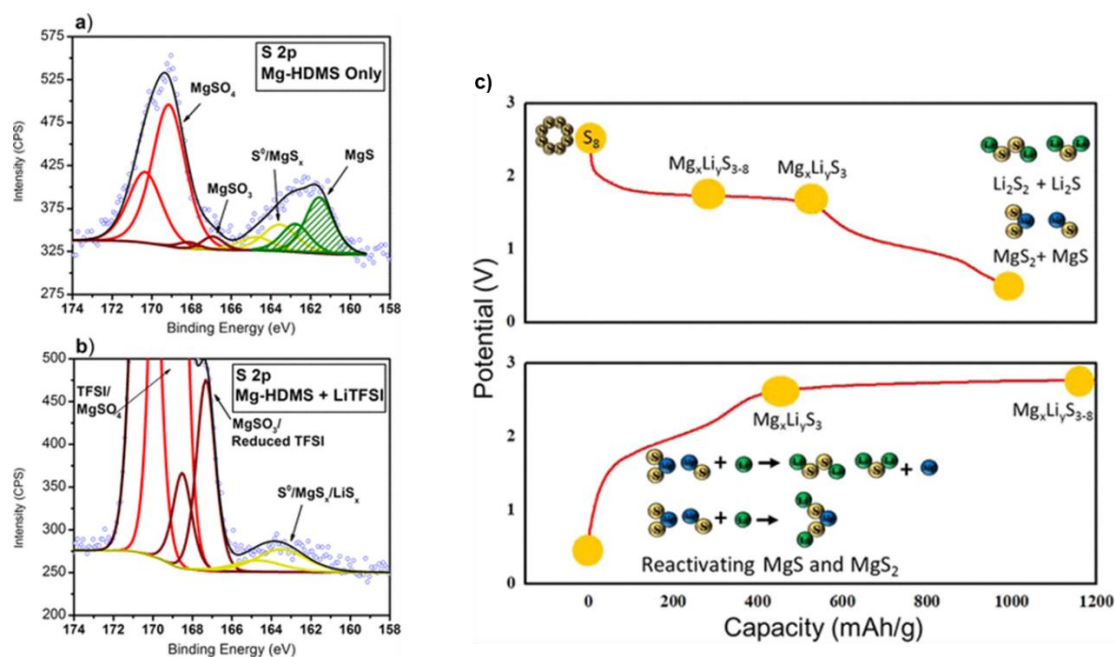


Figure 2.21: a) XPS analysis of the Mg anode cycled from a Mg-HMDS electrolyte; b) XPS analysis of the Mg anode cycled from a Mg-HMDS electrolyte with LiTFSI as additive; c) proposed charging and discharging voltage profile of a Mg-ACC/S cell using a Li-containing electrolyte.^[154] Reproduced with permission from ref.^[154]. Copyright (2015). American Chemical Society.

Based on the improved reversibility and *post-mortem* analysis, the authors also proposed a reaction sequence for Mg-ACC/S batteries with a LiTFSI-containing electrolyte (**Figure 2.21c**). During discharge process, similar to pure magnesium electrolytes, the elemental sulfur is first reduced to soluble high-order MgLi -polysulfides. Consequently, either short-chain lithium (poly)sulfides or magnesium (poly)sulfides form. However, during charging, the potentially formed short-chain lithium polysulfides are re-oxidized to long-chain lithium polysulfides. At the same time, the electrochemical inactive short-chain magnesium (poly)sulfides experience a re-activation process, either through an ion exchange process or coordination of Li^+ to the surface of S^{2-} or S_2^{2-} of MgS or MgS_2 . The reactivation process increases the solubility of the magnesium short-chain (poly)sulfides and reduces the kinetic barrier by forming MgLi -polysulfides.

Although the Mg-ACC/S cell using a LiTFSI-containing electrolyte in the study of Wang *et al.*^[154] only successfully cycled for 30 cycles and overcharging was observed, the use

of lithium salts as the additive in Mg-S cells is considered helpful to improve the reversibility and kinetics. In the following studies, different lithium salts, such as $\text{Li}[\text{BH}_4]$ [158], $\text{Li}[\text{CF}_3\text{SO}_3]$ [157, 192] and LiCl [200], have been used as additives to improve cell performance.

Apart from the use of lithium salts as the additives, *Fichtner et al.* [220] reported that the addition of iodine (I_2) to the electrolyte could help the formation of a more homogeneous, less corrosive and stable interfacial layer on the Mg anode. The authors galvanostatically cycled the Mg-Mg symmetric cells with 0.4 M $\text{Mg}[\text{B}(\text{hfp})_4]_2/\text{DME}$, 0.4 M $\text{Mg}[\text{B}(\text{hfp})_4]_2/\text{DME}$ + magnesium polysulfides, 0.4 M $\text{Mg}[\text{B}(\text{hfp})_4]_2/\text{DME}$ + I_2 , 0.4 M $\text{Mg}[\text{B}(\text{hfp})_4]_2/\text{DME}$ + magnesium polysulfides + I_2 , respectively. These measurements recorded that the overpotentials of cells containing 0.4 M $\text{Mg}[\text{B}(\text{hfp})_4]_2/\text{DME}$ with or without I_2 were very similar in the initial 300 cycles (*ca.* 0.08 V). [220] After 300 cycles, a slight increase in the overpotential to *ca.* 0.18 V was detected in cells with 0.4 M $\text{Mg}[\text{B}(\text{hfp})_4]_2/\text{DME}$ electrolyte; whereas the I_2 -containing cell showed a stable overpotential. More obvious differences were observed in cells containing magnesium polysulfides with or without I_2 . Mg-Mg cells using 0.4 M $\text{Mg}[\text{B}(\text{hfp})_4]_2/\text{DME}$ + magnesium polysulfides showed large and instable overpotentials (*ca.* 0.35 V). [220] In comparison, after adding I_2 , the overpotential of the cell was optimized, which was low and relatively stable (increasing slightly from 0.08 V to 0.18 V over 700 cycles). [220] These results indicated the beneficial effects of I_2 as the additive by means of reducing the passivation of the magnesium anodes, especially in the presence of magnesium polysulfide species. The authors stated the formation of a stable, thin and homogeneous SEI layer on the Mg anode in the presence of I_2 and magnesium polysulfides (**Figure 2.22b**). [220] In comparison, a resistive, inhomogeneous and thick layer formed on the Mg anode surface from the electrolyte in the presence of magnesium polysulfides (**Figure 2.22a**). [220]

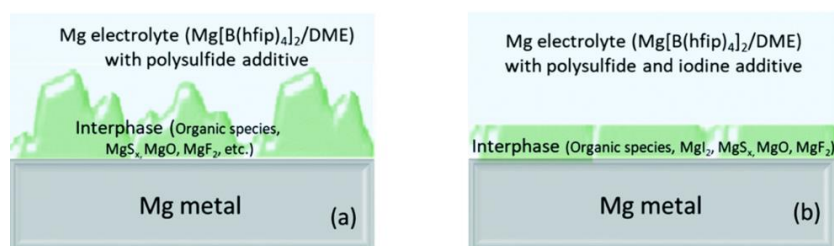


Figure 2.22: Illustration of **a)** a Mg anode cycled in a Mg electrolyte with polysulfide additive; **b)** a Mg anode cycled in a Mg electrolyte with polysulfide and I_2 additive. [220] Reproduced from the ref. [220]. Copyright (2017). Royal Society of Chemistry.

The authors also examined the chemical composition of the formed interfacial layers on the Mg anodes. Using the I₂ additive, the formation of MgI₂ on the Mg anode was observed. The authors stated that the MgI₂ layer was helpful to not only reduce the corrosion from magnesium polysulfide species to the Mg anode, but also to form an electrochemically stable and homogeneous SEI layer on the Mg anode.^[220]

Although some beneficial effects of the I₂ additive were observed in the symmetric cells, the Mg-S₈ cell using the 0.4 M Mg[B(hfip)₄]₂/DME electrolyte with the I₂ additive did not show much optimization. The authors cycled the cell at 0.05 C at room temperature. The cell delivered an initial discharge capacity of *ca.* 900 mAh g_s⁻¹, which, however, gradually dropped to only *ca.* 250 mAh g_s⁻¹ at the 100th cycle.^[220] A severe capacity decay still existed in the Mg-S cells although the use of the I₂ additive.

Chapter 3

Research Objectives

As discussed in **Chapter 2.5**, one major challenge in the field of Mg-S batteries is the lack of compatible electrolyte systems, although great efforts have been made over the last decade. Therefore, the objectives of this work were to develop and improve the electrolyte systems for the high-performance Mg-S batteries, especially for Mg-SPAN batteries and to understand the underlying mechanisms. The detailed objectives for each sub-project are listed as below.

In the first sub-project, the main objective was to investigate the use of SPAN cathodes in rechargeable Mg batteries. Based on the obtained results from this project, and despite an average cell performance, the possibility of reversible cycling of Mg-SPAN cells over 70 cycles was demonstrated.

In the second sub-project, the objective was to further improve the electrochemical performance of Mg-SPAN batteries, regarding cycle stability and specific capacities. By using a Mg²⁺/Li⁺ hybrid electrolyte (Li[BH₄] and Mg[BH₄]₂ in diglyme), the performance of the Mg-SPAN cells have been successfully improved (*ca.* 800 mAh g_s⁻¹ with > 99% Coulombic efficiency for 100 cycles at C/10).

In the third sub-project, the main objective was to understand the role of a lithium salt in a Mg-SPAN battery. At the same time, due to the low solubility of the Mg[BH₄]₂ (0.1 M) in the previous electrolyte system, an electrolyte, which can dissolve both magnesium and lithium salts had to be found. As a step further, the reaction mechanism of Mg-SPAN batteries containing a Mg²⁺/Li⁺ hybrid electrolyte was also an objective.

The application of a Mg²⁺/Li⁺ hybrid electrolyte, together with an SPAN cathode, resulted in outstanding electrochemical performance, with regards to cycle stability and rate capability, compared to existing reports. One of the main reasons leading to the high-

performance Mg-SPAN batteries was the successful suppression of the polysulfide shuttle. Since gel-polymer-electrolytes have also been reported to be able to reduce the polysulfide shuttle in Li-S batteries and there had barely reports on gel-polymer-electrolytes for Mg-S/ion batteries, the objectives for the fourth sub-project were the conceptualization and design of a gel-polymer-electrolyte for Mg-S and Mg-ion batteries.

Chapter 4

Magnesium-Sulfur Batteries Based on SPAN Cathodes

4.1 Motivation

In recent years, a few electrolyte systems have been developed for Mg-S batteries. Among these reported electrolytes, the electrolyte containing the non-corrosive conductive salt, $\text{Mg}[\text{B}(\text{hfip})_4]_2$, published by *Fichtner et al.*^[184, 194] in 2017 and 2018 respectively, showed several promising features. For example, the $\text{Mg}[\text{B}(\text{hfip})_4]_2$ -containing electrolyte allowed for a reversible magnesium plating and stripping in cyclic voltammetry (CV) using Pt as the working electrode (**Figure 4.1a**). In addition, the electrolyte showed relatively good oxidative stability against the common current collectors, such as copper (~2.8 V), carbon-coated aluminum foil (~3 V), stainless steel (~4 V) and Pt (3.5 V) (**Figure 4.1b**).^[194] These results suggested that electrolytes containing $\text{Mg}[\text{B}(\text{hfip})_4]_2$ showed promising compatibility with the Mg anodes.

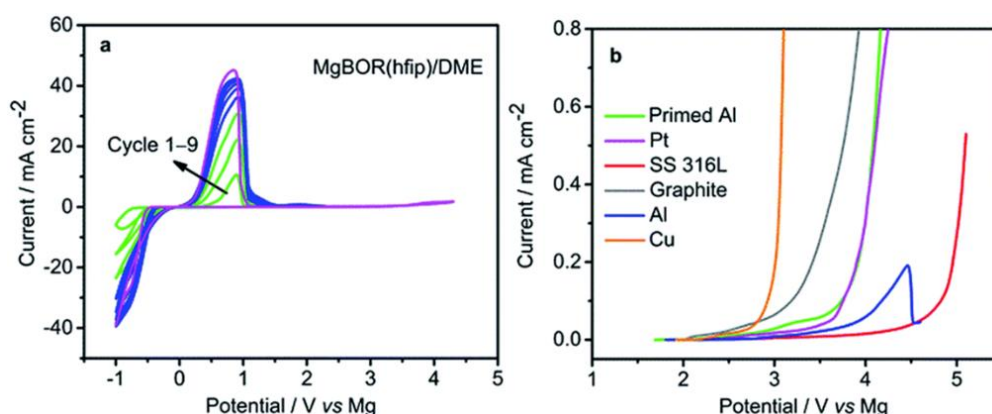


Figure 4.1: a) CV scans of Mg-Pt cell using the 0.6 M $\text{Mg}[\text{B}(\text{hfip})_4]_2/\text{DME}$ electrolyte at 25 mV s^{-1} ; b) LSV analysis of the 0.6 M $\text{Mg}[\text{B}(\text{hfip})_4]_2/\text{DME}$ against various current collectors.^[184] Reproduced with permission from ref.^[184]. Copyright (2017). Royal Society of Chemistry.

Further on, the $\text{Mg}[\text{B}(\text{hfp})]_4)_2$ -containing electrolytes also allowed for a reversible cycling of the Mg-S cells. **Figure 4.2** shows the voltage profiles and the cycle stability tests of Mg cells using a $\text{Mg}[\text{B}(\text{hfp})]_4)_2$ -based electrolyte at 0.1 C at room temperature with two different elemental sulfur-based cathodes, namely S-CMK-3 and ACC/S cathodes, respectively. In both cases, the plateaus at *ca.* 1.5 V and 1.2 V in the discharge curve indicated the stepwise reduction of the elemental sulfur (**Figure 4.2 a and c**). In addition, a gradual capacity fading and slight overcharging, especially in the initial cycles, were observed in both cell systems (**Figure 4.2 b and d**), which was most likely due to the polysulfide shuttle.^[194]

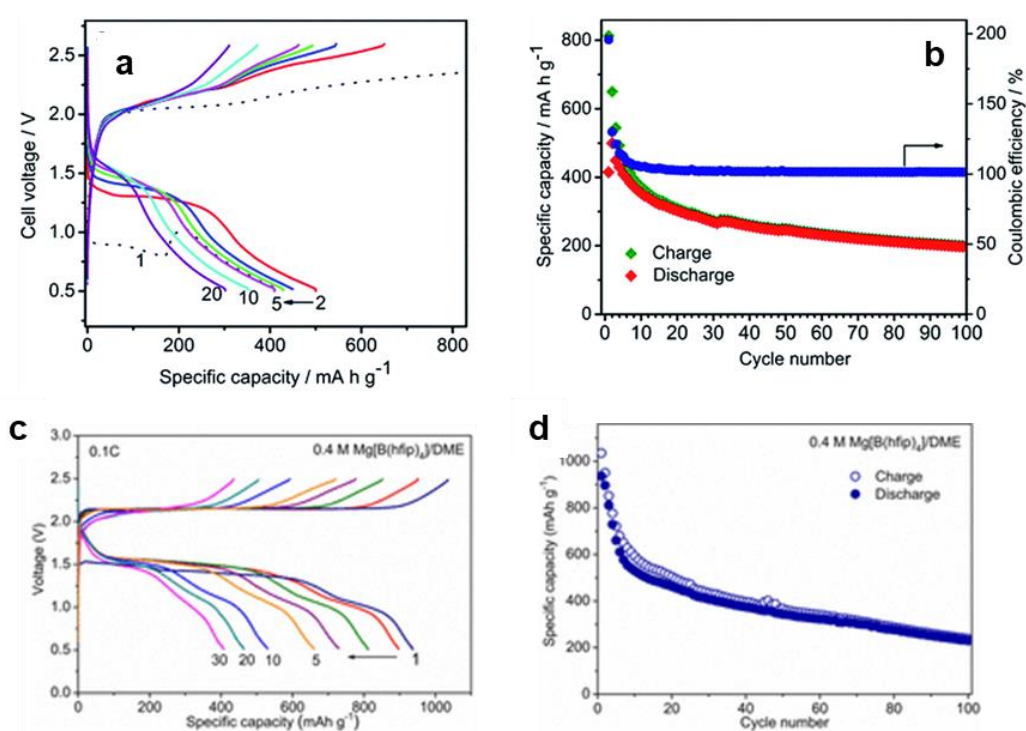


Figure 4.2: **a)** Voltage profile; **b)** cycle stability test of the Mg/S-CMK-3 cell using a $\text{Mg}[\text{B}(\text{hfp})]_4)_2$ /diglyme-tetraglyme (1-1, v-v) electrolyte at 0.1 C;^[184] Reproduced with permission from ref.^[184]. Copyright (2017). Royal Society of Chemistry. **c)** Voltage profile; **d)** cycle stability test of the Mg-ACC/S cell using 0.4 M $\text{Mg}[\text{B}(\text{hfp})]_4)_2$ /DME at 0.1 C.^[194] Reproduced with permission from ref.^[194]. Copyright (2018). American Chemical Society.

The promising properties of the $\text{Mg}[\text{B}(\text{hfp})]_4)_2$ -based electrolytes; however, the unsatisfactory cell performances of the Mg-S₈ cells, encouraged the further developments of Mg-S cells using this electrolyte.

4.2 Publication: “Characteristics of Magnesium-Sulfur Batteries Based on a Sulfurized Poly(acrylonitrile) Composite and a Fluorinated Electrolyte”

The use of SPAN-based cathodes in Li-S batteries showed high capacity retention and good cell reversibility due to the fact that sulfur is covalently bound to the carbonaceous matrix, which can better immobilize sulfur species than conventional cathodes based on elemental sulfur. However, in Mg-S batteries, SPAN has been barely reported as cathode materials.

In this sub-project, Mg-S cells were electrochemically characterized using an SPAN-based cathode, a Mg foil anode and the above-discussed $\text{Mg}[\text{B}(\text{hfp})]_4$ -based electrolyte. Electrochemical characterizations, such as cycle stability test, cyclic voltammetry analysis and rate capability test, *etc.*, were conducted. In addition, the cell performances of Mg-SPAN cells using a standard Mg foil anode and a Mg pressed anode, which possessed a larger surface area and more active sites, were studied. Furthermore, an understanding of the voltage profiles of Mg-SPAN cells, which differed from those of reported S_8 -based cathodes, was developed. Moreover, *post-mortem* analysis of the electrodes was conducted in order to understand the reaction mechanism of a Mg-SPAN battery.

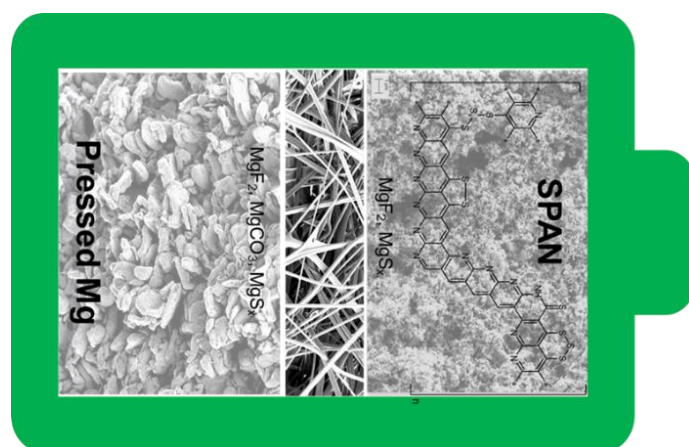


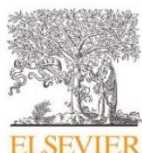
Figure 4.3: Graphical abstract of the publication “Characteristics of magnesium-sulfur batteries based on a sulfurized poly(acrylonitrile) composite and a fluorinated electrolyte”.

Publication

P. Wang, J. Kappler, B. Sievert, J. Häcker, K. Küster, U. Starke, F. Ziegler, M. R. Buchmeiser, *Electrochim. Acta* **2020**, *361*, 137024.

Author Contributions: P. Wang: Conceptualization, Investigation, Writing - original draft, Writing - review & editing; J. Kappler: Conceptualization, Writing - review; B. Sievert: Sample Preparation; J. Häcker: Sample preparation, Writing- review & editing; K. Küster: XPS Characterization, Writing - review & editing; U. Starke: XPS Characterization, Writing - review & editing; Felix Ziegler: BET Characterization; M. R. Buchmeiser: Conceptualization, Supervision, Writing - original draft, Writing - review & editing

Reprinted with permission from the © 2020 Elsevier Ltd.



Contents lists available at ScienceDirect

Electrochimica Acta

journal homepage: www.elsevier.com/locate/electacta

Characteristics of magnesium-sulfur batteries based on a sulfurized poly(acrylonitrile) composite and a fluorinated electrolyte

Peiwen Wang¹, Julian Kappler¹, Brigitta Sievert³, Joachim Häcker³, Kathrin Küster⁴, Ulrich Starke⁴, Felix Ziegler¹, Michael R. Buchmeiser^{1,2,*}

¹ Institute of Polymer Chemistry, University of Stuttgart, 70569, Stuttgart, Germany

² German Institutes of Textile and Fiber Research (DITF) Denkendorf, 73770 Denkendorf, Germany

³ Institute of Engineering Thermodynamics, German Aerospace Center, 70569 Stuttgart, Germany

⁴ Max Planck Institute for Solid State Research, 70569 Stuttgart, Germany

ARTICLE INFO

Article history:

Received 23 June 2020

Revised 24 August 2020

Accepted 26 August 2020

Available online 11 September 2020

Key words:

Magnesium foil
Pressed magnesium anode
Sulfur batteries
SPANBackspace
SEI formation

ABSTRACT

A magnesium-sulfur (Mg-S) battery system based on a sulfurized poly(acrylonitrile) ("SPAN") composite as cathode material is presented. Using magnesium tetrakis(hexafluoroisopropoxy) borate, $\text{Mg}[\text{B}(\text{hfp})_4]_2$, as conductive salt in the electrolyte, the cycle performance of Mg-S batteries based on SPAN and different types of Mg anodes, i.e. Mg foil and pressed Mg powder, respectively, were compared. A cell composed of Mg foil and SPAN delivered a discharge capacity around 300 $\text{mAh/g}_{\text{sulfur}}$ at C/30 while a cell based on SPAN and pressed Mg powder delivered ca. 500 $\text{mAh/g}_{\text{sulfur}}$ (energy density of ca. 422 $\text{mWh/g}_{\text{sulfur}}$) at C/30 and also possessed good rate capability. The higher discharge capacities of Mg-S cells based on pressed anodes are attributed to the substantially higher specific surface area of the pressed cells. *Post-mortem* analysis of aged cells based on SPAN and a pressed Mg anode indicates the formation of MgF_2 on both the cathode and the anode along with magnesium polysulfide species.

© 2020 Elsevier Ltd. All rights reserved.

1. Introduction

The growing demand for efficient energy storage materials currently results in substantial research in the area of *post-lithium* ion battery (LIB) technology. Rechargeable magnesium-sulfur (Mg-S) batteries are considered promising candidates due to the high earth abundance and high theoretical energy density of both sulfur ($1672 \text{ mA}\cdot\text{h}\cdot\text{g}^{-1}$) and magnesium ($3832 \text{ mA}\cdot\text{h}\cdot\text{cm}^{-3}$) compared to lithium ($2062 \text{ mA}\cdot\text{h}\cdot\text{cm}^{-3}$) or sodium ($1128 \text{ mA}\cdot\text{h}\cdot\text{cm}^{-3}$) [1]. At the same time, magnesium is predominantly reported to preferably plate in a non-dendritic manner, which translates into higher safety characteristics in commercial applications [2–4].

Despite their promising features, research activities on Mg-S batteries are so far quite limited, which is in stark contrast to Li-S battery technology. In terms of electrolytes, most of them comprise Al-, B- or Y-based Lewis acids together with a magnesium-derived Lewis base prepared via a transmetalation reaction [1, 5–14]. For example, the sole use of magnesium trifluoromethanesulfonate, $\text{Mg}(\text{CF}_3\text{SO}_3)_2$, resulted in poor electrochemical performance [15, 16] while the combination of $\text{Mg}(\text{CF}_3\text{SO}_3)_2$ with AlCl_3 , MgCl_2 ,

anthracene or LiCl, provided decent reversibility and discharge capacities [17, 18].

In terms of cathode materials, various porous, conductive, high-surface area carbon additives including carbon black [19], CMK-3 [13, 16, 20], nitrogen-doped graphene [21], carbon nanotubes [8], activated carbon clothes [7, 22], microporous carbon [11], reduced graphene oxide [23], graphdiyne [8], metal organic frameworks [24], dually nitrogen- and sulfur-doped carbon [25] and porous carbon modified with ionic surfactants [26] have been used to accommodate the sulfur. Generally, these carbonaceous materials are designed such that the final composite possesses high electrical conductivity and a good interaction with both the sulfur and the polysulfides to improve the utilization of active material and to reduce the diffusion of polysulfides [23]. At the same time, it should display substantial mechanical stability to uphold the volume change caused by the reduction and oxidation of sulfur during cycling [23].

Sulfurized poly(acrylonitrile) ("SPAN", Fig. 1) [27–29] has been thoroughly investigated as cathode material in Li-S batteries. The most important feature of SPAN is that the sulfur is not physisorbed to the material but *chemically* bound to the polymeric backbone, most probably in form of vinyllogous/phenylogous enolic thioamides, which allows for the formation of intra- and intermolecular polymer-S_x-polymer chains with $2 \leq x < 8$ (Fig. 1). It is this special feature, i.e. the thioamide bond in its enolate form, that

* Corresponding author.

E-mail address: michael.buchmeiser@ipoc.uni-stuttgart.de (M.R. Buchmeiser).

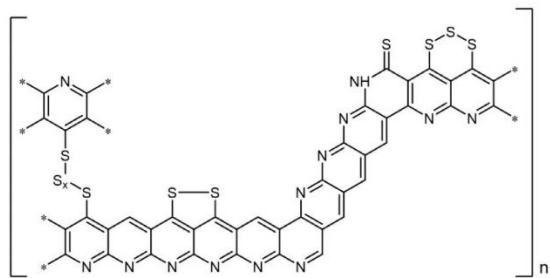


Fig. 1. Proposed structural motifs in SPAN, in which the sulfur is covalently bound to the matrix [30].

distinguishes SPAN from most other S-based cathodes. In fact, the anionic enolic thioamides or pyrid-2-ylthiolates serve as “docking stations” for sulfides during charging, which results in the reformation of the above-mentioned oligomeric sulfur chains attached to the polymeric backbone. In due consequence, SPAN allows for a poly(sulfide) shuttle-free cycling of cells up to discharge/charge rates of 8C for more than 1100 cycles with an overall loss of <10% [27–30]. Combination of this unique feature with the use of soluble organosulfides like dimethyltrisulfide (DMTS) allows for the realization of a DMTS-based catholyte that offers access to real capacities up to 4.3 mA h cm^{-2} [31].

In view of the promising properties of SPAN composites as the active cathode materials in Li-S batteries, it was worthwhile to study the electrochemical behavior of Mg-S batteries based on the same cathode material, which, to our best knowledge, has barely been exploited in the field of Mg-S batteries [32, 33]. Here, we report the electrochemical performance of Mg-SPAN cells using $\text{Mg}[\text{B}(\text{hfp})_4]_2$ as conductive salt in the electrolyte. The electrochemical performance of different types of Mg anodes including those based on Mg foil and pressed Mg anodes, are compared. The detailed surface chemistry study on both of the electrodes was also conducted by high resolution X-ray photoelectron spectroscopy.

2. Experimental

2.1. General

All samples were handled in an Ar-filled glove box with water and oxygen levels <0.1 ppm. Chemical syntheses were carried out using standard Schlenk techniques. All glassware was dried in an oven at 120°C . $\text{Mg}(\text{BH}_4)_2$ (95%), poly(acrylonitrile) (PAN, average $M_w=150,000 \text{ g/mol}$, $D=3.6$) and anhydrous 1,2-dimethoxyethane (DME, 99.5%) were purchased from Merck and used as received. 1,1,1,3,3,3-Hexafluoroisopropanol (99%, TCI) was distilled over 4 Å molecular sieves and stored inside the glovebox. Magnesium powder (325 mesh, 99.8%) was purchased from Alfa Aesar and used as received. Magnesium foil was polished thoroughly inside the glovebox prior to use.

^1H , ^{11}B , ^{19}F and ^{13}C nuclear magnetic resonance (NMR) measurements were recorded at 400, 128, 376 and 101 MHz on a Bruker Avance III 400 at room temperature. Attenuated total reflection-infrared spectroscopy (ATR-IR) spectra of PAN and SPAN were recorded on a Bruker ALPHA Platinum ATR spectrometer in the range of 4000 to 400 cm^{-1} . The weight percentage of elements (C, H, N, S) of SPAN and $\text{Mg}[\text{B}(\text{hfp})_4]_2$ were determined by an Elemental Analyzer (varioMACROcube) at the Institute of Inorganic Chemistry, University of Stuttgart. Scanning electron microscopy (SEM) was carried out on a Zeiss Auriga at the DITF Denkendorf, Germany. For the cross-section image, the pressed anode was cut from the middle and the cross section was measured. For *ex-situ* XPS mea-

surements, Mg-S cells were disconnected from the BasyTech after 7 cycles. Two different states of the electrodes were analyzed, (i) discharged to 1.5 V and (ii) discharged to 0.1 V. All cells were opened in an Ar-filled glovebox and the electrodes were thoroughly rinsed with DME, dried in vacuo overnight to remove all electrolyte and solvent. For XPS measurements, the electrodes were fixed on a sample holder and transferred under argon atmosphere directly into the X-ray photoelectron spectrometer to avoid any contamination with air. XPS was performed on a Kratos Axis Ultra system equipped with a monochromated $\text{Al } K_{\alpha}$ source using a pass-energy of 20 eV for high-resolution measurements. Data was analyzed using CasaXPS. Energy separation and determination of the peak areas of the $\text{S } 2p_{3/2}$ and $\text{S } 2p_{1/2}$ were accomplished according to the literature [34]. Signals were calibrated using the $\text{C } 1s$ signal at 284.8 eV. N_2 -gas adsorption measurements of the pressed Mg anode were conducted on an automated gas sorption analyzer (Autosorb iQ). The Mg powder was placed inside of the sample tube and outgassed for 16 h. Measurements was conducted at 77.35 K. The Brunauer-Emmett-Teller (BET) method was used for calculating the specific surface areas. The specific surface area of the Mg-foil was too low to be measured and was therefore calculated on the base of the area ($\sigma = 2\pi r^2$).

2.2. Preparation of SPAN-Based cathodes

SPAN was synthesized according to previous reports [30]. Briefly, a mixture of PAN and excess S_8 was reacted at 550°C for 5 h in a nitrogen atmosphere. Excess S_8 was removed by Soxhlet extraction using toluene. Electrode sheets were prepared by coating a mixture of SPAN: carbon black: poly(vinylidene difluoride) (PVDF, 70:15:15 wt.-%), in *N*-methyl-2-pyrrolidone (NMP) on an Al/C foil. After drying the coating at 60°C overnight, cathode chips 12 mm in diameter were punched out. The sulfur content in SPAN was ca. 40 wt.-%. The average sulfur content in each cathode was 0.6 mg/cm^2 .

2.3. Preparation of anodes based on mg powder

As-received magnesium powder was pressed with the aid of a hydraulic press and a homemade die with a diameter of 11 mm applying a pressure of 75 MPa.

2.4. Preparation of the electrolyte

The synthesis of $\text{Mg}[\text{B}(\text{hfp})_4]_2 \cdot 3 \text{ DME}$ was conducted according to the literature [13]. $\text{Mg}[\text{BH}_4]_2$ powder (0.4 g, 7.4 mmol) was dissolved into 30 mL anhydrous DME in a Schlenk flask. Excess $\text{HOC}(\text{H})(\text{CF}_3)_2$ (8.2 equivalents, 6.4 mL, 60.7 mmol) was added dropwise to a stirred solution of $\text{Mg}[\text{BH}_4]_2$ in DME over 30 min. Due to the exothermic reaction, the addition of $\text{HOC}(\text{H})(\text{CF}_3)_2$ was conducted in an ice bath. After stirring at room temperature for 1 h, the flask was equipped with a Dimroth condenser, and the reaction was refluxed at 80°C under Ar for 7 h. After the mixture had cooled to room temperature, the solvent was removed in vacuo. The solid was then ground and dried at 50°C for 5 h. ^1H NMR (400 MHz, $\text{DMSO}-d_6$) δ [ppm]: 3.23 (s, 18H, $\text{DME}-\text{CH}_3$), 3.42 (s, 12H, $\text{DME}-\text{CH}_2$), 4.63 (s, 8H, CH). ^{19}F -NMR (376 MHz, $\text{DMSO}-d_6$) δ [ppm]: -74.81 (48F, CF_3). ^{11}B -NMR (128.42 MHz, $\text{DMSO}-d_6$) δ [ppm]: 1.54. ^{13}C NMR (101 MHz, $\text{DMSO}-d_6$) δ [ppm]: 58.2 (s, DME), 69.6 (septet, CH, $J = 32.2 \text{ Hz}$), 70.2 (s, DME), 123.0 (q, CF_3 , $J = 284.6 \text{ Hz}$). The NMR spectra can be found in Figures S1–S4 (S.I.).

The conductive salt $\text{Mg}[\text{B}(\text{hfp})_4]_2 \cdot 3 \text{ DME}$ (1.3 g) was dissolved in a glass vial containing 1 mL of diglyme/tetraglyme (v/v, 1/1) inside the glovebox. The electrolyte was stirred overnight, filtered and then stored over molecular sieves for one day prior to use.

2.5. Electrochemistry

Cells were assembled in an Ar-filled glove box. Galvanostatic cycle and stress tests were conducted using Swagelok T-cells using either Mg foil or pressed Mg as anode and SPAN as cathode, separated by two pieces of Whatman glass fiber separators. The electrochemical data were recorded by a BasyTec XCTS-LAB system. For the charge process, a constant voltage step was added at the end, using the indicated cut off time and a current rate of 0.01 C.

Cyclic voltammetry measurements were performed with a three-electrode PAT cell from EL-cell® using Mg as both the counter and reference electrode and SPAN as the working electrode. Electrochemical impedance spectroscopy (EIS) data measured with a signal amplitude of 10 mV in a frequency range from 300 kHz to 100 mHz on Biologic VMP3. Data were fitted using the integrated EC-Lab software.

3. Results and discussion

3.1. Cathode material and electrolyte

The applied cathode material, SPAN, was synthesized according to previous studies [28, 29]. Notably, all excess elemental sulfur was removed by extensive Soxhlet extraction with toluene; consequently, all detected sulfur is covalently bound to the carbon structure. Elemental analysis data revealed a sulfur content of 40 wt.-%. A comparison of the infrared (IR) spectra of PAN and SPAN (Figure S5, S.I.) confirmed the successful synthesis of SPAN.

Magnesium tetrakis(hexafluoroisopropoxy) borate, $\text{Mg}[\text{B}(\text{hfip})_4]_2$ [14], containing a weakly coordinating anion, was used as conductive salt in a mixture of diethyleneglycol dimethyl ether (diglyme) and tetraethyleneglycol dimethyl ether (tetraglyme, v/v, 1/1). Tetraglyme was chosen because of its high dielectric constant ($\epsilon = 7.7$), which was expected to help dissolution of the conductive salt; whereas diglyme was used to lower the overall viscosity of the electrolyte system.

The anodic stability of a 0.8 M solution of $\text{Mg}[\text{B}(\text{hfip})_4]_2$ in diglyme/tetraglyme (v/v, 1/1) was examined by linear sweep voltammetry (Figure S6a, S.I.), which indicates that the electrolyte shows high stability (3.3 V vs. Mg/Mg^{2+}) on Al/C current collector. This result is in line with those of Zhao-Karger et al. [14]. To study the Mg plating and stripping performance of the electrolyte, cyclic voltammetry (CV) was performed using Al/C as working electrode and Mg foil as counter electrode at a scan rate of 1 mV s^{-1} (Figure S6b, S.I.). The first scan shows an oxidative current due to the Mg stripping starting at ca. 0.4 V and a reduction peak associated with Mg plating starting at ca. -0.72 V. Notably, the overpotential for Mg plating decreased to only ca. -0.1 V in the 4th cycle. At the same time, the current increased during cycling, indicating an improved Mg plating/stripping during scanning [13].

Further on, the polarization behavior of the electrolyte was also investigated using Swagelok-type symmetric Mg-Mg cells. Galvanostatic cycling experiments were carried out by discharging and charging at a constant current rate for 0.5 h respectively. As shown in Figure S7a (S.I.), the polarization overpotential of the system is around 0.1 V at 1 mA cm^{-2} for at least 60 cycles, indicating the small energy barrier for Mg plating and stripping and the stable cycling. For the determination of the Coulombic efficiency, asymmetric Mg-Al/C cells were built and cycled at 1 mA cm^{-2} . As shown in Figure S7b (S.I.), > 96% Coulombic efficiency was achieved upon cycling, indicating a comparably good reversibility.

3.2. Electrochemical behavior of the mg-span cells

The electrochemical performance of the Swagelok-type cell composed of an SPAN cathode, a Mg foil anode and 0.8 M

$\text{Mg}[\text{B}(\text{hfip})_4]_2$ in diglyme/tetraglyme (1/1, v/v) electrolyte was characterized at a current rate of C/30 at 25 °C (Figure S8a, S.I.). The reason to use a concentrated electrolyte (0.8 M $\text{Mg}[\text{B}(\text{hfip})_4]_2$ in diglyme/tetraglyme) was to suppress the dissolution of the magnesium polysulfides, a common issue in Mg-S batteries [14]. The cell delivered only ca. 100 $\text{mAh/g}_{\text{sulfur}}$ during the initial cycle; however, capacities gradually increased upon charging and discharging and reached a discharge capacity of ca. 300 $\text{mAh/g}_{\text{sulfur}}$ in the 30th cycle. In order to obtain a better insight into the cell behavior, the galvanostatic discharge/charge profile from the same cell is shown in Figure S8b (S.I.). It is worth to mention that the charging process includes two steps, i.e. a constant current step (0.1 – 3 V) and a constant voltage step (3 V). The use of a constant voltage step was also reported for other sulfur batteries [35, 36], in order to fully charge the batteries. As can be seen from the galvanostatic curves (Figure S8b, S.I.), the gap of the charge and discharge profile gradually decreased, indicating that the polarization of the system gradually decreased during cycling; consequently, less energy is needed for Mg plating and stripping, leading to a capacity increase during cycling.

Furthermore, in order to further understand the decreased polarization and the improved cycle behavior, electrochemical impedance spectroscopy (EIS) was carried out on the symmetric Mg-Mg cells containing the above-mentioned electrolyte. The Nyquist plot (Figure S9, S.I.) shows the resting Mg-Mg symmetric cell at OCV and after cycling. The plot was fitted according to the model shown in the inset, comprising the high frequency resistance (R_1) and two RC (resistor and capacitor in parallel) elements in series. The two RC elements model the charge transfer reaction (R_2 and Q_2) and a most likely blocking layer on the anode (R_3 and Q_3). The exact value of the fitting data can be found in Table S1 (S.I.). Interestingly, impedance decreased dramatically from 4233 Ω to 70 Ω after the first polarization cycle. This suggests the existence of an adsorption layer between the electrolyte and Mg anode surface before cycling. However, upon polarization, the layer is removed and Mg particles are depositing on the anode, leading to a fresh Mg surface with a higher surface area [37]. This phenomenon has also been observed by Häcker et al. [37]. During cycling, the impedance still dropped, which might be due to the activation of the Mg anode by the continuous Mg plating. This is also in accordance with the charge and discharge profile shown in Figure S8 (S.I.).

In view of the low specific surface area of Mg foils and the proposed non-dendritic growth of Mg during plating [3, 4], we surmised that an anode with a higher surface area might be beneficial. Consequently, the Mg foil was replaced by pressed Mg pellets to improve cell performance. Pressed Mg pellets were fabricated by hydraulically pressing the as-received Mg powder consisting of particles with an average size of 44 μm at 75 MPa.

Using again 0.8 M $\text{Mg}[\text{B}(\text{hfip})_4]_2$ in diglyme/tetraglyme (1/1, v/v) and SPAN as cathode, the cell was cycled between 0.1 – 3 V at C/30 (Fig. 2a). The cell successfully cycled over 70 cycles and delivered an initial discharge capacity of ca. 120 $\text{mAh/g}_{\text{sulfur}}$. The discharge capacity steadily increased to ca. 550 $\text{mAh/g}_{\text{sulfur}}$ (ca. 207 $\text{mAh/g}_{\text{SPAN}}$) over the first 20 cycles and then remained at that level. A detailed comparison between this work and the current state of the art in Mg-S batteries is provided in Table S2 (S.I.). The performance of the Mg-SPAN cells shown here is among the best in the field of Mg-S batteries, using a magnesium conductive salt as electrolyte.

In addition, in order to have further information about the electrochemical behavior of Mg-S battery at higher current rate and its rate capability, rate capability tests were carried out by cycling the cell between C/30 and C/5 (Fig. 2c). Discharge capacities also showed an increasing trend in the first 20 cycles, even when increasing the discharge/charge rate, which is in accordance with

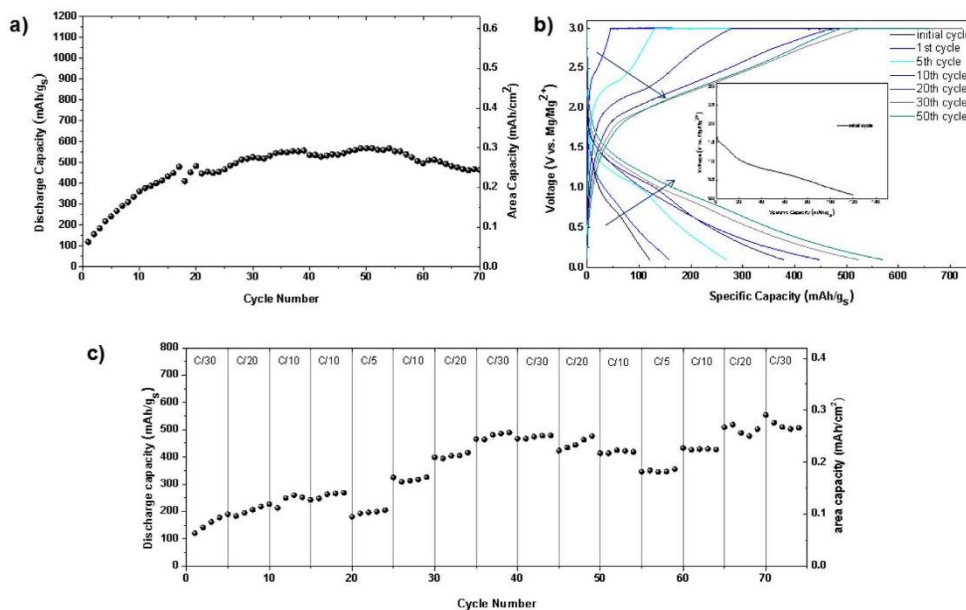


Fig. 2. Electrochemical behavior of a cell composed of a SPAN-based cathode, a pressed Mg anode and 0.8 M $\text{Mg}[\text{B}(\text{hfp})_4]_2$ in diglyme/tetraglyme (1/1, v/v); a) cycle stability of a cell cycled at C/30; b) typical charge and discharge profile of the cell containing 0.8 M $\text{Mg}[\text{B}(\text{hfp})_4]_2$ in diglyme/tetraglyme at C/30 (the charge process is composed of two steps: constant current step and constant voltage step at 3 V); c) rate capability test results of the cell cycling between C/30 to C/5. For all the cathodes, sulfur content was around 0.6 mg/cm^2 .

the previous cells. After the 20th cycle, higher discharge rates resulted in lower discharge capacities. The corresponding Coulombic efficiency is shown in Figure S10b (S.I.). The discharge capacity fully recovered up to 525 $\text{mAh}/\text{g}_{\text{sulfur}}$ (ca. 207 $\text{mAh}/\text{g}_{\text{SPAN}}$, 0.28 mAh/cm^2), when lowering the rate to C/30. At a relatively high rate of C/5, the cell still delivered a high discharge capacity of around 350 $\text{mAh}/\text{g}_{\text{sulfur}}$ (0.2 mAh/cm^2), indicating a good rate capability of the system.

The capacity increase phenomenon in the initial cycles is similar to the cell with the Mg foil anode. The galvanostatic charge and discharge profiles with the cell containing pressed anodes (Fig. 2b) shows similar features. This suggests that the voltage hysteresis (voltage gap between charge and discharge) also drops upon initial cycling, leading to a lower energy barrier for Mg plating/stripping and the increase of the discharge capacity. As discussed earlier, this might be due to the activation of the Mg surface by the continuous Mg plating, and the penetration of the electrolyte in to the cathode material [7].

Further on, the reason for the better cycle performance of cells based on a pressed Mg anode can be explained by its higher surface area compared to the one of a Mg-foil. As can be deduced from SEM images, the pressed magnesium anodes have a highly porous structure, the cross-section of which can be seen in Figure S11 (S.I.). The average particle size of the magnesium powder of 44 μm results in a higher specific surface area of the pressed Mg anode of 0.604 m^2/g (Figure S12, S.I.) as compared to the one of Mg foil (0.002 m^2/g). Clearly, the 300 times higher surface area of the Mg anode can be made accountable for the better electrochemical performance. In addition, during cycling, fresh Mg keeps depositing onto the Mg anode. Due to the much higher surface area in the pressed anode compared to Mg foil, there is higher possibility for fresh Mg deposition on the anode, resulting in a better charging behavior than in a cell based on Mg foil.

Similar to the discharge curves of SPAN-based Li-S batteries [27, 28, 38], the discharge curves obtained after twenty cycles were sloped instead of plateaued, starting around 1.6 V. By contrast, in the discharge curves of the first 20 cycles, some tiny voltage plateaus were observed (Fig. 2b insert). This suggests that in the first cycles, some polysulfides (MgS_4) might be formed during discharging [38]. The formed polysulfides tend to dissolve in ether-based solvents. At a certain point, however, the electrolyte is saturated and no polysulfides can be further dissolved due to the high concentration of the electrolyte. Therefore, from the 20th cycle on, only sloped potential curves were observed. This might be attributed to solid-to-solid single-phase reactions between SPAN and MgS or Mg_2S [38]. Indeed, according to the *ex-situ* UV-VIS study of the cycled electrolyte (after 40 cycles at a discharge state, Figure S13, S.I.), the peak corresponding to MgS can be detected [39]. By integrating the discharge curve, an energy density of ca. 422 $\text{mWh}/\text{g}_{\text{sulfur}}$ can be obtained.

To shed light on the different polysulfides species formed during the initial cycling, cyclic voltammetry (CV) was conducted with a three-electrode cell (PAT-cell from EL-CELL) using SPAN as the working electrode (WE) and Mg foil as the counter and reference electrode (Mg_{CE} and Mg_{RE}), respectively. Typical CV curves are presented in Fig. 3a. During the first five scans, the main reduction peak at 1.5 V can be observed. The oxidation peak appeared at around 2.4 V. In the subsequent cycles, the oxidative peak and reductive peak slightly shifted to lower and higher voltage, respectively, which is in accordance with the charge and discharge profile, suggesting the decrease of the voltage hysteresis. At the same time, the potentials vs. Mg_{CE} were measured, too (Fig. 3b). The reduction peaks appeared at a slightly lower potential of 1.3 V compared to the peak value vs. Mg_{RE} . Nevertheless, the oxidative peaks shifted to around 2.7 V, indicating that the recharge of the SPAN cathode is mainly restricted by the half-reaction at the Mg_{CE} . Furthermore, the potential change of Mg_{CE} (vs. Mg_{RE})

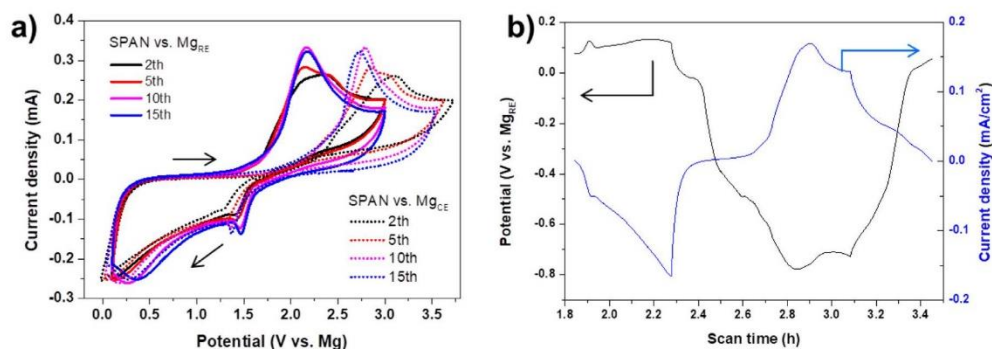
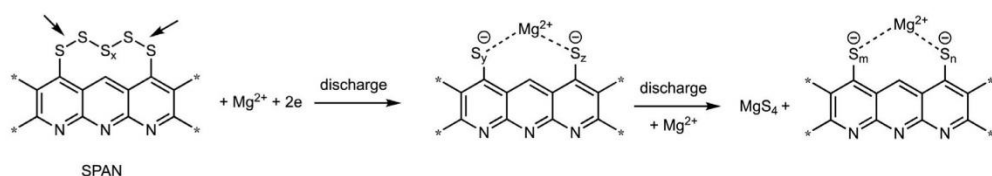
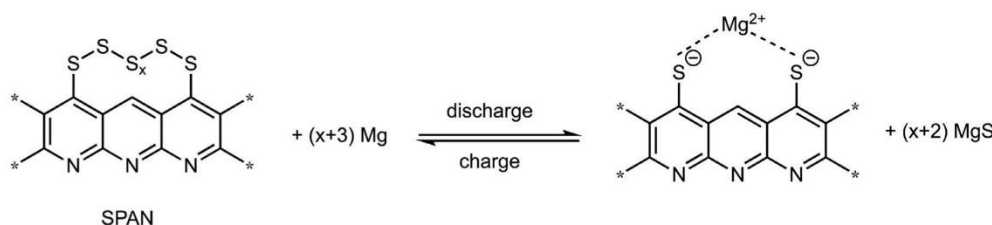


Fig. 3. a) CV of SPAN cathode using a three-electrode setup; b) potential change of Mg_{CE} and current wave of SPAN versus scan time. Scan rate was 1 mV/s.



Scheme 1. Proposed discharge reaction of SPAN.



Scheme 2. Proposed overall charge and discharge reaction of SPAN used in a Mg-S battery.

was also recorded simultaneously during the redox process with the three-electrode system. Fig. 3b shows the second CV cycle, where the voltage of Mg_{CE} was around 0.1 V when the reductive potential was applied, which is in line with the polarization potential value (Figure S7, S.I.). By contrast, a substantial potential drop of about -0.8 V was detected during the cathodic scan, indicating the sluggish reaction of the reduction of Mg^{2+} to $Mg(0)$. This might be due to the dissolved MgS_x species in the electrolyte [14].

In addition, the corresponding oxidation and reduction peaks shown in the CV curves in the initial cycles can also give some hints to the formed magnesium polysulfide species. Table S3 (S.I.) summarizes various magnesium polysulfide species during discharge, the theoretical discharge capacity delivered in each step, as well as the corresponding potentials at which they are formed, according to reported studies [6, 40]. In the second and fifth cycle of the CV test, two weak reductive peaks appeared around 1.3 V and 0.2 V, respectively. Their observation is consistent with the discharge profile of the initial cycle, which shows two short voltage plateaus and which suggests the formation of some lower order magnesium (poly)sulfide intermediates, MgS_4 , MgS [14]. Due to the similar Gibbs free energies [6], these different polysulfide species can co-exist in solution. In the following cycles, the main reduction peak at 1.3 V shifted to around 1.4 V in the corresponding CV, which can be correlated with the voltage plateau around 1.4 V. At the same time, this main reduction peak increases in intensity, in-

dicating an improved reversibility of the cell during cycling. Based on its potential of 1.4 V, the formation of MgS_4 is proposed [14]. The small shoulder around 0.4 V can be assigned to the formation of MgS or MgS_2 . In the reverse oxidative scan, the CV showed a large and broad signal around 1.8 - 2.5 V in the initial cycles, indicating the co-existence of different forms of Mg polysulfides, i.e. of MgS_4 , MgS_2 and MgS . In the following cycles, a broad peak at ca. 2.2 V were observed, indicating the conversion of MgS to MgS_4 and SPAN [14].

Overall, these observations are in line with the divalent nature of Mg. During discharge, as illustrated in Scheme 1, the sulfur chains in SPAN are proposed to be reductively broken at some point to form $^{-}S_y$ -SPAN- S_z^{-} species, which are further reduced stepwise from the end of the chain forming short chain polysulfides, i.e. MgS_2 and MgS , until all sulfur is fully reduced. At the same time, as outlined above, MgS_4 is formed during the initial cycles, along with MgS and MgS_2 . Upon cycling, only a sloped potential curve without any plateau was observed, both in the charge and discharge profile. We tentatively attribute that to a solid-solid, single-phase reaction, which has also been reported for Li-SPAN systems [38]. The overall reaction can be drawn as shown in Scheme 2. In the charge process, the polymer reacts with MgS and stepwise returns to the original structure. Therefore, the whole reduction and oxidation process takes place between the solid SPAN and MgS , without the formation of any intermediary magnesium polysulfides [38].

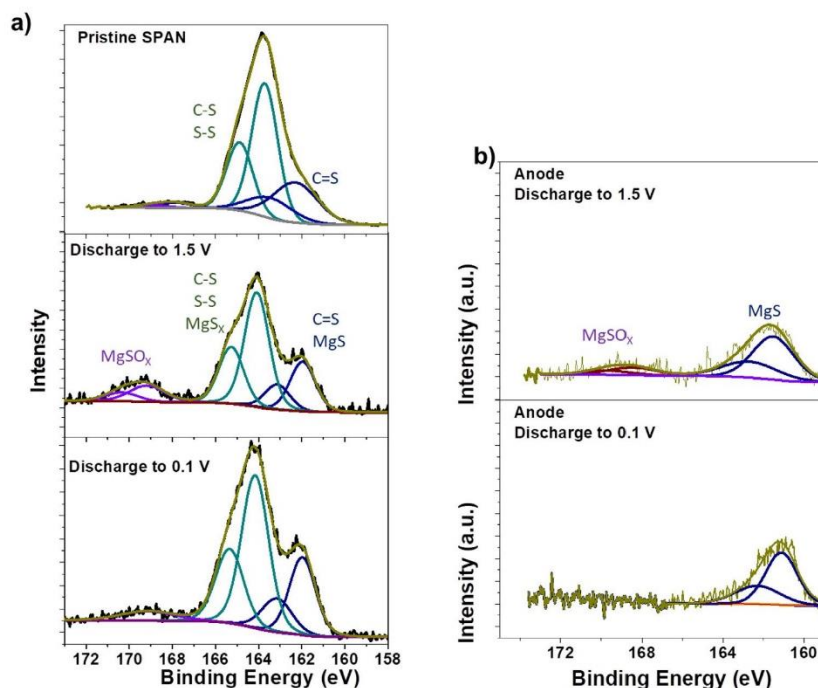


Fig. 4. High resolution *ex-situ* XPS (S 2p) spectra of a) a pristine SPAN cathode, after cycling to 1.5 V and 0.1 V, respectively; b) pressed Mg anodes after cycling to 1.5 V and 0.1 V, respectively. In order to have a direct comparison between each step, the figures were all plotted with the same total y-scale.

3.3. Post-Mortem analysis

To gain more insight to the chemical species formed on the surface of the electrodes, *ex-situ* X-ray photoelectron spectroscopy (XPS) was performed on a pristine electrode and on electrodes after seven cycles at different discharging stages, i.e. 1.5 V and 0.1 V, respectively. Fig. 4 shows the S 2p spectra of the pristine SPAN cathode, pressed Mg anodes and SPAN cathodes after cycling and is plotted with the same total y-scale allows for a direct comparison of the signals at different stages. On the cathode side, the peak of S $2p_{3/2}$ at ca. 164 eV can be assigned to C-S, S-S species and also to MgS_x ($4 \leq x \leq 8$). The formed polysulfides tend to dissolve in the electrolyte, diffuse to the anode and form MgS. As can be seen on the Mg anode surface, some MgS species were detected at ~161.9 eV at both discharge stages, although the signals were not particularly pronounced. This result fits the finding from the SEM/EDX mapping (Figure S14, S.I.). In addition, on the cathode side, the peak at 161.9 eV corresponds to the sulfur species with a double bond to carbon, C = S, in the SPAN structure and to MgS [41]. The intensity of this peak increased upon discharge compared to the pristine SPAN cathode, indicating the continuous formation of MgS during discharge. The identification of MgS and MgS_x on both electrodes is in good agreement with the report by Häcker et al., where the same conducting salt was used, but with elemental sulfur as cathode material [37]. In addition, the peak detected at around 168.3 eV most probably comes from $MgSO_x$ species, which has also been found on the aged Mg surface from Mg-S₈ system [7, 37]. Also, some silicon species from the glass fiber separator contribute to the signal around 153 eV (Figure S15, S.I.).

Apart from the detection of magnesium sulfides on the cycled electrodes, magnesium, carbon, fluorine and oxygen were also observed on the aged SPAN cathode and Mg anode surface (Fig. 5). According to the F 1s spectrum of the Mg anode, the peak at

685.5 eV indicates the formation of MgF_2 , which is in line with the signal at ~51 eV in the Mg 2p spectrum [37, 42]. MgF_2 is considered as the main components of the SEI layer. Interestingly, on the cathode side, small amounts of MgF_2 can also be detected. The formation of MgF_2 might be due to some decomposition of the electrolyte, with decomposition products depositing onto both of the electrodes. The signal around 688.2 eV on both electrodes originates from the $-CF_3$ group in the residual $Mg[B(hfp)_4]_2$ conductive salt. Further on, the O 1s spectrum of the Mg anode displayed a signal at ca. 531 eV, which arises from MgO. This is in line with the signal at 51 eV in the Mg 2p spectrum [42]. These MgO species might well be present on the pristine magnesium anode but might also form via the reaction between the electrolyte and the Mg anode. In addition, $MgCO_3$, which contributes to the peaks in the C 1s and O 1s spectra at 292.1 eV and 533.3 eV, respectively, was also found on the Mg anode [42]. These species, MgF_2 , MgO, $MgCO_3$ might come from the decomposition of the electrolyte and be part of the solid electrolyte interface (SEI) layer on both the cathode and anode surface [37]. On the cathode side, as depicted in the C 1s spectrum, the signal at 284.3 eV stems from carbon atoms binding to hydrogen, sulfur and to other carbon atoms, i.e. C-H, C-S and C-C, which exist in the SPAN structure; while the signal at 286.4 eV is attributed to the C = N and C-O groups in SPAN [41]. A detailed list of the XPS binding energies and the corresponding compounds, which were detected in the cell, are summarized in Table S4 (S.I.).

Based on the XPS study, the formation of MgS on the anode side can be confirmed during the initial cycles, which contributes to the SEI layer formation. Apart from the sulfur species, MgF_2 was found to be the main SEI component on both electrodes, even after few cycles. These inorganic solid magnesium species might play an important role during the electrochemical reaction. The as-formed SEI layer allows for a reversible Mg^{2+} transport and magnesium de-

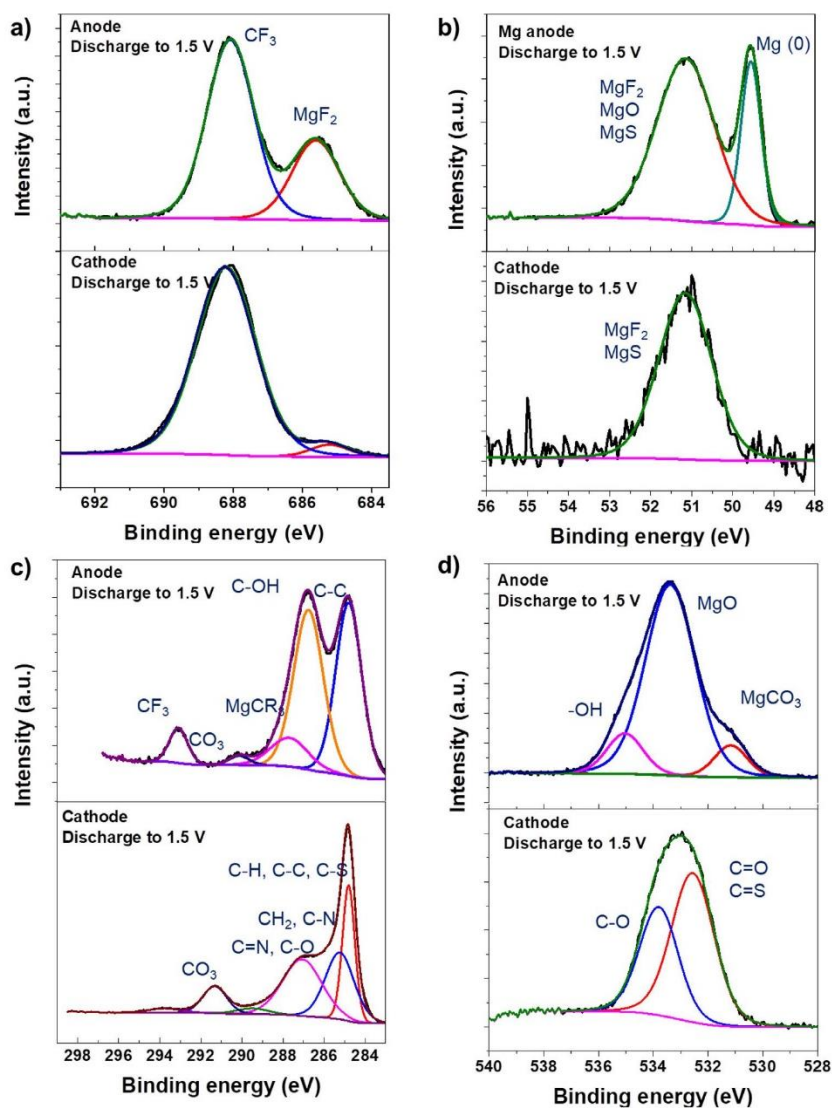


Fig. 5. High resolution ex-situ XPS spectra of the cycled SPAN cathode and the Mg anode; a) F 1 s; b) Mg 2p; c) C 1 s; d) O 1 s.

position. The provided picture of the Mg anode/electrolyte interface is expected to facilitate the future design of new electrolyte systems for Mg-SPAN batteries.

4. Conclusions

In conclusion, we investigated the cycle performance of SPAN-based Mg-S batteries using $\text{Mg}[\text{B}(\text{hfp})_4]_2$ as the conductive salt and a mixture of diglyme and tetraglyme as the solvent in the electrolyte. Using a polished Mg foil as the anode, the cell delivered around 300 $\text{mAh/g}_{\text{sulfur}}$ at C/30. When using a pressed Mg anode made from Mg powder, the cell was capable of delivering ca. 500 $\text{mAh/g}_{\text{sulfur}}$ (422 $\text{mWh/g}_{\text{sulfur}}$) with improved cycle stability. Also, stress test results indicated a good rate capability of the system. According to cyclic voltammetry and X-ray photoelectron spectroscopy data of the cycled Mg anode and SPAN cathode, magnesium (poly)sulfides, i.e. MgS_4 and MgS , are formed during initial

electrochemical cycling. To a certain point, the solid transition between SPAN and MgS is proposed. Furthermore, the XPS study of the aged SPAN cathode and the magnesium anodes indicated the formation of MgS , MgF_2 , MgCO_3 , MgO and MgSO_4 , which might at least in part form of the SEI layer on the electrodes. This study reveals a good compatibility of an SPAN cathode with Mg anodes for use in Mg-S batteries. Also, the importance of high surface areas as realized with pressed Mg anodes is demonstrated. The magnesium and electrolyte interface provide valuable hints for the future design of the electrolyte system.

Author statement

P. Wang: Conceptualization, Investigation, Writing - original draft, Writing - review & editing; J. Kappler: Conceptualization, Writing - review; B. Sievert: Sample Preparation; J. Häcker: Sample preparation, Writing- review & editing; K. Küster: XPS Charac-

terization, Writing - review & editing; U. Starke: XPS Characterization, Writing - review & editing; Felix Ziegler: BET Characterization; M. R. Buchmeiser: Conceptualization, Supervision, Writing - original draft, Writing - review & editing

Declaration of Competing Interest

The authors declare that they have no known competing financial interests or personal relationships that could have appeared to influence the work reported in this paper.

Acknowledgement

This work was financially support by the German Federal Ministry of Education and Research (project number 03XP0208J) and by the German Federal Ministry of Economic Affairs and Energy (project number 03ETE003E).

Supplementary materials

Supplementary material associated with this article can be found, in the online version, at doi:10.1016/j.electacta.2020.137024.

References

- H. Kim, T.S. Arthur, G.D. Allred, J. Zajicek, J.G. Newman, A.E. Rodniansky, A.G. Oliver, W.C. Boggess, J. Muldoon, Structure and compatibility of a magnesium electrolyte with a sulphur cathode, *Nat. Commun.* 427 (2011) 1–6.
- T. Gao, S. Hou, F. Wang, Z. Ma, X. Li, K. Xu, C. Wang, Reversible S(0)/MgSx Redox Chemistry in a MgTFSI2/MgCl2/DME Electrolyte for Rechargeable Mg/S Batteries, *Angew. Chem.* 129 (2017) 13711–13715.
- P. Wang, M.R. Buchmeiser, Rechargeable Magnesium-Sulfur Battery Technology: state of the Art and Key Challenges, *Adv. Funct. Mater.* 29 (2019) 1905248–1905275.
- P. Bonnick, J. Muldoon, A Trip to Oz and a Peak Behind the Curtain of Magnesium Batteries, *Adv. Funct. Mater.* 30 (2020) 1910510.
- Y. Xu, G. Zhou, S. Zhao, W. Li, F. Shi, J. Li, J. Feng, Y. Zhao, Y. Wu, J. Guo, Y. Cui, Y. Zhang, Improving a Mg/S Battery with YCl3 Additive and Magnesium Polysulfide, *Adv. Sci.* 6 (2019) 1800981–1800987.
- Z. Zhao-Karger, X. Zhao, O. Fuhr, M. Fichtner, Bisamide based non-nucleophilic electrolytes for rechargeable magnesium batteries, *RSC Adv.* 3 (2013) 16330.
- T. Gao, M. Noked, A.J. Pearce, E. Gillette, X. Fan, Y. Zhu, C. Luo, L. Suo, M.A. Schroeder, K. Xu, S.B. Lee, G.W. Rubloff, C. Wang, Enhancing the reversibility of Mg/S battery chemistry through Li(+) mediation, *J. Am. Chem. Soc.* 137 (2015) 12388–12393.
- A. Du, Z. Zhang, H. Qu, Z. Cui, L. Qiao, L. Wang, J. Chai, T. Lu, S. Dong, T. Dong, H. Xu, X. Zhou, G. Cui, An efficient organic magnesium borate-based electrolyte with non-nucleophilic characteristics for magnesium-sulfur battery, *Energ. Environ. Sci.* 10 (2017) 2616–2625.
- Y. Nuli, X. Zhao, Y. Yang, J. Yang, J. Wang, One kind of rechargeable magnesium battery electrolyte and rechargeable magnesium battery, *Shanghai Jiao Tong University China* (2019).
- L. Zeng, N. Wang, J. Yang, J. Wang, Y. Nuli, Application of a Sulfur Cathode in Nucleophilic Electrolytes for Magnesium/Sulfur Batteries, *J. Electrochem. Soc.* 164 (2017) A2504–A2512.
- W.Q. Wang, H.C. Yuan, Y. Nuli, J.J. Zhou, J. Yang, J.L. Wang, Sulfur@microporous Carbon Cathode with a High Sulfur Content for Magnesium-Sulfur Batteries with Nucleophilic Electrolytes, *J. Phys. Chem. C* 122 (2018) 26764–26776.
- H. Du, Z. Zhang, J. He, Z. Cui, J. Chai, J. Ma, Z. Yang, C. Huang, G. Cui., A Delicately Designed Sulfide Graphdiyne Compatible Cathode for High-Performance Lithium/Magnesium-Sulfur Batteries, *Small* 13 (2017) 1702277.
- Z. Zhao-Karger, M.E.G. Bardaji, O. Fuhr, M. Fichtner, A new class of non-corrosive, highly efficient electrolytes for rechargeable magnesium batteries, *J. Mater. Chem. A* 5 (2017) 10815–10820.
- Z. Zhao-Karger, R. Liu, W. Dai, Z. Li, T. Diemant, B.P. Vinayan, C. Bonatto Minella, X. Yu, A. Manthiram, R.J. Behm, M. Ruben, M. Fichtner, Toward Highly Reversible Magnesium-Sulfur Batteries with Efficient and Practical Mg[B(hfp)4]2 Electrolyte, *ACS Energy Lett.* 3 (2018) 2005–2013.
- I. Shterenberg, M. Salama, H.D. Yoo, Y. Gofer, J.-B. Park, Y.-K. Sun, D. Aurbach, Evaluation of (CF3SO2)2N–(TFSI) Based Electrolyte Solutions for Mg Batteries, *J. Electrochem. Soc.* 162 (2015) A7118–A7128.
- S.Y. Ha, Y.W. Lee, S.W. Woo, B. Koo, J.S. Kim, J. Cho, K.T. Lee, N.S. Choi, Magnesium(II) bis(trifluoromethane sulfonyl) imide-based electrolytes with wide electrochemical windows for rechargeable magnesium batteries, *ACS Appl. Mater. Interfaces* 6 (2014) 4063–4073.
- Y. Yang, W. Wang, Y. Nuli, J. Yang, J. Wang, High Active Magnesium Trifluoromethanesulfonate-Based Electrolytes for Magnesium-Sulfur Batteries, *ACS Appl. Mater. Interfaces* 11 (2019) 9062–9072.
- D. Huang, S. Tan, M. Li, D. Wang, C. Han, Q. An, L. Mai, Highly Efficient Non-Nucleophilic Mg(CF3SO3)2-Based Electrolyte for High-Power Mg/S Battery, *ACS Appl. Mater. Interfaces* 12 (2020) 17474–17480.
- D.-M. Kim, S.C. Jung, S. Ha, Y. Kim, Y. Park, J.H. Ryu, Y.-K. Han, K.T. Lee, Cointercalation of Mg2+ Ions into Graphite for Magnesium-Ion Batteries, *Chem. Mater.* 30 (2018) 3199–3203.
- X. Ji, K.T. Lee, L.F. Nazar, A highly ordered nanostructured carbon-sulphur cathode for lithium-sulphur batteries, *Nat. Mater.* 8 (2009) 500–506.
- W. Li, S. Cheng, J. Wang, Y. Qiu, Z. Zheng, H. Lin, S. Nanda, Q. Ma, Y. Xu, F. Ye, M. Liu, L. Zhou, Y. Zhang, Synthesis, Crystal Structure, and Electrochemical Properties of a Simple Magnesium Electrolyte for Magnesium/Sulfur Batteries, *Angew. Chem.* 128 (2016) 6516–6520.
- A.C. Kozen, C.F. Lin, A.J. Pearce, M.A. Schroeder, X. Han, L. Hu, S. Lee, G.W. Rubloff, M. Noked, Next-Generation Lithium Metal Anode Engineering via Atomic Layer Deposition, *ACS Nano* 9 (2015) 5884–5892.
- B.P. Vinayan, Z. Zhao-Karger, T. Diemant, V.S. Chakravadhanula, N.I. Schwarzburger, M.A. Cambaz, R.J. Behm, C. Kubel, M. Fichtner, Performance study of magnesium-sulfur battery using a graphene based sulfur composite cathode electrode and a non-nucleophilic Mg electrolyte, *Nanoscale* 8 (2016) 3296–3306.
- X. Zhou, J. Tian, J. Hu, C. Li, High Rate Magnesium-Sulfur Battery with Improved Cyclability Based on Metal-Organic Framework Derivative Carbon Host, *Adv. Mater.* 30 (2018) 1704166.
- M. Chen, S. Jiang, C. Huang, X. Wang, S. Cai, K. Xiang, Y. Zhang, J. Xue, Honeycomb-like Nitrogen and Sulfur Dual-Doped Hierarchical Porous Biomass-Derived Carbon for Lithium-Sulfur Batteries, *ChemSusChem* 10 (2017) 1803–1812.
- M. Chen, S. Jiang, S. Cai, X. Wang, K. Xiang, Z. Ma, P. Song, A.C. Fisher, Hierarchical porous carbon modified with ionic surfactants as efficient sulfur hosts for the high-performance lithium-sulfur batteries, *Chem. Eng. J.* 313 (2017) 404–414.
- L. Wang, X.M. He, J.J. Li, M. Chen, J. Gao, C.Y. Jiang, Charge/discharge characteristics of sulfurized polyacrylonitrile composite with different sulfur content in carbonate based electrolyte for lithium batteries, *Electrochim. Acta* 72 (2012) 114–119.
- J. Fanous, M. Wegner, M.B.M. Spera, M.R. Buchmeiser, High Energy Density Poly(acrylonitrile)-Sulfur Composite-Based Lithium-Sulfur Batteries, *J. Electrochem. Soc.* 160 (2013) A1169–A1170.
- J. Fanous, M. Wegner, J. Grimming, M. Rolff, M.B.M. Spera, M. Tenzer, M.R. Buchmeiser, Correlation of the electrochemistry of poly(acrylonitrile)-sulfur composite cathodes with their molecular structure, *J. Mater. Chem.* 22 (2012) 23240–23245.
- J. Fanous, M. Wegner, J. Grimming, A. Andresen, M.R. Buchmeiser, Structure-Related Electrochemistry of Sulfur-Poly(acrylonitrile) Composite Cathode Materials for Rechargeable Lithium Batteries, *Chem. Mater.* 23 (2011) 5024–5028.
- S. Warneke, R.K. Zenn, T. Leberer, K. Müller, A. Hintennach, U. Starke, R.E. Dinnebier, M.R. Buchmeiser, Hybrid Li/S Battery Based on Dimethyl Trisulfide and Sulfurized Poly(acrylonitrile), *Adv. Sustain. Syst.* 2 (2018) 1700144–1700149.
- Y. Nuli, Z. Guo, H. Liu, J. Yang, A new class of cathode materials for rechargeable magnesium batteries: organosulfur compounds based on sulfur-sulfur bonds, *Electrochem. Commun.* 9 (2007) 1913–1917.
- P. Wang, J. Truck, S. Niesen, J. Kappler, K. Kuster, U. Starke, F. Ziegler, A. Hintennach, M.R. Buchmeiser, High-Performance Magnesium-Sulfur Batteries Based on a Sulfurated Poly(acrylonitrile) Cathode, a Borohydride Electrolyte and a High-Surface Area Magnesium Anode, *Batteries & Supercaps*, 2020.
- J.F. Moulder, W.F. Stickle, P.E. Sobol, K.D. Bomben, *Handbook of X-ray Photoelectron Spectroscopy*, Physical Electronics Division, Perkin-Elmer Corporation, Minnesota (1992).
- X. He, W. Pu, J. Ren, L. Wang, J. Wang, C. Jiang, C. Wan, Charge/discharge characteristics of sulfur composite cathode materials in rechargeable lithium batteries, *Electrochim. Acta* 52 (2007) 7372–7376.
- D.-W. Xu, S. Xin, Y. You, Y. Li, H.-P. Cong, S.-H. Yu, Built-in Carbon Nanotube Network inside a Biomass-Derived Hierarchically Porous Carbon to Enhance the Performance of the Sulfur Cathode in a Li-S Battery, *ChemNanoMat* 2 (2016) 712–718.
- J. Häcker, C. Danner, B. Sievert, I. Biswas, Z. Zhao-Karger, N. Wagner, K.A. Friedrich, Investigation of magnesium-sulfur batteries using electrochemical impedance spectroscopy, *Electrochim. Acta* (2020) 135787.
- S. Zhang, Understanding of Sulfurized Polyacrylonitrile for Superior Performance Lithium/Sulfur Battery, *Energ.* 7 (2014) 4588–4600.
- G. Bieker, J. Wellmann, M. Kolek, K. Jalkanen, M. Winter, P. Bieker, Influence of cations in lithium and magnesium polysulfide solutions: dependence of the solvent chemistry, *Phys. Chem. Chem. Phys.* 19 (2017) 11152–11162.
- X. Yu, M. Arumugam, Performance Enhancement and Mechanistic Studies of Magnesium-Sulfur Cells with an Advanced Cathode Structure, *ACS Energy Lett.* 1 (2016) 431–437.
- M. Frey, R.K. Zenn, S. Warneke, K. Müller, A. Hintennach, R.E. Dinnebier, M.R. Buchmeiser, Easily Accessible, Textile Fiber-Based Sulfurized Poly(acrylonitrile) as Li/S Cathode Material: correlating Electrochemical Performance with Morphology and Structure, *ACS Energy Lett.* 2 (2017) 595–604.
- T. Gao, S. Hou, K. Huynh, F. Wang, N. Eidson, X. Fan, F. Han, C. Luo, M. Mao, X. Li, C. Wang, Existence of Solid Electrolyte Interphase in Mg Batteries: mg/S Chemistry as an Example, *ACS Appl. Mater. Interfaces* 10 (2018) 14767–14776.

4.3 Supporting Information to “Characteristics of Magnesium-Sulfur Batteries Based on a Sulfurized Poly(acrylonitrile) Composite and a Fluorinated Electrolyte”

Cathode and Electrolyte System

In the IR spectrum of PAN, the signal at 2244 cm^{-1} is attributed to the stretching of the nitrile group in the polymer chain.^[1, 2] The characteristic bands at 2935 cm^{-1} ($\nu_{\text{C-H}}$ in CH_2), 1452 cm^{-1} ($\delta_{\text{C-H}}$ in CH_2) and 1370 cm^{-1} ($\delta_{\text{C-H}}$ in CH) refer to the aliphatic groups of the PAN backbone.^[3] After the reaction with sulfur, the signal of the nitrile group disappears. At the same time, the signals for $\text{C}=\text{N}$ (1375 cm^{-1}), C-H (1228 cm^{-1}), $\text{C}=\text{C}$ (1504 cm^{-1}), which belong to the conjugated backbone including pyridine-like moieties, appear.^[4] In addition, the peaks at 512 and 939 cm^{-1} are attributed to S-S groups.^[4] The signal at 665 cm^{-1} refers to the covalent C-S bond.^[4]

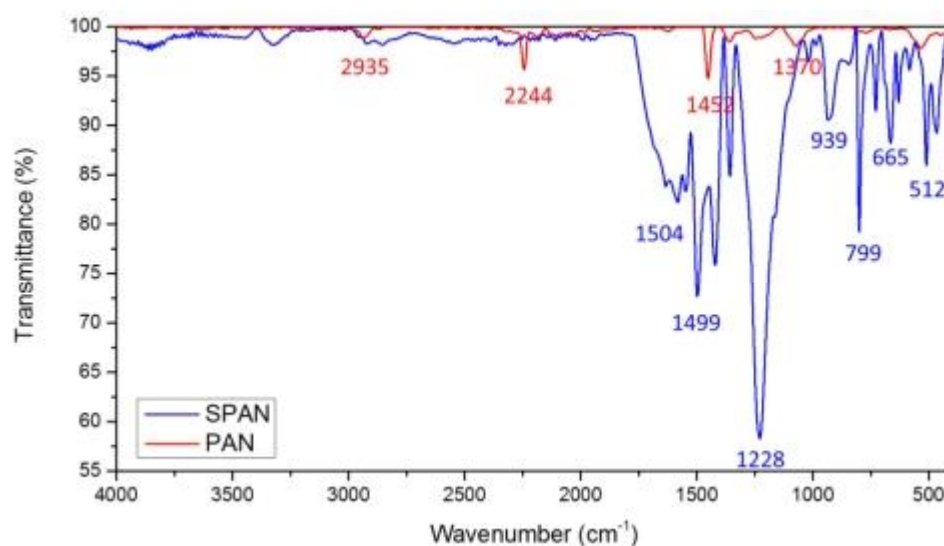


Figure S1: IR spectrum of PAN and SPAN.

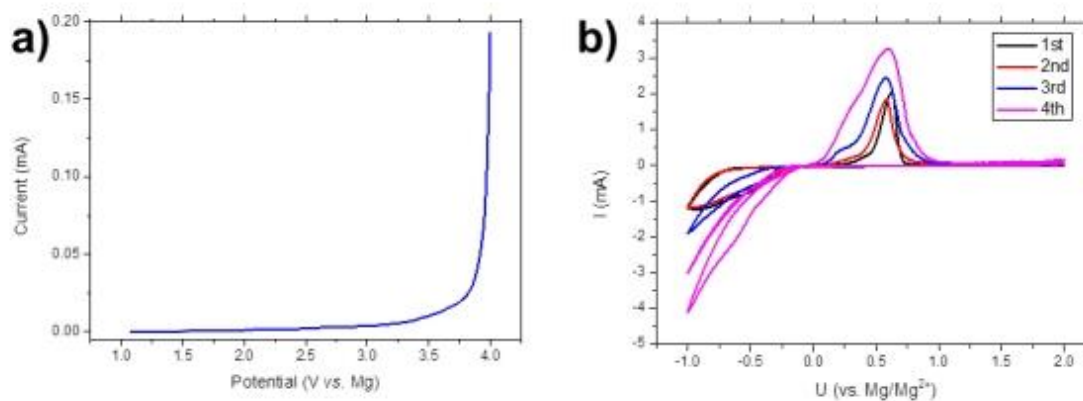


Figure S2: a) Linear sweep voltammograms of a cell containing 0.8 M $\text{Mg}[\text{B}(\text{hfip})_4]_2$ in diglyme/tetraglyme (1/1) and Al/C as working electrode at a scan rate of $1 \text{ mV} \cdot \text{s}^{-1}$; b) cyclic voltammograms of a cell containing 0.8 M $\text{Mg}[\text{B}(\text{hfip})_4]_2$ in diglyme/tetraglyme (1/1) and Al/C as the working electrode, Mg as counter and reference electrode at a scan rate of $1 \text{ mV} \cdot \text{s}^{-1}$.

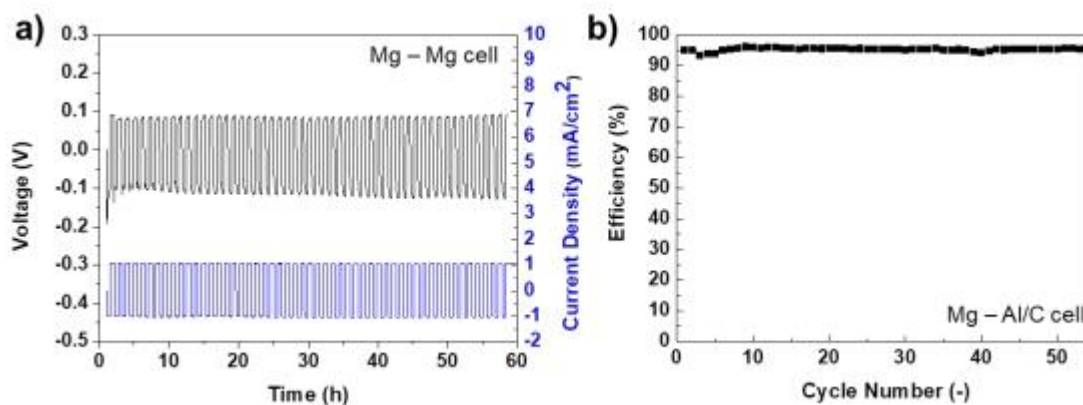


Figure S3: a) Mg plating and stripping test results using a symmetric Mg-Mg cell at a current rate of $1 \text{ mA}/\text{cm}^2$; b) Coulombic efficiency study using asymmetric Mg-Al/C cell.

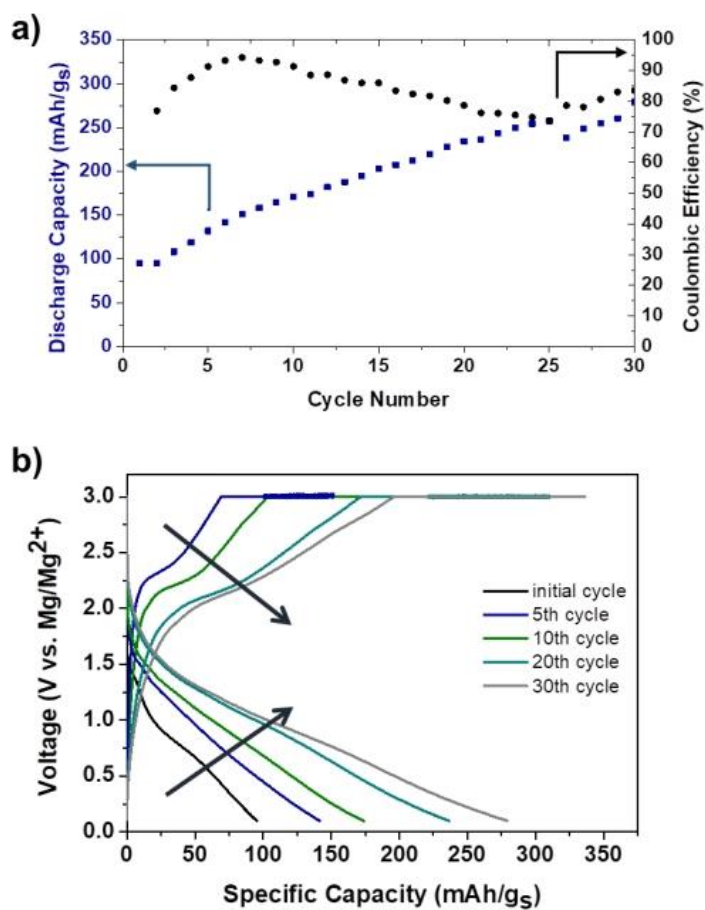


Figure S4: **a)** Electrochemical behavior of a cell composed of a SPAN cathode, a Mg foil and 0.8 M Mg[B(hfip)₄]₂ in diglyme/tetraglyme (1/1, v/v) at C/30; **b)** galvanostatic charge and discharge curves of the initial, 5th, 10th, 20th and 30th cycle.

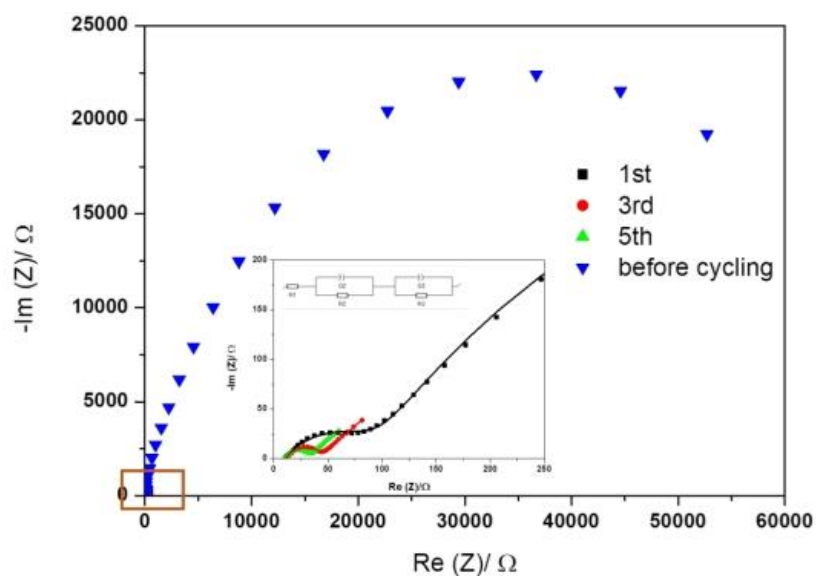


Figure S5: Nyquist plots of a symmetric Mg-Mg cell containing 0.8 M $\text{Mg}[\text{B}(\text{hfip})_4]_2$ in diglyme/tetraglyme before cycling and after the given number of cycles. Mg foils were fully polished before the measurements.

Table S1: Data fit of the EIS results.

measurement	R1 (Ohm)	R2 (Ohm)	$\chi^2/ Z $
Before cycling	10.1	4233	0.05
1 st cycle	10.52	69.95	0.04
3 rd cycle	10.54	34.14	0.03
5 th cycle	10.02	22.79	0.02

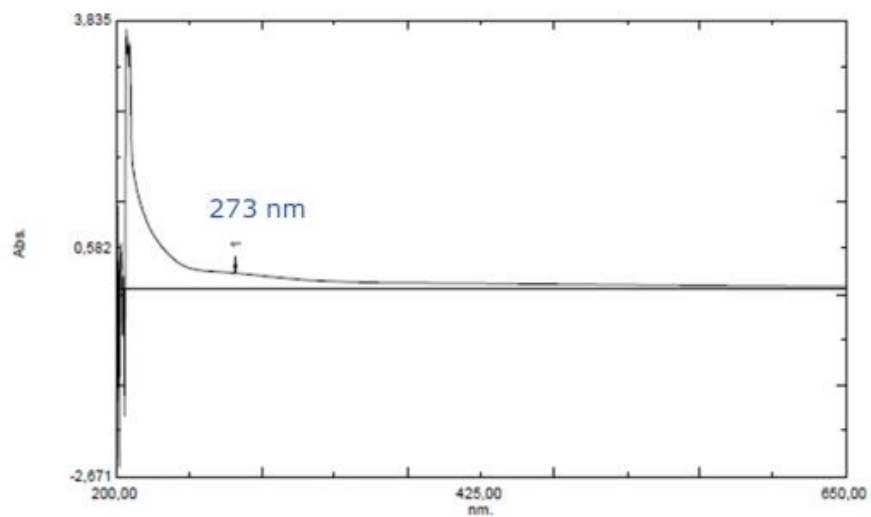


Figure S6: UV-VIS spectrum of the cycled electrolyte after 40 cycles. The peak at 273 nm corresponds to the MgS species.

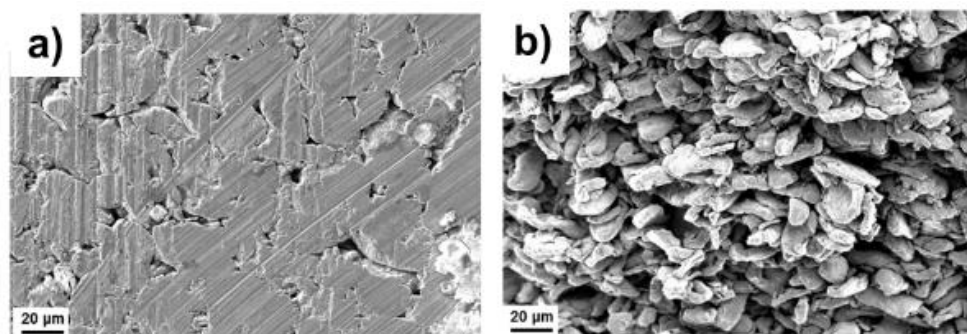


Figure S7: SEM images of **a)** a pressed Mg anode; **b)** cross-section of the pressed Mg anode.

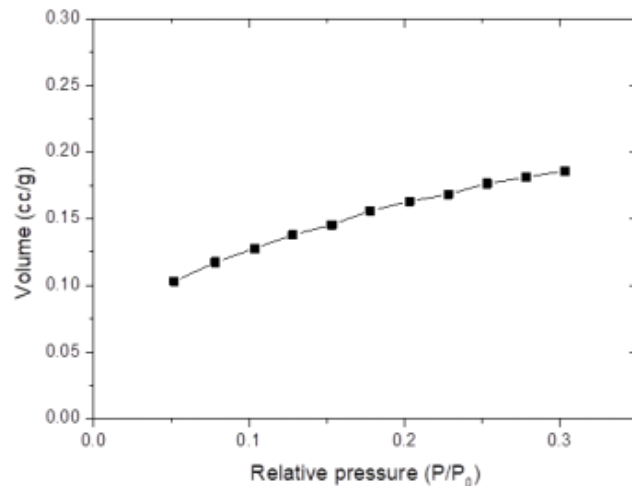


Figure S8: Adsorption curve for Mg powder used for the calculation of the specific surface area (BET method).

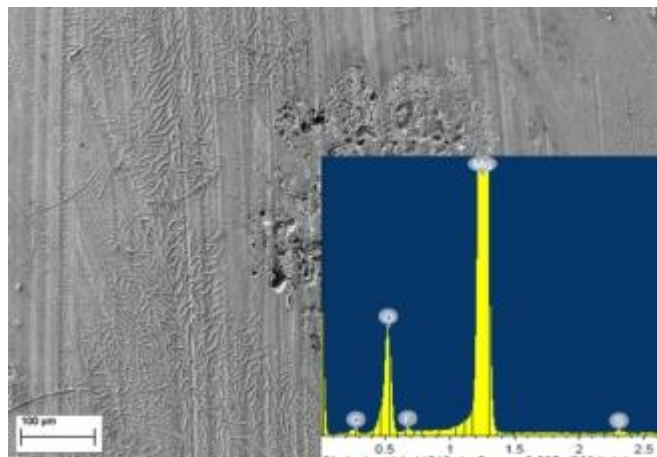


Figure S9: SEM image and EDX mapping of an aged Mg foil in a fully charged state after 7 cycles.

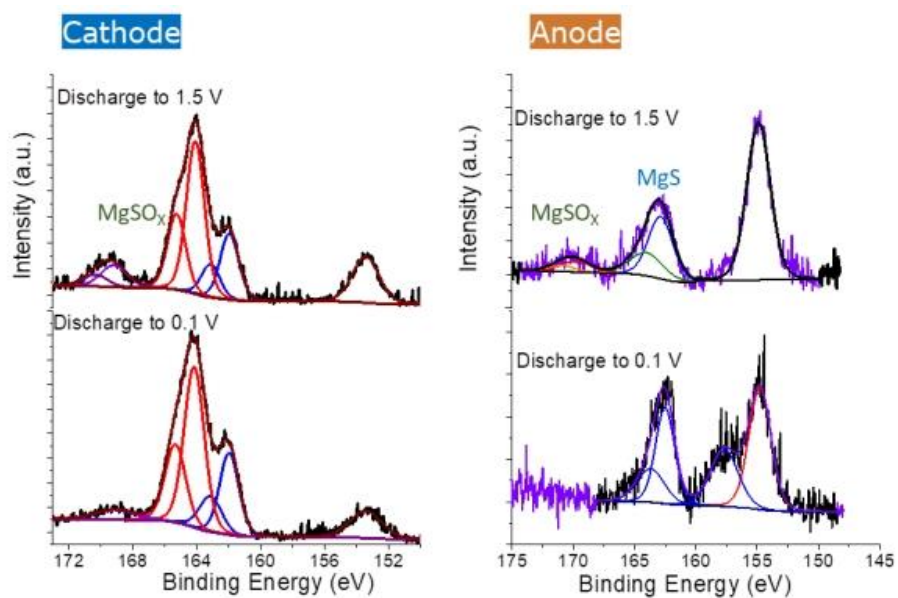


Figure S10: Complete *ex-situ* XPS spectra of a Mg anode after cycling to 1.5 V and 0.1 V, respectively. The peaks in the range of 160 eV to 150 eV correspond to Si species from the residual glass fiber separators.

Table S2: Mg polysulfide species, their reduction potentials and theoretical capacities. [5;

6]

Magnesium polysulfide species	Solubility in an ether-based electrolyte [5]	Reduction potential (V) [5]	Theoretical capacity (each step) (mAh/g _{sulfur}) [6]
S ₈	insoluble	1.8	
↓			
MgS ₈	insoluble	1.5-1.6	209
↓			
MgS ₆	soluble	1.5-1.6	70
↓			
MgS ₅	--	--	56
↓			
MgS ₄	soluble	1.4	84
↓			
MgS ₃	--	--	140
↓			
MgS ₂	insoluble	0.4	279
↓			
MgS	insoluble	0.4	837

Table S3: Important XPS binding energies and the corresponding compounds that are found in the anode and the SPAN cathodes.

Compound	F 1s [eV]	S 2p [eV]	O 1s [eV]	Mg 2p [eV]	C 1s [eV]	Ref.
MgF ₂	685.2		532.0	51.0		[7-9]
MgO						
MgS	161.9					
-CF ₃ from the conductive salt	688.2					[8]
C=S		161.9				[8; 10; 11]
MgS _x		164.0			284.2	[7; 10]
C-S						
S-S						
MgSO ₄		170.0				[8]
Mg				49.3		[8; 9; 12]
MgCO ₃			533.6		290.8	[9]
-OH			535.2			[13]
C-O			533.8		286.2	[7; 10]
C-H					284.2	[10]
C-C						
C-S						
CH ₂					284.7	[10]
C-N						
MgCR ₃					288.8	[7; 10]

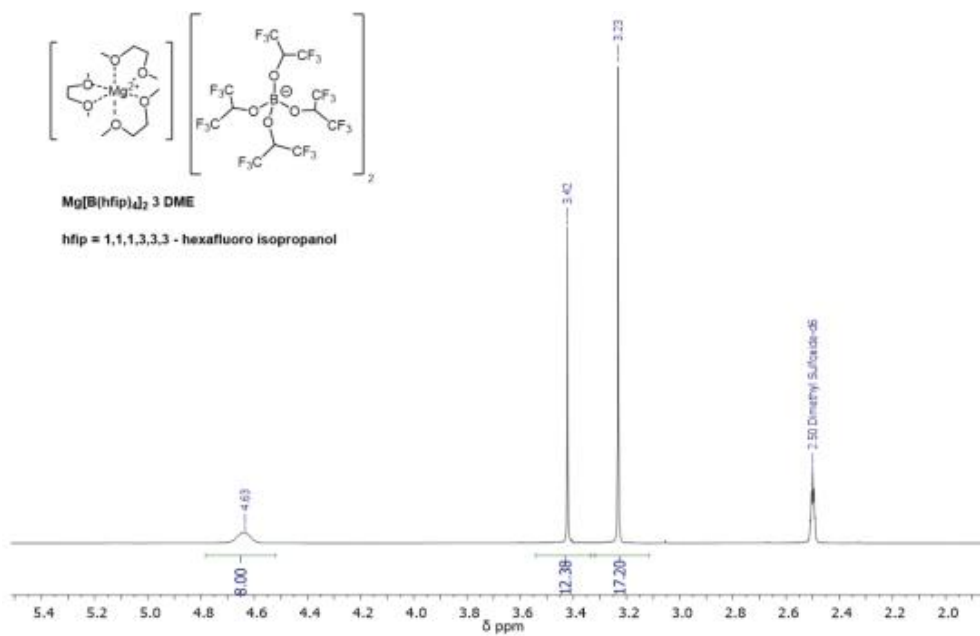


Figure S11: $^1\text{H-NMR}$ (400 MHz, DMSO-d_6) spectrum of $\text{Mg}[\text{B}(\text{hfip})_4]_2 \cdot 3\text{DME}$.

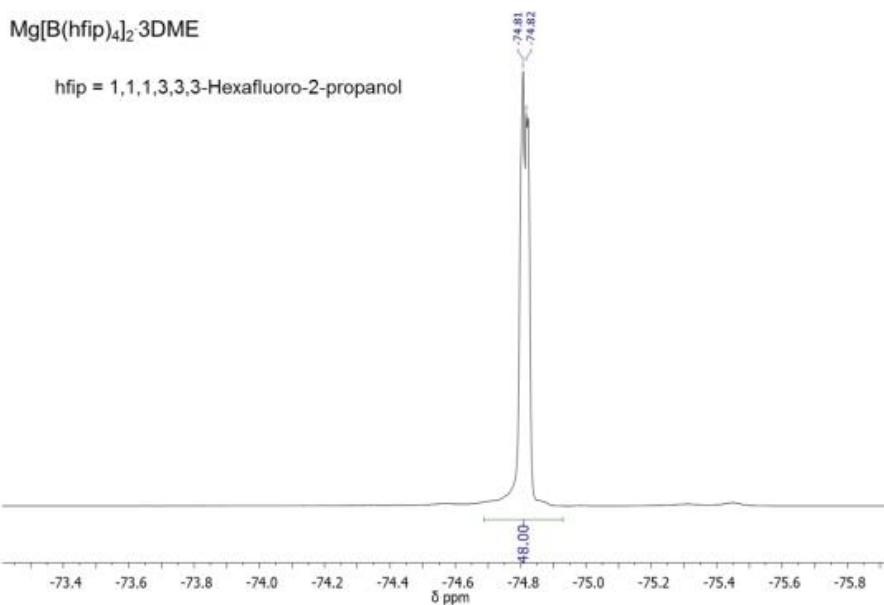


Figure S12: $^{19}\text{F-NMR}$ (376 MHz, DMSO-d_6) spectrum of $\text{Mg}[\text{B}(\text{hfip})_4]_2 \cdot 3\text{DME}$.

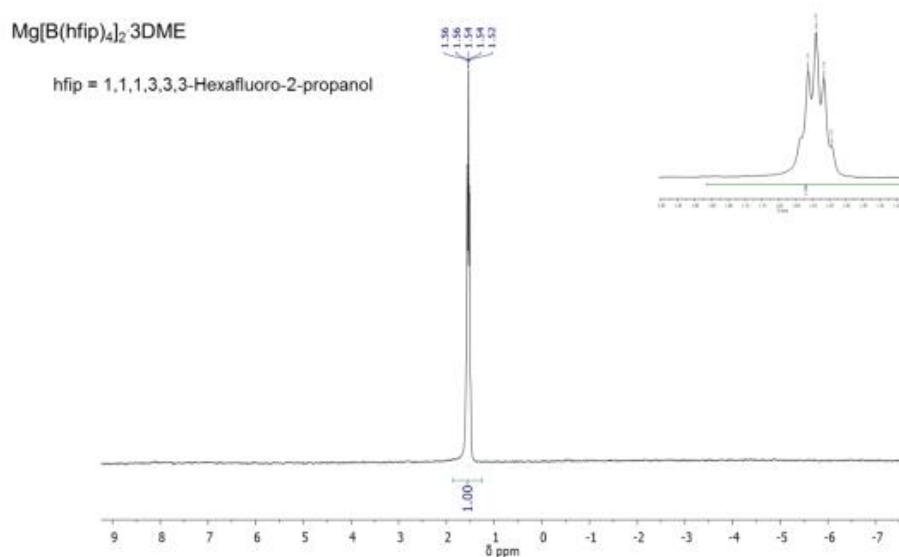


Figure S13: ¹¹B-NMR (128.42 MHz, DMSO-d₆) spectrum of Mg[B(hfip)₄]₂·3DME (the insert shows the enlarged version of the signal).

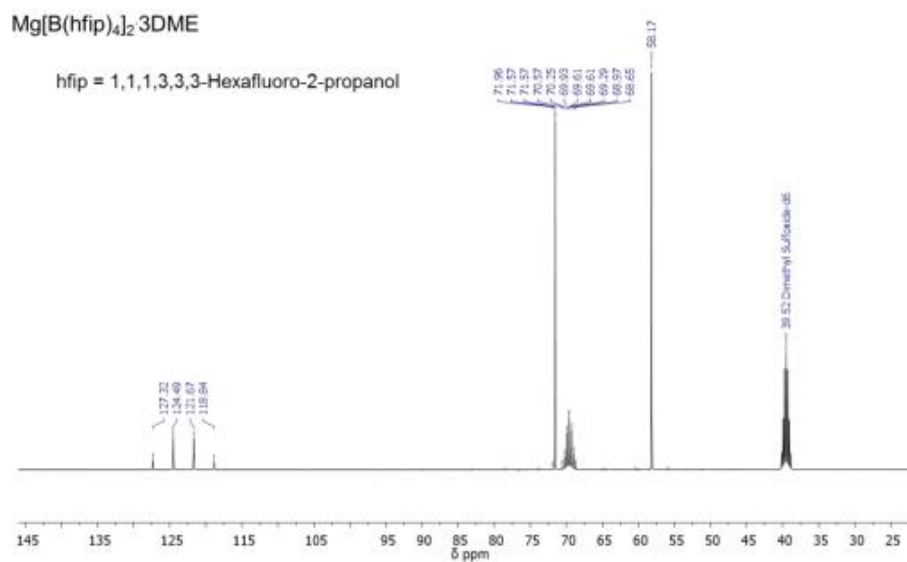


Figure S14: ¹³C-NMR (101 MHz, DMSO-d₆) spectrum of Mg[B(hfip)₄]₂·3DME.

References (Supporting Information)

1. Fanous J, Wegner M, Spera MBM, Buchmeiser MR. High Energy Density Poly(acrylonitrile)-Sulfur Composite-Based Lithium-Sulfur Batteries. *J Electrochem. Soc.* 160 (2013) A1169-A70.
2. Fanous J, M. Wegner, J. Grimminger, M. Rolff, M. B. M. Spera, et al. Correlation of the electrochemistry of poly(acrylonitrile)-sulfur composite cathodes with their molecular structure. *J. Mater. Chem.* 22 (2012) 23240-5.
3. Ribeiro R, Pardini L, Alves N, Brito J, Carlos A. Thermal Stabilization study of polyacrylonitrile fiber obtained by extrusion. *Polímeros* 25 (2015) 523-30.
4. Zhang YZ, Liu S, Li GC, Li GR, Gao XP. Sulfur/polyacrylonitrile/carbon multi-composites as cathode materials for lithium/sulfur battery in the concentrated electrolyte. *J. Mater. Chem.* 2 (2014) 4652-9.
5. Zhao-Karger Z, Zhao X, Fuhr O, Fichtner M. Bisamide based non-nucleophilic electrolytes for rechargeable magnesium batteries. *RSC Adv.* 3 (2013) 16330.
6. Yu X, Arumugam M. Performance Enhancement and Mechanistic Studies of Magnesium-Sulfur Cells with an Advanced Cathode Structure. *ACS Energy Lett.* 1 (2016) 431-7.
7. Warneke S, Zenn RK, Leberherz T, Müller K, Hintennach A, et al. Hybrid Li/S Battery Based on Dimethyl Trisulfide and Sulfurized Poly(acrylonitrile). *Adv. Sustain. Syst.* 2 (2018) 1700144.
8. Häcker J, Danner C, Sievert B, Biswas I, Zhao-Karger Z, et al. Investigation of magnesium-sulfur batteries using electrochemical impedance spectroscopy. *Electrochim. Acta* (2020) 135787.
9. Gao T, Hou S, Huynh K, Wang F, Eidson N, et al. Existence of Solid Electrolyte Interphase in Mg Batteries: Mg/S Chemistry as an Example. *ACS Appl. Mater. Interfaces* 10 (2018) 14767-76.
10. Frey M, Zenn RK, Warneke S, Müller K, Hintennach A, et al. Easily Accessible, Textile Fiber-Based Sulfurized Poly(acrylonitrile) as Li/S Cathode Material: Correlating

Electrochemical Performance with Morphology and Structure. *ACS Energy Lett.* 2 (2017) 595-604.

11. Zhao-Karger Z, Liu R, Dai W, Li Z, Diemant T, et al. Toward Highly Reversible Magnesium–Sulfur Batteries with Efficient and Practical $\text{Mg}[\text{B}(\text{hfiip})_4]_2$ Electrolyte. *ACS Energy Lett.* 3 (2018) 2005-13.

12. Moulder JF, Stickle WF, Sobol PE, Bomben KD. *Handbook of X-ray Photoelectron Spectroscopy*. Minnesota, USA: Perkin-Elmer Corporation

13. Schulze PD, Shaffer SL, Hance RL, Utley DL. *J. Vac. Sci. Technol. A* 1 (1983)

Chapter 5

Use of a Dual-Salt-Electrolyte in Mg-SPAN Batteries

5.1 Motivation

In **Chapter 4**, the electrochemical performance of a Mg battery based on an SPAN cathode and an electrolyte containing a pure magnesium conductive salt was studied. Reversible charging and discharging of Mg-SPAN cells proved possible. Unlike reported Mg cells using S₈-based cathodes, a severe capacity decay was observed. The Mg-SPAN cells delivered a relatively stable and high discharge capacity, especially in combination with a Mg pressed anode. However, the cell was cycled at a relatively low current rate. The overall cell performance therefore needed to be further improved.

According to the available publications, the addition of a lithium salt into a magnesium electrolyte by forming a hybrid electrolyte^[154] or the use of a pure lithium salt-based electrolyte in a magnesium cell to form an *in-situ* hybrid electrolyte^[221] could improve the cell performance of Mg cells by improving the reversibility of the system and forming a stable and homogeneous SEI layer on the Mg anodes.

A comparison between the cell performance of Mg-ACC/S cells using 0.1 M Mg-HMDS electrolyte (black) and those using a 0.1 M Mg-HMDS + 1 M LiTFSI electrolyte (red) is shown in **Figure 5.1a**. The addition of 1 M LiTFSI could significantly improve the cell performance with regards to discharge capacity and reversibility. *Gao et al.*^[154] pointed out that the lithium salt could reactivate the short-chain magnesium (poly)sulfides, which further improved the reversibility of the system.^[154] On the other hand, it is important to know whether the addition of a lithium salt into the electrolyte caused the formation of lithium dendrites on the magnesium anode, since a non-dendritic plating is of great benefit for the Mg cells. *Gao et al.*^[154] also characterized the surface and cross-section of the cycled Mg anode from the Mg-ACC/S cell with the lithium salt-containing electrolyte

(Figure 5.1 b and c). It is clear that the surface of the aged Mg anode showed some spheres with diameters around 2 μm instead of dendrites. In addition, the cross-section of the Mg anode also showed the absence of the dendrite formation.^[154]

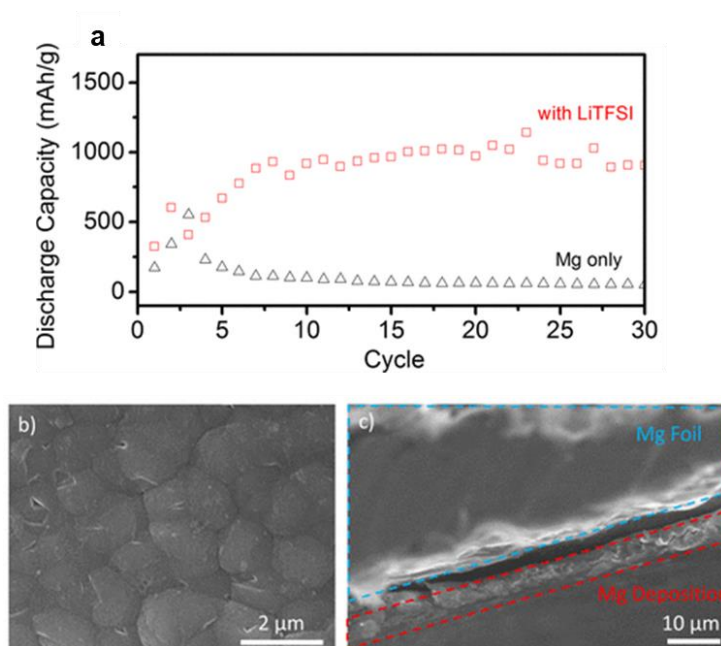


Figure 5.1: a) Comparison of the cell performance of Mg-ACC/S cells using a pure magnesium electrolyte (black) and a Mg-HMDS electrolyte with the LiTFSI additive (red); b) SEM image of the surface of the Mg anode using the Mg-HMDS electrolyte with the LiTFSI additive; c) SEM image of the cross-section of the cycled Mg anode from the Mg-ACC/S cell using the Mg-HMDS electrolyte with the LiTFSI additive.^[154] Reproduced with permission from ref.^[154]. Copyright (2015) American Chemical Society.

In view of these, the addition of a lithium salt in a Mg-S battery could improve cell performance, and at the same time, it does not cause dendrite formation. This novel idea opens a new avenue for Mg-S cells, which is worth to be further investigated.

5.2 Publication: “High-Performance Magnesium-Sulfur Batteries Based on a Sulfurated Poly(acrylonitrile) Cathode, a Borohydride Electrolyte, and a High-Surface Area Magnesium Anode”

It has been reported that the addition of a lithium salt into the electrolyte of the Mg-ACC/S cell can significantly improve both reversibility and discharge capacity.^[154] However, the combination of a Mg²⁺/Li⁺ hybrid electrolyte together with the use of an SPAN cathode has not yet been reported. On the other hand, the use of a Mg pressed anode is also beneficial for the cell performance. Therefore, in this sub-project, a major goal was to improve the performance of Mg-SPAN cells by combining a Mg²⁺/Li⁺ hybrid electrolyte, an SPAN cathode and a Mg pressed anode in one cell system.

In this study, the compatibility of a Mg²⁺/Li⁺ hybrid electrolyte (0.1 M Mg[BH₄]₂ + 1.5 M Li[BH₄] in diglyme) with Mg metal anodes was analyzed using Mg-Mg symmetric cells. These cells showed low and stable overpotentials over 200 cycles, indicating good compatibility of the electrolyte with Mg anodes. *Post-mortem* SEM analysis of aged Mg anodes also confirmed the absence of the dendrites after Mg plating. In addition, Mg-S cells based on an SPAN cathode, a Mg²⁺/Li⁺ hybrid electrolyte and a Mg foil anode were further characterized. The cell showed stable and outstanding cycle performance (*ca.* 800 mAh g⁻¹ at 0.1 C for 100 cycles with almost 100% Coulombic efficiency). More strikingly, the replacement of the Mg foil by a Mg pressed anode made of Rieke Mg powder could further improve the cell performance. Further on, *post-mortem* XPS analysis proved the absence of lithium metal on the Mg anode, indicating the dominated magnesium chemistry during cycling. The stable SPAN structure, according to *post-mortem* XPS analysis, also explained the stable cycling performance.

Publication

P. Wang, J. Trück, S. Niesen, J. Kappler, K. Küster, U. Starke, F. Ziegler, A. Hintennach, M. R. Buchmeiser, *Batter. Supercaps* **2020**, 3, 1239-1247.

P. Wang and J. Trück contributed equally to this publication.

Author Contributions: P. Wang: Electrolyte part, Conceptualization, Investigation, Writing - original draft, Writing - review & editing; J. Trück: Anode part, Conceptualization, Investigation, Writing - original draft, Writing - review & editing; S. Niesen, A. Hintennach: Writing – review & editing; J. Kappler: Writing – review & editing; K. Küster: XPS Characterization, Writing - review & editing; U. Starke: XPS Characterization, Writing - review & editing; Felix Ziegler: BET Characterization; M. R. Buchmeiser: Conceptualization, Supervision, Writing - original draft, Writing - review & editing

Reprinted with permission from the © 2020 WILEY-VCH Verlag GmbH & Co. KGaA, Weinheim.

High-Performance Magnesium-Sulfur Batteries Based on a Sulfurated Poly(acrylonitrile) Cathode, a Borohydride Electrolyte, and a High-Surface Area Magnesium Anode

Peiwen Wang,^[a] Janina Trück,^[a, c] Stefan Niesen,^[a, c] Julian Kappler,^[a] Kathrin Küster,^[d] Ulrich Starke,^[d] Felix Ziegler,^[a] Andreas Hintennach,^[c] and Michael R. Buchmeiser^{*[a, b]}

Post-lithium-ion battery technology is considered a key element of future energy storage and management. Apart from high gravimetric and volumetric energy densities, economic, ecological and safety issues become increasingly important. In that regards, both the anode and cathode materials must be easily available, recyclable, non-toxic and safe, which renders magnesium-sulfur (Mg-S) batteries a promising choice. Herein, we present Mg-S cells based on a sulfurated poly(acrylonitrile) composite cathode (SPAN), together with a halogen-free electrolyte containing both Mg[BH₄]₂ and Li[BH₄] in diglyme and

a high-specific surface area magnesium anode based on Rieke magnesium powder. These cells deliver discharge capacities of 1400 and 800 mAh/g_{sulfur} with >99% Coulombic efficiency at 0.1 C and 0.5 C, respectively, and are stable over at least 300 cycles. Energy densities are 470 and 400 Wh/kg_{sulfur} at 0.1 C and 0.5 C, respectively. Rate tests carried out between 0.1 C and 2 C demonstrate good rate capability of the cells. Detailed mechanistic studies based on X-ray photoelectron spectroscopy and electric impedance spectroscopy are presented.

1. Introduction

There is a growing demand for efficient energy storage materials in the era of post-lithium-ion battery technology. Because of the high theoretical energy density of both, sulfur and magnesium,^[1–2] rechargeable magnesium sulfur (Mg-S) batteries are attractive candidates. At the same time, magnesium is considered a safer choice in commercial applications due to its predominantly non-dendritic plating.^[3] However, compared to Li-S batteries, the accomplishments in the field of Mg-S batteries are still quite limited, mainly due to the lack of suitable electrolytes that improve the sluggish kinetics of the bivalent Mg²⁺ ions and the poor plating performance of Mg anodes.^[2]

Most cathode materials for Mg-S batteries reported so far accommodate the sulfur in different porous and highly

conductive carbon materials, such as carbon black,^[1] CMK-3,^[4–6] nitrogen-doped graphene,^[7] carbon nanotubes,^[8] carbon nanofibers,^[9–10] activated carbon cloths^[11–12] or reduced graphene oxide.^[13] General important features of these cathode materials are that they possess good electrical conductivity, impede the polysulfide diffusion and show high mechanical stability.^[13]

Anodes for Mg-S cells are mostly based on low specific surface area Mg foils. Upon contact with traces of oxygen or air, however, Mg immediately forms a passivating layer (approximately 10 nm) containing oxides, carbonates and hydroxides.^[11,14–17] To remove the passivation layer and to activate the Mg, the foils are usually scratched under an inert atmosphere. However, this approach is of limited reproducibility and hard to scale.

Currently used electrolytes comprise Al-, B- or Y-based Lewis acids together with a magnesium-derived Lewis base, such as Mg bis(hexamethyldisilazide), Mg[HMDMS]₂, prepared via a transmetalation reaction.^[8,18–19] Complementary, the use of magnesium salts containing a weakly coordinating anion such as Mg bis(tetrakis(hexafluoropropoxyborate)), Mg[B(hfip)₄]₂, has also been outlined.^[6,20] Unfortunately, with this type of salt, capacity fading has been observed.^[20] Finally, the addition of some lithium salts, e.g. lithium bis(trifluoromethylsulfon)imide, LiTFSI, and LiCl, to a magnesium salt-containing electrolyte has been reported to result in improved reversibility and discharge capacities.^[4,11,21–22]

Here, we present a halogen-free dual salt electrolyte system based on Mg[BH₄]₂ and Li[BH₄] together with an alternative active cathode materials based on a sulfur-carbon composites, e.g., sulfur-poly(acrylonitrile) ("SPAN").^[23–26] In SPAN, the sulfur is not physisorbed but chemically bound to the carbonaceous backbone, predominantly as vinyllogous/phenylogous enolic

[a] P. Wang,^{*} J. Trück,^{*} S. Niesen, J. Kappler, F. Ziegler, Prof. M. R. Buchmeiser
Institute of Polymer Chemistry, University of Stuttgart
Pfaffenwaldring 55, 70569 Stuttgart, Germany
E-mail: michael.buchmeiser@ipoc.uni-stuttgart.de

[b] Prof. M. R. Buchmeiser
German Institutes of Textile and Fiber Research (DITF) Denkendorf
Körschtalstraße 26, 73770 Denkendorf, Germany

[c] J. Trück,^{*} S. Niesen, Prof. A. Hintennach
Daimler AG, RD/EBT
Hanns-Klemm-Straße 45, 71034 Böblingen, Germany

[d] K. Küster, Prof. U. Starke
Max Planck Institute for Solid State Research
Heisenbergstraße 1, 70569 Stuttgart, Germany

□ These authors contributed equally to this work.

Supporting information for this article is available on the WWW under
<https://doi.org/10.1002/batt.202000097>

© 2020 The Authors. Published by Wiley-VCH Verlag GmbH & Co. KGaA. This is an open access article under the terms of the Creative Commons Attribution License, which permits use, distribution and reproduction in any medium, provided the original work is properly cited.

thioamides, which allows for the formation of intra- and intermolecular polymer- S_x -polymer chains ($2 \leq x \leq 8$). The thioamide bond in its enolate form distinguishes SPAN from most other S-based cathodes. We also present a novel approach to high specific surface area Mg anodes. It comprises the synthesis of Rieke Mg powder via the reduction of magnesium chloride under inert atmosphere.^[27] Its particle size is in the sub-micro meter range resulting in a comparably large specific surface area.

2. Results and Discussion

Because of the divalent nature of the Mg^{2+} cation, ion pair formation with the oligosulfides, S_x^{2-} ($1 \leq x \leq 8$), that form during discharge results in different oligomeric structures ($S_x^{2-}Mg^{2+}$), ($n \geq 1$). Their solubility strongly depends on the solvent used. Also, the predominantly non-dendritic plating of Mg imposes a challenge.^[3] While this is highly beneficial in terms of battery safety, it results in a comparably low specific surface area of the anode and limited formation of fresh Mg surface during charging. Together with its pronounced ability to form an oxide/hydroxide-based passivation layer, Mg-S batteries suffer from poor cycle stability and very limited rate capability.^[2]

2.1. Electrolyte

One way to remove Mg hydroxide/oxide layers is the use of hydrides, e.g. $Mg[BH_4]_2$. Unfortunately, the solubility of $Mg[BH_4]_2$ is only 0.01 M in diglyme.^[28] However, with the addition of $Li[BH_4]$, its solubility increases to 0.1 M. Moreover, due to the mediating role of Li^+ , its presence can be expected to promote the formation of mixed cation, i.e. of Li^+/Mg^{2+} (poly)sulfides. Previous research demonstrated that this type of electrolyte is electroactive, but performs poorly with standard sulfur-containing carbonaceous materials.^[28] However, in view of the excellent long-time cycle stability of Li-SPAN cells with an LiTFSI/ether-based electrolyte,^[24,29] an SPAN-based cathode material was chosen and expected to display a similar performance in Mg-S cells using this Mg^{2+}/Li^+ hybrid electrolyte.

The influence of the concentration of the Li salt on cycle performance was studied using three different electrolyte systems: (i) 0.1 M $Mg[BH_4]_2/0.5$ M $Li[BH_4]$, (ii) 0.1 M $Mg[BH_4]_2/1$ M $Li[BH_4]$ and (iii) 0.1 M $Mg[BH_4]_2/1.5$ M $Li[BH_4]$. Diglyme was chosen as solvent due to its high dielectric constant ($\epsilon = 7.23$ at 298 K) compared to 1,2-dimethoxyethane ($\epsilon = 5.02$ at 298 K).^[30] Electrolytes with high ionic conductivity can lower the internal resistance.^[6] The ionic conductivity of the three diglyme-based electrolyte systems at room temperature was 670, 1610 and 1700 $\mu S/cm$, respectively (Figure 1a). Scanning electron microscopy (SEM) images of the surface of a charged Mg anode after 200 cycles (Figure 1b) revealed the presence of Mg spheres approximately 150 nm in diameter. Only spherical but no dendritic structures were observed. The overpotential was measured by cycling symmetric Mg-Mg cells and proved high

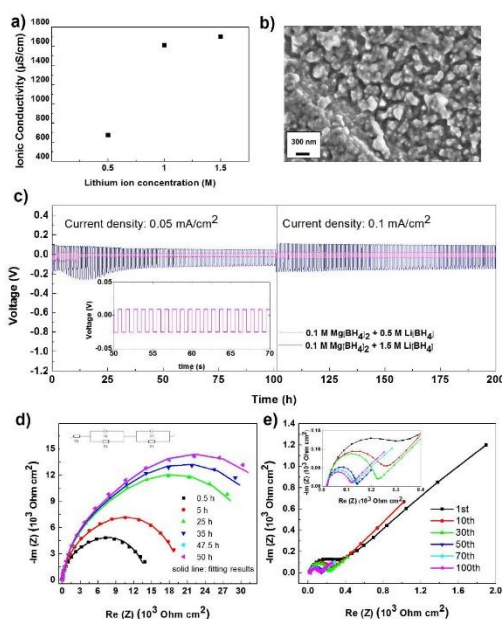


Figure 1. a) Ionic conductivity of the electrolytes: 0.1 M $Mg[BH_4]_2$ with 0.5 M, 1 M and 1.5 M of lithium ions in diglyme; b) SEM image of a Mg foil after long-term Mg plating and stripping test; no dendrite formation was observed within 200 cycles; c) long-term Mg plating and stripping over 200 cycles in 0.1 M $Mg[BH_4]_2/0.5$ M $Li[BH_4]$ /diglyme, and 0.1 M $Mg[BH_4]_2/1.5$ M $Li[BH_4]$ /diglyme at a current density of 0.05 and 0.1 mA/cm^2 , respectively, using symmetric Mg-Mg cells. Measurements were started directly after assembling the cells; d) Nyquist plots of a symmetric Mg-Mg cell containing 0.1 M $Mg[BH_4]_2/1.5$ M $Li[BH_4]$ /diglyme with resting times between 0.5 and 50 hours at OCV; e) Nyquist plots of a symmetric Mg-Mg cell containing 0.1 M $Mg[BH_4]_2/1.5$ M $Li[BH_4]$ /diglyme after the given number of cycles. Mg foils were applied in the measurements.

efficiency of the electrolyte. Thus, cells containing 0.1 M $Mg[BH_4]_2/1.5$ M $Li[BH_4]$ (Figure 1c pink, left) showed good cycle stability with a very low overpotential < 0.04 V at a current density of 0.05 mA/cm^2 for 100 hours. The inset of the voltage profile shows a rectangular potential profile, indicating smooth Mg plating and stripping. In comparison, cells containing 0.1 M $Mg[BH_4]_2/0.5$ M $Li[BH_4]$ showed a higher polarization potential up to 0.13 V (Figure 1c blue, left) indicating poorer Mg plating and stripping performance. It is worth to point out that the overpotential of the 0.1 M $Mg[BH_4]_2/1.5$ M $Li[BH_4]$ electrolyte is substantially lower than the one reported for the $Mg[B(hfp)]_2$ system (around 0.1 V).^[20]

2.2. Electrochemical Impedance Spectroscopy

Since the overpotential of a symmetric Mg-Mg cell based on 0.1 M $Mg[BH_4]_2/1.5$ M $Li[BH_4]$ up to cycle fifteen was higher than during the following 185 cycles (0.08 V vs. 0.04 V), electrochemical impedance spectroscopy (EIS) was applied,

both during open circuit voltage (OCV) and after cycling. Figure 1d shows the Nyquist plot of a resting symmetrical Mg–Mg cell at OCV (dots). The plot was fitted according to the model shown in the inset, comprising the high frequency resistance (R_1) and two RC (resistor and capacitor in parallel) elements in series. The two RC elements model the charge transfer reaction (R_2 and Q_2) and most likely a blocking layer on the anode (R_3 and Q_3).

Since the charge transfer resistance is several orders of magnitude higher than other resistance contributions,^[31–32] only one clear semicircle is visible and a distinction between the two resistances is not possible. For the following discussions, the sum of R_2 and R_3 will be described as the overall charge transfer resistance. Fits are shown as solid lines. For more clarity, the high frequency resistance (R_1) was subtracted from all measurements. The exact values of the resistance can be found in Table S1 in the Supporting Information. Impedance measurements clearly show an increase in impedance with increasing resting time of the cell at OCV. Impedance became constant after 47.5 hours, indicating a stabilization of the interface or fully wetting of the electrodes. Nonetheless, impedance decreased dramatically after cycling the cell, as shown in Figure 1e. These data can be interpreted in that some ion-blocking layer partially blocks the interface between the electrolyte and the Mg surface during resting the cell at OCV. However, after cycling, fresh and highly conductive Mg metal surfaces are reformed, leading to the pronounced drop in impedance. Similar observations, though with different electrolyte systems, have been reported by Oscar et al.^[33] and Zhao-Karger et al.^[6] and appear to be quite unique for Mg systems.

2.3. Electrochemical Characterization

Figure 2a shows that the cells with 0.1 M Mg[BH₄]₂/0.5 M Li[BH₄] (lower blue) and 0.1 M Mg[BH₄]₂/1.5 M Li[BH₄] in diglyme (lower red) deliver a discharge capacity of ca. 420 and 800 mAh/g_{sulfur} at 0.1 C, respectively, both with virtually >99.8% Coulombic efficiency (Figure 2a top). In addition, the use of a coin cell setup with a reduced amount of electrolyte results in a virtually identical electrochemical performance (Figure S1 in the Supporting Information). This strongly indicates the high stability of the system and renders extensive sacrificial consumption of the electrolyte unlikely. The electrochemical performance of cells based on a 1 M Li[BH₄] electrolyte was also measured (Figure S2). Performance of cells based on 1 M and 1.5 M Li[BH₄], respectively, was very similar. Nonetheless, for further studies, the electrolyte with the highest lithium salt concentration (1.5 M) was used in order to prevent the potential dissolution of polysulfides.^[2] The rate tests in Figure 2b show the capacities fully recovered once the current rate was decreased, indicating good rate capability. For Coulombic efficiency see, Figure S3. The better performance of cells containing higher concentration of Li[BH₄] are attributable to the higher ionic conductivity of the electrolyte (Figure 1a), which results in higher ion mobility. The capacity contributed by the potential intercalation of Li⁺ or Mg²⁺ ions into the

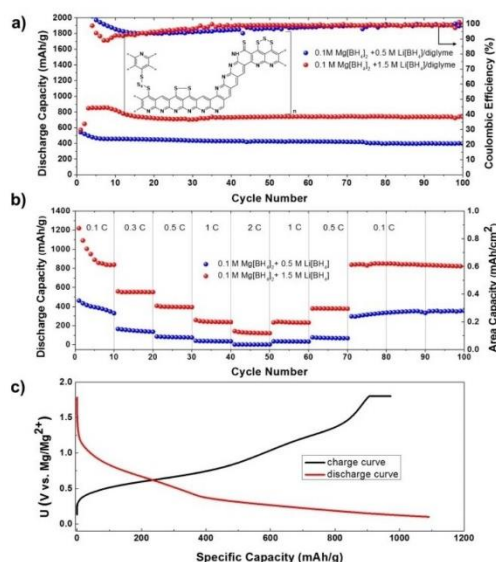


Figure 2. a) Long-term cycle stability of SPAN–Mg cells at 0.1 C, 22 °C, inset: structural features of SPAN, where $2 \leq x < 8$ ^[28] b) rate test between 0.1 C and 2 C, 28 °C. All cells contained 0.1 M Mg[BH₄]₂/0.5 M Li[BH₄]/diglyme and 0.1 M Mg[BH₄]₂/1.5 M Li[BH₄]/diglyme, respectively. The sulfur content of all cathodes was 0.6 mg/cm²; c) typical discharge and charge profiles at 0.1 C of a cell containing 0.1 M Mg[BH₄]₂/1.5 M Li[BH₄]/diglyme.

graphite current collector was determined for an SPAN-free system consisting of a Mg foil, a graphite current collector and 0.1 M Mg[BH₄]₂/1.5 M Li[BH₄]/diglyme; only a minor contribution of 0.04 mAh/cm² was found (Figure S4). The charge and discharge voltage profiles (Figure 2c) as well as cyclic voltammetry (CV) measurements (Figure S5) of a Mg foil-SPAN cell using the 0.1 M Mg[BH₄]₂/1.5 M Li[BH₄] electrolyte provide some insight into the chemical reactions inside the cell. The first striking feature is that the voltage plateau around 1.5 V, which corresponds to the formation of long-chain polysulfides (e.g. MgS₈), is not observed.^[20] Similar was observed in Li-SPAN cells, in which only LiS_x species with $1 \leq x \leq 4$ were identified.^[24] This is attributed to the unique structure of SPAN that does not possess any elemental sulfur but only chemically bound sulfur chains (Figure 2a inset). Since the sulfur chain length in the SPAN structure has an upper limit of eight ($x \leq 6$) and the C–S bond is hard to break, no long-chain polysulfides, such as MgS₈ are formed with SPAN cathodes. Indeed, elemental analysis of the SPAN-based cathode of fully discharged Mg–SPAN cells contain ca. 11 wt-% of S and show an atomic ratio of N:S close to unity (0.98). This clearly indicates that the final C–S bonds in the SPAN structure are not broken even after full discharge. This is in line with a recent paper by Wang et al. on Li–S batteries.^[35] Instead, in the discharge curve, two distinct sloped regions were observed, one at 1.2–0.4 V and a second at 0.4–0.1 V. The first region is most probably attributable to the

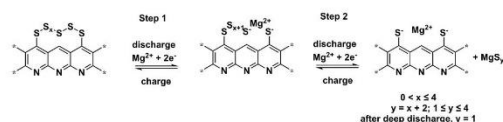
formation of magnesium polysulfides, such as MgS_4 or Mg_3S_8 .^[36] Scheme 1 outlines the proposed redox process of the SPAN cathode. After incorporation of Mg ions into the SPAN structure (step 1), MgS_4 and Mg_3S_8 , respectively, are proposed to form (Scheme 1, step 2). During further discharge, the sulfur species are released via breakage of the S–S but not of the C–S bond, due to the higher bonding energy of C–S bonds (Scheme 1, $y = 4$ or $8/3$). Since the potential of Li is similar to that of Mg, some Li polysulfides might also coexist inside the electrolyte. The second region of the discharge curve starts at around 0.4 V, which is the deep discharge of the system. This region indicates the formation of low-order magnesium sulfides, i.e., MgS and MgS_2 . MgS is stable and crystalline and therefore hard to re-oxidize to amorphous Mg_3S_8 and eventually also passivates the Mg anode.

Due to the existence of Li^+ ions inside of the system, however, some lithiation of the MgS is proposed to happen in this voltage range, which might also contribute to the overall capacity.^[4,36–38] The charge curve shows an almost constant increase from 0.4 to 1.8 V, suggesting multiple reactions in this voltage range. In the presence of Li^+ ions, (lithiated) MgS or MgS_2 react reversibly back to the polysulfides, such as Mg_3S_8 , contributing to the observed high reversibility. Overall, by integrating the discharge curve, an energy density of ca. 430 mWh/g_{sulfur} or 14 mWh/g_{cathode} at 0.1 C is obtained.

2.4. XPS Post-Mortem Analysis

To gain an insight of the sulfur species forming on the electrodes, ex situ high resolution X-ray photoelectron spectroscopy (XPS) was conducted on the pristine SPAN powder, as well as on anodes and cathodes fully charged and deep discharged over seven cycles. The sulfur-containing fragments S–S/S–C and S=C featured by the S 2p_{3/2} and S 2p_{1/2} signals in SPAN are shown in Figure 3a.

In particular the S 2p_{3/2} signals were used to monitor variations in the sulfur species during cycling.^[18,20] On the pristine SPAN powder, the S 2p_{3/2} signals at 161.7 and 163.4 eV are attributable to the S=C and C–S/S–S bonds.^[29] It should be noted that the pristine SPAN powder was pressed onto indium foil whereas the cycled SPAN was mixed with carbon black and coated onto a graphite current collector. This leads to a shift in binding energy compared to the pristine SPAN powder. After seven cycles, at a deep discharged state (0.1 V), the signal at 161.7 eV appears to be more pronounced than the one at 163.4 eV, suggesting that large amounts of lithium/magnesium



Scheme 1. Proposed redox process of the SPAN cathode. For simplicity, Mg^{2+} ions were used as model ion; MgS , could transform to short sulfides ($y = 1, 2$). In the deep discharge state, it is in the form of MgS .

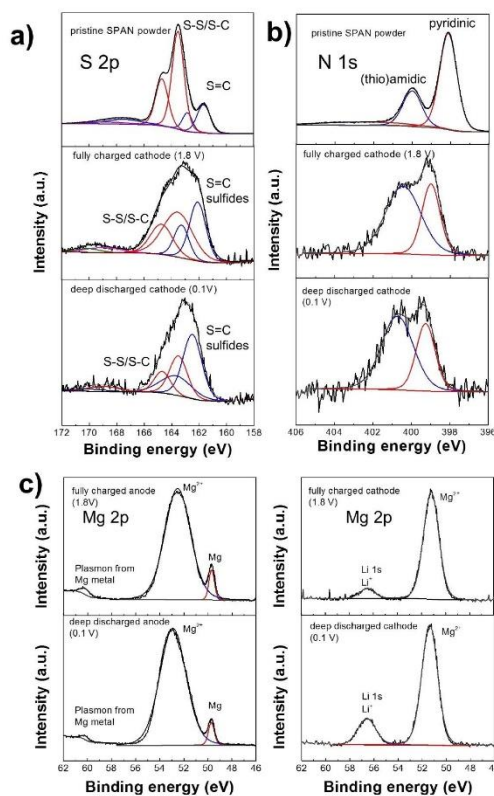


Figure 3. a) High-resolution S 2p (upper left) and b) N 1s (upper right) ex situ XPS spectra of pristine SPAN powder and aged cathodes and anodes after seven cycles at the fully charged and deep-discharged state, respectively. The pristine SPAN powder was pressed onto indium foil whereas the cycled SPAN was mixed with carbon black and coated onto graphite foil, which is partially conductive, resulting in the broader peaks of the cycled cathodes and the shift in binding energy compared to the pristine SPAN powder; c) Mg 2p (down) ex situ XPS spectra of pristine SPAN powder and aged cathodes and anodes after seven cycles at the fully charged and deep-discharged state, respectively.

sulfides are formed at 0.1 V on the cathode side, which is in line with the above-proposed redox process. Notably, after seven cycles and in the fully charged state (1.8 V), the detected peak positions are similar to those in pristine SPAN, in which the sulfur exists in the form of S=C, S–S and S–C species.^[29] This suggests that the SPAN framework as such is stable over the entire redox process. Further on, N 1s spectra of both pristine SPAN powder and aged cathodes (Figure 3b) suggest that the main features of SPAN structure including (thio)amidic (401.5 eV) and pyridinic (399.1 eV) chemical units are stable over the entire redox process. Figure 3c shows high resolution XPS spectra in the energy region of the Mg 2p and Li 1s core levels of aged electrodes after seven cycles at different voltage states. The spectrum of the Mg anode at a fully charged state

(1.8 V) shows a signal at 51.5 eV and a smaller one at 48.5 eV, which is assignable to Mg^{2+} (MgO , MgS or $\text{Mg}[\text{BH}_4]_2$) and Mg (0), respectively. Also, a small signal at 59.2 eV associated with the plasmon excitation of the magnesium nanoparticles might indicate the presence of plated Mg on the surface.^[39] In view of the redox potentials of Li (-3.04 V) and Mg (-2.36 V) and the maximum charging voltage of 1.8 V, the formation of Li (0) seems highly unlikely. On the cathode side, both samples (0.1 V and 1.8 V) contain substantial amounts of Li^+ observed at 56.1 eV. During discharge, more lithium polysulfide species are formed on the cathode, resulting in a more pronounced signal of the Li 1s peak at the discharged cathode. The Li species on the cathode at the charged state might stem from the electrolyte, lithium oxide and/or residual lithium polysulfides.

2.5. Role of the Mg Anodes

Apart from the cathode and the electrolyte, the anode plays a crucial role in electrochemical performance.^[40–42] Generally, a large specific surface area is highly desired since this offers a large number of sites for plating and stripping, thereby impeding the build-up of a passivation layer at the anode and reducing the resistance for charge transfer. In order to determine the influence of specific surface area on electrochemical performance, three different anode materials, i.e., Rieke Mg, commercial Mg powder and Mg foil, were used. Scanning electron micrographs show the plate-shaped particles of Rieke Mg, which were 30–50 nm thick and had a diameter of 0.3–2 μm (Figure 4a), while commercial Mg powder (Figure S6) consisted of substantially larger particles, typically 44 μm in diameter. The X-ray diffraction (XRD) spectrum of Rieke Mg powder shows the expected signals (Figure S7). N_2 -adsorption measurements (BET method) revealed a specific surface area of 13.43 m^2/g for Rieke Mg, which is more than one order of magnitude higher than the one of conventional Mg powder (325 mesh, 0.60 m^2/g). In sharp contrast, the surface area of Mg

foil was only 0.002 m^2/g and thus almost 7000 times smaller than the one of Rieke Mg. To investigate the effect of the specific surface area of the anode on electrochemical behavior, Mg anodes were prepared from Rieke Mg applying different pressures. According to Figure 4b–d, the surface gets smoother with increasing pressure. For the lowest pressure (13.8 MPa), the surface shows rough features with holes between the individual powder particles. Some cavities even form deep channels, where the individual particles can still be detected. This creates a larger surface area compared to a regular metal foil. The higher the pressure applied, the more cavities are closed. This occurs even at a low pressure of 55.1 MPa, while the surface of the Mg anode prepared 96.5 MPa is even flatter. N_2 -adsorption measurements (BET method) of the anodes prepared with different pressures support this trend.

Thus, the parent Mg powder had a specific surface area of 13.4 m^2/g , while anodes prepared at 13.8, 55.1 and 96.5 MPa had specific surface areas of 11.3, 11.6 and 9.4 m^2/g , respectively (Figure S8). However, it is important to note that the pellets had to be divided into two parts prior to measurements. This inevitably induces some error to all the measurements, especially for pellets prepared at high pressures, since the newly created cross-section area adds to the original surface area.

To study the impedance of the Mg powder anodes prepared at different pressures, symmetrical Mg–Mg cells were measured at OCV. Similar to the measurement presented in Figure 1d, a time-dependent increase of the impedance was also detected for the pressed anodes. For a more lucid comparison between the different types of anodes, only the impedance after resting for 1 hour at OCV is presented in Figure 5a. The Nyquist plots were fitted as described in Figure 1d; the exact fitting data are given in Table S2. Obviously, the impedance of all pressed Mg powder anodes is one order of magnitude lower than that of the foil. The inset shows a higher resolution of the curves of the pressed anodes. Clearly, impedance increased with increasing pressure during anode preparation. The charge transfer resistances were 331, 773 and 1150 Ω for the Mg anodes prepared at 13.8, 55.1 and 96.5 MPa, respectively. This clearly indicates that the higher the surface area of the anode is, the lower the resistance for the charge transfer of the Mg^{2+} becomes. Notably, the charge transfer resistance did not linearly increase with increasing preparation pressure. Instead, a more pronounced increase of the impedance between the anodes prepared at 13.8 and 55.1 MPa, compared to the impedance increase between the 55.1 and 96.5 MPa, was found. This can be explained by SEM: at pressures higher than 13.8 MPa, the individual particles progressively fuse together, resulting in a much smaller surface area. Notably, this is to the best of our knowledge the first correlation between anode morphology and the charge transfer resistance reported so far.

To determine the influence of the different charge transfer resistance on cycle stability, the electrochemical performance of Mg–S cells prepared from pressed Mg-anodes fabricated at different pressures was studied applying a discharge rate of 0.5 C. Results are shown in Figure 5b.

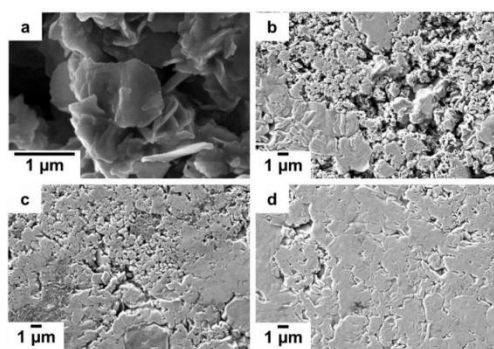


Figure 4. SEM images of the surfaces of pressed anodes prepared from Rieke Mg with different preparation pressures: a) pristine Rieke Mg powder, b) 13.8 MPa, c) 55.1 MPa, d) 96.5 MPa.

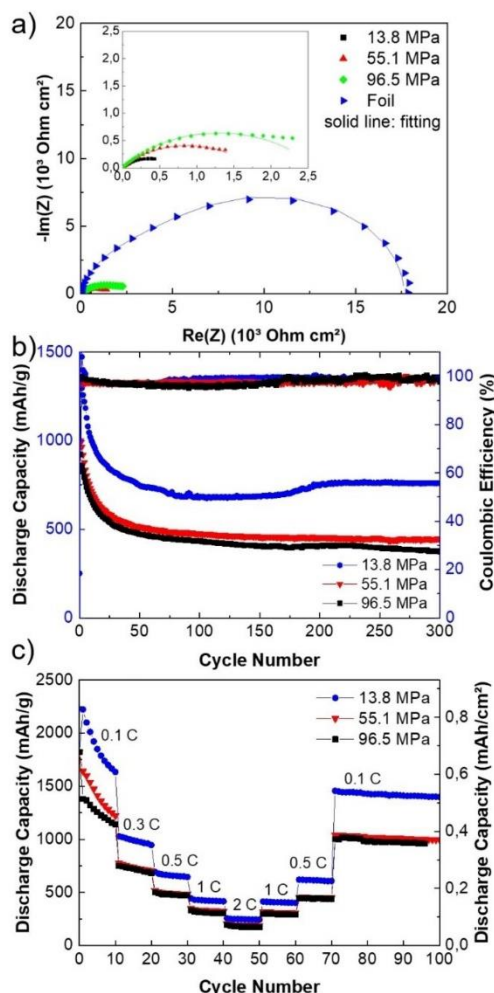


Figure 5. a) Nyquist plots of a symmetric Mg–Mg cell containing 0.1 M Mg [BH₄]₂/1.5 M Li[BH₄]₂/diglyme after 1 hour resting time at OCV with Mg anodes prepared from Rieke Mg at different pressure and from a Mg foil for comparison. Inset: Enlarged part of the plot showing only the impedance of the powder anodes and the equivalent circuit for fitting. b) Long-term cycle stability of SPAN–Mg cells with pressed Mg anode at 0.5 C, 22 °C; c) rate tests between 0.1 C and 2 C, 22 °C. All cells contained 0.1 M Mg[BH₄]₂/1.5 M Li[BH₄]₂/diglyme.

The Coulombic efficiency remained constant at ca. 100%, suggesting that the system is stable. On top of that, a higher cycle stability than with cells based on a Mg-foil was observed: more than 300 cycles could be run without any signs of decomposition. For all pressed anodes, the discharge capacity was higher compared to the foil anode. Cells containing anodes compacted with the lowest pressure (13.8 MPa) show discharge

capacities of ca. 800 mAh/g_{sulfur} at 0.5 C. With increasing fabrication pressure of the anodes, decreasing capacities were observed, though still with good cycle stability. In line with the results for charge transfer resistance and with the observations from SEM, the differences in capacity became less pronounced with increasing fabrication pressure. In addition, the difference in capacity for the differently prepared anodes become smaller at higher C-rates (Figure 5c). Cells containing a Mg-anode prepared at 13.8 MPa delivered 1400 mAh/g_{sulfur} at 0.1 C, and 250 mAh/g_{sulfur} at 2 C. Notably, upon cycling between 0.1 C and 2 C, capacity reestablishes to 1500 mAh/g_{sulfur} after 70 cycles when returning to 0.1 C for a cathode prepared at 13.8 MPa.

Differences in capacity between a cell containing a Mg-anode prepared at 13.8 MPa and one prepared at 96.5 MPa were 400 mAh/g_{sulfur} and 70 mAh/g_{sulfur} at 0.1 C and 2 C, respectively. The Coulombic efficiency for the rate test was ca. 100% for every tested C-rate (Figure S9). These observations clearly reveal the importance of anode morphology and specific surface area to allow a fast and reversible Mg plating. Similar to what was found for the Mg-foil, the capacity contributed by any possible Li-ion intercalation into the graphite current collector was negligible, as can be deduced from Figure S10.

Finally, it is worth to mention that the charge and discharge voltage profiles of cells based on SPAN and pressed Mg anodes (Figure S11) were similar as those obtained with cells based on SPAN and a standard Mg foil anode, confirming that the same electrochemical reactions occur during cycling. By integrating the discharge curve, a power density of ca. 400 mWh/g_{sulfur} or 13 mWh/g_{cathode} though at a discharge rate of 0.5 C, was determined. A summary of the electrochemical performance of the different anodes is given in Table S3.

3. Conclusions

The first long-lasting Mg–SPAN cell based on a Mg[BH₄]₂/Li[BH₄]₂ electrolyte in diglyme has been developed. The tailored electrolyte features a low overpotential of only 0.04 V and efficiently removes any blocking layer on the surface of the Mg foil. SPAN-based Mg–S cells based on the novel electrolyte deliver around 800 mAh/g_{sulfur} at 0.1 C and also show very good rate capability. Compared to Mg foils, the utilization of the pressed Rieke Mg anodes further improves cell performance, allowing for ca. 800 mAh/g_{sulfur} at 0.5 C over 300 cycles. Post-mortem analysis supports the proposed redox mechanism of the SPAN cathodes. In summary, the combination of SPAN as cathode material with this particular “dual” electrolyte and high surface area Mg anodes clearly offers new opportunities for Mg–S cells.

Experimental Section

Chemicals

All samples were handled in an Ar-filled glove box with water and oxygen levels < 0.1 ppm. All glassware was dried in an oven at 120 °C. Mg(BH₄)₂ (95%), Li[BH₄] (> 95%) PAN (*M_n* = 36,500 g/mol, \bar{D} = 3.6), MgCl₂, naphthalene and anhydrous diethyleneglycol dimethyl ether (diglyme, 99.5%, anhydrous) were purchased from Merck and used as received. Li foils were purchased from Alfa Aesar and were polished before use. Mg foil (0.25 mm thick, 99.9%) and graphite foil (0.13 mm, 99.8%) were purchased from Alfa Aesar Germany. The Mg chips were polished with a ceramic knife inside a glovebox to remove the oxide layer before assembling the cells.

Preparation of Mg[BH₄]₂/Li[BH₄] solutions in diglyme

In an argon-filled glovebox, 21.6 mg Mg(BH₄)₂ (0.1000 mol) and 132 mg Li[BH₄] (1.500 mol) were dissolved in 4 mL diglyme. The mixture was stirred at room temperature overnight, then filtered through a glass fiber filter and stored over molecular sieves for at least one day in the glovebox. The preparation of 0.1 M Mg[BH₄]₂/1 M Li[BH₄] and 0.1 M Mg[BH₄]₂/0.5 M Li[BH₄] solutions in diglyme was conducted in the similar way. The ¹H NMR spectrum of the electrolyte can be found in Figure S12. The ionic conductivity of the electrolyte solutions with different concentrations was measured using an InLab Sensor conductometer (Mettler Toledo).

Preparation of SPAN

The active material in the cathode, sulfurated poly(acrylonitrile) (SPAN) was prepared via a two-step reaction. First, 1.00 g of poly(acrylonitrile) (PAN) powder was thoroughly mixed with excess (ca. 15 g) sulfur powder inside a high-temperature resistant quartz glass tube, which was heated to 150 °C under Ar. After the sulfur in the glass tube was fully molten, the tube was cooled to room temperature and placed inside a furnace apparatus. The temperature of the oven was first increased to 150 °C within 30 minutes and then held for 30 minutes. Then, the temperature was gradually increased to 550 °C over 3 hours and held for another 5 hours. The oven was allowed to cool to room temperature overnight and the quartz glass tube was removed from the oven. Then, a heat gun was used to melt and remove the obtained SPAN (black) with excess sulfur (yellow). After that, in order to remove excess sulfur, the material was extracted in a Soxhlet apparatus using hot toluene for 2 days until no further sulfur could be extracted. The obtained SPAN compound was further dried in vacuo overnight and then manually ground with the aid of a mortar and a pestle in order to reduce the particle size of the SPAN particles. To achieve a more homogeneous particle size distribution, the SPAN particles were sieved by a 63 μm sieve. Elemental analysis of SPAN: C, 44.08%; H, 1.048%; N, 13.66%; S, 38.32%.

Preparation of the cathodes

For preparing the coated cathodes, the weight ratio of SPAN: carbon black: binder was set to 70:15:15. The weight ratio of N-methyl-2-pyrrolidone (NMP): SPAN was set to 10:1. The dispersion of the SPAN, the conductive material, the binder and NMP was thoroughly mixed at 20,000 rpm for 6 minutes. Then the slurry was coated on a graphite foil. The wet coating was dried on a vacuum plate at 60 °C and under air suction for several hours. After the coating was nearly dry, it was transferred to an oven at 60 °C for further drying. Then, round chips 12 mm in diameter were punched out. The average sulfur content was around 0.6 mg/cm²

per cathode, corresponding to 1.0 mAh/cm². The binder used for all measurements was poly(vinylidene difluoride) (PVDF), except for cathodes subjected to post-mortem elemental analysis; for these, poly(acrylic acid) (PAA) was used.

Preparation of pressed anodes

Rieke Mg was synthesized by the reduction of MgCl₂ with Li and naphthalene as an electron carrier.¹²⁷ All chemicals were dried prior to use and the procedure was conducted in an Ar-filled glovebox. Naphthalene (27.7 g, 216 mmol) was dissolved in 150 mL of dry THF. To this solution, freshly polished Li (1.5 g, 216 mmol) was added in pieces. MgCl₂ (10.3 mg, 108 mmol) was added slowly to keep the exothermic reduction under control. After vigorous stirring for at least 15 h, the precipitated Mg powder was washed several times with THF and diethyl ether. The XRD pattern of the synthesized Mg powder is shown in Figure S7. The synthesized powder was then pressed with the aid of a hydraulic press in an argon filled glovebox, applying 13.8, 55.1 and 96.5 MPa, respectively.

Electrochemistry

Cells were assembled in an Ar-filled glovebox. Both the overpotential and the long-term cycle stability were tested using symmetric Mg–Mg Swagelok-type cells using two pieces of Mg foils containing the corresponding electrolyte. Discharging and charging of the cells was performed at a constant current for 0.5 h at 0.05 and 0.1 mA/cm², respectively.

For testing cycle stability and for investigating the influence of different concentrations of the [BH₄][−] anion in the electrolytes, Swagelok cells were built from an SPAN cathode and Mg foil using 0.1 M Mg[BH₄]₂ and 1.5 M Li[BH₄]/0.5 M Li[BH₄] dissolved in diglyme as electrolyte. Cells comprised one Mg foil (12 mm diameter), one SPAN cathode (12 mm diameter) and two Whatman glass fiber separators. 100 μL of electrolyte were added onto each of the separators. The Mg foil was thoroughly scratched with a ceramic knife inside a glovebox to remove the oxide layer. For comparison, coin cells using the same system were manufactured using 130 μL of electrolyte. All cycling data were recorded on a BasyTec XCTS-LAB system. Cells were cycled at a potential window of 0.1–1.8 V to avoid decomposition of the electrolyte at higher voltage.¹⁴³ Long-term cycle stability testing was performed at 0.1 C at room temperature (22 °C) using two electrolytes with different concentrations. CV-measurements were conducted using a three-electrode cell set-up (PAT cell from EL-CELL ©) with SPAN as working electrode (WE), Mg foil as the counter and reference electrodes (Mg_{CE} and Mg_{RE}).

Rate capability testing of the cells was investigated using a stress test that comprised cycling ten times each at 0.1 C, 0.3 C, 0.5 C, 1 C, 2 C and then back to 0.1 C for another 30 cycles. (0.1 C = 0.1 mA/cm²).

Electrochemical impedance spectroscopy (EIS) data of the open circuit voltage (OCV) were measured with a signal amplitude of 10 mV in a frequency range from 300 kHz to 100 mHz with no current applied on Biologic VMP3. Data were fitted using the integrated EC-Lab software. The resistance data were normalized to the geometrical area of the electrode.

Measurement of the powder surface area by nitrogen adsorption

Nitrogen adsorption analyses were performed at 77 K on a Quantachrome Instruments Autosorb iQ MP automatic volumetric instrument. Magnesium samples were degassed for 16 hours at 150 °C under vacuum prior to the gas adsorption studies. Surface areas were evaluated using the eleven-point Brunauer-Emmett-Teller (BET) model implemented in the ASiQwin software version 3.01.

Ex situ XPS measurements

For ex situ XPS measurements, Mg-S cells were disconnected from the BasyTech after seven cycles. All cells were opened in an Ar-filled glovebox and the electrodes were thoroughly rinsed with DME and dried in vacuo overnight to remove all the solvent. The electrodes were then fixed on a sample holder and transferred under argon atmosphere directly into the X-ray photoelectron spectrometer to avoid any contamination with air. Pristine SPAN spectra were obtained by measuring pure SPAN powder stabilized on indium foil. XPS was performed on a Kratos Axis Ultra system equipped with a monochromatic Al K_α source using a pass-energy of 20 eV for the high-resolution measurements. Data were analyzed using CasaXPS. The energy separation and peak area of the S 2p_{3/2} and S 2p_{1/2} were constrained according to the literature.^[44] Broader peaks and spikes in the Mg 2p spectra were a result of the charging of the anodes. Characteristic C1s signals of SPAN were calibrated to 284.8 eV according to the literature.^[29]

Post-mortem analysis of the discharged cathodes

Mg-SPAN cells based on Mg foil anodes were disconnected at a fully discharged state (0.1 V) after two cycles. The cathodes were thoroughly washed with DME and dried. The coating was then removed from the graphite current collector. Elemental analysis of the obtained powder revealed 4.75 wt% N and 11.12 wt% S, respectively. The corresponding molar ratio of N to S was ca. 0.98.

Acknowledgements

Financial support by the German Federal Ministry of Education and research (project number 03XP0208J) and by the German Federal Ministry of Economic Affairs and Energy (project number 03ETE003E) is gratefully acknowledged. The authors would also like to thank the Ministry of Science, research and Arts of the Federal State of Baden-Württemberg for the financial support of the projects within the InnovationsCampus Mobilität der Zukunft. Finally, we wish to thank Mr. U. Hageroth from the German Institutes of Textile and Fiber Research (DITF) Denkendorf and Mr. B. Fenk from the Max Planck Institute for Solid State Research, Stuttgart, for the SEM measurements. Open access funding enabled and organized by Projekt DEAL.

Conflict of Interest

The authors declare no conflict of interest.

Keywords: magnesium · sulfur · sulfurized polyacrylonitrile · SPAN · borohydride · batteries

- [1] H. Kim, T. S. Arthur, G. D. Allred, J. Zajicek, J. G. Newman, A. E. Rodnyansky, A. G. Oliver, W. C. Bogges, J. Muldoon, *Nat. Commun.* **2011**, *2*, 1–6.
- [2] P. Wang, M. R. Buchmeiser, *Adv. Funct. Mater.* **2019**, *29*, 1905248–1905275.
- [3] T. Gao, S. Hou, F. Wang, Z. Ma, X. Li, K. Xu, C. Wang, *Angew. Chem.* **2017**, *129*, 13711–13715; *Angew. Chem. Int. Ed.* **2017**, *13526*–13530.
- [4] S. Y. Ha, Y. W. Lee, S. W. Woo, B. Koo, J. S. Kim, J. Cho, K. T. Lee, N. S. Choi, *ACS Appl. Mater. Interfaces* **2014**, *6*, 4063–4073.
- [5] X. Ji, K. T. Lee, L. F. Nazar, *Nat. Mater.* **2009**, *8*, 500–506.
- [6] Z. Zhao-Karger, M. E. G. Bardaji, O. Fuhr, M. Fichtner, *J. Mater. Chem. A* **2017**, *5*, 10815–10820.
- [7] W. Li, S. Cheng, J. Wang, Y. Qiu, Z. Zheng, H. Lin, S. Nanda, Q. Ma, Y. Xu, F. Ye, M. Liu, L. Zhou, Y. Zhang, *Angew. Chem.* **2016**, *128*, 6516–6520; *Angew. Chem. Int. Ed.* **2016**, *55*, 6406–6410.
- [8] A. Du, Z. Zhang, H. Qu, Z. Cui, L. Qiao, L. Wang, J. Chai, T. Lu, S. Dong, T. Dong, H. Xu, X. Zhou, G. Cui, *Energy Environ. Sci.* **2017**, *10*, 2616–2625.
- [9] X. Yu, M. Arumugam, *ACS Energy Lett.* **2016**, *1*, 431–437.
- [10] P. Zuo, Y. Li, M. He, R. Li, Y. Ma, C. Du, Y. Gao, G. Yin (Harbin Institute of Technology), CN107910535A, **2018**.
- [11] T. Gao, M. Noked, A. J. Pearce, E. Gillette, X. Fan, Y. Zhu, C. Luo, L. Suo, M. A. Schroeder, K. Xu, S. B. Lee, G. W. Rubloff, C. Wang, *J. Am. Chem. Soc.* **2015**, *137*, 12388–12393.
- [12] A. C. Kozen, C. F. Lin, A. J. Pearce, M. A. Schroeder, X. Han, L. Hu, S. Lee, G. W. Rubloff, M. Noked, *ACS Nano* **2015**, *9*, 5884–5892.
- [13] B. P. Vinayan, Z. Zhao-Karger, T. Diemant, V. S. Chakravadhanula, N. I. Schwarzburger, M. A. Cambaz, R. J. Behm, C. Kubel, M. Fichtner, *Nanoscale* **2016**, *8*, 3296–3306.
- [14] Y. Cheng, Y. Shao, J. G. Zhang, V. L. Sprenkle, J. Liu, G. Li, *Chem. Commun.* **2014**, *50*, 9644–9646.
- [15] Z. Zhao-Karger, X. Zhao, D. Wang, T. Diemant, R. J. Behm, M. Fichtner, *Adv. Energy Mater.* **2014**, *5*, 1401155–1401164.
- [16] C. Fotea, J. Callaway, M. R. Alexander, *Surf. Interface Anal.* **2006**, *38*, 1363–1371.
- [17] M. Santamaria, F. Di Quarto, S. Zanna, P. Marcus, *Electrochim. Acta* **2007**, *53*, 1314–1324.
- [18] Y. Xu, G. Zhou, S. Zhao, W. Li, F. Shi, J. Li, J. Feng, Y. Zhao, Y. Wu, J. Guo, Y. Cui, Y. Zhang, *Adv. Sci.* **2019**, *6*, 1800981–1800987.
- [19] L. Zeng, N. Wang, J. Yang, J. Wang, Y. NuLi, *J. Electrochem. Soc.* **2017**, *164*, A2504–A2512.
- [20] Z. Zhao-Karger, R. Liu, W. Dai, Z. Li, T. Diemant, B. P. Vinayan, C. Bonatto Minella, X. Yu, A. Manthiram, R. J. Behm, M. Ruben, M. Fichtner, *ACS Energy Lett.* **2018**, *3*, 2005–2013.
- [21] I. Shterenberg, M. Salama, H. D. Yoo, Y. Gofer, J.-B. Park, Y.-K. Sun, D. Aurbach, *J. Electrochem. Soc.* **2015**, *162*, A7118–A7128.
- [22] Y. Yang, W. Wang, Y. Nuli, J. Yang, J. Wang, *ACS Appl. Mater. Interfaces* **2019**, *11*, 9062–9072.
- [23] L. Wang, X. M. He, J. J. Li, M. Chen, J. Gao, C. Y. Jiang, *Electrochim. Acta* **2012**, *72*, 114–119.
- [24] J. Fanous, M. Wegner, M. B. M. Spera, M. R. Buchmeiser, *J. Electrochem. Soc.* **2013**, *160*, A1169–A1170.
- [25] J. Fanous, M. Wegner, J. Grimming, M. Rolff, M. B. M. Spera, M. Tenzerb, M. R. Buchmeiser, *J. Mater. Chem.* **2012**, *22*, 23240–23245.
- [26] J. Fanous, M. Wegner, J. Grimming, A. Andresen, M. R. Buchmeiser, *Chem. Mater.* **2011**, *23*, 5024–5028.
- [27] R. D. Rieke, *Science* **1989**, *246*, 1260–1264.
- [28] Y. Shao, T. Liu, G. Li, M. Gu, Z. Nie, M. Engelhard, J. Xiao, D. Lv, C. Wang, J. G. Zhang, J. Liu, *Sci. Rep.* **2013**, *3*, 1–7.
- [29] M. Frey, R. K. Zenn, S. Warneke, K. Müller, A. Hintennach, R. E. Dinnebie, M. R. Buchmeiser, *ACS Energy Lett.* **2017**, *2*, 595–604.
- [30] C. F. Riadigos, R. Iglesias, M. A. Rivas, T. P. Iglesias, *J. Chem. Thermodyn.* **2011**, *43*, 275–283.
- [31] B. T. Habte, F. Jiang, *Solid State Ionics* **2018**, *314*, 81–91.
- [32] B. Yan, M. Li, X. Li, Z. Bai, L. Dong, D. Li, *Electrochim. Acta* **2015**, *164*, 55–61.
- [33] O. Tutusaus, R. Mohtadi, N. Singh, T. S. Arthur, F. Mizuno, *ACS Energy Lett.* **2016**, *2*, 224–229.
- [34] S. Warneke, R. K. Zenn, T. Leberz, K. Müller, A. Hintennach, U. Starke, R. E. Dinnebie, M. R. Buchmeiser, *Adv. Sustain. Syst.* **2018**, *2*, 1700144–1700149.

- [35] W. Wang, Z. Cao, G. A. Elia, Y. Wu, W. Wahyudi, E. Abou-Hamad, A.-H. Emwas, L. Cavallo, L.-J. Li, J. Ming, *ACS Energy Lett.* **2018**, *3*, 2899–2907.
- [36] Y. Xu, Y. Ye, S. Zhao, J. Feng, J. Li, H. Chen, A. Yang, F. Shi, L. Jia, Y. Wu, X. Yu, P. A. Glans-Suzuki, Y. Cui, J. Guo, Y. Zhang, *Nano Lett.* **2019**, *19*, 2928–2934.
- [37] M. Helen, M. Fichtner, *Electrochim. Acta* **2015**, *169*, 180–185.
- [38] M. Wang, X. Li, M. Gao, H. Pan, Y. Liu, *J. Alloys Compd.* **2014**, *603*, 158–166.
- [39] J. Chang, R. T. Haasch, J. Kim, T. Spila, P. V. Braun, A. A. Gewirth, R. G. Nuzzo, *ACS Appl. Mater. Interfaces* **2015**, *7*, 2494–2502.
- [40] P. Saha, M. K. Datta, O. I. Velikokhatnyi, A. Manivannan, D. Alman, P. N. Kumta, *Prog. Mater. Sci.* **2014**, *66*, 1–86.
- [41] H. D. Yoo, I. Shterenberg, Y. Gofer, G. Gershinsky, N. Pour, D. Aurbach, *Energy Environ. Sci.* **2013**, *6*, 2265–2279.
- [42] J. Song, E. Sahadeo, M. Noked, S. B. Lee, *J. Phys. Chem. Lett.* **2016**, *7*, 1736–1749.
- [43] F. Tuerxun, Y. Abulizi, Y. NuLi, S. Su, J. Yang, J. Wang, *J. Power Sources* **2015**, *276*, 255–261.
- [44] J. F. Moulder, W. F. Stickle, P. E. Sobol, K. D. Bomben, *Handbook of X-ray Photoelectron Spectroscopy*, Physical Electronics Division, Perkin-Elmer Corporation, Minnesota, **1992**, pp. 1–261.

Manuscript received: May 5, 2020
Revised manuscript received: July 3, 2020
Accepted manuscript online: July 3, 2020
Version of record online: July 22, 2020

5.3 Supporting Information to: “High-Performance Magnesium-Sulfur Batteries Based on a Sulfurated Poly(acrylonitrile) Cathode, a Borohydride Electrolyte, and a High-Surface Area Magnesium Anode”

Table S1: Data fit of the EIS results for the Mg foil.

OCV (h)	R1 (Ohm)	R2+R3 (Ohm)	$\chi^2/ Z $
0.5	9.8	5120	0.0040
5	9.4	7550	0.0039
25	8.9	12690	0.0049
35	9.0	14060	0.0039
47.5	9.0	15300	0.0028
50	9.0	15340	0.0032

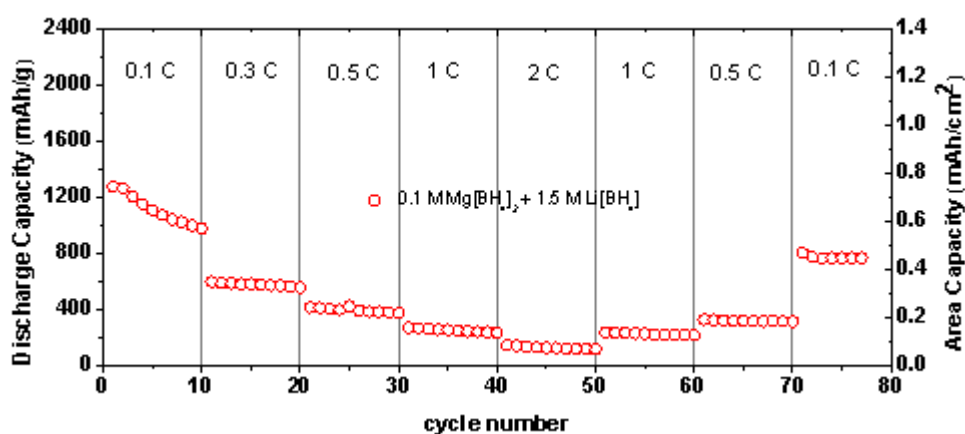


Figure S1: Results of the rate capability test using a coin cell setup; anode: Mg foil, cathode: SPAN coated on graphite foil; electrolyte: 0.1 M Mg[BH₄]₂ and 1.5 M Li[BH₄] in diglyme.

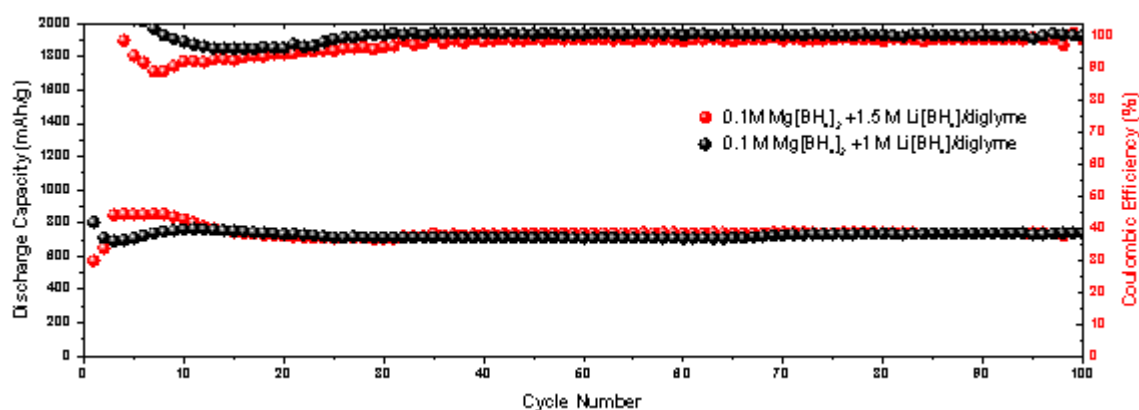


Figure S2: Comparison of the cell performance of an SPAN-Mg foil cell with 0.1 M $\text{Mg}[\text{BH}_4]_2$ / 1 M $\text{Li}[\text{BH}_4]$ in diglyme and 0.1 M $\text{Mg}[\text{BH}_4]_2$ / 1.5 M $\text{Li}[\text{BH}_4]$ in diglyme, respectively.

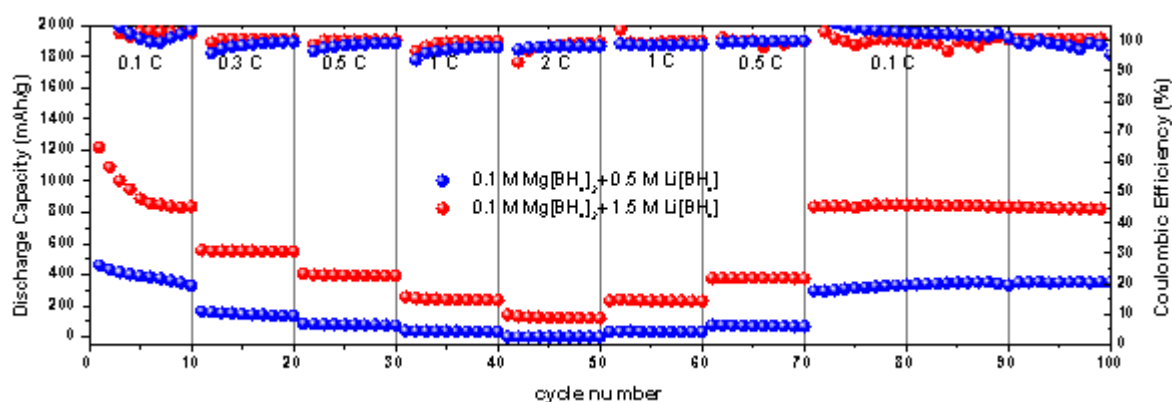


Figure S3: Rate test between 0.1 C and 2 C, 28 °C, showing the discharge capacity and the Coulombic efficiency. The cells contained 0.1 M $\text{Mg}[\text{BH}_4]_2$ / 0.5 M $\text{Li}[\text{BH}_4]$ / diglyme and 0.1 M $\text{Mg}[\text{BH}_4]_2$ / 1.5 M $\text{Li}[\text{BH}_4]$ / diglyme, respectively. The sulfur content of all cathodes was 0.6 mg/cm².

To quantify the capacity that stems from a potential intercalation and deintercalation of the Li^+ or Mg^{2+} ions into the graphite current collector, Swagelok-cells using Mg foil, a graphite current collector without SPAN and 0.1 M $\text{Mg}[\text{BH}_4]_2$ / 1.5 M $\text{Li}[\text{BH}_4]$ / diglyme electrolyte were cycled following the same test plan. Only a negligible discharge capacity of 0.04 mAh/cm² based on the weight of graphite was measured, indicating that the overall measured discharge capacity of ca. 800 mAh/g virtually solely stems from the redox reaction of sulfur.

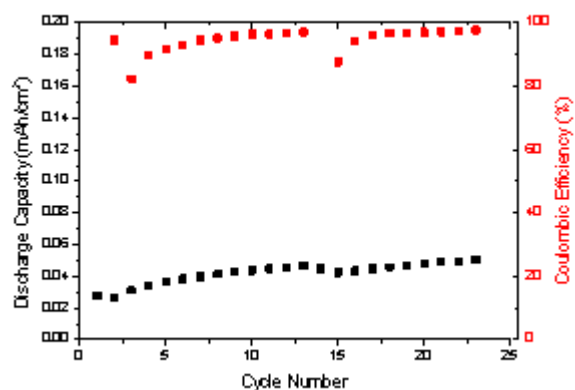


Figure S4: Cycle behavior of a Mg-graphite current collector without SPAN.

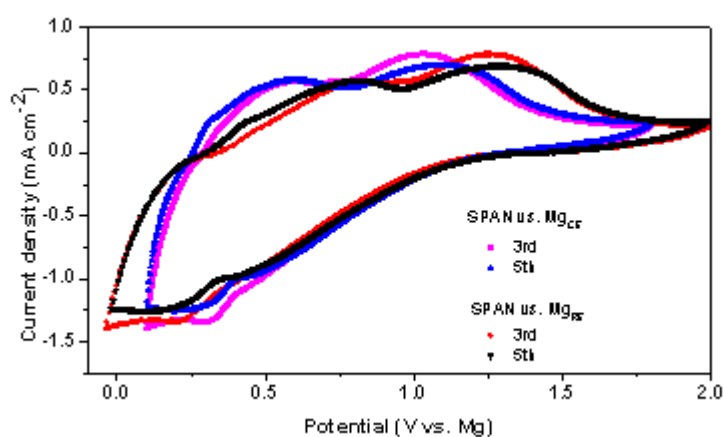


Figure S5: Cyclic voltammogram of a SPAN cathode using a three-electrode set-up at a scan rate of 1 mVs^{-1} . The cells contained SPAN, $0.1 \text{ M Mg[BH}_4\text{]}_2 / 1.5 \text{ M Li[BH}_4\text{]} / \text{diglyme}$ and a Mg foil anode. The Figure shows the typical CV result using a three-electrode cell set-up (PAT cell from EL-CELL), with SPAN as working electrode (WE), Mg foil as the counter and reference electrodes (Mg_{CE} and Mg_{RE}). In the third scan, two reduction regions, were observed at $1.2 \text{ V} - 0.5 \text{ V}$ and, $0.4 \text{ V} - 0.1 \text{ V}$ (vs. Mg_{CE}), which is in line with the discharge profile in Figure 2c. This indicates multi-step sulfur reactions. Also, in the reverse scan, two oxidation regions at $0.4 - 0.7 \text{ V}$ and $0.7 - 1.5 \text{ V}$ (vs. Mg_{CE}) can be detected. Concomitantly, the potential vs. Mg_{CE} was recorded. The reduction peak is located at slightly lower potential (0.1 V difference) compared to the voltage region vs. Mg_{RE} . Nonetheless, the oxidative signal is shifted by *ca.* 0.3 V , indicating the recharge of the cathode is restricted to the half reaction at the Mg_{CE} .^[1]

Table S2: Data fit of the EIS results with pressed Mg anodes and Mg foils.

Anode	R1 (Ohm)	R2+R3 (Ohm)	$\chi^2/ Z $
Pressed Rieke Mg 13.8 MPa	23	330	0.0008
Pressed Rieke Mg 55.1 MPa	20	770	0.0131
Pressed Rieke Mg 96.5 MPa	1	1150	0.0381
Mg foil	17	5590	0.4026

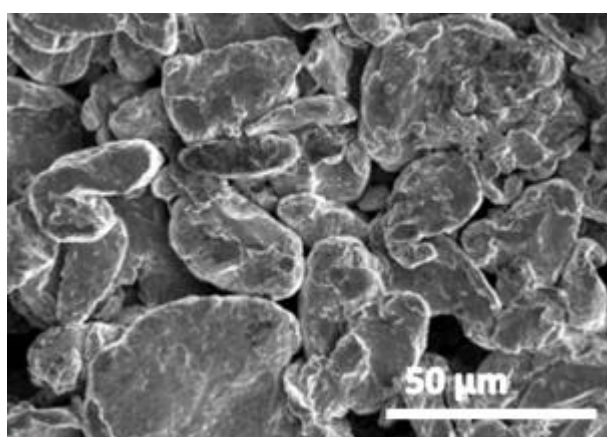


Figure S6: SEM image of customized Mg powder (Alfa Aesar, 325 mesh).

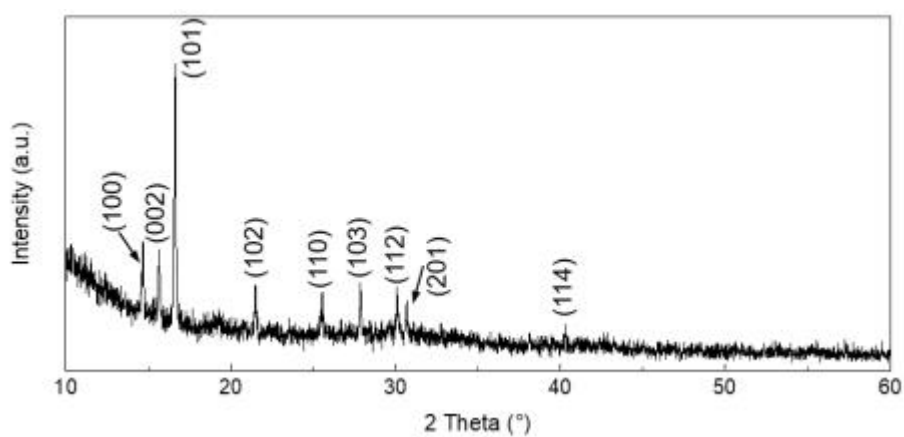


Figure S7: XRD pattern of the synthesized Rieke Mg powder.

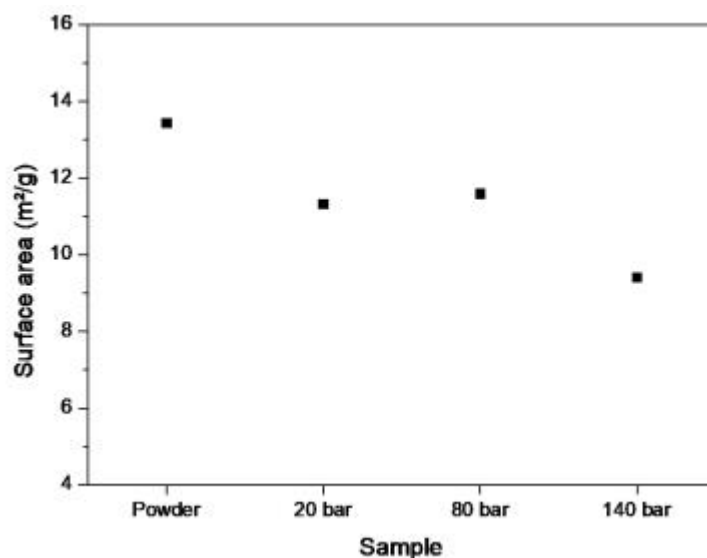


Figure S8: Values of the surface area of the Rieke Mg anodes prepared at different pressures compared to the raw Rieke Mg powder. Measured by N₂-adsorption and evaluated using the Brunauer-Emmett-Teller (BET) method.

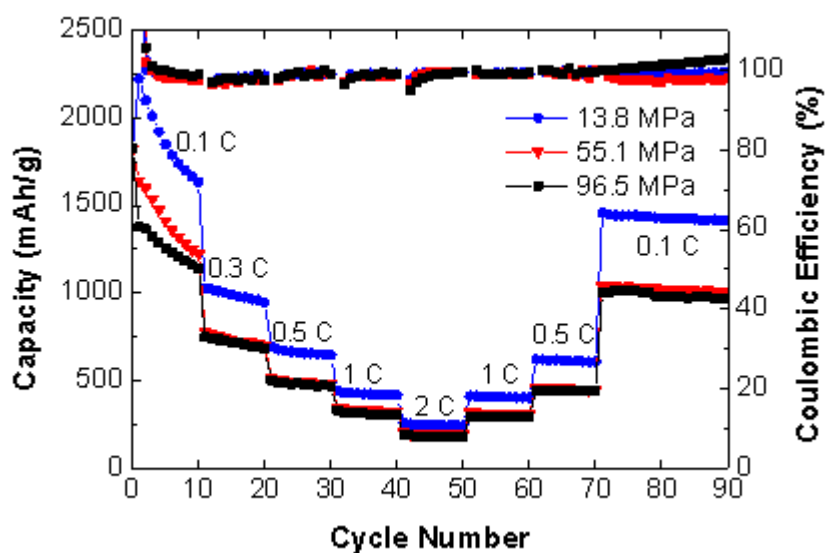


Figure S9: Rate tests of SPAN-Mg cells with pressed Mg anode between 0.1 C and 2 C, 22 °C. All cells contained 0.1 M Mg[BH₄]₂ / 1.5 M Li[BH₄] / diglyme.

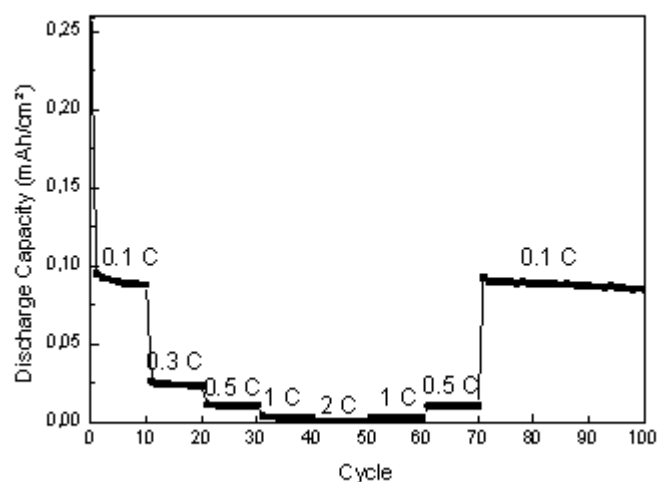


Figure S10: Contribution of the Li ion intercalation to the total capacity in the graphite current collector using Rieke Mg (13.8 MPa) and graphite current collector without SPAN.

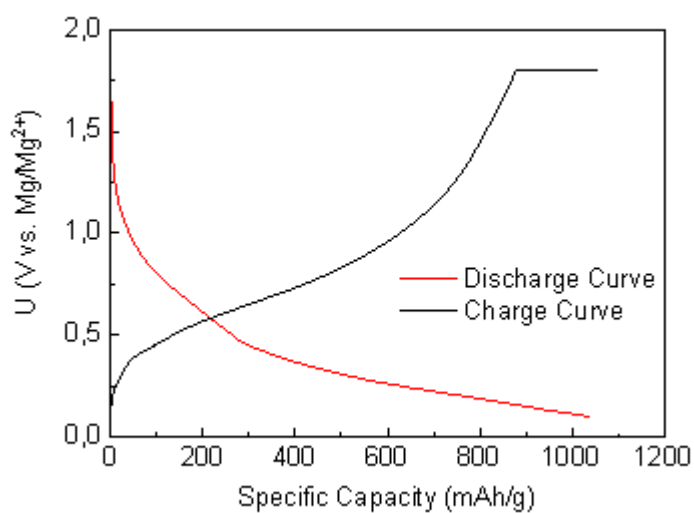


Figure S11: Discharge and charge profiles at 0.5 C of a cell containing 0.1 M Mg[BH₄]₂ / 1.5 M Li[BH₄] in diglyme and a pressed Rieke Mg anode at 55.1 MPa.

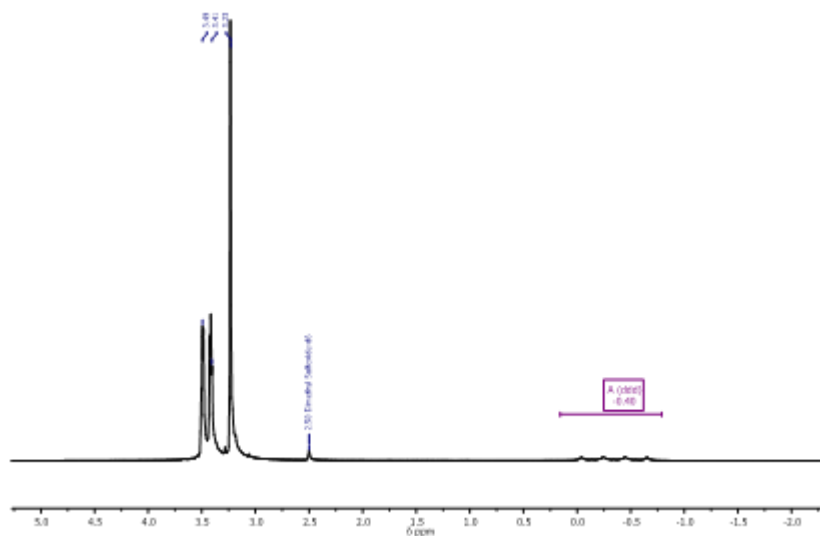


Figure S12: ^1H NMR spectrum of the electrolyte 0.1 M $\text{Mg}[\text{BH}_4]_2$ and 1.5 M $\text{Li}[\text{BH}_4]$ in diglyme (DMSO_{d6}).

Table S3: Summary of the electrochemical performance of the different anodes using 0.1 M $\text{Mg}[\text{BH}_4]_2$ / 1.5 M $\text{Li}[\text{BH}_4]$ in diglyme as electrolyte and SPAN as cathode.

Anode	Rieke Mg, pressed at 13.8 MPa	Rieke Mg, pressed at 55.1 MPa	Rieke Mg, pressed at 96.5 MPa	Foil
Resistance [Ohm]	330	770	1150	5120
Discharge Capacity (0.1 C) [mAh/g]	1400	1100	1000	800
Discharge Capacity (0.5 C) [mAh/g]	800	500	480	400

[1] Z. Zhao-Karger, R. Liu, W. Dai, Z. Li, T. Diemant, B. P. Vinayan, C. Bonatto Minella, X. Yu, A. Manthiram, R. J. Behm, M. Ruben, M. Fichtner, *ACS Energy Lett.* **2018**, 3, 2005-2013.

Chapter 6

Understanding the Role of a Lithium Salt in Mg-SPAN

Batteries

6.1 Motivation

As presented in **Chapter 5**, the use of a $\text{Mg}^{2+}/\text{Li}^+$ dual salt-electrolyte in a Mg-SPAN cell resulted in an outstanding electrochemical performance. However, the question why a dual salt electrolyte improved the cell performance in borohydride systems could not be investigated because of the extremely low solubility of $\text{Mg}[\text{BH}_4]_2$ in ether-based solvents. Without the addition of the $\text{Li}[\text{BH}_4]$ salt, even 0.1 M $\text{Mg}[\text{BH}_4]_2$ could hardly be dissolved in diglyme. On the other hand, the role of a lithium salt in Mg-SPAN batteries have not been studied in detailed. Although *Gao et al.*^[154] observed a better electrochemical performance with the addition of 1 M LiTFSI to Mg-HMDS-based electrolytes, their cells showed severe overcharging and the functions of the lithium salt were not investigated. Hence, a different electrolyte system, which can dissolve both lithium and magnesium salts, and at the same time, show good compatibility with the Mg-SPAN cells, had to be developed in order to gain a better understanding of the role of a lithium salt in Mg-SPAN batteries.

The electroactive species $[\text{Mg}_2(\mu_2\text{-Cl})_2(\text{DME})_4]^{2+}$ reportedly allowed for a reversible Mg plating and stripping.^[89] *Huang et al.*^[192] further reported on an electrolyte composed of $\text{Mg}(\text{CF}_3\text{SO}_3)_2$, MgCl_2 and AlCl_3 , which also contained the electroactive species $[\text{Mg}_2(\mu_2\text{-Cl})_2(\text{DME})_4]^{2+}$ after the synthesis of the electrolyte. They outlined the possible reaction routine of the formation of the electroactive species (**Figure 6.1a**). The authors also simulated the possible chemical structure of the corresponding electroactive species (**Figure 6.1b**). Further on, they have investigated the cycle stability of a Mg-S₈ cell using

the electrolyte ($\text{Mg}(\text{CF}_3\text{SO}_3)_2$, MgCl_2 and AlCl_3 dissolved in DME). The results shown in **Figure 6.1c**, suggested a stable cycling of the cell, which delivered *ca.* 500 mAh g^{-1} for 100 cycles at 500 mA g^{-1} (*ca.* 0.3 C) with almost 100% Coulombic efficiency, indicating good compatibility of the electrolyte with Mg anodes and sulfur-based cathodes.^[192]

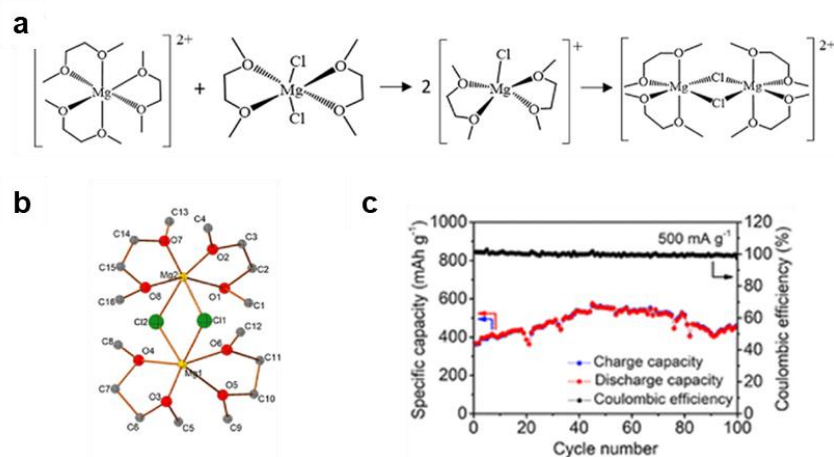


Figure 6.1: **a)** Proposed formation of the electroactive species; **b)** simulated molecular structure of the electroactive species $[\text{Mg}_2(\mu_2\text{-Cl})_2(\text{DME})_4]^{2+}$; **c)** cell stability test of a Mg-S cell with a $\text{Mg}(\text{CF}_3\text{SO}_3)_2$, MgCl_2 and AlCl_3 -based electrolyte at 0.3 C .^[192] Reproduced with permission from ref^[192]. Copyright (2020) American Chemical Society.

In view of the reported outstanding compatibility of the electrolyte ($\text{Mg}(\text{CF}_3\text{SO}_3)_2$, MgCl_2 and AlCl_3 in DME) with Mg anodes and sulfur-based cathodes, together with the unsaturation of the electrolyte,^[192] a similar electrolyte system was used to test the compatibility with SPAN cathodes and to investigate the functions of the lithium salt in Mg-SPAN batteries.

Consequently, two electrolytes, *i.e.* a pure magnesium salt-based electrolyte ($\text{Mg}(\text{CF}_3\text{SO}_3)_2$, MgCl_2 and AlCl_3 in DME) and a $\text{Mg}^{2+}/\text{Li}^+$ hybrid electrolyte prepared on the basis of $\text{Mg}(\text{CF}_3\text{SO}_3)_2$, MgCl_2 , AlCl_3 and $\text{Li}(\text{CF}_3\text{SO}_3)$, have been investigated. For simplicity, $\text{Li}(\text{CF}_3\text{SO}_3)$, which has the same anion as the $\text{Mg}(\text{CF}_3\text{SO}_3)_2$ was selected as the source of the lithium ions.

6.2 Publication: “Performance Enhancement of Rechargeable Magnesium-Sulfur Batteries Based on a Sulfurized Poly(acrylonitrile) Composite and a Lithium Salt”

In order to investigate the specific role of a lithium salt in Mg-SPAN batteries, a pure magnesium electrolyte ($\text{Mg}(\text{CF}_3\text{SO}_3)_2$, MgCl_2 and AlCl_3 in DME) and a $\text{Mg}^{2+}/\text{Li}^+$ hybrid electrolyte ($\text{Mg}(\text{CF}_3\text{SO}_3)_2$, MgCl_2 , AlCl_3 and $\text{Li}(\text{CF}_3\text{SO}_3)$ in DME) were prepared. The electrochemical performances of Mg-SPAN cells containing these two different electrolytes were compared and investigated.

In good accordance with the findings in **Chapter 5**, in this study, the addition of a lithium salt also greatly improved the performance of Mg-SPAN cells. The Mg-SPAN cells containing the $\text{Mg}^{2+}/\text{Li}^+$ hybrid electrolyte delivered *ca.* 1100 mAh g_s^{-1} for 100 cycles with almost 100% Coulombic efficiency. In contrast, Mg-SPAN cells containing the pure Mg electrolyte showed severe capacity decay in the initial few cycles. These results again indicated the beneficial effects of the addition of a lithium salt.

In order to understand the reasons behind, Mg-Mg symmetric cells were first studied to exclude the influences from the sulfur species. Surprisingly, with both electrolytes, the symmetric cells showed similar low overpotentials (0.15 V) when the same current conditions were applied to the cells. In both symmetric cells, the overpotentials were low and stable, suggesting that both electrolytes did not passivate Mg anodes. Hence, the poor cycle performance of the Mg-SPAN cell containing the pure Mg electrolyte should be caused by the *in-situ* formed sulfur species.

In order to further confirm this assumption, magnesium polysulfide species (MgS_x) were synthesized and added to both electrolytes to mimic a sulfur species-containing environment. The Mg-Mg symmetric cells with the pure Mg electrolyte + MgS_x showed large and unstable overpotentials; whereas the cell with the $\text{Mg}^{2+}/\text{Li}^+$ hybrid electrolyte + MgS_x showed stable and much lower overpotentials (*ca.* 0.15 V) under the same current conditions. These data strongly suggested that the magnesium polysulfide species are harmful to the Mg anode in the absence of a lithium salt. Impedance spectroscopy analysis

of these two symmetric cells at the OCV state also confirmed that the magnesium polysulfide species tended to passivate the Mg anode surface in the absence of a lithium salt in the electrolyte.

The overpotentials of Mg-SPAN cells with both electrolyte systems (pure Mg electrolyte and $\text{Mg}^{2+}/\text{Li}^+$ hybrid electrolyte) have also been evaluated by galvanostatic intermittent titrations technique (GITT), which showed that cells with the pure Mg electrolyte possessed much higher overpotentials than those with the $\text{Mg}^{2+}/\text{Li}^+$ hybrid electrolyte, which could also explain the better cycling performance of the cell with the hybrid electrolyte.

Next, *post-mortem* XPS analysis of the Mg anodes from both electrolytes was conducted to investigate whether the use of a lithium salt reduced the amount of sulfur species, which potentially passivated the Mg anodes. The Mg anode from the Mg-SPAN cell using the hybrid electrolyte showed much lower amount of MgS species than those using the pure Mg electrolyte. MgS species are known to be corrosive, electrochemically inactive and hard to be re-oxidized to higher-order polysulfides, consequently reducing the reversibility of the system. These XPS results, however, suggested that the final reduction product, MgS, was most likely lithiated or dissolved in the presence of lithium ions in the electrolyte, which helped in the further re-oxidizations in the following cycles.

At the same time, SEM analysis on the cycled Mg anodes from Mg-SPAN cells based on the $\text{Mg}^{2+}/\text{Li}^+$ hybrid electrolyte was carried out to exclude dendrite formations. On the cycled Mg anode, agglomerates of spheres rather than dendrites were observed. Also, *post-mortem* XPS analysis of the aged Mg anode from a Mg-SPAN cell containing the $\text{Mg}^{2+}/\text{Li}^+$ hybrid electrolyte also confirmed the absence of lithium metal. Further on, the three-electrode CV analysis also confirmed that the redox reactions are based on the Mg/Mg^{2+} . All these results suggested the whole chemistry inside of Mg-SPAN cells were dominated by the magnesium chemistry, even when the lithium salt was inside of the electrolyte.

A detailed discussion and introduction to this sub-project is presented in the following publication.

Publication

P. Wang, K. Küster, U. Starke, C. Liang, R. Niewa, M. R. Buchmeiser, *J. Power Sources* **2021**, 515, 230604.

Author Contributions: P. Wang: Conceptualization, Investigation, Writing - original draft, Writing - review & editing; K. Küster, U. Starke: XPS Characterization, Writing - review & editing; C. Liang, R. Niewa: XRD Characterization; M. R. Buchmeiser: Conceptualization, Supervision, Writing - original draft, Writing - review & editing

Reprinted with permission from the © 2021 Elsevier Ltd.



Contents lists available at ScienceDirect

Journal of Power Sources

journal homepage: www.elsevier.com/locate/jpowsour



Performance enhancement of rechargeable magnesium–sulfur batteries based on a sulfurized poly(acrylonitrile) composite and a lithium salt

Peiwen Wang^a, Kathrin Küster^b, Ulrich Starke^b, Chen Liang^c, Rainer Niewa^c, Michael R. Buchmeiser^{a,d,*}

^a Institute of Polymer Chemistry, University of Stuttgart, 70569, Stuttgart, Germany

^b Max Planck Institute for Solid State Research, 70569, Stuttgart, Germany

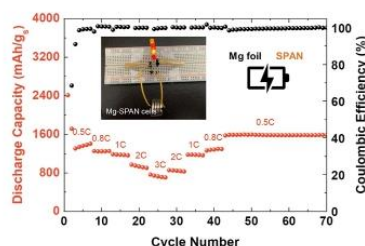
^c Institute of Inorganic Chemistry, University of Stuttgart, 70569, Stuttgart, Germany

^d German Institutes of Textile and Fiber Research (DITF) Denkendorf, 73770, Denkendorf, Germany

HIGHLIGHTS

- Roles of lithium salt in magnesium-SPAN batteries are discussed in detail.
- The lithium salt can lower the resistance and overpotential when MgS_x is present.
- The Mg-sulfur batteries stably delivered 1100 mAh g^{-1} for 100 cycles.
- The lithium salt promotes the formation of an SEI layer.
- First in-depth electrochemical, thermodynamic and kinetic study of a Mg-SPAN battery.

GRAPHICAL ABSTRACT



ARTICLE INFO

Keywords:

Sulfur-poly(acrylonitrile) composite
Magnesium battery
Lithium salt
Overpotential
SEI layer

ABSTRACT

Research on magnesium-sulfur (Mg-S) batteries has gained great attention due to the high theoretical gravimetric and volumetric energy densities (1700 Wh kg^{-1} and 3200 Wh L^{-1}), as well as because of their economic, ecologic and safety advantages. In this study, we present room-temperature Mg-S batteries with a sulfurized poly(acrylonitrile) composite (SPAN) cathode and a $\text{Mg}^{2+}/\text{Li}^{+}$ hybrid electrolyte (magnesium trifluoromethanesulfonate, $(\text{CF}_3\text{SO}_3)_2\text{Mg}$), lithium trifluoromethanesulfonate, MgCl_2 and AlCl_3 in 1,2-dimethoxyethane (DME)). These cells deliver high discharge capacities and energy densities of 1100 mAh g^{-1} and 700 Wh kg^{-1} at 1 C, respectively, with $>99.9\%$ Coulombic efficiency. Electrochemical and kinetic measurements as well as *post-mortem* analysis revealed that utilization of SPAN and a lithium salt in the electrolyte is crucial and beneficial for the prevention of the polysulfide shuttle. It also dramatically reduces the cell resistance and the overpotential via the formation of MgLiS_x species. Concomitantly, this system supports the formation of a solid electrolyte interface (SEI) layer, which greatly improves the reaction kinetics of the Mg^{2+} ions and the cycle performance.

* Corresponding author. Institute of Polymer Chemistry, University of Stuttgart, 70569, Stuttgart, Germany.
E-mail address: michael.buchmeiser@ipoc.uni-stuttgart.de (M.R. Buchmeiser).

<https://doi.org/10.1016/j.jpowsour.2021.230604>

Received 9 June 2021; Received in revised form 20 August 2021; Accepted 4 October 2021

Available online 8 October 2021

0378-7753/© 2021 Elsevier B.V. All rights reserved.

1. Introduction

Rechargeable magnesium-sulfur (Mg-S) batteries are attractive among other post-Li-ion batteries due to their high theoretical energy density (3200 Wh l⁻¹), which is higher than that of the Li-S cells (2800 Wh l⁻¹) [1]. Also, magnesium is more abundant and safer than lithium because it tends to plate non-dendritically [2,3]. Motivated by these potentials, several concept cells have been reported [2,4–10]. Nonetheless, in comparison to Li-S batteries, the investigations on Mg-S batteries are still limited, mainly because of unsuitable cathodes and electrolytes that can effectively prevent the polysulfide shuttle and improve the kinetics of the Mg²⁺ ions [2,11,12].

The cathode materials reported in Mg-S batteries generally accommodate the elemental sulfur in the porous and conductive carbon matrixes (carbon black [1], CMK-3 [13–15], Ketjen black [16], nitrogen-doped graphene [17], carbon nanotubes [18] or activated carbon cloths [19,20]). Recently, a sulfur-carbon composite, e.g., sulfur-poly(acrylonitrile) (“SPAN”, Fig. 1a inset) [21–26] has been reported as a novel cathode material in the Mg-S batteries [5,8,9]. Notably, in SPAN, the sulfur is covalently bound and not physisorbed to the N-containing carbonaceous backbone, avoiding a ‘free sulfur’ system. Indeed, intra- and intermolecular polymer-bound sulfur chains are formed, which can effectively prevent the polysulfide shuttle. This is why SPAN outperforms most other S₈-based cathodes.

Recent reported electrolytes in Mg-S batteries include magnesium salts containing a weakly coordinating anion dissolved in ether-based solvents [4,9,15,16]. The use of a Lewis acid (Al- or B- based) and a Lewis base (such as Mg bis(hexamethyldisilazide)) has also been reported [18,27,28]. In addition, an all-inorganic Mg²⁺ electrolyte consisting of MgCl₂ and AlCl₃, abbreviated as ‘MACC electrolyte’, has been used in Mg batteries, which allows reversible Mg plating and stripping and shows a high anodic stability (3.4 V vs. Mg) [29,30]. However, an additional electrochemical conditioning process is necessary, which is difficult to be scaled up [31]. Luo et al. [32] reported that treating the MACC electrolyte with reductive Mg powder could effectively remove the deleterious species present in the electrolytes to avoid the conditioning process and also achieve low overpotential and high Coulombic efficiency. Moreover, the utilization of a lithium salt (e.g. lithium bis(trifluoromethanesulfonyl)imide (LiTFSI), Li[BH₄], and LiCl) in a

magnesium cell can improve the reversibility of the system [5,6,13,19,33].

Here, we present a novel Mg-SPAN system containing a Mg²⁺/Li⁺ hybrid electrolyte (magnesium trifluoromethanesulfonate, (CF₃SO₃)₂Mg), lithium trifluoromethanesulfonate, CF₃SO₃Li), MgCl₂ and AlCl₃ in 1,2-dimethoxyethane (DME)), which shows superior energy density of 700 Wh kg⁻¹ (1100 mAh g_s⁻¹) at a current rate of 1 (1 C) with >99.9% Coulombic efficiency, and good rate capability. Notably, the cell could deliver ca. 800 mAh g_s⁻¹ at 3 C, which is among the best Mg-S batteries so far. In addition, we discuss the functions of the lithium salt by means of electrochemical and kinetic measurements, as well as post-mortem analysis. Notably, the use of a lithium salt in the electrolyte effectively suppresses the polysulfide shuttle in SPAN-based cells, improves the kinetics and helps forming the solid electrolyte interface (SEI) layer, thereby improving the cycle performance and reversibility.

2. Materials and methods

2.1. Materials

All chemicals were handled in an Ar-filled glovebox with H₂O and O₂ levels below 0.1 ppm. Poly(acrylonitrile) (PAN, M_n = 36,500 g mol⁻¹, Đ = 3.6), 1,2-dimethoxyethane (DME, anhydrous, 99.5%, inhibitor free), magnesium chloride (MgCl₂, anhydrous, >98%) and aluminum chloride (AlCl₃, anhydrous, powder, 99.999% trace metals basis) were purchased from Merck. Magnesium trifluoromethanesulfonate (magnesium triflate, 97%) and lithium trifluoromethanesulfonate (lithium triflate, 99.995% trace metal basis) were purchased from Merck and dried at 100 °C for 10 h before use. Magnesium foils (0.25 mm thick, 99.9%) were purchased from Alfa Aesar Germany and thoroughly polished inside the glovebox.

2.2. Preparation of cathodes and electrolytes

The active cathode material (SPAN) was synthesized by a facile and low-cost method, which has been reported in previous work [5,9,22,24,34,35]. Elemental analysis revealed a sulfur content of 38 wt% (Table S6). For the preparation of the cathode slurry, a dispersion of SPAN, super C65 conducting carbon and poly(vinylidene fluoride)

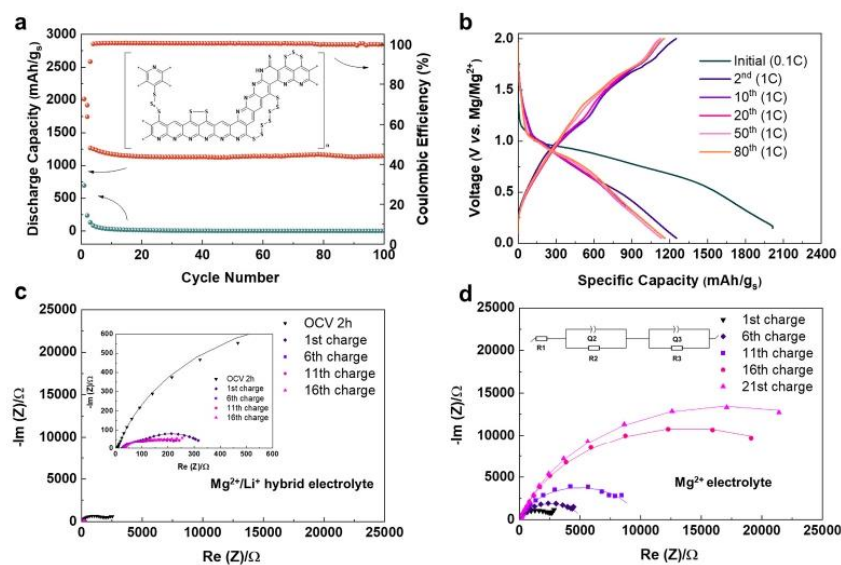


Fig. 1. a) Cycling performance of Mg-SPAN cell using the Mg²⁺/Li⁺ hybrid electrolyte (red) and the Mg²⁺ electrolyte (blue) at 1 C (initial cycle at 0.1C); inset: proposed SPAN structure; b) voltage profile from a) with the Mg²⁺/Li⁺ hybrid electrolyte; c) Nyquist plot of a Mg-SPAN cell with the Mg²⁺/Li⁺ hybrid electrolyte measured at OCV and after each cycle (1 C) in the charged state (2 V), inset: enlarged version of the curves at high frequency; d) Nyquist plot of the Mg-SPAN cell using the Mg²⁺ electrolyte measured after each cycle (1 C) in the charged state (2 V). The dots are the measured values; the lines are fitted by the equivalent circuit shown in the inset in d). (For interpretation of the references to color in this figure legend, the reader is referred to the Web version of this article.)

(PVDF) in 1-methyl-2-pyrrolidinone in a weight ratio of 70:15:15 was mixed with a planetary mixer (Thinky) at 2000 rpm for 6 min. The dispersion was then cast onto a carbon-coated copper foil (Cu/C) with a wet thickness of 200 μm . The coating was then dried in an oven at 60 $^{\circ}\text{C}$ overnight. Cathode chips 12 mm in diameter were punched out with an average sulfur content of 0.5–0.6 mg cm^{-2} per cathode (areal capacity: 1.0 mAh cm^{-2}). To increase the sulfur content, a thicker coating was also prepared (300 μm), resulting in a sulfur content of 1 mg cm^{-2} . The reference cathodes based on elemental sulfur were prepared by the same procedure except replacing SPAN powder by elemental sulfur.

All the electrolytes were all prepared in the Argon-filled glovebox. The electrolyte containing 0.2 M magnesium triflate, 0.4 M MgCl_2 , 0.4 M AlCl_3 and 1.6 M lithium triflate in DME [36], referred to as $\text{Mg}^{2+}/\text{Li}^+$ hybrid electrolyte, was obtained by dissolving magnesium triflate in anhydrous DME, followed by adding anhydrous MgCl_2 . Afterwards, AlCl_3 and lithium triflate was slowly added to the above mixture. After 12 h stirring at room temperature, a transparent solution was obtained. For comparison, an electrolyte without any lithium salt, i.e. 0.2 M magnesium triflate – 0.4 M MgCl_2 – 0.4 M AlCl_3 /DME, referred to as Mg^{2+} electrolyte, was prepared using similar procedures. Excess of magnesium powder was then added to both electrolytes to remove residual water and was filtered off prior to use. The prepared electrolytes were sealed and stored in a glovebox. ^{19}F nuclear magnetic resonance spectroscopy (^{19}F NMR) was measured in CD_3CN at 376 MHz and showed one signal at $\delta = -79.43$ ppm (Fig. S1a) for the CF_3SO_3^- group. Electrospray ionization mass spectroscopy (ESI-MS) showed the following signals: positive mode m/z (calculated for $[\text{Mg}_2(\mu_2\text{-Cl})_2(\text{DME})_4]$: 239.1; m/z (measured): 240.9; negative mode m/z (calculated for CF_3SO_3^-): 148.9; m/z (measured): 148.9. (Figs. S1c and d).

The MgS_x species were synthesized by ball milling 1.0 g (32 mM) sulfur and 0.090 g (8.0 mM) magnesium powder at 300 rpm for 3 h under an Ar atmosphere. Afterwards, the obtained grey powder was transferred into a glovebox. 0.1 g grey powder was added to 6 mL anhydrous bis(2-methoxyethyl) ether (diglyme). The whole mixture was stirred at 60 $^{\circ}\text{C}$ for 7 days, after which the solid materials were filtered off before use [4]. The filtrate showed an orange-red color (Fig. S2a inset). For comparison, Fig. S2b shows the filtrate of the mixture of magnesium powder and elemental sulfur in diglyme, which is colorless. UV–vis analysis (Fig. S2a) confirmed the filtration in Fig. S2a being an MgS_x solution.

2.3. Electrochemical measurements

All cells were assembled inside the Ar-filled glovebox. Symmetric Mg–Mg cells were assembled with two pieces of Mg foils, two pieces of glass fiber separator (GF/C) and the corresponding electrolytes (130 μL per cell) in a Swagelok-type cell. They were characterized galvanostatically at different current densities. Cyclic voltammetry (CV) was measured by means of a Biologic VMP-3 with a three-electrode PAT cell (EL-CELL) with Mg metal as both counter and reference electrodes. Mg–S cells were fabricated with one SPAN cathode, a Mg foil anode and two pieces of glass fiber separators with 130 μL corresponding electrolytes using Swagelok cells, which were measured at a constant temperature of 23 ± 0.2 $^{\circ}\text{C}$ with the aid of a Basytech XCT-LAB system. Electrochemical impedance spectroscopy (EIS) data were acquired with a signal amplitude of 10 mV in a frequency range from 100 kHz to 100 MHz by a Biologic VMP-3.

2.4. Characterization

X-ray diffraction (XRD) spectra were measured by a STOE STADI P (STOE GmbH & Cie, Darmstadt). Molybdenum ($\lambda = 70.93$ pm) was used as the anode target material. The sample was placed between two grease-covered foils and enclosed in an airtight sample holder. The ionic conductivity of the electrolytes was determined by an InLab Sensor

conductometer (Mettler Toledo). Scanning electron microscopy (SEM) images were recorded on an Auriga type field emission scanning electron microscope from Zeiss. For *ex-situ* X-ray photoelectron spectroscopy (XPS) measurements, the cells were disconnected after one cycle or ten cycles, respectively. All electrodes were thoroughly washed, dried, and fixed on a sample holder under Ar. The samples were transferred under argon to avoid any contamination with air. XPS was performed on a Kratos Axis Ultra system equipped with a monochromic Al K_{α} source. Spectra were analyzed using the CasaXPS software. The energy separation and peak area of the S 2p $_{3/2}$ and S 2p $_{1/2}$ were constrained to 1.18 eV and 2:1, respectively [37].

3. Results and discussion

3.1. Cathodes and electrolytes

XRD results of the SPAN cathode (Fig. S3a, blue curve) did not show any signals for elemental sulfur (Fig. S3a, black curve), but one significant peak at approximately 20 $^{\circ}$ corresponding to the graphitic PAN structure, indicating the absence of elemental sulfur and the successful synthesis of the SPAN material [35]. SEM images and the elemental mapping of the SPAN cathode (Figs. S3b–f) suggest that the SPAN powder, carbon black and PVDF binder are well distributed within the cathode material. Fig. S4 shows the enlarged feature of an SPAN cathode, which consisted of spherical SPAN particles approximately 200 nm in diameter.

Electrospray ionization mass (ESI-MS) spectroscopy of the $\text{Mg}^{2+}/\text{Li}^+$ hybrid electrolyte showed a signal with an m/z ratio of 240.9 in the positive mode (Fig. S1c), corresponding to the $[\text{Mg}_2(\mu_2\text{-Cl})_2(\text{DME})_4]^{2+}$ complex that has been verified as electroactive species in the Mg batteries [38]. In the negative mode, the signal at 148.9 corresponds to the $[\text{CF}_3\text{SO}_3]^-$ anion. The $\text{Mg}^{2+}/\text{Li}^+$ hybrid electrolyte possessed a high ionic conductivity of ca. 6.5 mS cm^{-1} at 23 $^{\circ}\text{C}$. In comparison, the ionic conductivity of the Mg^{2+} electrolyte was somewhat lower (5.5 mS cm^{-1}), indicating that the addition of 1.6 M lithium salt can increase the ionic conductivity. Cyclic voltammetry (CV) curves (Fig. S5) for the Mg plating and stripping on Pt and Cu–C disks using the $\text{Mg}^{2+}/\text{Li}^+$ hybrid electrolyte indicated that the electrolyte allows for the magnesium deposition and dissolution. Linear sweep voltammetry (LSV) was also tested at 10 mV s^{-1} (Fig. S6) on common current collectors (stainless steel, Al/C and Cu/C discs), showing that the $\text{Mg}^{2+}/\text{Li}^+$ hybrid electrolyte is oxidatively stable up to 2.3 V, 2.8 V and 3.5 V with stainless steel, Al–C and Cu/C, respectively. Since Cu/C possesses a better stability and copper is reported to be beneficial to the conversion kinetics for sulfur-based batteries [39,40], Cu/C was selected as the current collector in this study. Coulombic efficiency tests showed approximately 100% Coulombic efficiency from the initial cycle on without any conditioning process, which could be thanks to the removal of deleterious species in the electrolyte by pre-treatment with Mg powder (Fig. S7) [32]. In addition, the transfer number of Mg^{2+} in the Mg^{2+} electrolyte, which is a value examining the mobility of the cations, was determined to be 0.7 via the Bruce-Vincent method (Fig. S8, Table S1), which is high for Mg-based electrolytes [2].

3.2. Mg-SPAN batteries

In order to examine the compatibility of the $\text{Mg}^{2+}/\text{Li}^+$ hybrid electrolyte and Mg^{2+} electrolyte with the SPAN cathode, cells comprising one SPAN cathode, one polished Mg foil and the corresponding electrolytes were fabricated and charged/discharged at a current rate of 1 C (1670 mA cm^{-2}) at 23 $^{\circ}\text{C}$ (Fig. 1a). The current rate for the initial cycle was 0.1 C to produce an SEI layer. Using the $\text{Mg}^{2+}/\text{Li}^+$ hybrid electrolyte, a discharge capacity of about 1100 mAh g_s^{-1} (700 Wh kg_s^{-1}) was delivered by the Mg-SPAN cell with virtually 100% Coulombic efficiency, illustrating high reversibility and high energy density of the system. A cell using an SPAN cathode with a higher sulfur

content (1 mg cm^{-2}) also delivered around 700 mAh g_s^{-1} at 1 C (Fig. S21), indicating excellent performance of this system. In sharp contrast, cells based on the Mg^{2+} electrolyte delivered only around 700 mAh g_s^{-1} in the initial cycle at 0.1 C and the capacity dropped to almost zero within the next 10 cycles, showing that the system solely based on the Mg^{2+} electrolyte is not reversible. To get more insight into the systems, the galvanostatic voltage profile of cells based on the $\text{Mg}^{2+}/\text{Li}^+$ hybrid electrolyte and the Mg^{2+} electrolyte, respectively, were recorded (Fig. 1b and Fig. S9). The galvanostatic discharge curves of cells based on a $\text{Mg}^{2+}/\text{Li}^+$ hybrid electrolyte display three sloped regions starting at 1.6 V, 1.1 V and 0.5 V, respectively. In comparison, the discharge profile of a cell with the Mg^{2+} electrolyte shows the sloped regions at lower voltage starting from 1.2 V, 0.8 V and 0.4 V, respectively. However, the sloped regions in the Mg^{2+} electrolyte cell gradually shortened and finally vanished upon cycling (Fig. S9), indicating the dissolution of magnesium polysulfides (MgS_x) in the Mg^{2+} electrolyte, which might corrode/block the Mg anode surface and prevent the reversible plating and stripping of the Mg ions in the system. For further comparison, a Mg- S_8 cell containing the $\text{Mg}^{2+}/\text{Li}^+$ hybrid electrolyte was also tested using the same cycling program (Fig. S10). The cell delivered ca. 500 mAh g_s^{-1} in the initial cycle; the voltage profile (Fig. S10b) displayed typical features of elemental sulfur: several long plateaus (1.2 V, 0.6 V and 0.2 V) instead of sloped regions. However, the capacity quickly dropped to ca. 10 mAh g_s^{-1} in the second cycle, indicating the non-reversibility of the S_8 system even in the presence of a Li salt-containing electrolyte, and the superior electrochemical performance of the SPAN cathodes. In order to show that the lithium triflate in the electrolyte is not electroactive, a Mg-SPAN cell using 0.2 M magnesium triflate and 1.6 M lithium triflate/DME, which excluded MgCl_2 and AlCl_3 , was cycled (Fig. S11). An initial discharge capacity of only 50 mAh g_s^{-1} , followed by fast capacity fading to nearly 0 mAh g_s^{-1} suggests that the electroactive $[\text{Mg}_2(\mu_2\text{-Cl})_2(\text{DME})_4]^{2+}$ complex is crucial for the Mg-SPAN system and the capacity from the cell is solely contributed by Mg. Also, due to the use of a Cu/C current collector, copper sulfide might form, which is known to suppress the polysulfide shuttle [41,42]. To exclude the capacity contribution from the *in-situ* formed copper sulfide, a cell composed of a copper sulfide cathode, a Mg foil and the $\text{Mg}^{2+}/\text{Li}^+$ hybrid electrolyte was prepared and cycled (Fig. S24). Compared to Mg-SPAN cells, it delivered only one tenth of the capacity, indicating that the majority of the capacity comes from the SPAN cathode.

To understand the superior electrochemical performance of Mg-SPAN cells containing the $\text{Mg}^{2+}/\text{Li}^+$ hybrid electrolyte, *in-situ* electrochemical impedance spectroscopy (EIS) was applied using the $\text{Mg}^{2+}/\text{Li}^+$ hybrid electrolyte and the Mg^{2+} electrolyte, respectively. Cells were kept for 30 min before the EIS measurement to reach an equilibrium state. Fig. 1c shows the Nyquist plots of the cells at open circuit voltage (OCV, 2 h) and after cycling in the charged state (2 V) with the $\text{Mg}^{2+}/\text{Li}^+$ hybrid electrolyte. For comparison, the impedance of the cell with the Mg^{2+} electrolyte after cycling was also analyzed (Fig. 1d). The Nyquist plots were fitted by the equivalent circuit (Fig. 1d inset). R_1 accounts for the bulk resistance. The semicircle at the high frequency region represents the diffusion of ions through the SEI to the active material (R_2) and to the capacitance in parallel (Q_2). A constant phase element (Q_2) instead of ideal capacitors was used due to the suppressed semicircle coming from the surface roughness [43]. The semicircle observed at lower frequency region can be assigned to the charge transfer resistance (R_3) between the electrode and the electrolyte, together with the double-layer capacitance (Q_3). The corresponding resistance values are summarized in Tables S2 and S3, respectively.

Cells based on the $\text{Mg}^{2+}/\text{Li}^+$ hybrid electrolyte (Fig. 1c) showed relatively high impedance at OCV for 2 h. However, after cycling, the charge transfer resistance (R_3) and the resistance of the SEI layer (R_2) dramatically decreased and stayed at that level during cycling, suggesting the formation of a stable interface between the electrodes and the electrolyte. In addition, the bulk resistance (R_1) slightly increased after polarization, indicating the formation of some polysulfides in the

electrolyte. R_1 , however, remained almost constant over cycling, suggesting that the electrolyte system reached an equilibrium state and barely changed in composition during cycling; *i.e.* the amount of the dissolved polysulfides species did not further increase after the initial cycle. In sharp contrast, cells with the Mg^{2+} electrolyte (Fig. 1d) showed a dramatic increase in the charge transfer resistance (R_3) and the resistance of the SEI layer over cycling (R_2), which indicates the formation and dissolution of polysulfides and the gradual blocking of the electrodes. The Nyquist plots of the cells using the two electrolytes at the discharged state also show similar behavior (Fig. S12).

The rate capability is another important factor to determine battery performance. Fig. 2a and b shows the rate capability results and the galvanostatic voltage profile of the Mg-SPAN system based on the $\text{Mg}^{2+}/\text{Li}^+$ hybrid electrolyte, cycled from 0.5 C to 3 C then back to 0.5 C. The discharge capacity decreased from ca. $1500 \text{ mAh g}_s^{-1}$ (0.5 C) to ca. 700 mAh g_s^{-1} (3 C) and reversed back to the original state when the current rate decreased, indicating good rate capability of the Mg-SPAN battery with the $\text{Mg}^{2+}/\text{Li}^+$ hybrid electrolyte.

3.3. Roles of the lithium salt in the electrolyte

As discussed above, addition of 1.6 M lithium triflate into the Mg^{2+} electrolyte significantly improved the performance of a Mg-SPAN cell. In order to shed light on this issue, Swagelok-type symmetric Mg-Mg cells based on the $\text{Mg}^{2+}/\text{Li}^+$ hybrid electrolyte and the Mg^{2+} electrolyte, respectively, were assembled. Galvanostatic cycling experiments were conducted by applying a current (0.1 mA cm^{-2}) for 30 min during charging/discharging the half cells (Fig. 3a).

The galvanostatic cycling profile for the $\text{Mg}^{2+}/\text{Li}^+$ hybrid electrolyte (Fig. 3a, red curve) shows an initial high plating overpotential of approximately -0.39 V , which dropped subsequently to -0.18 V in the second cycle. Afterwards, the overpotential of plating and stripping continuously decreased to approximately $\pm 0.11 \text{ V}$ and stayed constant at that level for more than 500 h. This strongly points towards the formation of a stable interphase between the Mg surface and the electrolyte [44]. The morphology of the Mg foil surface after polarization was examined by SEM (Fig. 3a, inset), which revealed the presence of spherical rather than dendritic structures. Agglomeration of Mg spheres with $<100 \text{ nm}$ dimensions can be detected on the Mg surface.

Since the initial overpotential is substantially higher than in the subsequent cycles, electrochemical impedance spectroscopy analysis was applied to the symmetric Mg-Mg cell containing the $\text{Mg}^{2+}/\text{Li}^+$ hybrid electrolyte at OCV state and after polarization (Fig. 3b). Curves were fitted using the same equivalent circuit model shown in Fig. 1d (inset); the corresponding fitted values can be found in Table S4. In the equivalent circuit, R_1 , R_2 and R_3 represent the bulk resistance, charge transfer resistance and resistance from the adsorption layer, respectively. Q_2 and Q_3 represent the constant phase element and the double layer capacitance. As displayed in Fig. 3b, the Nyquist plots of the Mg-Mg cell show a clear increase in impedance in the OCV state. Specifically, the charge transfer resistance (R_2) increased from 712.5Ω to $21 \text{ k}\Omega$ during 50 h in the OCV state (Table S4). This strongly indicates the formation of an inactive adsorption layer on the Mg surface. However, this layer could be partially removed after the application of a current, leading to a dramatic drop in resistance by several orders of magnitude and a relatively high overpotential in the initial cycles. Indeed, this phenomenon has also been observed with other electrolyte systems in Mg batteries [4,5,16].

At the same time, a Mg-Mg cell containing the Mg^{2+} electrolyte exhibited a surprisingly good cycling stability with a similar low polarization potential of ca. $\pm 0.1 \text{ V}$ for 500 h (Fig. 3a, blue curve). The polarization potential decreased from 0.46 V to 0.05 V within the first 60 cycles; however, it gradually increased again to 0.1 V in the following cycles. The change in the overpotential hints towards the formation of an unstable SEI layer in the initial cycles, which slowly changed until reaching a new equilibrium state.

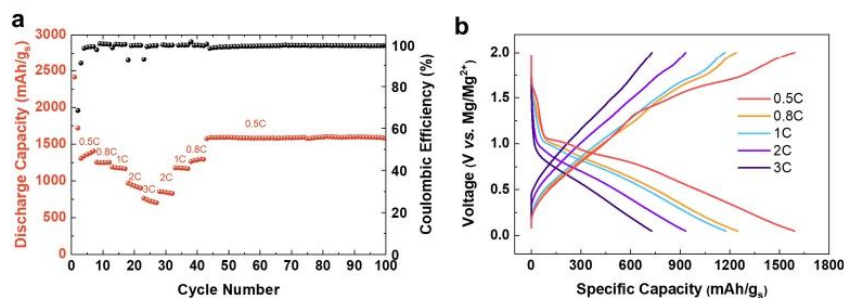


Fig. 2. a) Rate capability test of the Mg-SPAN cell using the Mg²⁺/Li⁺ hybrid electrolyte (0.5 C–3 C); b) voltage profile from a).

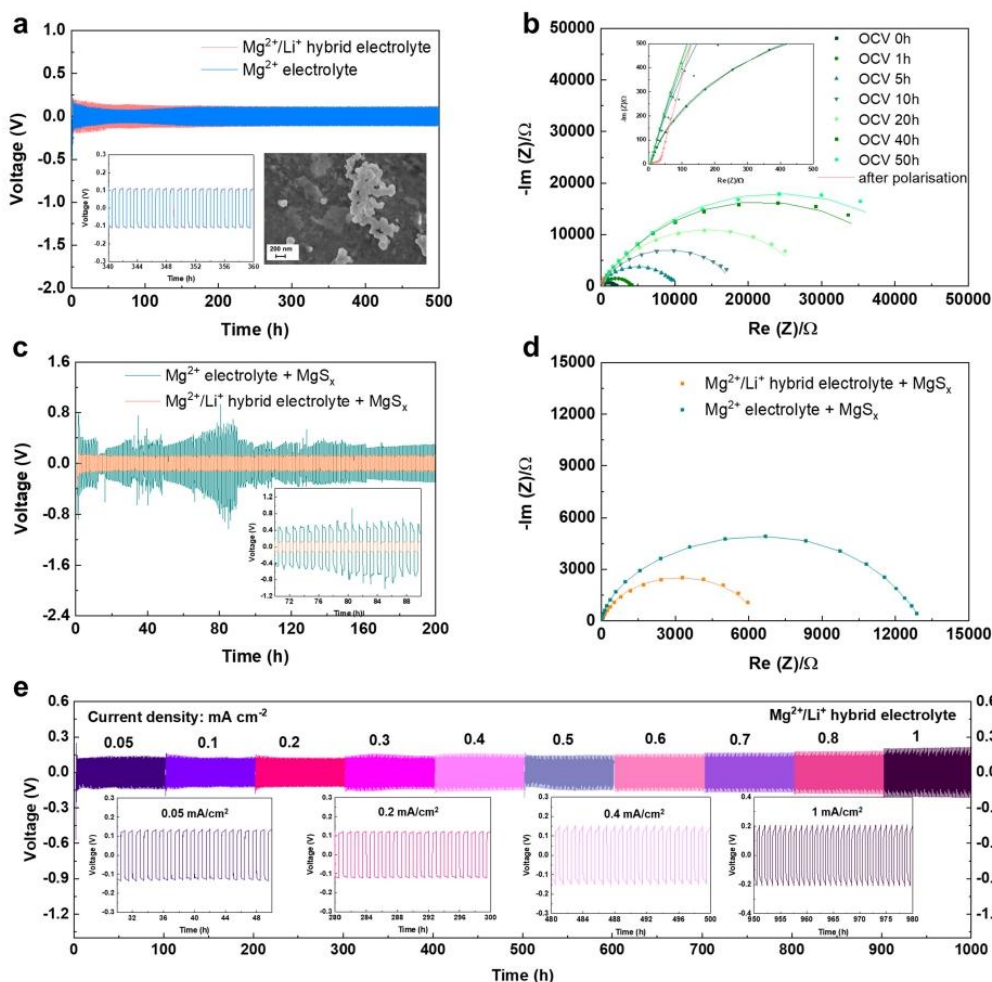


Fig. 3. a) Long-term Mg plating/stripping measurements of a Mg–Mg symmetric cell with the Mg²⁺/Li⁺ hybrid electrolyte (red) and the Mg²⁺ electrolyte (blue) at a constant current density of 0.1 mA/cm², with 30 min plating/stripping time; inset: SEM image of the Mg anode from Mg²⁺/Li⁺ hybrid electrolyte after 100 times polarization; b) Nyquist plots and the equivalent circuit of Mg–Mg symmetric cell with Mg²⁺/Li⁺ hybrid electrolyte at OCV and after polarization (enlarged curve is in inset); c) Mg plating/stripping galvanostatic cycling of the Mg–Mg symmetric cell with the Mg²⁺/Li⁺ hybrid electrolyte + MgS_x solution (orange) and with the Mg²⁺ electrolyte + MgS_x solution (green) at 0.1 mA/cm² with 30 min plating/stripping time; d) Nyquist plots of the Mg²⁺/Li⁺ hybrid electrolyte + MgS_x solution (orange) and with the Mg²⁺ electrolyte + MgS_x solution (green) at OCV for 1 h; e) Mg plating/stripping measurement of the Mg–Mg symmetric cell at different current densities (0.05 mA/cm² – 0.5 mA/cm²). (For interpretation of the references to color in this figure legend, the reader is referred to the Web version of this article.)

Notably, the low overpotential (0.1 V) of the Mg^{2+} electrolyte system in the prolonged cycling indicates that the poor reversibility observed in Mg-SPAN cells might not stem from the interaction between the pristine electrolyte and the Mg foil or the decomposition of the electrolyte, but rather be a result of the presence of sulfur species (most likely magnesium polysulfides) in the electrolyte formed after cycling. The *in-situ* formed sulfur species in the Mg-SPAN cells with the Mg^{2+} electrolyte are hypothesized to have a negative influence on the reversibility of the system, which could be greatly improved by the addition of lithium triflate. In order to shed more light on this issue, a MgS_x solution was added to both the Mg^{2+} and $\text{Mg}^{2+}/\text{Li}^+$ hybrid electrolyte and the resulting electrolytes were applied to the symmetric Mg-Mg cells (Fig. 3c). Cells were polarized using the same testing program: discharging and charging the cells for 30 min at a constant current density of 0.1 mA cm^{-2} . Cells containing the Mg^{2+} electrolyte + MgS_x solution (Fig. 3c, green curve) clearly showed an unstable and deteriorating electrochemical behavior. In the initial cycles, the plating/stripping overpotential was at approximately $\pm 0.81 \text{ V}$, which slightly decreased to $\pm 0.42 \text{ V}$ after 10 cycles. A possible reason is that the Mg anodes reacted with the magnesium polysulfides species and formed a highly resistive film on the Mg surface, which partially blocks the Mg foil. Indeed, a charge transfer resistance (R_c) of ca. 5630Ω was detected in the Mg-Mg symmetric cell containing this electrolyte after OCV for 1 h (Fig. 3d, green, Table S5). A high initial overpotential is required to break this insulating blocking layer to allow the diffusion of the Mg^{2+} ions. It was also noticed that some sudden fluctuations and bumps shows in Fig. 3c (green), attributable to the sudden breaking of the insulating layer [44]. And indeed, after 18 cycles, the overpotential generally showed an increasing trend, up to 1.2 V at around 80 cycles, indicating the continuous formation or accumulation of resistive species on the Mg surface. The insulating species formed on the Mg anodes gradually stabilized after 85 cycles, resulting in a quasi-stable but highly resistive interphase. In sharp contrast, the Mg-Mg symmetric cell containing the $\text{Mg}^{2+}/\text{Li}^+$ hybrid electrolyte + MgS_x solution (Fig. 3c orange), cycled under the same experimental conditions, showed smooth and stable Mg plating and stripping. Despite the initial relatively high plating overpotential (-0.38 V), which might result from the adsorption layer on the Mg surface, the plating/stripping overpotential gradually dropped to approximately $\pm 0.13 \text{ V}$ and stayed at that level for at least 200 cycles, which is in good agreement with the stable cycling of Mg-SPAN cells using the $\text{Mg}^{2+}/\text{Li}^+$ hybrid electrolyte + MgS_x solution (Fig. S13). We propose that in the presence of Li^+ ions, the added magnesium polysulfides exist in form of MgLi -polysulfides, which have a low tendency to passivate the magnesium surface and allow the diffusion of Mg^{2+} ions [5]. Actually, the Nyquist plots shown in Fig. 3d (orange) hint towards a much lower resistance of the Mg-Mg cell containing the $\text{Mg}^{2+}/\text{Li}^+$ hybrid electrolyte + MgS_x solution compared to cells with the Mg^{2+} electrolyte + MgS_x solution. The changes in the resistance of the Mg-Mg symmetric cells using the two electrolytes during the OCV state (0 h–24 h) were recorded (Fig. S14). In both systems, the resistance substantially increased during the first 20 h at OCV but stabilized after 20 h, indicating the formation of an equilibrium state. Notably, the resistance of the cell containing Mg^{2+} electrolyte + MgS_x solution was nearly twice as high as the one with the $\text{Mg}^{2+}/\text{Li}^+$ hybrid electrolyte + MgS_x solution (Fig. S14); and was four times the one with the $\text{Mg}^{2+}/\text{Li}^+$ hybrid electrolyte (Fig. 3b) after reaching the equilibrium state (OCV 20 h). This suggests that the presence of MgS_x in general has a negative influence on the Mg surface while the addition of a lithium salt compensates for the influence of MgS_x by reactivation of the Mg anodes.

The polarization behavior at various current densities was also examined for a Mg-Mg cell based on the $\text{Mg}^{2+}/\text{Li}^+$ hybrid electrolyte (Fig. 3e). Increasing the current density from 0.05 to 1 mA cm^{-2} , the polarization of the cell did not increase significantly, indicating the superior cycle stability and rate capability of the system. The enlarged voltage versus time profile shown in the insets show nearly flat potential curves, especially at low current rates, suggesting a smooth Mg plating

and stripping process.

3.4. Proposed working mechanism

In order to further understand the Mg-SPAN system using both the $\text{Mg}^{2+}/\text{Li}^+$ hybrid and the Mg^{2+} electrolyte, three-electrode cells were fabricated with SPAN as working electrode (WE) as well as with Mg foils as counter (Mg_{CE}) and reference electrode (Mg_{RE}). A CV curve of the $\text{Mg}^{2+}/\text{Li}^+$ hybrid electrolyte is shown in Fig. 4a. Two reduction peaks located at 1 V and 0.8 V (vs. Mg_{RE}), respectively, and two small shoulders at 1.6 V and 0.4 V (vs. Mg_{RE}), respectively, were observed. The main oxidation peaks can be found at 1.6 V and 1.0 V (vs. Mg_{RE}), respectively, indicating the stepwise oxidation of the sulfur species at the SPAN cathodes. Notably, when comparing the CV curves to those acquired with the Mg^{2+} electrolyte (Fig. S15), the current density measured for the $\text{Mg}^{2+}/\text{Li}^+$ hybrid electrolyte is much higher than that of the Mg^{2+} electrolyte, which is in agreement with the better cycling behavior in the $\text{Mg}^{2+}/\text{Li}^+$ hybrid electrolyte. In addition, the potential between the working electrode and the Mg_{CE} was also measured in cells containing the $\text{Mg}^{2+}/\text{Li}^+$ hybrid electrolyte (Fig. 4a, blue curve). The oxidation peaks shift only 0.2 V to higher voltage, indicating the smooth recharge of the SPAN cathode. Finally, the potential of the magnesium counter electrode (Mg_{CE} vs. Mg_{RE}) was also monitored (Fig. 4b, blue curve) and found to be approximately 0.05 V and -0.15 V in the anodic and cathodic scan, respectively. These values are comparably low for the oxidization of Mg metal and reduction of Mg^{2+} , which is also indicative for the low polarization potential of the Mg anode [4,9]. Also, the Mg_{CE} returned back to the original voltage after each scan, indicating the plated and stripped species are Mg^0 metal and Mg^{2+} ions, respectively, rather than Li^0 and Li^+ . These results are also consistent with those previously discussed for Mg-SPAN cells containing only Mg triflate and Li triflate in the electrolyte, which delivered no capacity (Fig. S11). Hence, the capacity contribution from lithium is neglectable. CVs with multiple scans and the potential of Mg_{CE} vs. Mg_{RE} can be found in Fig. S16.

To further explain the superior performance of the Mg-SPAN cell using the $\text{Mg}^{2+}/\text{Li}^+$ hybrid electrolyte, Galvanostatic Intermittent Titrations Technique (GITT) (Fig. 4c) was applied by polarizing the cell for 10 min, followed by 10 min resting time. Fig. 4c shows the thermodynamics of the SPAN cathode at different stages. The equilibrium potential of SPAN (red) shows some staging features, which can be distinguished by the differences in the slopes. In the discharge process, one initial short sloped region (1.8 V – 1.1 V , stage I), followed by two further sloped regions (1.1 V – 0.8 V , 0.8 V – 0.4 V , stage II and III) and a fourth short sloped region (0.4 V – 0.1 V , stage IV) can be detected. In the reversed charge process, also four stages can be detected. For comparison, the thermodynamic features of SPAN in the Mg^{2+} electrolyte were recorded, too (Fig. S17). In the Mg^{2+} electrolyte, using the same equilibrium condition, a complete discharge and charge is impossible, suggesting that the short chain polysulfides are electrochemically difficult to address [45]. At the same time, the overpotential during the electrochemical reaction of the two systems was also measured by comparing the equilibrium potential (Fig. 4c, red curve, Fig. S17 light blue) and the transient potential (Fig. 4c, black curve, Fig. S17 dark blue) [45]. The corresponding results are shown in Fig. 4d (discharge process) and Fig. S18 (charge process). During charging and discharging, the overall overpotential measured in the Mg^{2+} electrolyte is higher than the one measured in the $\text{Mg}^{2+}/\text{Li}^+$ hybrid electrolyte. Specifically, in the discharge process, the overpotentials of both systems reveal a decreasing trend in stages I and II. In the following stages (corresponding to the formation of short-chain polysulfides), the overpotential measured in the Mg^{2+} electrolyte greatly increases, whereas the overpotential in the $\text{Mg}^{2+}/\text{Li}^+$ hybrid electrolyte does not show any increase. This suggests that the overall reaction kinetics are much faster with the $\text{Mg}^{2+}/\text{Li}^+$ hybrid electrolyte than with the Mg^{2+} electrolyte, especially in stages III and IV.

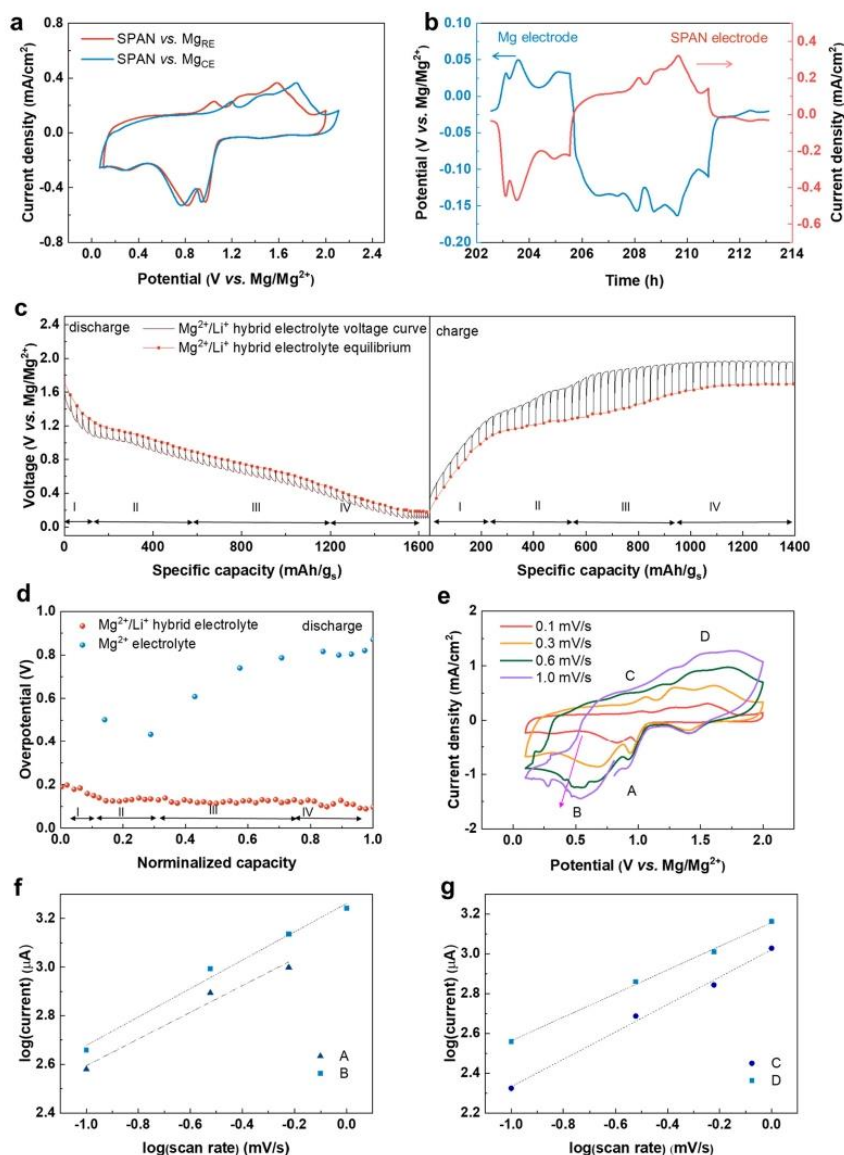
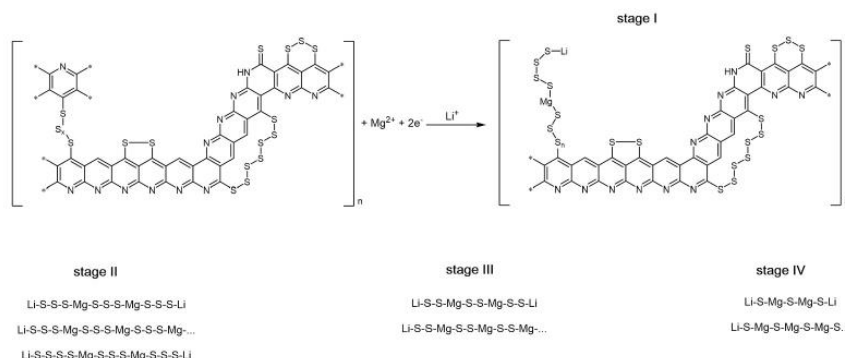


Fig. 4. a) CV results for Mg-SPAN cells using the Mg²⁺/Li⁺ hybrid electrolyte using a three-electrode cell (scan rate: 0.1 mV s⁻¹); b) voltage change of the Mg_{CE} (vs. Mg_{RE}) and current density of SPAN cathode (vs. time); c) GITT curve of a Mg-SPAN cell using the Mg²⁺/Li⁺ hybrid electrolyte cycled at 0.1 C, discharge and charge time: 10 min, resting time: 10 min; d) overpotential of the GITT curve (discharge); e) CVs of Mg-SPAN cell using the Mg²⁺/Li⁺ hybrid electrolyte at different scan rates using a three-electrode setup; f) and g) logarithm of the anodic/cathodic peak current versus the logarithm of the scan rate from d).

CV measurements with the Mg²⁺/Li⁺ hybrid electrolyte at various scan rates (Fig. 4e) revealed two main reduction peaks (A, B) and two main oxidation peaks (C, D). In a double logarithmic plot, the current densities of the anodic peaks (Fig. 4f) and cathodic peak (Fig. 4g) increase linearly with increasing scan rate. By fitting the data through the equation $y = a \times x^b$, the obtained b-value indicates the kinetic factor that controls the reaction, in which $b = 1$ corresponds to a surface-controlled reaction (capacitive behavior); and $b = 0.5$ corresponds to a diffusion-controlled reaction [46]. In the redox process, the b values for peaks A, B and D were 0.55, 0.59 and 0.59, respectively, suggesting that the conversion kinetics between polysulfides and SPAN are relatively more diffusion-controlled. In comparison, the b value for peak C is higher (0.69), indicating a faster kinetic of the reoxidation of the short-chain polysulfides to long-chain polysulfides, which we attribute to the incorporation of the lithium salt in the system.

In SPAN, the sulfur chains have an upper limit of eight sulfur units [24]; also, the C-S bond is difficult to break [24]. Consequently, the long-chain polysulfides (e.g. MgS₈), which typically form in the S₈ system, do not form with SPAN cathodes. Actually, elemental analysis of the SPAN cathode from fully discharged cells (0.1 V) show a residual sulfur content of 13 wt-% and an atomic ratio of N:S of nearly unity (0.93). This strongly suggests the final C-S bonds in the SPAN structure did not break even after fully discharge provided the voltage is ≥ 0.1 V. This is in line with recent findings on Li-S batteries [47]. Based on these SPAN features, the voltage profiles and the kinetic studies, the following four stages during cell discharge are proposed (Scheme 1):

In stage I, the SPAN cathode, which contains sulfur chains of different length, starts to be reduced by breaking the S-S bonds and creating Mg-S bonds, leading to a mixture of different polysulfides (MgLiS_x, MgS₄) and the typical sloped voltage curve for SPAN. In stages



Scheme 1. Proposed four stages for the reduction of SPAN in Mg-SPAN cell (with $2 < x < 8, 0 < n < 2$) in the Mg^{2+}/Li^+ hybrid electrolyte.

II and III, the sulfur species from the previous stages are further shortened, forming a mixture of various polysulfides ($MgLiS_3, Mg_2Li$), which reflects the sloped regions in the voltage profile instead of plateaus in the elemental sulfur system. In stage IV, the crystalline mixed sulfides species, MgS and $Mg-Li-S$, are further produced. A detailed computational study on the working mechanism of Mg-SPAN cells will be presented in a future work.

Actually, lithium becomes concomitantly incorporated into the

cathode structure in the Mg^{2+}/Li^+ hybrid electrolyte, from the initial discharge, as demonstrated by *post-mortem* XPS analysis (Fig. 5a). All the electrodes were sputtered for 15 min, indicating the removal of all the residual electrolyte species. The Mg 2p spectrum of the SPAN cathode after the initial discharge (Fig. 5a upper) shows both lithium and magnesium species, which can be detected at ca. 56 eV and 51 eV, respectively. These two peaks were also observed in the Mg 2p spectrum of the cathode after 10 cycles (Fig. 5a middle), indicating that the lithium and

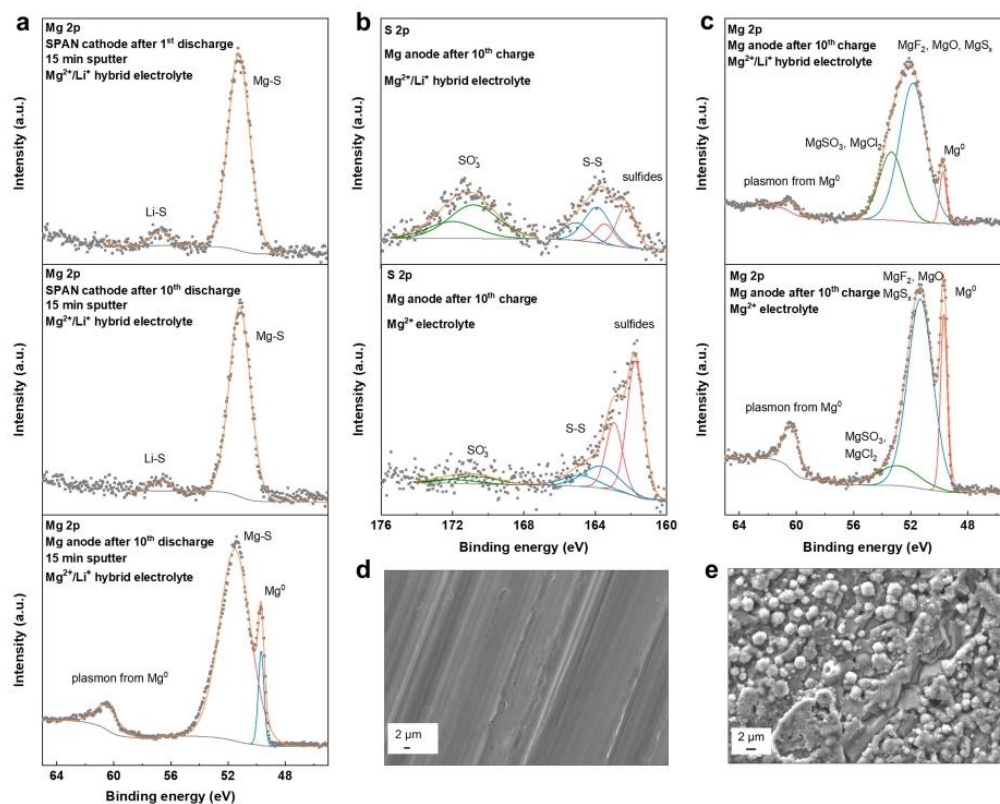


Fig. 5. a) Mg 2p spectra of Mg anode and SPAN cathodes at discharged state cycled in the Mg^{2+}/Li^+ hybrid electrolyte; b) S 2p spectra of the Mg anodes cycled in the Mg^{2+}/Li^+ hybrid electrolyte (upper) and a Mg^{2+} electrolyte (lower), respectively; c) Mg 2p spectra of a Mg anode from the cell with a Mg^{2+}/Li^+ hybrid electrolyte (upper) and a Mg^{2+} electrolyte (lower), respectively; d) SEM image of a pristine, scratched Mg anode; e) SEM image of the aged Mg anode cycled in a Mg^{2+}/Li^+ hybrid electrolyte (50 cycles at charged state).

magnesium species both remained in the cathode over cycling. Most likely, lithium serves as counter ion for the sulfur chains, i.e. $\text{SPAN-S}_x^- \text{Li}^+$.

In addition, the Mg anodes from cells containing the $\text{Mg}^{2+}/\text{Li}^+$ hybrid electrolyte and the Mg^{2+} electrolyte, respectively, were analyzed by XPS after 10 cycles. The S 2p spectra (Fig. 5b) of the Mg anode of cells based on the $\text{Mg}^{2+}/\text{Li}^+$ hybrid electrolyte showed only small amounts of sulfide species (161.9 eV), along with some long chain poly(sulfides) (163.8 eV) [5]. In contrast, a much larger quantity of magnesium sulfides compared to polysulfides can be detected on the Mg anode from the Mg^{2+} electrolyte, which could eventually passivate the Mg surface. These results further support our findings that the addition of a lithium salt can reactivate the short chain magnesium (poly)sulfides (MgS_x , $x < 4$), and increase their solubility, thereby eventually refreshing the Mg anode surface. The solubility tests shown in Fig. S19 (S.I.) verified an increasing solubility of the magnesium polysulfides with the addition of the lithium-salt containing electrolyte. Similar performance has also been found with the Mg bis(hexamethyldisilazide) system with the addition of Li[TFSI] [19].

Fig. 5c shows the Mg 2p spectra of the Mg anodes with both electrolytes. Three peaks could explicitly be observed on the Mg surface: Mg metal (49.6 eV), $\text{MgF}_2/\text{MgO}/\text{MgS}/\text{MgS}_x$ (51.2 eV), and $\text{MgCO}_3/\text{MgCl}_2$ (52.1 eV) [10,48]. The organomagnesium species detected on the Mg surface suggest the presence of an SEI layer on the Mg anode [10]. The corresponding F 1s, Cl 2p C 1s and O 1s spectra (Fig. S20, S.I.) support the SEI layer composition. It is worth to mention that neither lithium metal, nor lithium salt was observed around 55–58 eV, indicating that predominantly, if not solely, Mg joins the electrochemical reaction (Fig. 5c upper and Fig. 5a lower). Lithium in the system does not plate on the Mg surface therefore, it therefore does not contribute to the overall capacity. Notably, formation of the SEI layer proceeded to a larger extent with the $\text{Mg}^{2+}/\text{Li}^+$ hybrid electrolyte compared to the Mg^{2+} electrolyte as can be judged from the higher relative signal intensity of the different Mg-species in the SEI with respect to those for Mg. These results suggest that the addition of lithium salt promotes the formation of a stable SEI layer, which protects the Mg anode during long-term electrochemical cycling [49].

Complementary, SEM images were recorded for a pristine, freshly scratched Mg anode (Fig. 5d) and an anode aged over 50 cycles in the charged state (Fig. 5e). Compared to a pristine Mg foil, on such a cycled anode spherically shaped depositions in the nanometer range but no dendrites were observed, which provides better safety. The elemental mapping results (Fig. S24) confirmed that the surface of the cycled Mg foil is solely composed of Mg, which is in line with previous XPS results. Last but not least, the cycled cathode material in a charged state was analyzed by XRD (Fig. S3); no differences to the pristine cathode were observed. Overall, the *post-mortem* analysis is in line with the good cycle stability of the system and a neglectable shuttle effect in the Mg-SPAN system using the $\text{Mg}^{2+}/\text{Li}^+$ hybrid electrolyte.

4. Conclusions

The electrochemistry of a Mg-S battery system using a sulfurized poly(acrylonitrile) composite (SPAN cathode) and a $\text{Mg}^{2+}/\text{Li}^+$ hybrid electrolyte consisting of magnesium triflate, lithium triflate, MgCl_2 and AlCl_3 in DME has been elucidated. Cells delivered discharge capacities of 1100 mAh g_s^{-1} (energy density: 700 Wh kg_s^{-1}) with over 99.9% Coulombic efficiency at 1 C for at least 100 cycles. Cells cycled between 0.5 C and 3 C demonstrated good rate capability. This work also provides the first in-depth electrochemical, thermodynamic and kinetic study of an SPAN cathode in combination with the $\text{Mg}^{2+}/\text{Li}^+$ hybrid electrolyte for Mg battery applications. The addition of a lithium salt could effectively lower the resistance and the overpotential of the batteries, when magnesium polysulfides are present in the electrolyte. Utilization of a lithium salt in the electrolyte in combination with the SPAN system also significantly improves reaction kinetics, especially in

the conversion of short chain polysulfides.

CRedit authorship contribution statement

Peiwen Wang: Conceptualization, Investigation, Writing – original draft, Writing – review & editing. **Kathrin Küster:** Resources, Writing – review & editing. **Ulrich Starke:** Resources, Writing – review & editing. **Chen Liang:** Resources. **Rainer Niewa:** Resources. **Michael R. Buchmeiser:** Supervision, Writing – review & editing.

Declaration of competing interest

The authors declare that they have no known competing financial interests or personal relationships that could have appeared to influence the work reported in this paper.

Acknowledgement

Financial support by the German Federal Ministry of Education and Research (project number 03XP0208J) and by the German Federal Ministry of Economic Affairs and Energy (project number 03ETE003E) is gratefully acknowledged. We also thank Mr. U. Hageroth from the German Institutes of Textile and Fiber Research (DITF) Denkendorf for the SEM/EDX measurements. We wish to thank Miss J. Trück for the productive discussion.

Appendix A. Supplementary data

Supplementary data to this article can be found online at <https://doi.org/10.1016/j.jpowsour.2021.230604>.

References

- [1] H. Kim, T.S. Arthur, G.D. Allred, J. Zajicek, J.G. Newman, A.E. Rodnyansky, A. G. Oliver, W.C. Boggess, J. Muldoon, Nat. Commun. 427 (2011) 1–6.
- [2] P. Wang, M.R. Buchmeiser, Adv. Funct. Mater. 29 (2019) 1905248–1905275.
- [3] Y. Lu, C. Wang, Q. Liu, X. Li, X. Zhao, Z. Guo, Small Methods 5 (2021) 2001303.
- [4] Z. Zhao-Karger, R. Liu, W. Dai, Z. Li, T. Diemant, B.P. Vinayan, C. Bonatto Minella, X. Yu, A. Manthiram, R.J. Behm, M. Ruben, M. Fichtner, ACS Energy Lett. 3 (2018) 2005–2013.
- [5] P. Wang, J. Trück, S. Niesen, J. Kappler, K. Küster, U. Starke, F. Ziegler, A. Hintennach, M.R. Buchmeiser, Batteries Supercaps 3 (2020) 1239–1247.
- [6] Y. Yang, W. Wang, Y. Nuli, J. Yang, J. Wang, ACS Appl. Mater. Interfaces 11 (2019) 9062–9072.
- [7] J. Sun, C. Deng, Y. Bi, K.-H. Wu, S. Zhu, Z. Xie, C. Li, R. Amal, J. Luo, T. Liu, D.-W. Wang, ACS Appl. Energy Mater. 3 (2020) 2516–2525.
- [8] S. Zhang, Y. Huang, Y. Nuli, B. Wang, J. Yang, J. Phys. Chem. C 124 (2020) 20712–20721.
- [9] P. Wang, J. Kappler, B. Sievert, J. Häcker, K. Küster, U. Starke, F. Ziegler, M. R. Buchmeiser, Electrochim. Acta 361 (2020) 137024.
- [10] T. Gao, S. Hou, K. Huynh, F. Wang, N. Eidson, X. Fan, F. Han, C. Luo, M. Mao, X. Li, C. Wang, ACS Appl. Mater. Interfaces 10 (2018) 14767–14776.
- [11] Z. Zhao-Karger, M. Fichtner, MRS Commun. 7 (2017) 770–784.
- [12] T. Gao, S. Hou, F. Wang, Z. Ma, X. Li, K. Xu, C. Wang, Angew. Chem. 129 (2017) 13711–13715. Angew. Chem. Int. Ed. 2017, 129, 13526–13530.
- [13] S.Y. Ha, Y.W. Lee, S.W. Woo, B. Koo, J.S. Kim, J. Cho, K.T. Lee, N.S. Choi, ACS Appl. Mater. Interfaces 6 (2014) 4063–4073.
- [14] X. Ji, K.T. Lee, L.F. Nazar, Nat. Mater. 8 (2009) 500–506.
- [15] Z. Zhao-Karger, M.E.G. Bardaji, O. Fuhr, M. Fichtner, J. Mater. Chem. A 5 (2017) 10815–10820.
- [16] J. Häcker, C. Danner, B. Sievert, I. Biswas, Z. Zhao-Karger, N. Wagner, K. A. Friedrich, Electrochim. Acta 338 (2020) 135787.
- [17] W. Li, S. Cheng, J. Wang, Y. Qiu, Z. Zheng, H. Lin, S. Nanda, Q. Ma, Y. Xu, F. Ye, M. Liu, L. Zhou, Y. Zhang, Angew. Chem. 128 (2016) 6516–6520. Angew. Chem. Int. Ed. 2016, 55, 6406–6410.
- [18] A. Du, Z. Zhang, H. Qu, Z. Cui, L. Qiao, L. Wang, J. Chai, T. Lu, S. Dong, T. Dong, H. Xu, X. Zhou, G. Cui, Energy Environ. Sci. 10 (2017) 2616–2625.
- [19] T. Gao, M. Noked, A.J. Pearce, E. Gillette, X. Fan, Y. Zhu, C. Luo, L. Suo, M. A. Schroeder, K. Xu, S.B. Lee, G.W. Rubloff, C. Wang, J. Am. Chem. Soc. 137 (2015) 12388–12393.
- [20] A.C. Kozen, C.F. Lin, A.J. Pearce, M.A. Schroeder, X. Han, L. Hu, S. Lee, G. W. Rubloff, M. Noked, ACS Nano 9 (2015) 5884–5892.
- [21] L. Wang, X.M. He, J.J. Li, M. Chen, J. Gao, C.Y. Jiang, Electrochim. Acta 72 (2012) 114–119.
- [22] J. Fanous, M. Wegner, M.B.M. Spera, M.R. Buchmeiser, J. Electrochem. Soc. 160 (2013) A1169–A1170.

- [23] J. Fanous, M. Wegner, J. Grimminger, M. Rolf, M.B.M. Spera, M. Tenzerb, M. R. Buchmeiser, *J. Mater. Chem.* 22 (2012) 23240–23245.
- [24] J. Fanous, M. Wegner, J. Grimminger, A. Andresen, M.R. Buchmeiser, *Chem. Mater.* 23 (2011) 5024–5028.
- [25] S. Warneke, M. Eusterholz, R.K. Zenn, A. Hintennach, R. Dinnebier, M. R. Buchmeiser, *J. Electrochem. Soc.* 165 (2018) A6017–A6020.
- [26] S. Zhang, *Energy* 7 (2014) 4588–4600.
- [27] Y. Xu, G. Zhou, S. Zhao, W. Li, F. Shi, J. Li, J. Feng, Y. Zhao, Y. Wu, J. Guo, Y. Cui, Y. Zhang, *Adv. Sci.* 6 (2019) 1800981–1800987.
- [28] L. Zeng, N. Wang, J. Yang, J. Wang, Y. NuLi, *J. Electrochem. Soc.* 164 (2017) A2504–A2512.
- [29] T. Liu, Y. Shao, G. Li, M. Gu, J. Hu, S. Xu, Z. Nie, X. Chen, C. Wang, J. Liu, *J. Mater. Chem.* 2 (2014) 3430.
- [30] R.E. Doe, R. Han, J. Hwang, A.J. Gmitter, I. Shterenberg, H.D. Yoo, N. Pour, D. Aurbach, *Chem. Commun.* 50 (2014) 243–245.
- [31] I. Shterenberg, M. Salama, Y. Gofer, E. Levi, D. Aurbach, *MRS Bull.* 39 (2014) 453–460.
- [32] J. Luo, S. He, T.L. Liu, *ACS Energy Lett.* 2 (2017) 1197–1202.
- [33] I. Shterenberg, M. Salama, H.D. Yoo, Y. Gofer, J.-B. Park, Y.-K. Sun, D. Aurbach, *J. Electrochem. Soc.* 162 (2015) A7118–A7128.
- [34] T. Lebzherz, M. Frey, A. Hintennach, M.R. Buchmeiser, *RSC Adv.* 9 (2019) 7181–7188.
- [35] M. Frey, R.K. Zenn, S. Warneke, K. Müller, A. Hintennach, R.E. Dinnebier, M. R. Buchmeiser, *ACS Energy Lett.* 2 (2017) 595–604.
- [36] D. Huang, S. Tan, M. Li, D. Wang, C. Han, Q. An, L. Mai, *ACS Appl. Mater. Interfaces* 12 (2020) 17474–17480.
- [37] J.F. Moulder, W.F. Stickle, P.E. Sobol, K.D. Bomben, *Handbook of X-Ray Photoelectron Spectroscopy*, Physical Electronics Division, Perkin-Elmer Corporation, Minnesota, 1992, pp. 1–261.
- [38] Y. Cheng, R.M. Stolley, K.S. Han, Y. Shao, B.W. Arey, N.M. Washton, K.T. Mueller, M.L. Helm, V.L. Sprenkle, J. Liu, G. Li, *Phys. Chem. Chem. Phys.* 17 (2015) 13307–13314.
- [39] B. Lee, J. Choi, S. Na, D.-J. Yoo, J.H. Kim, B.W. Cho, Y.-T. Kim, T. Yim, J.W. Choi, S.H. Oh, *Appl. Surf. Sci.* 484 (2019) 933–940.
- [40] P. He, H.O. Ford, L.C. Merrill, J.L. Schaefer, *ACS Appl. Energy Mater.* 2 (2019) 6800–6807.
- [41] W.Q. Wang, H.C. Yuan, Y. Nuli, J.J. Zhou, J. Yang, J.L. Wang, *J. Phys. Chem. C* 122 (2018) 26764–26776.
- [42] Z. Zhou, B. Chen, T. Fang, Y. Li, Z. Zhou, Q. Wang, J. Zhang, Y. Zhao, *Adv. Energy Mater.* 10 (2019) 1902023.
- [43] J. Chai, Z. Liu, J. Zhang, J. Sun, Z. Tian, Y. Ji, K. Tang, X. Zhou, G. Cui, *ACS Appl. Mater. Interfaces* 9 (2017) 17897–17905.
- [44] V. Bhaghavathi Parambath, Z. Zhao-Karger, T. Diemant, M. Jäckle, Z. Li, T. Scherer, A. Gross, R.J. Behm, M. Fichtner, *J. Mater. Chem. A* 8 (2020) 22998–23010.
- [45] T. Gao, X. Ji, S. Hou, X. Fan, X. Li, C. Yang, F. Han, F. Wang, J. Jiang, K. Xu, C. Wang, *Adv. Mater.* 30 (2018) 1704313.
- [46] S. Li, Z. Zeng, J. Yang, Z. Han, W. Hu, L. Wang, J. Ma, B. Shan, J. Xie, *ACS Appl. Energy Mater.* 2 (2019) 2956–2964.
- [47] Y.Z. Zhang, S. Liu, G.C. Li, G.R. Li, X.P. Gao, *J. Mater. Chem.* 2 (2014) 4652–4659.
- [48] D.-T. Nguyen, A.Y.S. Eng, M.-F. Ng, V. Kumar, Z. Sofer, A.D. Handoko, G. S. Subramanian, Z.W. Seh, *Cell Rep.* 1 (2020) 100265.
- [49] K. Tang, A. Du, S. Dong, Z. Cui, X. Liu, C. Lu, J. Zhao, X. Zhou, G. Cui, *Adv. Mater.* 32 (2019), e1904987.

6.3 Supporting Information to: “Performance Enhancement of Rechargeable Magnesium-Sulfur Batteries Based on a Sulfurized Poly(acrylonitrile) Composite and a Lithium Salt”

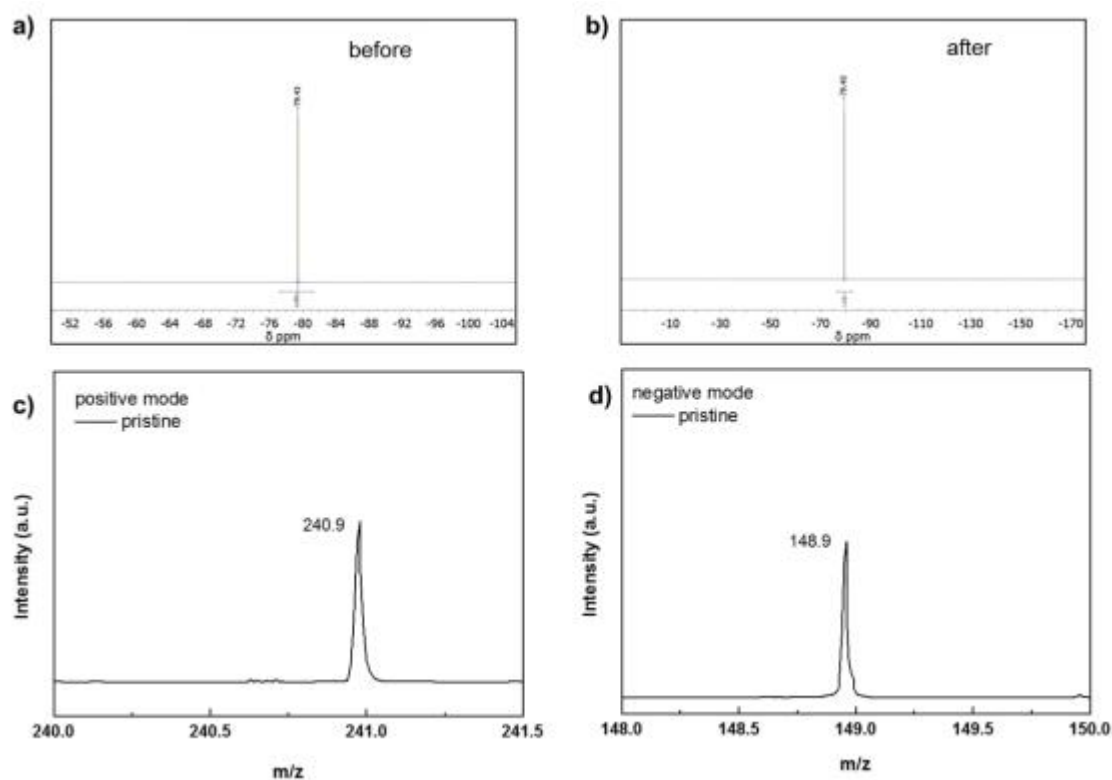


Figure S1: a,b) ¹⁹F-NMR spectra of a Mg²⁺/Li⁺ hybrid electrolyte before and after cycling; c,d) ESI-MS (positive and negative modes) of the pristine Mg²⁺/Li⁺ hybrid electrolyte.

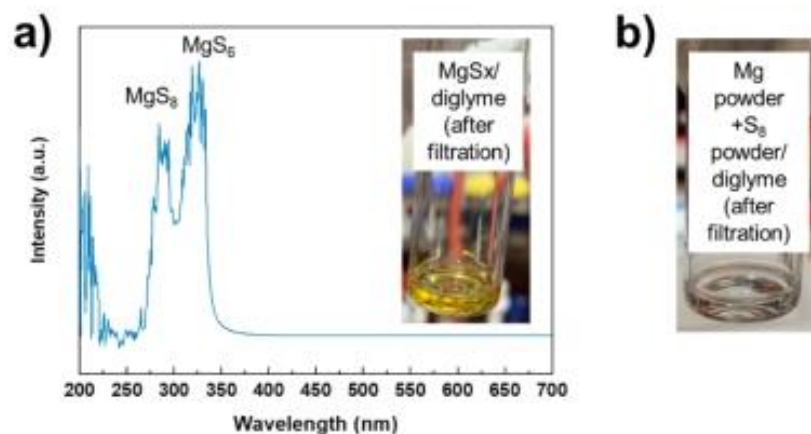


Figure S2: a) UV-vis spectrum of a MgS_x-diglyme solution; inset: orange-red color of the MgS_x-diglyme solution after filtration; b) transparent color of the filtrate of a mixture of Mg and S₈ powder.

Preparation of a Mg²⁺/Li⁺ hybrid electrolyte containing MgS_x and of a Mg²⁺ electrolyte containing MgS_x

As described in the experimental section, after dissolving 0.1 g MgS_x in 6 mL diglyme, there remains still some undissolved MgS_x in the mixture; consequently, the filtered MgS_x/diglyme solution is saturated. The mixtures containing the Mg²⁺/Li⁺ hybrid electrolyte + MgS_x solution and the Mg²⁺ electrolyte + MgS_x solution, respectively, were prepared by mixing the corresponding electrolytes and the MgS_x solutions in a volumetric ratio of 2:1. In each cell, 130 μL electrolyte were used.

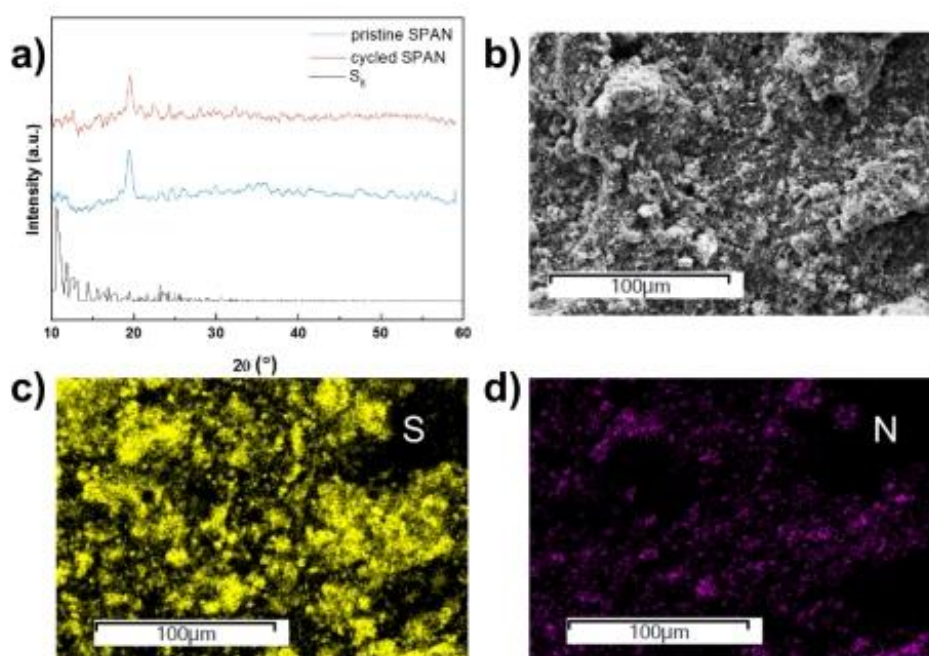


Figure S3: a) XRD pattern of a pristine SPAN cathode, a cycled SPAN cathode and an elemental sulfur reference; b) SEM image of an SPAN cathode; c-f) elemental mapping of S and N. The covalently bound sulfur, nitrogen from SPAN are all evenly distributed in the SPAN.

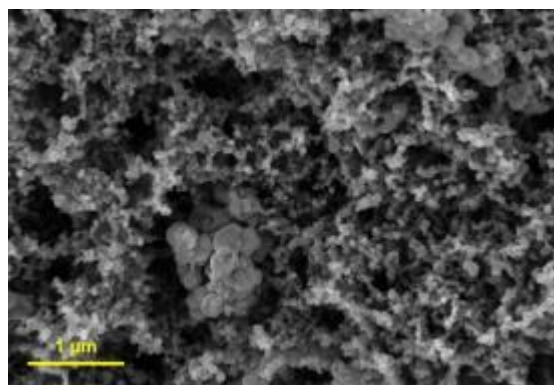


Figure S4: Higher resolution SEM image of a SPAN cathode.

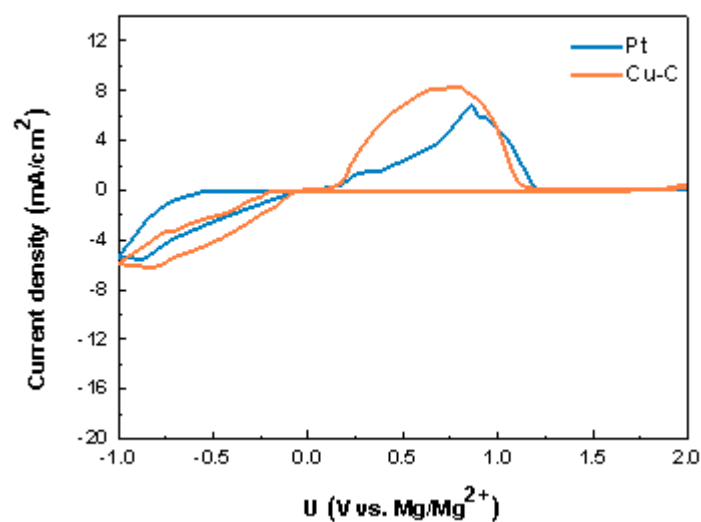


Figure S5: CV of the Mg electrochemical plating and stripping of Mg at 0.5 mV/s in a Mg²⁺/Li⁺ hybrid electrolyte on Pt and Cu/C disc electrodes, respectively.

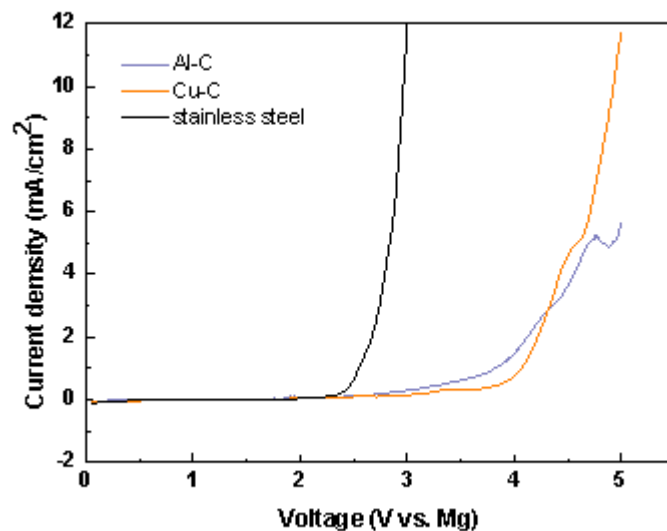


Figure S6: Linear sweep voltammetry on stainless steel, Al-C and Cu-C electrodes.

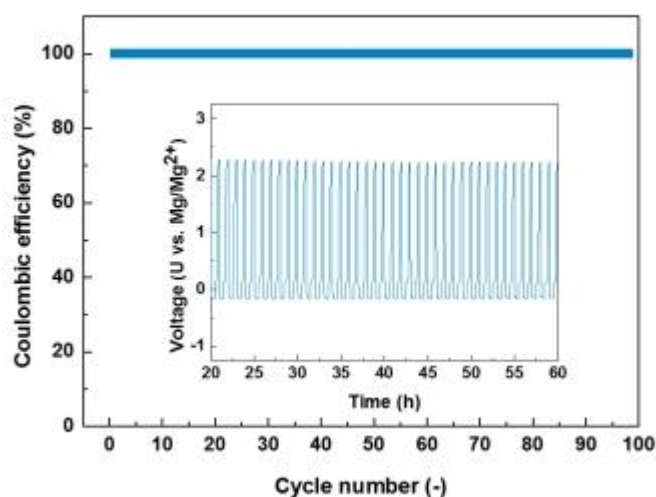


Figure S7: Coulombic efficiency of stainless steel-Mg cells using the $\text{Mg}^{2+}/\text{Li}^+$ hybrid electrolyte by charging and discharging the cell at 0.1 mA/cm^2 (0.05 mAh/cm^2); inset: voltage profile.

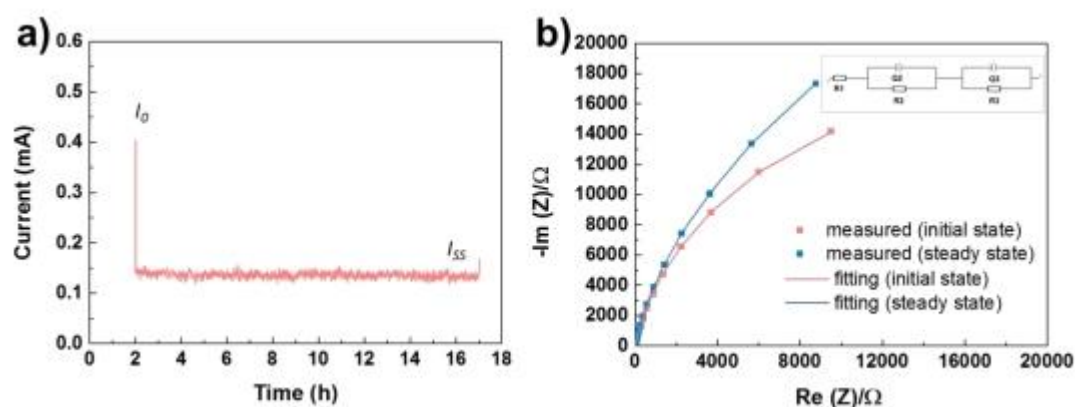


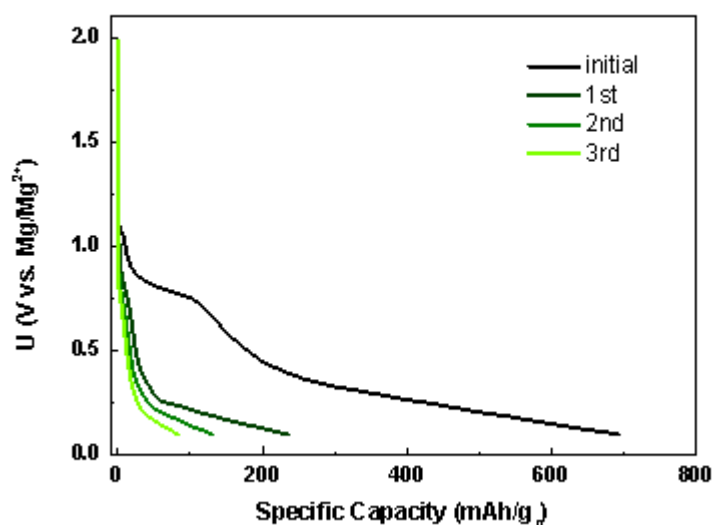
Figure S8: a) Chronoamperogram of a Mg^{2+} electrolyte with an applied voltage of 10 mV. I_0 indicates the initial current; I_{ss} is the steady state current; b) Nyquist plots of the Mg^{2+} electrolyte. The red curve shows the impedance spectrum before polarization. The blue curve shows the impedance spectrum after polarization at steady state. Inset: equivalent circuit of the electrode resistance.

Table S1: Fitted resistance values before and after polarization.

	R1 (electrolyte resistance, Ω)	R2 + R3 (electrode resistance, Ω)
Before polarization	6.433	$(2.59 + 39564)/2 = 19783$
Steady state	6.383	$(1.185 + 57114)/2 = 28557$

In order to exclude the influence of Li^+ , the transfer number of Mg^{2+} was measured based on the Bruce and Vincent method (Eq.1) using a Mg^{2+} electrolyte. A small constant potential (10 mV) was applied to the electrolyte between two magnesium electrodes, leading to a decrease of the initial current value (0.4 mA) until steady state (0.14 mA) after 15 hours (Figure S8). Since the anions are not involved into the redox reaction, the anion current vanishes after reaching the steady state and the total current is only caused by the Mg^{2+} cations. The contact resistance was measured before and after polarization. Figure S8 shows the chronoamperometric and impedance measurement using the Mg^{2+} electrolyte. The fitted resistance values are listed in Table S1. The transfer number of the Mg^{2+} was further determined by Eq. 1:

$$t_{\text{Mg}^{2+}} = \frac{I_{SS}(\Delta V - I_0 R_{P,0})}{I_0(\Delta V - I_{SS} R_{P,SS})} = \frac{140 \mu\text{A} \times (10 \text{ mV} - 400 \mu\text{A} \times 19.8 \text{ k}\Omega)}{400 \mu\text{A} \times (10 \text{ mV} - 140 \mu\text{A} \times 28.6 \text{ k}\Omega)} = 0.7 \quad \text{Eq 1}$$


Figure S9: Voltage profile of a Mg-SPAN cell using a Mg^{2+} electrolyte.

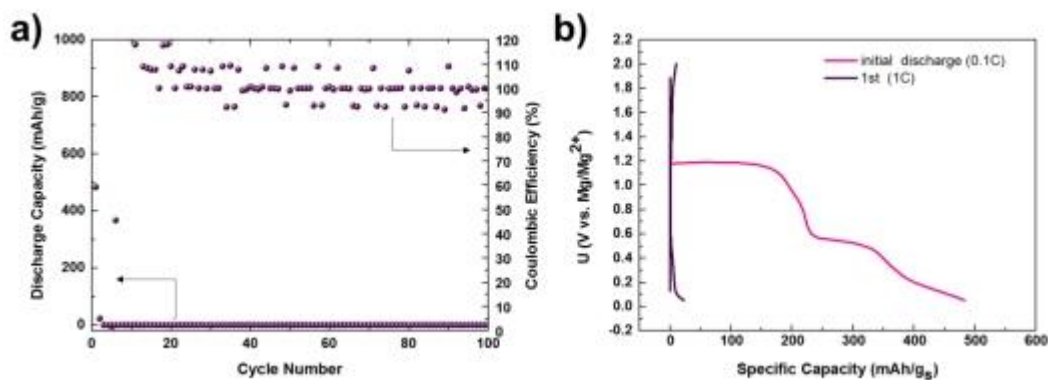


Figure S10: a) Mg-S₈ cell using a Mg²⁺/Li⁺ hybrid electrolyte, cycled at 1 C; b) voltage profile of the cell in a). The fast capacity decay is attributed to the fast loss of sulfur during cycling.

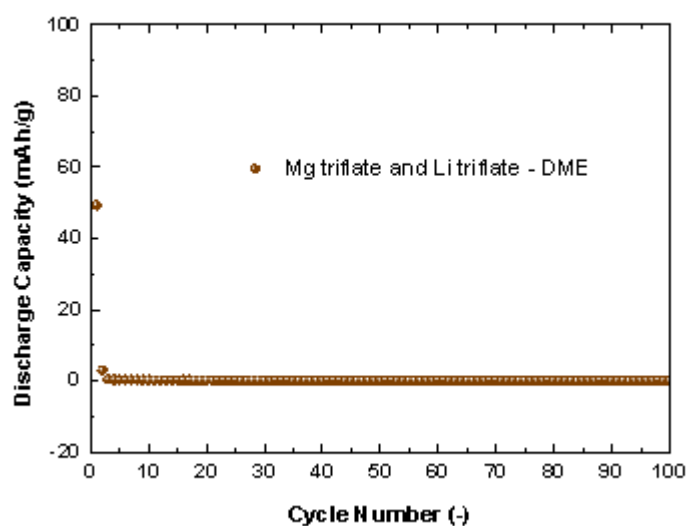


Figure S11: Mg-SPAN cell containing 0.2 M Mg triflate and 1.6 M Li triflate cycled at 0.5 C. Neglectable capacity was detected, indicating the importance of the electroactive species.

Table S2: Resistance values of a Mg-SPAN cell using a Mg²⁺/Li⁺ hybrid electrolyte.

	R1 (Ω)	R2 (Ω)	R3 (Ω)	 χ²/z
OCV 2h	6.76	1413	1538	0.02121
1st charge	24.33	86.74	233.40	0.00024
6th charge	27.15	36.60	236.50	0.00019
11th charge	28.73	59.18	232.10	0.00026
16th charge	29.34	66.99	265.20	0.00016
1st discharge	27.52	231.80	260.10	0.01082
6th discharge	30.54	299.10	153.90	0.00029
11th discharge	31.60	302.70	158.00	0.00038
16th discharge	32.22	318.80	165.10	0.00041

Table S3: Resistance values of the Mg-SPAN cell using the Mg²⁺ electrolyte.

	R1 (Ω)	R2 (Ω)	R3 (Ω)	 χ²/z
1st charge	2.18	5.06	3239	0.38000
6th charge	9.06	49.94	5102	0.04988
11th charge	11.19	73.32	9760	0.02845
16th charge	13.75	93.39	27839	0.00028
21st charge	16.96	110.20	34324	0.00034
1st discharge	7.51	7.62	1969	0.55770
6th discharge	9.37	37.34	5491	0.04232
11th discharge	11.55	61.01	12214	0.02829
16th discharge	14.22	104.80	28043	0.00079
21st discharge	17.05	125.20	36075	0.01435

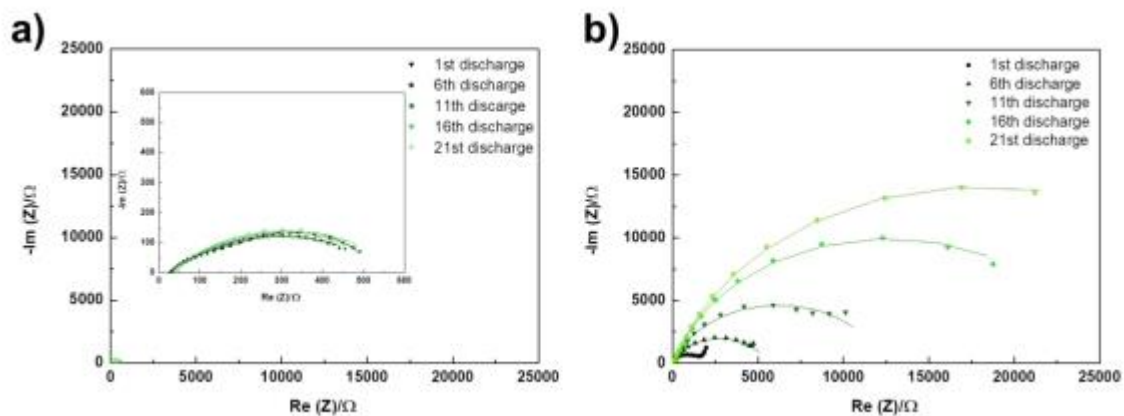


Figure S12: Nyquist plots of cells after each cycle at the discharged state, using **a)** a $\text{Mg}^{2+}/\text{Li}^+$ hybrid electrolyte; **b)** a Mg^{2+} electrolyte.

Table S4: Resistance values of a symmetric Mg-Mg cell containing a $\text{Mg}^{2+}/\text{Li}^+$ hybrid electrolyte.

	R1 (Ω)	R2 (Ω)	R3 (Ω)	$ \chi^2/z $
OCV 0h	2.7	712.5	277.9	0.0252
OCV 1h	2.7	1633.0	412.3	0.0088
OCV 5h	2.7	5335.0	343.9	0.0155
OCV 10h	2.8	8896.5	592.5	0.0109
OCV 20h	2.9	13474.0	821.0	0.0116
OCV 40h	2.9	19507.0	1248.5	0.0176
OCV 50h	2.9	21674.0	1417.5	0.0220
after polarization	2.9	4060.5	19.9	0.1918

Table S5: Resistance values of a symmetric Mg-Mg cell containing a Mg²⁺/Li⁺ hybrid electrolyte + MgS_x and the Mg²⁺ electrolyte + MgS_x.

	R1 (Ω)	R2 (Ω)	R3 (Ω)	χ ² /z
Mg ²⁺ /Li ⁺ hybrid electrolyte + MgS _x (1h OCV)	3.3	3180.5	495.9	0.0288
Mg ²⁺ electrolyte + MgS _x (1h OCV)	4.6	5630.0	683.5	0.00047

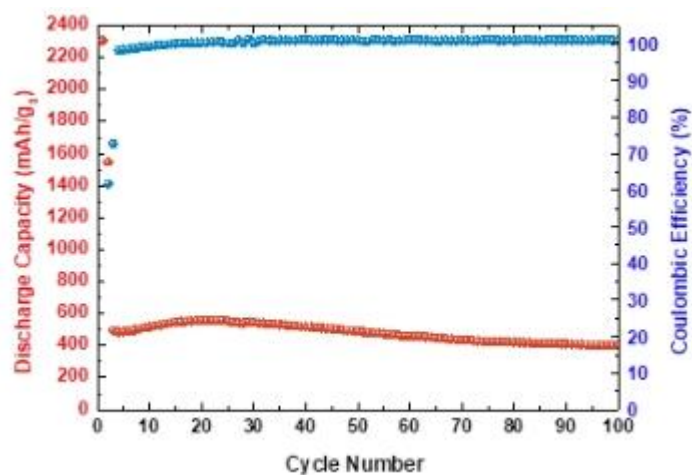


Figure 13: Mg-SPAN cell using a Mg²⁺/Li⁺ hybrid electrolyte + MgS_x solution cycled at 1 C.

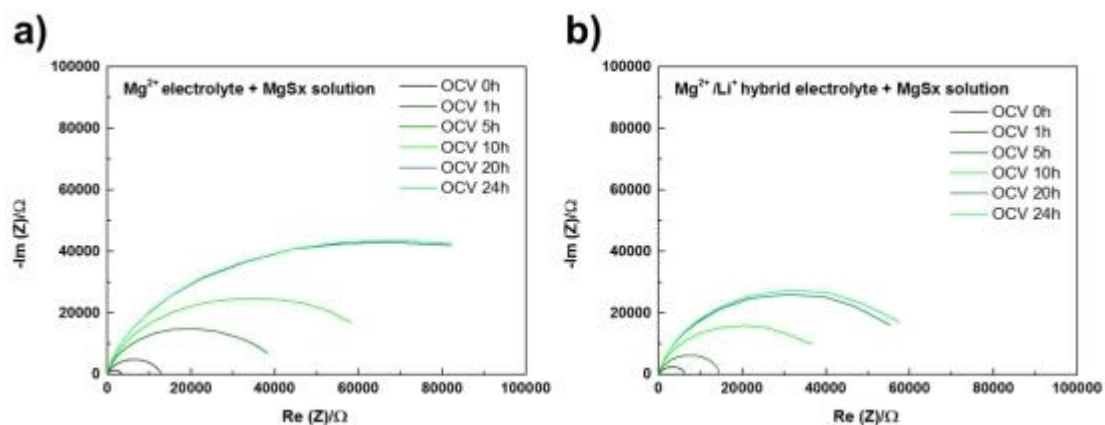


Figure S14: Nyquist plots of a symmetric Mg-Mg cell at the OCV state with **a)** a Mg^{2+} electrolyte + MgS_x solution; **b)** a $\text{Mg}^{2+}/\text{Li}^+$ hybrid electrolyte + MgS_x solution.

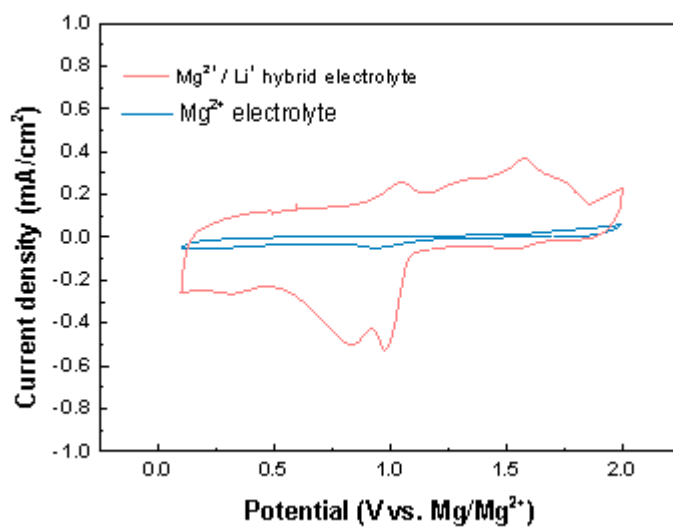


Figure S15: CVs of the Mg-SPAN three-electrode cell using a $\text{Mg}^{2+}/\text{Li}^+$ hybrid electrolyte and a Mg^{2+} electrolyte, respectively, applying a scan rate of 0.1 mV/s.

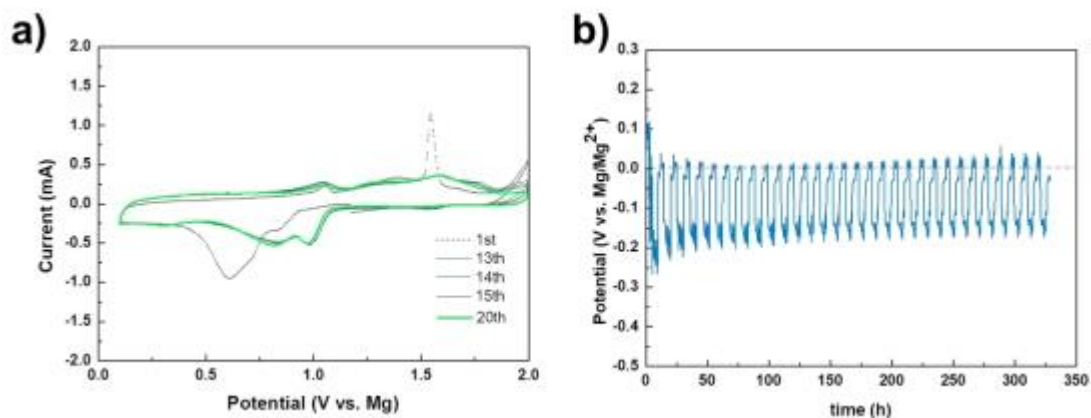


Figure S16: a) CVs of a three-electrode Mg-SPAN cell. Differences between the initial cycle and the following cycles are attributed to the formation of an SEI layer; b) potential change of the Mg_{CE} (vs. Mg_{RE}) versus time. After each cycle, the Mg_{CE} returns back to the original state, showing only Mg joins the plating and stripping.

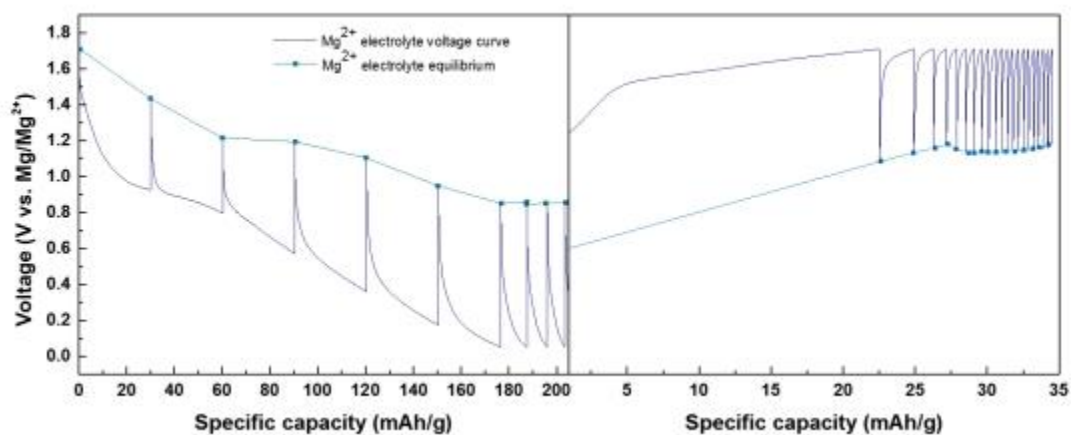


Figure S17: GITT curve of a Mg-SPAN cell using a Mg²⁺ electrolyte cycled at 0.1 C.

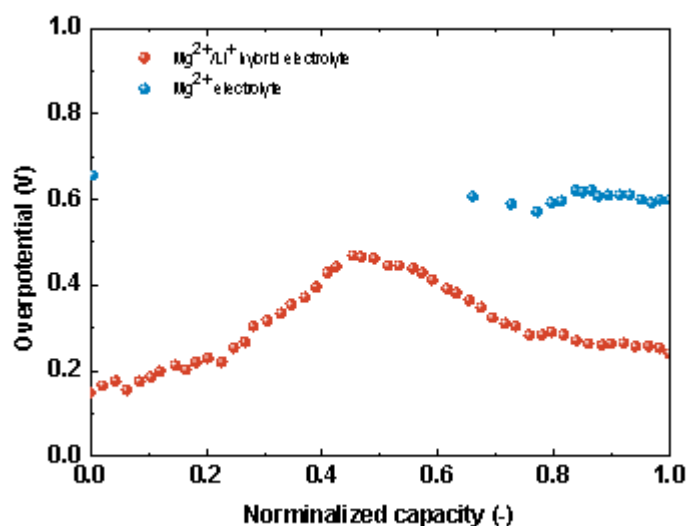


Figure S18: Overpotential in the GITT curve (charge).

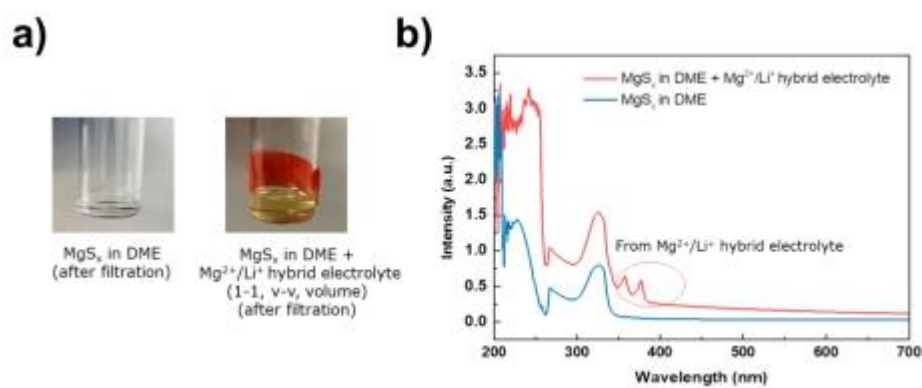


Figure S19: a) Comparison between a solution of MgS_x in DME (left) and MgS_x in DME with the addition of the $\text{Mg}^{2+}/\text{Li}^+$ hybrid electrolyte (right); b) UV-Vis spectra of the two solutions.

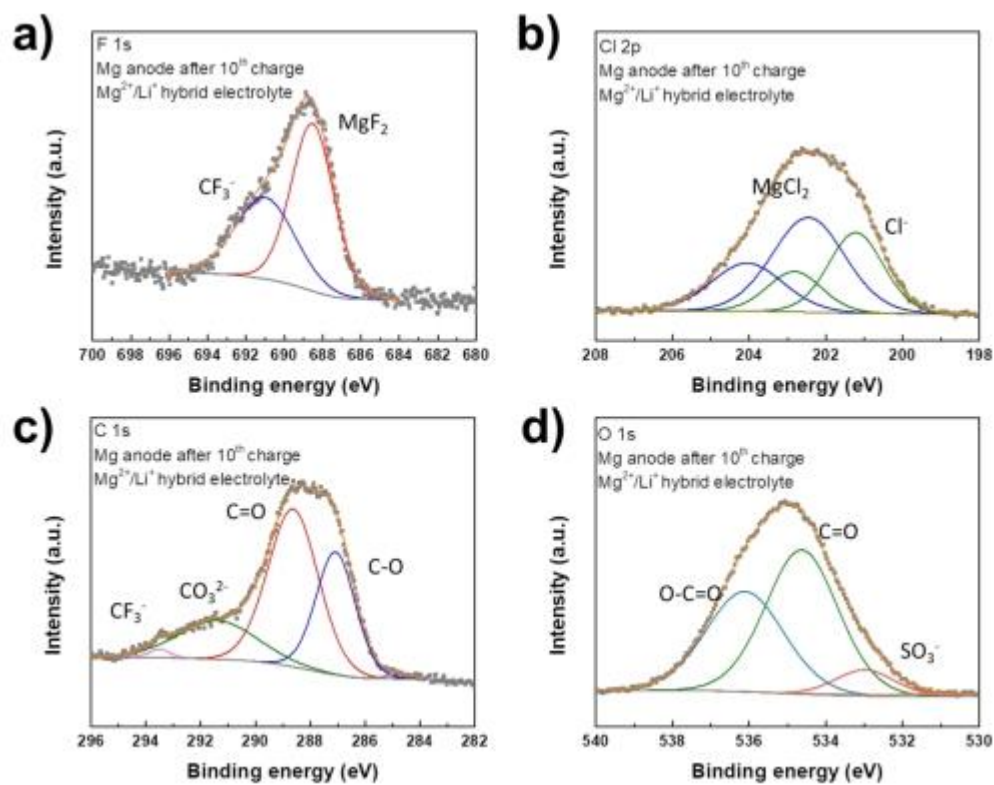


Figure S20: High resolution XPS spectra of a Mg anode after 10 cycles in the charged state; a) F1s; b) Cl 2p; c) C1s; d) O1s.^[1-2]

Table S6: Elemental analysis of SPAN.

Element	Composition (%)
C	42.6
H	1.1
N	13.8
S	38.0

In order to compare the battery performance of cathodes with a higher sulfur loading, an SPAN slurry was prepared using the same composition (SPAN:carbon black:PVDF=70:15:15), but a thicker coating thickness (300 μm wet). The sulfur loading was around 1 mg/cm^2 , which is comparable with the state of the art.^[3] Figure S21 shows the corresponding cycling data. The cell delivered around 700 $\text{mAh}/\text{g}_\text{s}$ discharge capacity for over 50 cycles with 100% Coulombic efficiency at 1 C, indicating superior cycling performance and good combination between SPAN and the lithium-containing hybrid electrolyte.

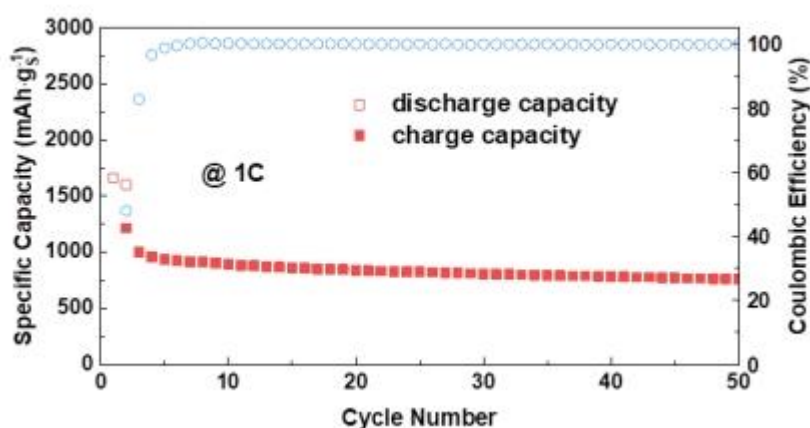


Figure S21: long-term cycling data of Mg-SPAN cell with higher sulfur loading (1 mg/cm^2).

In order to investigate the electrolyte with different lithium salt concentrations, 0.8 M lithium triflate was added to the hybrid electrolyte. Figure S22 shows a Mg-SPAN cell using the 0.8 M lithium triflate electrolyte. The cell showed some capacity decay in the initial cycles but stabilized around 450 $\text{mAh}\cdot\text{g}_\text{s}^{-1}$ in the following cycles. It is known that an unsaturated electrolyte can further dissolve polysulfides, which leads to the polysulfide shuttle.^[3] Therefore, a saturated electrolyte concentration was selected: 0.2 M magnesium triflate, 0.4 M MgCl_2 , 0.4 M AlCl_3 and 1.6 M lithium triflate in DME.

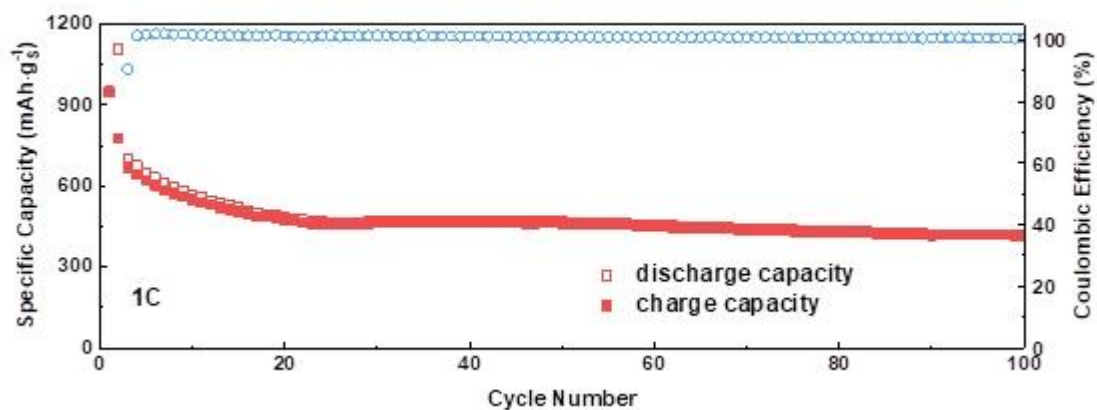


Figure S22: Long term cycling of Mg-SPAN at 1 C using 0.2 M magnesium triflate, 0.4 M MgCl₂, 0.4 M AlCl₃ and 0.8 M lithium triflate.

In order to exclude the capacity contribution from the *in-situ* formed copper sulfide, the CuS cathode was prepared with carbon black and PVDF. The cell composed of a CuS cathode, a Mg anode and Mg²⁺/Li⁺ hybrid electrolyte was cycled between 0.05 V to 2 V at 0.5 C. Figure S23 shows that the capacity contribution from the CuS is minor, suggesting that the copper sulfide in the system only catalyzes the reversible reactions and suppresses the polysulfide shuttle.

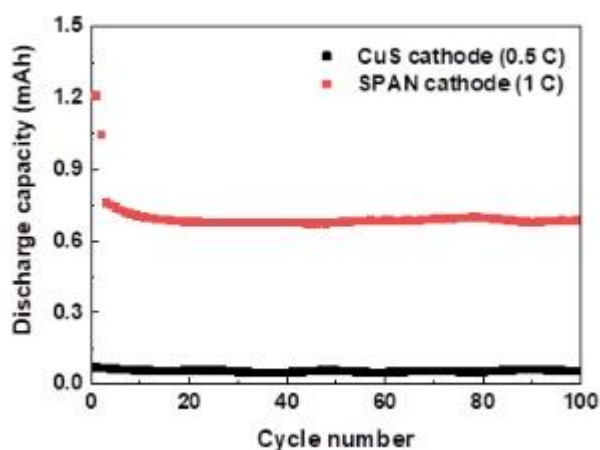


Figure S23: Comparison of cells with an SPAN cathode and a CuS cathode.

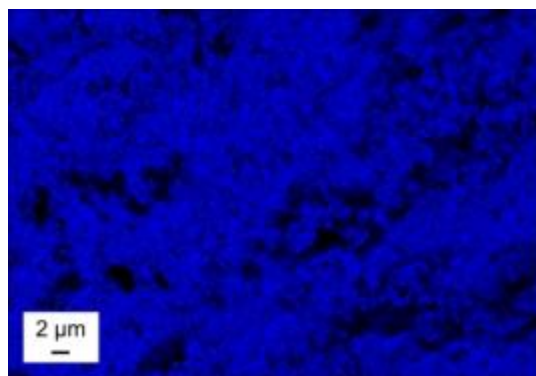


Figure S24: Elemental mapping of the cycled Mg foil from Figure 5e.

References (Supporting Information):

- [1] T. Gao, S. Hou, K. Huynh, F. Wang, N. Eidson, X. Fan, F. Han, C. Luo, M. Mao, X. Li, C. Wang, *ACS Appl. Mater. Interfaces* 2018, **10**, 14767-14776.
- [2] P. Wang, J. Kappler, B. Sievert, J. Häcker, K. Küster, U. Starke, F. Ziegler, M. R. Buchmeiser, *Electrochim. Acta* 2020, **361**, 137024.
- [3] Z. Zhao-Karger, R. Liu, W. Dai, Z. Li, T. Diemant, B. P. Vinayan, C. Bonatto Minella, X. Yu, A. Manthiram, R. J. Behm, M. Ruben, M. Fichtner, *ACS Energy Lett.* 2018, **3**, 2005-2013.

Chapter 7

Design of a Gel Polymer Electrolyte for Magnesium-Sulfur/Ion Batteries

7.1 Motivation

Based on the outstanding electrochemical performance of Mg-SPAN cells presented in **Chapter 5-6**, SPAN cathodes proved to be well compatible with Mg anodes together with the liquid $\text{Mg}^{2+}/\text{Li}^{+}$ hybrid electrolytes. However, the liquid electrolytes for Mg-S batteries, which are mostly investigated so far, have shown some inevitable shortcomings, such as potential leakage and polysulfide shuttle, which lead to the cycle performance decay.

There are barely reports on the solid-state electrolytes for Mg-S batteries. At the same time, polysulfide shuttle and leakage issues are common challenges in both Li-S and Mg-S batteries containing liquid electrolytes. In Li-S systems, one possible solution to overcome these issues is the replacement of traditional liquid electrolytes by solid-state electrolytes.^[222] By using a solid-state electrolyte, the dissolution of polysulfides is substantially reduced; consequently, the shuttle effect can be eliminated. The internal short circuit and electrolyte leakage can also be inhibited by using a solid-state electrolyte. Concerning low ion conductivity and poor contact between electrodes and electrolytes in the majority of the all-solid-state batteries, an *in-situ* prepared gel-polymer-electrolyte (GPE) is designed for Mg-S batteries in this sub-project.

In view of the outstanding electrochemical performance of Mg-SPAN cells containing the $\text{Mg}^{2+}/\text{Li}^{+}$ borohydride-based hybrid electrolyte (**Chapter 5**), it is interesting to investigate the compatibility of a borate-based GPE, prepared *via* an *in-situ* crosslinking reaction between the $\text{Mg}[\text{BH}_4]_2/\text{Li}[\text{BH}_4]$ solution and poly(tetrahydrofuran) solution, with Mg-SPAN cells.

7.2 Publication: “A Design Concept for Halogen-Free Mg²⁺/Li⁺-Dual Salt-Containing Gel-Polymer-Electrolytes for Rechargeable Magnesium Batteries”

Solid-state electrolytes can effectively promote the development of Mg-S batteries because of the improved safety and reduced polysulfide shuttle effect. However, electrolyte leakage issue and shuttle effect in Mg-S cells containing traditional liquid electrolytes prohibit their further development. Here, a new borate-based GPE, *in-situ* prepared by mixing Mg[BH₄]₂/Li[BH₄] and poly(tetrahydrofuran) solutions, has been designed. Due to the reported beneficial effects of the nanofillers in the solid-state electrolytes^[222], TiO₂ nano powder has also been embedded.

The as-prepared GPE possessed relatively high ionic conductivities from 0 to 40 °C, excellent polarization behavior and good reversibility. More remarkably, the GPE displayed outstanding compatibility not only with sulfur-based cathodes, but also with intercalation cathodes (TiS₂, LTO, Mo₆S₈). Specifically, Mg-SPAN and Mg-ACC/S cells containing the GPE stably delivered *ca.* 600 and 420 mAh g_s⁻¹ at 0.2 C for 140 and 50 cycles, respectively. *Post-mortem* XPS analysis of the Mg anode from the Mg-SPAN cell also confirmed the successful suppression of polysulfides. In addition, the Mg-SPAN system containing the GPE featured low self-discharge, high flexibility and safety characteristics.

The graphical abstract, which well summarized the sub-project, is shown in **Figure 7.1**. A detailed discussion and introduction to this sub-project is presented in the following publication.

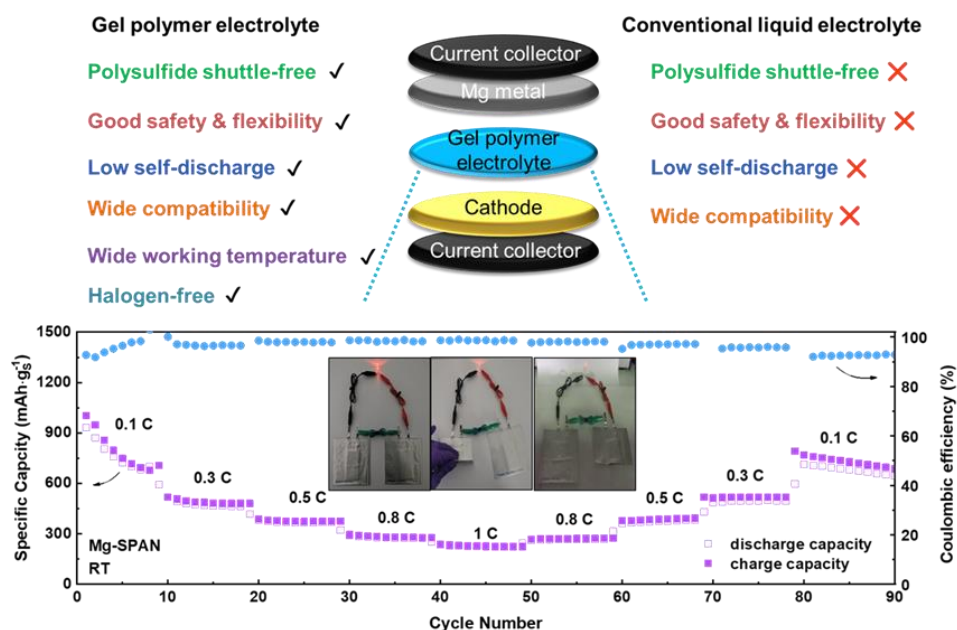


Figure 7.1: Graphical abstract of the publication “A design concept for halogen-free Mg^{2+}/Li^{+} -dual salt-containing gel-polymer-electrolytes for rechargeable magnesium batteries”.

Publication

P. Wang, J. Trück, J. Häcker, A. Schlosser, K. Küster, U. Starke, L. Reinders, M. R. Buchmeiser, *Energy Storage Mater.* **2022**, 49, 509-517.

Author Contributions: Peiwen Wang: Conceptualization; Data curation; Formal analysis; Investigation; Methodology; Roles/Writing - original draft; Writing - review & editing; Janina Trück: Resources; Joachim Häcker: Resources; Writing - review & editing; Anja Schlosser: Methodology; Resources; Writing - review & editing; Kathrin Küster: Methodology; Writing - review & editing; Ulrich Starke: Methodology; Writing - review & editing; Leonie Reinders: Methodology; Writing - review & editing; Michael R. Buchmeiser: Funding acquisition; Project administration; Supervision; Validation; Writing - review & editing

Reprinted with permission from the © 2022 Elsevier Ltd.



Contents lists available at ScienceDirect

Energy Storage Materials

journal homepage: www.elsevier.com/locate/ensm

A design concept for halogen-free $\text{Mg}^{2+}/\text{Li}^+$ -dual salt-containing gel-polymer-electrolytes for rechargeable magnesium batteries

Peiwen Wang^a, Janina Trück^{a,c}, Joachim Häcker^d, Anja Schlosser^e, Kathrin Küster^f, Ulrich Starke^f, Leonie Reinders^b, Michael R. Buchmeiser^{a,b,*}

^a Institute of Polymer Chemistry, University of Stuttgart, 70569, Stuttgart, Germany

^b German Institutes of Textile and Fiber Research (DITF), 73770 Denkendorf, Germany

^c Dainler AG, 70327 Stuttgart, Germany

^d Institute of Engineering Thermodynamics, German Aerospace Center, 70569 Stuttgart, Germany

^e Customcells Holding GmbH, 25524 Itzehoe, Germany

^f Max Planck Institute for Solid State Research, 70569 Stuttgart, Germany

ARTICLE INFO

Key words:

gel polymer electrolyte

in-situ crosslinking

halogen free

room-temperature magnesium-sulfur/ion batteries

ABSTRACT

Polymer-based electrolytes can greatly promote the development of rechargeable metal-sulfur batteries owing to the improved safety and high flexibility; however, liquid electrolytes, which are mostly investigated so far, often hinder practical application due to the severe shuttling effect and possible leakage of the electrolytes. Herein, a new cell design is presented, that bridges the gap between lab cells and application by a novel halogen-free gel-polymer-electrolyte (GPE) with outstanding electrochemical performance. The GPE was prepared *via an in-situ* crosslinking reaction between lithium/magnesium borohydrides and poly(tetrahydrofuran). This GPE displays outstanding ionic conductivities in a wide temperature range, superior polarization behavior, remarkable reversibility and more strikingly, excellent compatibility with different sulfur containing and intercalation cathodes: S_8 @activated carbon cloth (ACC/S), sulfur poly(acrylonitrile) (SPAN) composite, titanium disulfide, Chevrel phase Mo_6S_8 and lithium titanate. The effective suppression of the ‘polysulfide shuttle’ by the GPE allows for a stable cycling of $\text{Mg}|\text{SPAN}$ and $\text{Mg}|\text{ACC/S}$ cells at room temperature with high discharge capacities (600 and 420 $\text{mAh}\cdot\text{g}_s^{-1}$ after 140 and 50 cycles, respectively). Remarkably, the $\text{Mg}|\text{GPE}|\text{SPAN}$ system features low self-discharge, excellent flexibility and safety characteristics, which significantly improve the possibility for practical applications.

1. Introduction

Current electric energy storage technology in electric vehicles is mostly based on lithium-ion batteries. However, considering both safety issues and the limited resources of raw materials for lithium batteries, rechargeable magnesium batteries have received considerable attention as a viable alternative by virtue of their improved safety and high earth-abundance of the electrode material [1]. Growing attention has recently been devoted to Mg-S batteries owing to the low toxicity and the high theoretical volumetric energy density ($3200 \text{ Wh}\cdot\text{L}^{-1}$) [2–4]. Several prototypes of Mg-S cells have been developed to prove the concept; however, they are still suffering from some critical issues.

In the reported prototypes, sulfur is generally directly adopted by either physical adsorption (e.g. sulfur@multiporous carbon [5],

sulfur@activated carbon cloth (ACC/S) [6]) or covalently bound to the carbon backbone (e.g. sulfur@poly(acrylonitrile) (SPAN) [7–9]). Using bulk sulfur-based cathodes generally results in the loss of active materials, self-discharge and severe polysulfide shuttle [8, 10]. Complementary, several groups reported on the use of SPAN-based cathodes in Mg batteries. Similar to lithium-sulfur batteries, the different sulfur species occurring can be better controlled due to the covalently bound sulfur in the carbon matrix [7–9, 11]. The development of electrolytes so far still focused on liquid systems, such as the halogen-containing magnesium aluminum chloride complex (MACC) or magnesium tetraakis(hexafluoroisopropoxy) ($\text{Mg}[\text{B}(\text{hfp})_4]_2$) electrolytes [6, 12, 13]. Here, for the first time, the polysulfide shuttle as well as cell leakage and safety problems can be greatly reduced by the combination of SPAN with a halogen-free quasi-solid-state $\text{Mg}^{2+}/\text{Li}^+$ dual salt electrolyte system.

* Corresponding author.

E-mail address: michael.buchmeiser@ipoc.uni-stuttgart.de (M.R. Buchmeiser).

<https://doi.org/10.1016/j.ensm.2022.04.034>

Received 9 February 2022; Received in revised form 12 April 2022; Accepted 20 April 2022

Available online 22 April 2022

2405-8297/© 2022 Elsevier B.V. All rights reserved.

Mg-S cells are in general suffering from the polysulfide shuttle, and poor safety, especially in the combination with conventional bulk sulfur-based cathodes. One attractive way to reduce the polysulfide shuttle that has already been employed in Li-S batteries entails the use of gel polymer electrolytes (GPEs), by which the diffusion of the polysulfides is hindered and the anode is consequently protected [14]. Apart from polysulfide suppression, GPE also reduces the risk of internal short circuits and electrolyte leakage, which greatly improve the safety of this type of cells [15]. Furthermore, GPEs exhibit a high ion conductivity, especially compared to all-solid state electrolytes [3]. Nonetheless, the application of the concept of GPEs in Mg-S batteries is highly recommended, but rarely investigated so far.

Herein, we present a halogen-free $\text{Mg}^{2+}/\text{Li}^+$ dual-salt borate-based gel polymer electrolyte for Mg batteries, showing high ionic conductivities for a wide operating temperature range and superior electrochemical performance. Most important, the developed electrolyte is compatible with not only different intercalation cathodes, but also various types of sulfur-based cathodes. The electrolyte is prepared via a straightforward *in-situ* crosslinking reaction between lithium and magnesium borohydrides and poly(tetrahydrofuran) (PTHF) with TiO_2 nanoparticles as additive, using a glass fiber separator as mechanically stable support (magnesium/lithium/ TiO_2 GPE, referred to *MLT-GPE*). This electrolyte exhibits superior compatibility with Mg anodes and shows negligible overpotential (<0.06 V) over more than 1100 cycles. The successful suppression of the polysulfide shuttle by the MLT-GPE allows for a stable room/low temperature cycling of $\text{Mg}||\text{MLT-GPE}||\text{SPAN}$ and $\text{Mg}||\text{MLT-GPE}||\text{ACC/S}$ cells with approx. $600 \text{ mAh} \cdot \text{g}_s^{-1}$ and $420 \text{ mAh} \cdot \text{g}_s^{-1}$, respectively. More important, the $\text{Mg}||\text{MLT-GPE}||\text{SPAN}$ system shows low self-discharge, excellent flexibility and greatly

improved safety issues. Additionally, the MLT-GPE is also well compatible with various intercalation cathodes at ambient temperature, like $\text{Mg}||\text{MLT-GPE}||\text{Mo}_6\text{S}_8$, $\text{Mg}||\text{MLT-GPE}||\text{TiS}_2$ and $\text{Mg}||\text{MLT-GPE}||\text{LTO}$ ($\text{Li}_4\text{Ti}_5\text{O}_{12}$) cells, which all show excellent cycle stability and high discharge capacities.

2. Results and discussion

2.1. Characterization of the MLT-GPE

For the successful realization of the halogen-free GPE, we took advantage of the high basicity of borohydrides, which allows for a crosslinking reaction with the hydroxyl group in poly(tetrahydrofuran) (PTHF) [15]. More important, the utilization of a $\text{Mg}^{2+}/\text{Li}^+$ dual salt electrolyte in a Mg battery has not only been shown to greatly improve the kinetics of the bivalent Mg^{2+} ions, but also to reduce the passivation of the Mg anode from the sulfur species in a sulfur battery, especially short-chain polysulfides, which have been studied in detail previously [8, 9, 16]. Furthermore, it has been reported that the addition of nano-sized TiO_2 particles can significantly improve the ionic conductivity and mechanical properties of the Mg solid-state electrolyte [17, 18]. Moreover, the formed polysulfide species in sulfur batteries are reported to be successfully trapped by nano-sized TiO_2 . Consequently, a better capacity retention and a protected anode can be achieved [17, 18]. We therefore designed a reaction system based on $\text{Mg}[\text{BH}_4]_2$, Li $[\text{BH}_4]$, TiO_2 and PTHF, which reacts *in-situ* in a glass fiber separator, resulting in a gel-like electrolyte (Figure 1a). Also, due to the evolution of hydrogen, a porous structure forms (Fig. 1b), which possesses a different morphology than the pristine glass fiber separator (Fig. S1a).

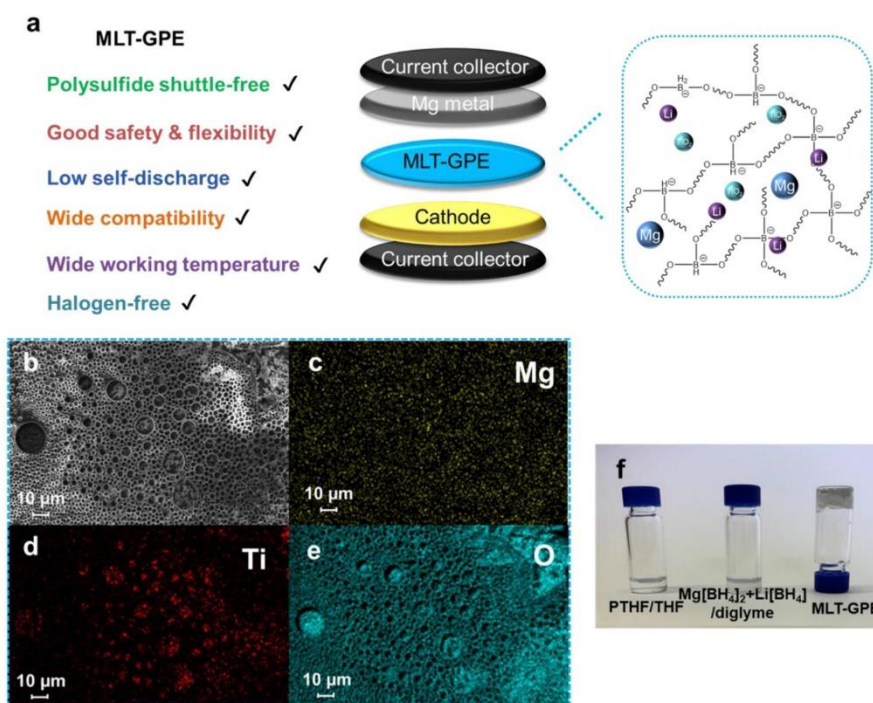


Fig. 1. a) Drawing of a magnesium cell with the crosslinked MLT-GPE; b-e) SEM image and elemental mappings of the MLT-GPE; f) photographs of the PTHF/THF solution (left), $\text{Mg}[\text{BH}_4]_2 + \text{Li}[\text{BH}_4]$ / diglyme solution (middle) and MLT-GPE (right).

The bubbles inside the GPE are a result of the evolution of hydrogen and might have an influence on the properties of the MLT-GPE; hence control over the amount and distribution of the bubbles is important. Indeed, the bubbles might be removed by the application of low vacuum during synthesis. In addition, elemental mapping of the MLT-GPE (Fig. 1c–1e) confirms that all the elements are homogeneously distributed. For clarity, the components of the pristine glass fiber separator (Na, Si) have been neglected. Fig. 1f clearly demonstrates that the liquid hybrid borohydride electrolyte (middle) reacts with the liquid PTHF/THF solution (left), resulting in the immobilized GPE (right). This was additionally confirmed by the cross-section scanning electron microscopy (SEM) images of the MLT-GPE (Fig. S1b, S.I.), where the glass fiber skeletons are thoroughly infiltrated by the cross-linked GPE and become

almost invisible. Further on, thermal stability analysis (Fig. S2, S.I.) indicates good thermal stability of the MLT-GPE, which could be attributed to the crosslinked polymer network [15].

Ionic conductivity is an important parameter to evaluate the feasibility and efficiency of a solid-state electrolyte, since it can quantify the ion mobility inside the electrolyte. The ionic conductivities of the MLT-GPE were measured in a temperature range of 0 °C to 40 °C using electrochemical impedance spectroscopy (EIS) employing an MLT-GPE sandwiched between two stainless steel (SS) plates. The Nyquist plot (Fig. 2a) shows straight lines without semi-circles in the high frequency range. This indicates that only ions are the current carrier and the obtained conductivity is based solely on ion conductivity, which has also been observed in other solid-state batteries [19–21]. This could be

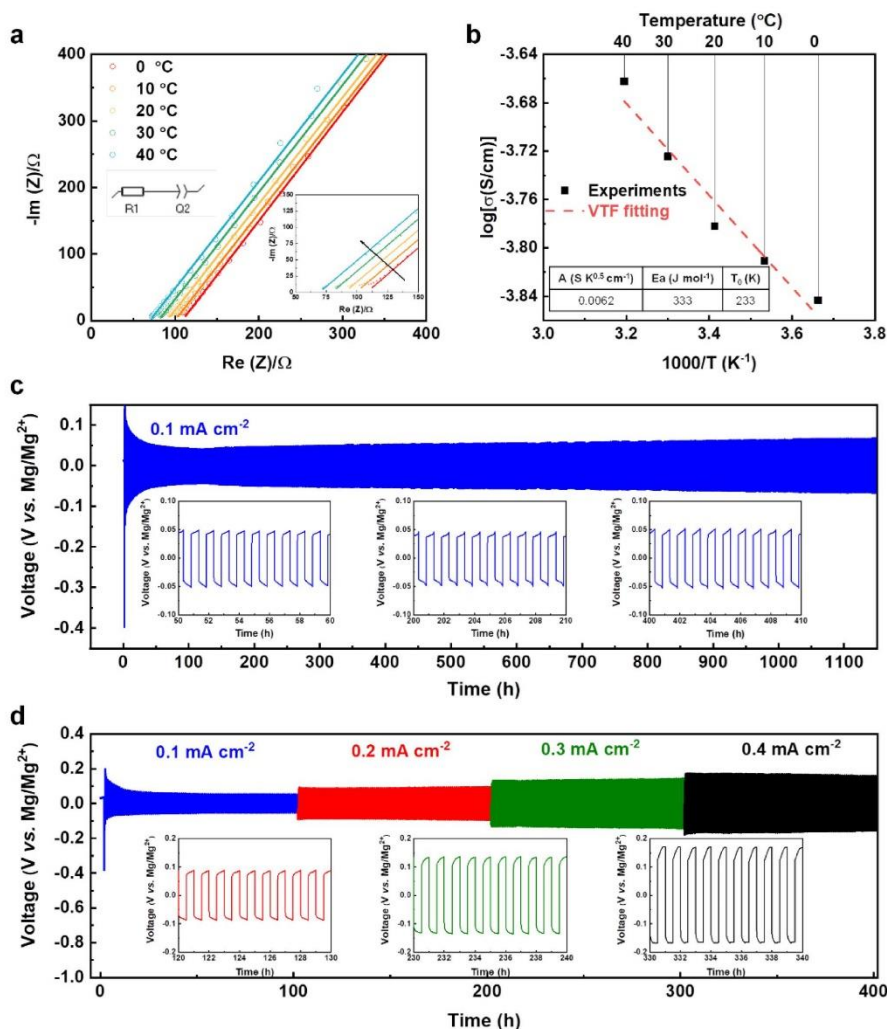


Fig. 2. a) Nyquist plots of SS||MLT-GPE||SS at various temperatures; dots: measured values; lines: fitted values (by the inset model); b) temperature-dependent ionic conductivity for MLT-GPE; c) long-term galvanostatic cycling of a Mg||MLT-GPE||Mg symmetric cell at a current density of 0.1 mA cm⁻²; d) galvanostatic cycling test of a Mg||MLT-GPE||Mg symmetric cell at various current densities.

attributed to the low glass transition temperature (T_g) of the MLT-GPE (9°C), which ensures a high mobility of the polymer segments and fast relaxation at the high frequency region [20]. The Nyquist plots were fitted using the equivalent circuit model shown in the inset of Fig. 2a; the corresponding fitted values are listed in Table S1. The ionic conductivity increased from $0.15 \text{ mS}\cdot\text{cm}^{-1}$ to $0.22 \text{ mS}\cdot\text{cm}^{-1}$ when the temperature was increased from 0°C to 40°C. In addition, the temperature-dependent ionic conductivity follows the Vogel-Tammann-Fulcher (VTF) empirical equation (Eq. (1)) [22]:

$$\sigma = AT^{-0.5} \exp\left[\frac{-E_a}{R(T-T_0)}\right] \quad (1)$$

where A is the pre-factor of the ionic conductivity; E_a is the activation energy which is related to the mobility of the polymer chains; T_0 is the temperature which is normally 10 K to 50 K below T_g of the polymer; R is the ideal gas constant [15]. The parameters according to the VTF fitting are listed in the inset of Fig. 2b. The super-low activation energy ($0.333 \text{ kJ}\cdot\text{mol}^{-1}$) indicates a low energy barrier for the movements of the cations. The calculated T_0 is 233 K, which is 49 K below the T_g (282 K).

In addition, symmetric Mg||Mg cells with MLT-GPE were fabricated to investigate the polarization behavior (Fig. 2c and 2d). Fig. 2c shows that the MLT-GPE exhibits an extremely low overpotential ($< 0.06 \text{ V}$) and very good long-term cycling durability (> 1100 cycles) at room temperature. The polarization behavior of the MLT-GPE at higher/different current densities was also evaluated (Fig. 2d) by a Mg||Mg cell. When the current density was successively increased from $0.1 \text{ mA}\cdot\text{cm}^{-2}$ to $0.4 \text{ mA}\cdot\text{cm}^{-2}$, the overpotential of the MLT-GPE did not exceed 0.2 V , confirming the excellent polarization behavior of the MLT-GPE. Additionally, the enlarged potential curves shown in the insets of Fig. 2c, 2d generally show flat features, indicating a smooth Mg plating and stripping. Noticeably, a high overpotential of ca. -0.4 V can be observed in the initial few cycles, followed by a substantial decrease over cycling, which has also been observed in the cases of many liquid magnesium electrolytes [6–8]. To understand this phenomenon, EIS analysis was applied for the Mg||MLT-GPE||Mg symmetric cell before and after cycling (Fig. S3, S.I.). A well-defined semi-circle was observed in the high frequency region after cycling, indicating that an equilibrium state and a perfect contact between the MLT-GPE and the Mg metal have been reached [21]. More important, a sharp decrease of the interfacial resistance after cycling was recorded. Obviously, the adsorption layer and the intrinsic oxide layer on the Mg surface that cause the initial high overpotential, were reduced through the Mg plating and stripping.

Next, the influence of TiO_2 nanoparticles on the electrochemical performance was examined. At first, the ionic conductivity of the GPE without TiO_2 was determined using the same method as for the MLT-GPE (Fig. S4 and Table S2, S.I.). Upon the addition of 10 wt% of TiO_2 nanoparticles, the ionic conductivity increased by one order of magnitude at all temperatures, which is in line with previous studies [17, 18]. Additionally, the magnesium plating/stripping behavior of the GPE with and without TiO_2 nanoparticles was compared using symmetric Mg||Mg and Mg||stainless steel (SS) cells, respectively (Figure S5, Figure S6, S.I.). Addition of the TiO_2 nanoparticles substantially decreased the overpotential from 0.15 V to 0.05 V and increased the oxidative peak current. In view of the positive influence of TiO_2 nanoparticles on electrochemical performance, the following studies focused on GPEs containing 10 wt.% TiO_2 .

The oxidative stability of the MLT-GPE was tested with different current collectors by linear sweep voltammetry (LSV, Fig. S7a, S.I.). The MLT-GPE was stable up to 3.5 V on the standard SS current collector, which was further applied as the current collector for the cathode materials. In addition, the reversibility of the MLT-GPE was examined by plating/stripping of Mg on the SS substrate. Fig. S7b (S.I.) displays the cyclic voltammetry (CV) curves between -1 V to 2 V , showing almost overlapping curves from the initial cycle. Furthermore, the Coulombic efficiency of the MLT-GPE was determined (Fig. S7c, S.I.) and turned out

to be stable at $\sim 99.8\%$. Also, the transference number of Mg^{2+} in a pure magnesium electrolyte was measured by EIS (Fig. S8 and Table S3, S.I.), revealing a good transference number of 0.5 [23].

2.2. Mg-SPAN battery performance with the MLT-GPE

To examine the electrochemical performance of the Mg-S batteries, SPAN was first selected as cathode material to test its compatibility with the MLT-GPE, because SPAN (see Fig. 3b inset) has been reported to show good capacity retention in magnesium batteries due to its covalently bound sulfur, which in turn can be well immobilized in the cathode [8, 11]. The SPAN cathodes, comprising SPAN active material, a conventional binder PVDF and conductive carbon black, were analyzed by SEM and elemental mapping (Fig. S9, S.I.), showing good homogeneity. The SPAN cathode was then applied in a Swagelok-type cell together with a polished Mg foil and the MLT-GPE. The Mg||MLT-GPE||SPAN cell was charged and discharged at 0.2 C at 22°C for long-term cycling testing ($1 \text{ C} = 1672 \text{ mA}\cdot\text{g}_s^{-1}$, Fig. 3a, voltage curves in Fig. S10, S.I.). The cell delivered an initial discharge capacity of $908 \text{ mAh}\cdot\text{g}_s^{-1}$ and showed a slight capacity decay within the initial 10 cycles (ca. $750 \text{ mAh}\cdot\text{g}_s^{-1}$ at the 10^{th} cycle). After that, the cell cycled stable for another 130 cycles, with only 0.1% capacity decay per cycle, indicating superior capacity retention (ca. $580 \text{ mAh}\cdot\text{g}_s^{-1}$ at 140^{th} cycle). These values are so far unprecedented in a quasi-solid-state Mg-S battery, even compared to current state of the art Mg batteries based on liquid electrolytes (Table S4, S.I.) [2, 24]. Generally, the capacity contribution from the MLT-GPE is believed to be negligible. In order to verify this, a cell with a Mg anode, an SS current collector as cathode and MLT-GPE as the electrolyte was cycled using the same electrochemical conditions as the previous Mg||SPAN cells (Fig. S7d, S.I.), showing indeed negligible discharge/charge capacities ($< 1 \text{ mAh}\cdot\text{g}^{-1}$). Also, CV curves of the Mg||MLT-GPE||SS cell in Fig. S7d (S.I.) inset do not show any redox peaks in the applied voltage window. Based on these investigations, one can conclude that the capacities from the Mg||MLT-GPE||SPAN cells solely stem from SPAN, but not from the electrolyte.

The cell resistance of the Mg||MLT-GPE||SPAN cell after each cycle at the charged state was also recorded *in-situ*. The corresponding Nyquist plot and the fitted values are shown in Fig. S11 and Table S5, S.I., respectively. The bulk resistance (R_1) in the high frequency region increased slightly, which can be attributed to the formation and dissolution/accumulation of magnesium polysulfides on the MLT-GPE. However, the resistance of the solid electrolyte interphase (SEI) layer (R_2) at the middle frequency range stayed almost constant and low during cycling, indicating the formation of a stable SEI layer on the Mg surface. This implies that the formed sulfide species do not passivate or interact with the Mg metal anode but are instead blocked by the MLT-GPE, leading to a ‘polysulfide shuttle-free’ system. A comparison of the cycling performance of Mg||SPAN cells using the MLT-GPE and the liquid electrolyte, respectively (Fig. S12, S.I.), revealed that with the liquid electrolyte ($0.1 \text{ M Mg}[\text{BH}_4]_2$, $1.5 \text{ M Li}[\text{BH}_4]$, $10 \text{ wt}\%$ TiO_2 in diglyme), the cell showed high discharge capacities ($\sim 1150 \text{ mAh}\cdot\text{g}_s^{-1}$) in the initial three cycles, implying better sulfur utilization due to the liquid electrolyte. However, the discharge capacity sharply decreased to only $\sim 450 \text{ mAh}\cdot\text{g}_s^{-1}$ in the 50^{th} cycle, indicating poorer sulfur addressability and capacity retention compared to cells based on the MLT-GPE. These findings again confirm the successful suppression of the polysulfide shuttle by the MLT-GPE.

In addition, the aged Mg anode removed from the MLT-GPE electrolyte after 10 cycles was investigated by *ex-situ* X-ray photoelectron spectroscopy (XPS, Fig. 3e and f). On the aged Mg anode, a thin layer consisting of several sulfur species was identified in the S 2p spectra. Apart from a sulfone species ($\sim 169 \text{ eV}$), only magnesium polysulfides (MgS_x) ($\sim 163.6 \text{ eV}$) were detected. These magnesium polysulfides originate most likely from the residual GPE, which is hard to remove due to its gel-like structure. Notably, no MgS , which is the major harmful species leading to the shuttle effect since it is hard to be re-oxidized

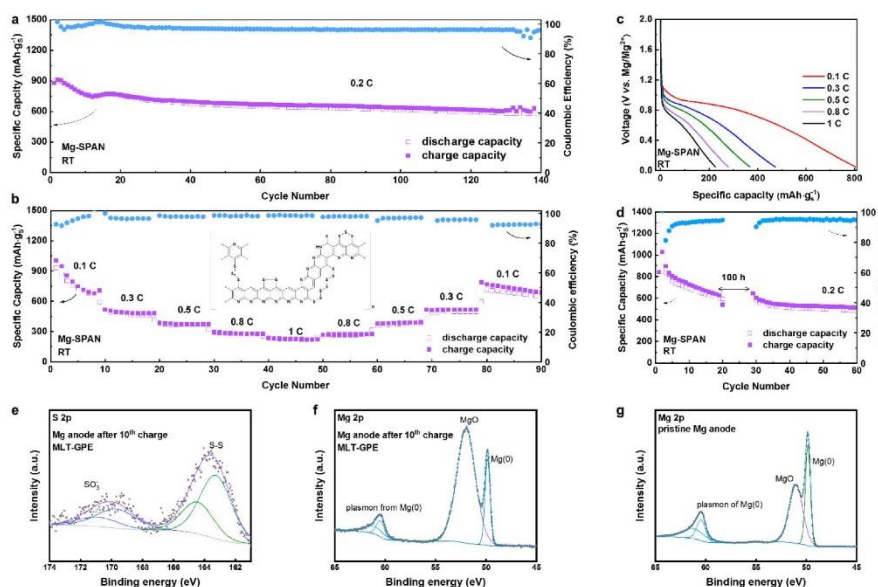


Fig. 3. a–d) Electrochemical characterization of a Mg||MLT-GPE||SPAN cell at room temperature (RT, 22°C); a) long-term galvanostatic cycling (charging/discharging at 0.2 C); b) rate capability test from 0.1 C to 1 C; inset: chemical structure of SPAN; c) corresponding potential curves at different current densities; d) self-discharge analysis of the Mg||MLT-GPE||SPAN cell; e) S 2p XPS spectra of a cycled Mg anode; f) Mg 2p XPS spectra of an aged Mg anode after 10 cycles in the charged state using an MLT-GPE electrolyte; g) Mg 2p XPS spectra of a pristine Mg anode.

during charging [16, 25], was found on the aged Mg anode at ~ 160 eV [9]. The absence of MgS on the aged Mg anode strongly suggests that the Mg anode is well protected, which helps in the successful suppression of the shuttle effect by the MLT-GPE [9].

According to our previous study, the addition of a lithium salt to a magnesium electrolyte can significantly improve the redox kinetics, increase the solubility of the magnesium (poly)sulfides by lithiation and reduce the passivation of the Mg anode [9]. At the same time, it is important to know whether lithium species join the redox reaction. To obtain more direct chemical proof of the redox chemistry, *ex-situ* XPS was applied to both, pristine and aged Mg anodes. Fig. 3f and g shows the XPS spectra of an aged Mg anode cycled in the MLT-GPE electrolyte in the charged state and of a pristine Mg anode. Both spectra show similar features; Mg(O) and MgO species can be detected at approx. 49.8 eV and 51 eV, respectively. Importantly, no peaks were found at about 55.3 eV, where the Li 1s signal would be expected [9]. This indicates that no lithium species, especially lithium metal, are formed during cycling. Consequently, the entire redox process is solely governed by the Mg chemistry, which is in line with results reported for Mg batteries using Li-containing liquid electrolytes [8, 9, 16, 26]. Due to the strong physical interaction between the MLT-GPE and the SPAN cathode coating, *post-mortem* analysis of the SPAN cathode could not be conducted.

Next, the rate capability of the Mg||MLT-GPE||SPAN cell was also evaluated by charging and discharging the cell at different current rates at room temperature. As depicted in Fig. 3b, the battery delivered a capacity of ca. 800, 480, 380, 290 and 230 $\text{mAh}\cdot\text{g}_s^{-1}$ at current rates of 0.1, 0.3, 0.5, 0.8 and 1 C, respectively. The capacity successfully reversed back when the current rate decreased, demonstrating the superior rate capability of the Mg||MLT-GPE||SPAN system. Fig. 3c shows the discharge profile of a Mg||MLT-GPE||SPAN cell at various current rates. Only one smoothly sloped profile around 1 V instead of several plateaus in conventional bulk sulfur cells can be observed. This sloped

voltage profile is characteristic for SPAN cathodes and is in good agreement with the voltage profiles observed in solid-state Li-SPAN cells and liquid-state Mg-SPAN cells [7, 9, 27, 28].

Low temperature durability is another important factor for any practical use of a battery system. Thanks to the relatively high ionic conductivity of the MLT-GPE at low temperatures, the performance of the Mg||MLT-GPE||SPAN cell was also examined at 0°C. The cells stably delivered a considerably high discharge capacity of approx. 300 $\text{mAh}\cdot\text{g}_s^{-1}$ (Fig. S13a, S.I.). The rate capability of the Mg||MLT-GPE||SPAN cell was also investigated at 0°C, cycling between 0.1 C and 1 C (Fig. S13b, S.I.). Although the cell delivered lower discharge capacity at a higher current rate, which might be due to the lower diffusivity, the capacity was still able to return back when the current rate decreased, showing relatively good rate capability. These data illustrates the wide application temperatures of the Mg||MLT-GPE||SPAN cell.

Furthermore, CV measurements of the Mg||MLT-GPE||SPAN cell at different scan rates (Fig. S14a, S.I.) revealed one distinct oxidation peak starting from 1.4 V and one reduction peak starting from 1.1 V. The redox peak positions are in good agreement with the voltage plateaus in Fig. 3c, indicating the redox reactions between SPAN and lower-order poly(sulfides). Also, the current densities of the redox peaks increase linearly with an increasing scan rate in a double logarithmic diagram (Fig. S14b, S.I.), indicating that both redox reactions are diffusion-controlled and not surface-limited adsorption processes [29].

The extent of self-discharging is another crucial feature in the evaluation of energy-storage devices, especially with sulfur batteries using ether-based electrolytes, such as DME or diglyme [30]. The extent of self-discharge of the Mg||MLT-GPE||SPAN cell was investigated by resting the cell in the fully charged state after 20 cycles for 100 hours (Fig. 3d). After 100 hour resting time, the cell still stably delivered ca. 580 $\text{mAh}\cdot\text{g}_s^{-1}$, showing negligible capacity decay, indicating the absence of any self-discharge.

Besides its electrochemical performance, safety is one of the most

important aspects of a battery system. In order to further examine the safety properties of the Mg||MLT-GPE||SPAN system, soft package Mg||MLT-GPE||SPAN (Pouch) cells were assembled and tested. In Fig. 4a, using two Mg||MLT-GPE||SPAN cells connected in series, a red light emitting diode (LED) light can be successfully lightened up. Moreover, the situation when the cells are under external mechanical force was examined by bending one or even both of the Pouch cell(s). As shown in Fig. 4b and in the video (Supporting Information), the LED is still successfully lightened with the same brightness, indicating the excellent flexibility of the Mg||MLT-GPE||SPAN pouch cells.

Further on, the soft-package cell was half-cut, as shown in Fig. 4c. The cell was still capable of powering the LED light, illustrating that cutting does not lead to an internal-short circuit. Fig. 4d shows the cross-section of the cut Mg||MLT-GPE||SPAN cell, where a gel-like structure instead of liquid leakage can be observed. All of these experiments show that the Mg||MLT-GPE||SPAN batteries possess excellent safety characteristics.

2.3. Performance of Mg-sulfur/ion batteries with an MLT-GPE

The outstanding electrochemical performance of the Mg||MLT-GPE||SPAN cell encouraged us to further examine the polysulfide suppression effect of the MLT-GPE with a conventional elemental sulfur system. A binder-free cathode, i.e. sulfur@activated carbon cloth (ACC/S), which has already been applied in several metal-sulfur systems, was employed in a magnesium battery together with the MLT-GPE. The Mg||MLT-GPE||ACC/S cell was also cycled at 0.2 C at room temperature. As shown in Fig. 5a and Fig. S15a (S.I.), the cell delivered an initial discharge capacity of around $600 \text{ mAh}\cdot\text{g}_{\text{S}}^{-1}$ at 0.2 C. Strikingly, the cell then delivered an almost constant capacity of $420 \text{ mAh}\cdot\text{g}_{\text{S}}^{-1}$ for more than 50 cycles with >99% Coulombic efficiency. In sharp contrast, the Mg||ACC/S cell with the liquid electrolyte (0.1 M $\text{Mg}[\text{BH}_4]_2$, 1.5 M Li $[\text{BH}_4]$, 10 wt% TiO_2 in diglyme) delivered a higher initial discharge capacity ($\sim 800 \text{ mAh}\cdot\text{g}_{\text{S}}^{-1}$) due to a better sulfur utilization (Fig. 5b). However, from the third cycle on, the cell showed very poor Coulombic efficiency (<60%), caused by a severe polysulfide shuttling compared to the Mg||liquid electrolyte||SPAN system. Clearly, the SPAN structure retains sulfur much better than the free elemental sulfur system in a liquid electrolyte. Nonetheless, the MLT-GPE was capable of suppressing the polysulfide shuttle in a sulfur cell, resulting in a stable system with good capacity retention.

Intercalation cathode materials are also good candidates for rechargeable magnesium batteries beyond sulfur cathodes [31–33]. A feasible and practical electrolyte should show good electrochemical performance and also good compatibility with these electrodes. To verify the compatibility of the MLT-GPE with intercalation cathode materials, the MLT-GPE was also utilized in several types of intercalation cathodes, namely Chevrel phase Mo_6S_8 (Fig. S16, S.I.), TiS_2 and spinel $\text{Li}_4\text{Ti}_5\text{O}_{12}$ (LTO) cathodes. As shown in Fig. 5c and Fig. S17a (S.I.),

the Mg||MLT-GPE|| TiS_2 cell stably delivered $235 \text{ mAh}\cdot\text{g}^{-1}$ with approximately 98% Coulombic efficiency at 0.5 C at room temperature. (1 C = $239 \text{ mA}\cdot\text{g}^{-1}$) for 70 cycles, representing outstanding specific capacities and cycle stability. In the rate capability test, the cell delivered discharge capacities of 235, 205, 190, 180 $\text{mAh}\cdot\text{g}^{-1}$ at 0.5 C, 1 C, 2 C and 3 C, respectively (Fig. 5d and Fig. S17b, S.I.). The capacity fully recovered when the current rate decreased, demonstrating the good rate capability of the system. The corresponding voltage profiles and the CV curves (Fig. S17c, S.I.) show two distinct plateaus at 1.4 V and 0.9 V during discharge, indicating the stepwise intercalation of Mg into the TiS_2 lattice. The observed plateaus are in line with the reported Mg- TiS_2 cells with the liquid all phenyl complex (APC) electrolyte characterized via *in-situ* methods [31]. Overall, excellent compatibility of the MLT-GPE with the insertion cathodes was observed.

As a step further, spinel $\text{Li}_4\text{Ti}_5\text{O}_{12}$ (LTO), which is known as a “zero-strain” ion insertion-type anode material for the full cell applications, was utilized as electrode material together with Mg metal and the MLT-GPE to examine its possible application for Mg full cells [34, 35]. Fig. 5e displays the Mg||MLT-GPE||LTO cell cycled at 0.2 C (1 C = $175 \text{ mAh}\cdot\text{g}_{\text{LTO}}^{-1}$) at room temperature. The discharge capacity increased from 80 to $120 \text{ mAh}\cdot\text{g}_{\text{LTO}}^{-1}$ over the initial 10 cycles and stayed almost constant during the following 60 cycles with 99.5% Coulombic efficiency, resulting in ca. $100 \text{ mAh}\cdot\text{g}_{\text{LTO}}^{-1}$ at the 70th cycle. The increase in capacity during the initial cycles is attributed to the decrease of polarization over cycling, as can be deduced from the corresponding voltage profiles (Fig. S18a, S.I.) and the CV curves (Fig. S18c, S.I.). Additionally, the Mg||MLT-GPE||LTO cell delivered 110, 105, 85, 70 $\text{mAh}\cdot\text{g}_{\text{LTO}}^{-1}$ at 0.2, 0.5, 1 and 2 C, respectively (Fig. 5f). The capacity also fully recovered with a decreasing current rate, indicating outstanding rate capability of the system. The potential curves of the cell (Fig. S18a,b, S.I.) display distinct plateaus at 0.8 V and 0.9 V during discharge and charge, respectively, which show very similar characteristic with the Mg||LTO system based on a lithium-containing liquid electrolyte [34]. The role of the lithium salt in a magnesium electrolyte for the applications of magnesium ion batteries was discussed already in several publications [26, 33, 34]. To date it is assumed that reversible magnesium plating/stripping takes only place at the anode side due to the thermodynamic redox potential difference between Mg^{2+}/Mg and Li^+/Li in a $\text{Mg}^{2+}/\text{Li}^+$ hybrid electrolyte [33, 34].

3. Experimental Section

3.1. Chemicals

All samples were handled inside an Ar-filled glovebox with H_2O and O_2 levels ≤ 0.1 ppm. All cells were fabricated in the same glovebox. Glassware was dried in an oven at 120°C . Magnesium borohydride ($\text{Mg}[\text{BH}_4]_2$, 95%), lithium borohydride ($\text{Li}[\text{BH}_4]$, >95%), anhydrous diethylene glycol dimethyl ether (diglyme, 99.5%), poly(tetrahydrofuran)

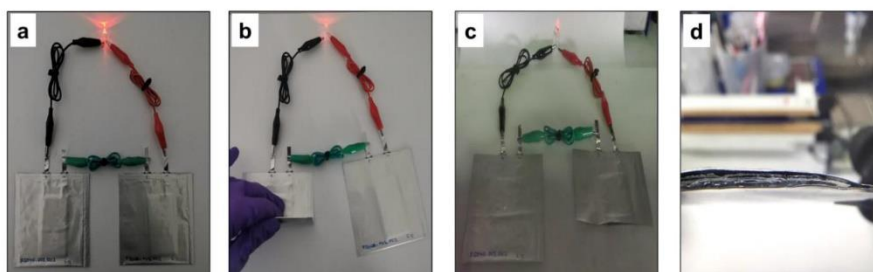


Fig. 4. a-d) Illustrations of two soft-package Mg||MLT-GPE||SPAN cells connected in series at room temperature a) at normal conditions; b) under bending conditions; c) after cutting one cell; d) cross-section of the cut soft package cell.

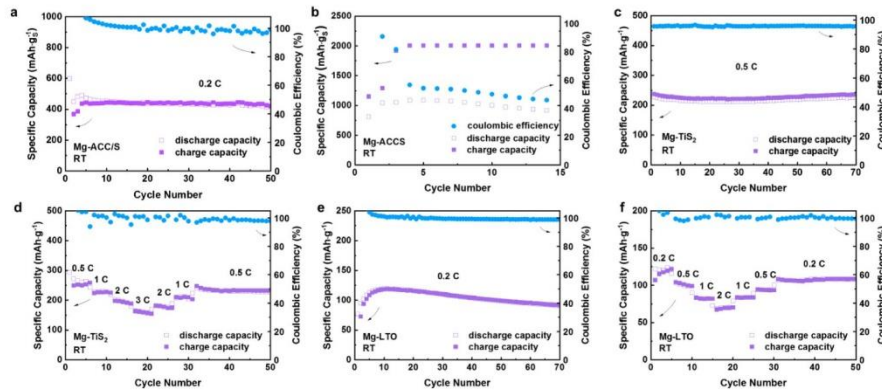


Fig. 5. Compatibility of the MLT-GPE with bulk sulfur-based and intercalation cathodes: **a)** long-term cycling stability test of Mg||MLT-GPE||ACC/S cell at room temperature, charging/discharging at 0.2 C; **b)** long-term cycling stability test of Mg||liquid electrolyte||ACC/S cell at room temperature, charging/discharging at 0.2 C; **c)** cycle stability test of Mg||MLT-GPE||TiS₂ cells, charge/discharge at 0.5 C (1 C = 239 mA·g⁻¹); **d)** rate capability test Mg||MLT-GPE||TiS₂ cells from 0.5 C to 3 C; **e)** cycle stability test of Mg||MLT-GPE||LTO cells, charge/discharge at 0.2 C (1 C = 175 mA·g⁻¹); **f)** rate capability test of Mg||MLT-GPE||LTO cells from 0.5 C to 3 C. All the cells were characterized at room temperature (22°C).

(PTHF, Mn~2900 g/mol), titanium dioxide nanopowder (21 nm, >99.5% trace metals basis), titanium disulfide (TiS₂), lithium titanate (LTO) and poly(acrylonitrile) (PAN, Mn=36,500 g/mol, \bar{D} =3.6) were purchased from Merck and used as received. Chevrel phase Mo₆S₈ was purchased from NEI Corporation and used as received. Anhydrous tetrahydrofuran (THF) was obtained from Solvent Purification System. Magnesium foils (0.25 mm, 99.9%, Advent Research Materials) were punched into chips 12 mm in diameter and thoroughly scratched with a ceramic knife before use. Glass fiber separators (Whatman, GF/C) were punched into chips 13 mm in diameter and dried at 120°C under vacuum for 40 h.

3.2. Preparation of electrolytes

0.1 M Mg[BH₄]₂ and 1.5 M Li[BH₄] solutions in diglyme were prepared inside an Ar-filled glovebox. The preparation method follows our previous reports [8], where the use of this specific salt ratio showed the best electrochemical performance. After one day of stirring, 10 wt% of TiO₂ was added; the mixture is referred to as *MLT/diglyme*. 1 g PTHF was then dissolved in 5 mL THF, the solution is referred to as *PTHF/THF*. The gel polymer electrolyte, referred to as MLT-GPE, was synthesized by the *in-situ* crosslinking reaction between MLT/diglyme and PTHF/THF inside the glass fiber separator. The glass fiber separator was used as mechanical reinforcement. In detail, 45 μ L MLT/diglyme and 45 μ L PTHF/THF were pipetted to one piece of glass fiber separator. Based on the components in the above synthesis, the molar quantities of Mg [BH₄]₂, Li[BH₄], and the -CH₂-CH₂-CH₂-CH₂-O- unit from PTHF were 0.0045 mmol, 0.0675 mmol and 0.625 mmol, respectively.

3.3. Preparation of various cathodes

Sulfurized poly(acrylonitrile) composite (SPAN) was synthesized according to the literature [7, 8]. SPAN cathodes were prepared by mixing 70 wt% SPAN powders, 15 wt% super C65 carbon black and 15 wt% poly(vinylidene fluoride) (PVDF) in 1-methyl-2-pyrrolidinone at 2,000 rpm for 6 minutes with a mixer (Thinky). The obtained slurry was then casted onto a stainless-steel foil with a wet thickness of 300 μ m. The coating was dried in an oven at 60°C for 24 h. Cathodes were punched into chips 12 mm in diameter. The average sulfur content was around 0.7~1 mg/cm².

For the ACC/S cathode preparation, activated carbon cloth (ACC

507-20, Kynol) was cut in electrodes with 12 mm diameter and dried at 120°C in vacuum for 12 h. In an argon-filled glovebox (O₂ < 1 ppm, H₂O < 1 ppm), sulfur powder (99.5 %, Alfa Aesar) was distributed on the ACC surface (approx. 1.6 mg/cm²) and melt infiltrated into the microporous carbon at 155°C for 24 h applying an autoclave vessel. Subsequently, the infiltrated ACC/S cathodes were placed in a glass tube under argon atmosphere and transferred to a tubular furnace to evaporate residual sulfur from the carbon surface at 330°C for 3 h (5 K/min heating rate). Thus, ACC/S cathodes with a sulfur loading of approx. 0.6 mg/cm² result.

TiS₂ insertion cathodes, LTO cathodes and Chevrel phase Mo₆S₈ cathodes were prepared by mixing the active material, super C65 carbon black and poly(vinylidene fluoride) (PVDF) in 1-methyl-2-pyrrolidinone in a weight ratio of 70:15:15, 80:10:10 and 70:15:15, respectively. The slurry was mixed at 2,000 rpm for 6 minutes with a mixer (Thinky) and then casted onto a stainless-steel current collector with a wet thickness of 200 μ m, 300 μ m and 300 μ m, respectively. The coating was dried in an oven at 60°C for at least 24 h. Cathodes were punched into chips 12 mm in diameter. The active material per cathode was around 2 mg, 2 mg and 7.4 mg, respectively.

3.4. Electrochemical measurements

The ionic conductivity of the MLT-GPE was measured by electrochemical impedance spectroscopy on a Biologic VMP-3. The MLT-GPE was sandwiched between two stainless steel electrodes in a Swagelok-type cell. The impedance was recorded in a frequency range between 100 kHz and 100 mHz at different temperatures (0°C to 40°C). The ionic conductivity was calculated by the equation 2:

$$\sigma = \frac{l}{SR} \quad (2)$$

where σ is the ionic conductivity (S/cm); l is the thickness of the MLT-GPE; S is the area of the stainless-steel disc; R is the resistance obtained from the impedance measurement.

The stability of the MLT-GPE was determined by Linear Sweep Voltammetry (LSV) using a Biologic VMP-3. A two-electrode cell with stainless steel foil/graphite foil/platinum foil and Mg foil as electrodes and MLT-GPE as electrolyte was employed and swept at 5 mV/s.

Cyclic Voltammetry (CV) was measured on a Biologic VMP-3 using two-electrode or three-electrode cells comprising stainless steel or SPAN

as working electrodes, freshly polished Mg foil as counter and reference electrodes and MLT-GPE as electrolyte. Scan rates between 0.2 mV/s and 0.8 mV/s were applied.

The electrochemical performance of Mg-S batteries and Mg-ion batteries was evaluated by Swagelok-Type cells comprising the respective cathode material, a freshly scratched Mg foil as anode and MLT-GPE as electrolyte. When preparing the cell, 45 μ L MLT/diglyme and 45 μ L PTHF/THF were consecutively added to the glass fiber disc. All the cells were allowed to rest for at least 3 hours before testing.

The flexibility and safety of the Mg||MLT-GPE||SPAN system were evaluated with the aid of pouch cells. For their assembly, cathodes ($31 \times 56 \text{ mm}^2$) and anodes ($32.5 \times 57 \text{ mm}^2$) of the specified size were obtained by die-cutting. Afterwards, Al tabs (AME energy) were connected to the electrode foils by ultrasonic welding. The separator (Whatman GF/C) was cut into pieces with a size of $67 \times 37 \text{ mm}^2$. Before introduction into the glovebox, the electrodes and separators were dried in vacuum at 60°C for 20 h and 80°C for 48 h, respectively. The further cell assembly was carried out in an Argon filled glovebox ($\text{O}_2 < 1 \text{ ppm}$, $\text{H}_2\text{O} < 1 \text{ ppm}$). The Mg anode was first thoroughly scratched with a ceramic knife. Afterwards, the separator was placed on the activated side of the anode. Then, 600 mL MLT/diglyme and PTHF/THF were added dropwise onto the separator, respectively. The cathode was then placed on the separator and the cell stack was stabilized with a chemical-resistant adhesive tape. Finally, the stacks were inserted into a pouch bag ($7 \times 20 \text{ cm}^2$, $184 \mu\text{m}$, DNP), which was afterwards sealed under vacuum.

3.5. Materials characterizations

Scanning electron microscopy (SEM) images and energy dispersive X-ray (EDX) spectra were obtained on an Auriga type field emission scanning electron microscope from Zeiss. The samples were stored in Ar-filled glass vials, and measured under air. For *ex-situ* XPS measurements, the cells were disconnected after ten cycles in the charged state. The pristine Mg anode was thoroughly scratched by a ceramic knife inside a glovebox. The Mg anodes were then washed by DME, dried, and fixed on a sample holder under Ar. Due to the stickiness of the MLT-GPE, some residual electrolyte remained on the Mg anode. The samples were transferred under argon to avoid any contamination with air. XPS measurements were performed on a Kratos Axis Ultra system equipped with a monochromic Al K_{α} source. Spectra were analyzed using the CasaXPS software. The energy separation and peak area of the S $2p_{3/2}$ and S $2p_{1/2}$ were constrained to 1.18 eV and 2:1, respectively [36].

4. Conclusions

In summary, we outlined the effectiveness of a halogen-free $\text{Mg}^{2+}/\text{Li}^+$ dual salt-containing GPE in Mg-S and Mg-ion batteries. The novel design concept effectively solves the major issues in metal-sulfur batteries by reducing the shuttle effect and the risks of electrolyte leakage. The novel MLT-GPE with outstanding electrochemical performance has been synthesized via an *in-situ* crosslinking reaction between $\text{Li}[\text{BH}_4]$, $\text{Mg}[\text{BH}_4]_2$ and the hydroxyl groups of PTHF in a glass fiber membrane with TiO_2 nanoparticles as additive. The MLT-GPE exhibited high ionic conductivities over a wide temperature range, excellent polarization behavior, good reversibility and outstanding compatibility with sulfur and intercalation cathodes. The Mg||MLT-GPE||SPAN cells and the Mg||MLT-GPE||ACC/S cells showed good cycling stability, rate capability and high discharge capacities by suppressing the polysulfide shuttle. Detailed impedance and XPS, measurements have been conducted to verify the concept. Moreover, the Mg||MLT-GPE||SPAN pouch cells show low self-discharge, good flexibility and safety properties, which benefit the practical use of this system. Further on, the Mg||MLT-GPE|| Mo_6S_8 cells, Mg||MLT-GPE|| TiS_2 cells and Mg||MLT-GPE||LTO cells all showed superior cycle stability and rate capability at room temperature. The MLT-GPE presented here not only narrows the gap between the lab cells and a practical use, but also sets directions for future developments

in the area of high-performance room-temperature rechargeable solid-state magnesium batteries.

CRedit authorship contribution statement

Peiwen Wang: Conceptualization, Data curation, Formal analysis, Investigation, Methodology, Writing – original draft, Writing – review & editing. **Janina Trück:** Resources. **Joachim Häcker:** Resources, Writing – review & editing. **Anja Schlosser:** Methodology, Resources, Writing – review & editing. **Kathrin Küster:** Methodology, Writing – review & editing. **Ulrich Starke:** Methodology, Writing – review & editing. **Leonie Reinders:** Methodology, Writing – review & editing. **Michael R. Buchmeiser:** Funding acquisition, Project administration, Supervision, Validation, Writing – review & editing.

Declaration of Competing Interest

The authors declare no competing financial interests or personal relationships that could have appeared to influence the work reported in this paper.

Acknowledgment

We gratefully acknowledge financial support by the German Federal Ministry of Education and Research (project number 03XP0208J) and by the German Federal Ministry of Economic Affairs and Energy (project number 03ETE003E). The authors would also like to thank the Ministry of Science, Research and Arts of the Federal State of Baden-Württemberg for financial support within the InnovationsCampus Mobilität der Zukunft. We also wish to thank Mr. U. Hageroth from the German Institutes of Textile and Fiber Research (DITF), Denkendorf, for SEM/EDX measurements. We also acknowledge Dr. Annika Baumann from EL-Cell GmbH and Mr. Felix Kampmann from Schäffler Technologies AG & Co. KG for the kind material supplement.

Supplementary materials

Supplementary material associated with this article can be found, in the online version, at doi:10.1016/j.ensm.2022.04.034.

References

- [1] P. Bonnick, J. Muldoon, *Adv. Funct. Mater.* 30 (2020), 1910510.
- [2] P. Wang, M.R. Buchmeiser, *Adv. Funct. Mater.* 29 (2019) 1905248–1905275.
- [3] P.W. Jaschin, Y. Gao, Y. Li, S. H. Bo, *J. Mater. Chem. A* 8 (2020) 2875–2897.
- [4] Y. Lu, C. Wang, Q. Liu, X. Li, X. Zhao, Z. Guo, *Small Methods* 5 (2021), 2001303.
- [5] W.Q. Wang, H.C. Yuan, Y. Nuli, J.J. Zhou, J. Yang, J.L. Wang, *J. Phys. Chem. C* 122 (2018) 26764–26776.
- [6] Z. Zhao-Karger, R. Liu, W. Dai, Z. Li, T. Diemant, B.P. Vinayan, C. Bonatto Minella, X. Yu, A. Manthiram, R.J. Behm, M. Ruben, M. Fichtner, *ACS Energy Lett* 3 (2018) 2005–2013.
- [7] P. Wang, J. Kappler, B. Sievert, J. Häcker, K. Küster, U. Starke, F. Ziegler, M. R. Buchmeiser, *Electrochim. Acta* 361 (2020), 137024.
- [8] P. Wang, J. Trück, S. Niesen, J. Kappler, K. Küster, U. Starke, F. Ziegler, A. Hintennach, M.R. Buchmeiser, *Batter. Supercaps* 3 (2020) 1239–1247.
- [9] P. Wang, K. Küster, U. Starke, C. Liang, R. Niewa, M.R. Buchmeiser, *J. Power Sources* 515 (2021), 230604.
- [10] L. Kong, C. Yan, J. Q. Huang, M. Q. Zhao, M.-M. Titirici, R. Xiang, Q. Zhang, *Energy Environ. Mater.* 1 (2018) 100–112.
- [11] S. Zhang, Y. Huang, Y. Nuli, B. Wang, J. Yang, J. Wang, *J. Phys. Chem. C* 124 (2020) 20712–20721.
- [12] J. Luo, S. He, T.L. Liu, *ACS Energy Lett* 2 (2017) 1197–1202.
- [13] Y. Yang, W. Wang, Y. Nuli, J. Yang, J. Wang, *ACS Appl. Mater. Interfaces* 11 (2019) 9062–9072.
- [14] S. Li, W. Zhang, J. Zheng, M. Lv, H. Song, L. Du, *Adv. Energy Mater.* 11 (2020), 2000779.
- [15] A.B. Du, H.R. Zhang, Z.H. Zhang, J.W. Zhao, Z.L. Cui, Y.M. Zhao, S.M. Dong, L. L. Wang, X.H. Zhou, G.L. Cui, *Adv. Mater.* 31 (2019), 1805930.
- [16] T. Gao, M. Noked, A.J. Pearce, E. Gillette, X. Fan, Y. Zhu, C. Luo, L. Sui, M. A. Schroeder, K. Xu, S.B. Lee, G.W. Rubloff, C. Wang, *J. Am. Chem. Soc.* 137 (2015) 12388–12393.
- [17] F. Lee, M.-C. Tsai, M.-H. Lin, Y.-L. Ni'mah, S. Hy, C.-Y. Kuo, J.-H. Cheng, J. Rick, W.-N. Su, B.-J. Hwang, *J. Mater. Chem. A* 5 (2017) 6708–6715.

- [18] R. Deivanayagam, M. Cheng, M. Wang, V. Vasudevan, T. Foroozan, N.V. Medhekar, R. Shahbazian-Yassar, *ACS Appl. Energy Mater.* 2 (2019) 7980–7990.
- [19] K. Karuppasamy, P.A. Reddy, G. Srinivas, R. Sharma, A. Tewari, G.H. Kumar, D. Gupta, *J. Solid State Electrochem* 21 (2016) 1145–1155.
- [20] B. Huang, Y. Zhang, M. Que, Y. Xiao, Y. Jiang, K. Yuan, Y. Chen, *RSC Adv.*, 7 (2017) 54391–54398.
- [21] G.P. Pandey, R.C. Agrawal, S.A. Hashmi, *J. Solid State Electrochem.* 15 (2010) 2253–2264.
- [22] S. Huang, Z. Cui, L. Qiao, G. Xu, J. Zhang, K. Tang, X. Liu, Q. Wang, X. Zhou, B. Zhang, G. Cui, *Electrochim. Acta* 299 (2019) 820–827.
- [23] Y.G. Cho, C. Hwang, D.S. Cheong, Y.S. Kim, H.K. Song, *Adv. Mater.* 31 (2019), e1804909.
- [24] Z. Ma, D.R. MacFarlane, M. Kar, *Batteries & Supercaps* 2 (2019) 115–127.
- [25] A. Robba, A. Vizintin, J. Bitenc, G. Mali, I. Arçon, M. Kavčič, M. Žitnik, K. Bučar, G. Aquilanti, C. Martineau-Corcoss, A. Randon-Vitanova, R. Dominko, *Chem. Mater.* 29 (2017) 9555–9564.
- [26] J. Triick, P. Wang, E. Buch, J. Groos, S. Niesen, M.R. Buchmeiser, *J. Electrochem. Soc.* 169 (2022), 010505.
- [27] S. Zhang, *Energy* 7 (2014) 4588–4600.
- [28] Z. Liu, Z. Liu, W. Fu, N.J. Dudney, C. Liang, *Angew. Chem.* 125 (2013) 7608–7611.
- [29] S. Li, Z. Zeng, J. Yang, Z. Han, W. Hu, L. Wang, J. Ma, B. Shan, J. Xie, *ACS Appl. Energy Mater.* 2 (2019) 2956–2964.
- [30] S. Wei, S. Xu, A. Agrawal, S. Choudhury, Y. Lu, Z. Tu, L. Ma, L.A. Archer, *Nat Commun* 7 (2016) 11722.
- [31] X. Sun, P. Bonnick, L.F. Nazar, *ACS Energy Lett* 1 (2016) 297–301.
- [32] Z.L. Tao, L.N. Xu, X.L. Gou, J. Chen, H.T. Yuan, *ChemComm* (2004) 2080.
- [33] H.D. Yoo, Y. Liang, Y. Li, Y. Yao, *ACS Appl. Mater. Interfaces* 7 (2015) 7001–7007.
- [34] N. Wu, Z.Z. Yang, H.R. Yao, Y.X. Yin, L. Gu, Y.G. Guo, *Angew. Chem. Int. Ed.* 54 (2015) 5757–5761.
- [35] M. Rashad, M. Asif, *J. Energy Chem.* 56 (2021) 383–390.
- [36] J.F. Moulder, W.F. Stickle, P.E. Sobol, K.D. Bomben, *Handbook of X-ray Photoelectron Spectroscopy*, Physical Electronics Division, Perkin Elmer Corporation, Minnesota, 1992.

7.3 Supporting Information to: “A Design Concept for Halogen-Free Mg^{2+}/Li^+ - Dual Salt-Containing Gel-Polymer-Electrolytes for Rechargeable Magnesium Batteries”

Section 1. Supporting Figures

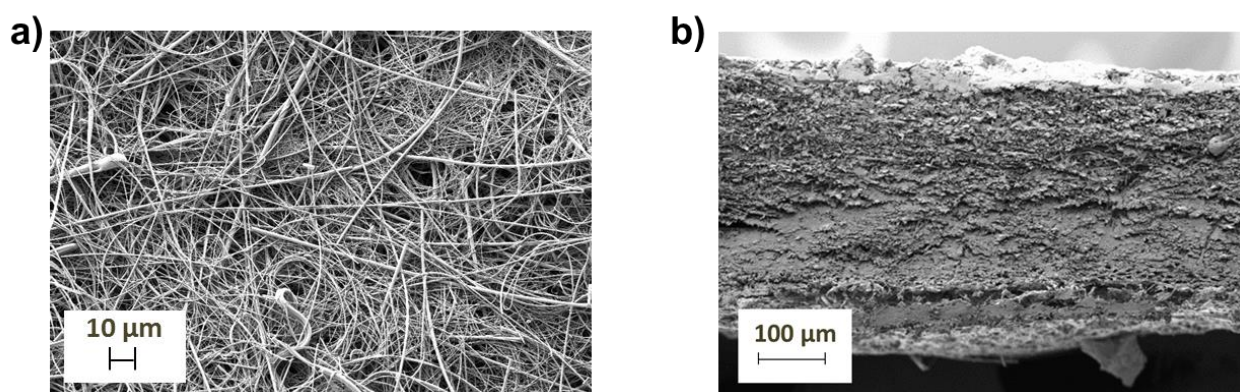


Figure S1. SEM images of **a)** the surface of a pristine glass fiber separator; **b)** a cross-section of the MLT-GPE.

The comparison between a pristine glass fiber separator and a magnesium, lithium, TiO_2 -gel polymer electrolyte (MLT-GPE) (Figure S1a), together with the SEM image of the cross-section of the MLT-GPE, confirms that the pores in the glass fiber separator are infiltrated by the MLT-GPE after the *in-situ* cross-linking reaction.

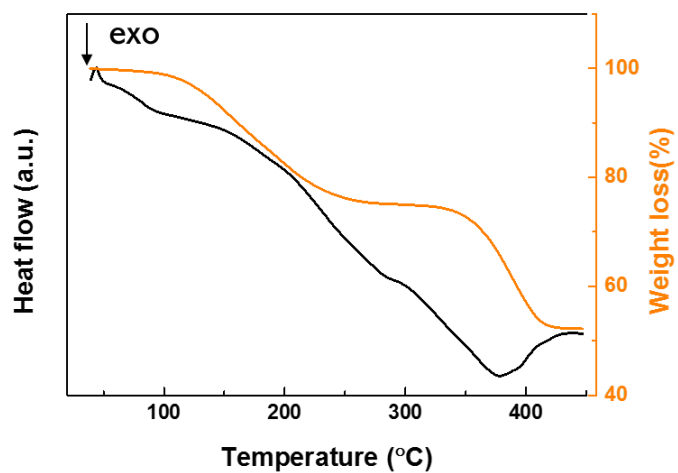


Figure S2. TGA-DSC analysis of the MLT-GPE.

Figure S2 shows the TGA-DSC results of the MLT-GPE. The crosslinked MLT-GPE shows a higher melting temperature (380 °C) than the reactants (PTHF, 28 °C).[1]

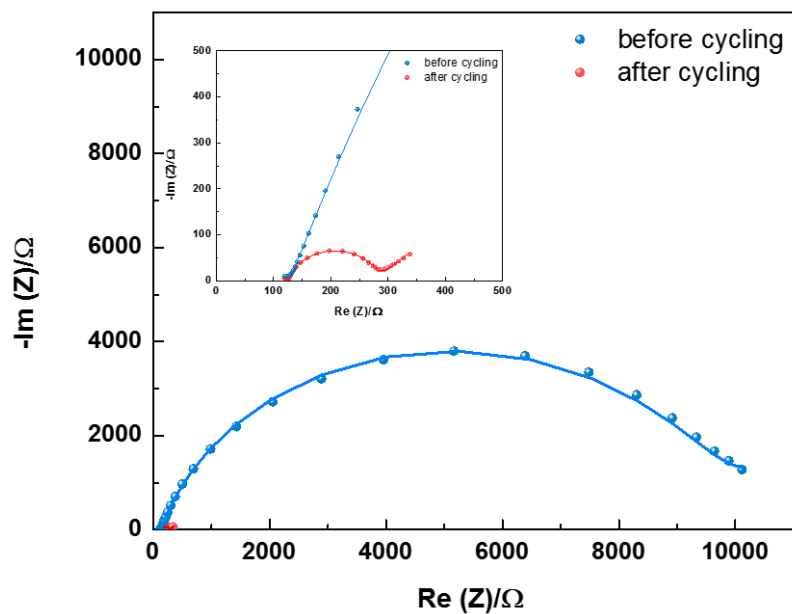


Figure S3. Nyquist plots of the Mg|| MLT-GPE || Mg cell with an before and after cycling.

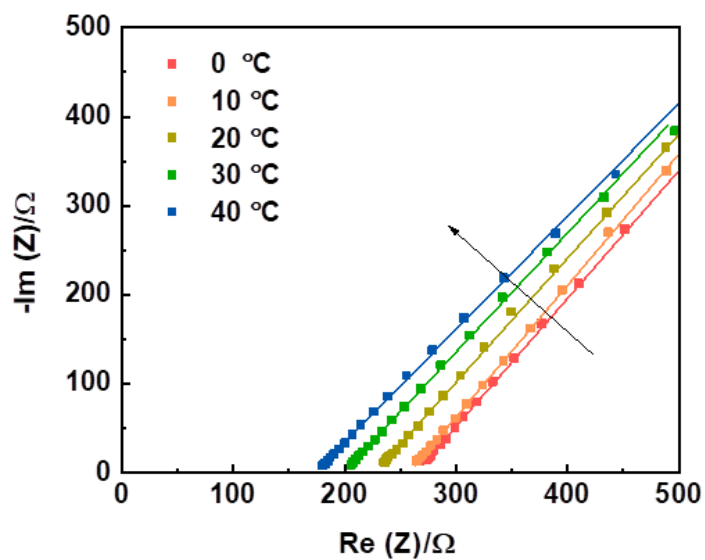


Figure S4. Nyquist plots of the SS||GPE||SS cell without TiO_2 at different temperatures.

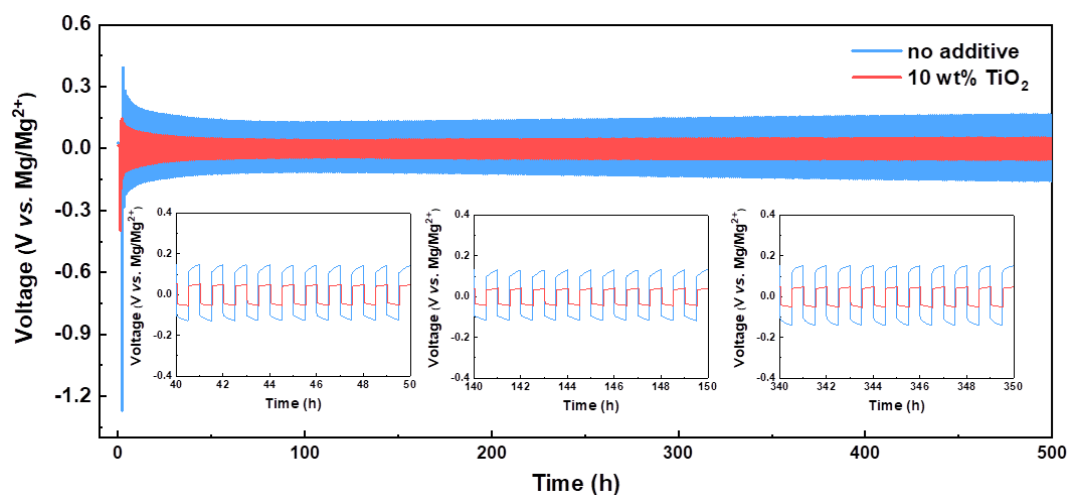


Figure S5. Long-term galvanostatic cycling of symmetric Mg||Mg cells at 0.1 mA cm^{-2} with various amounts of TiO_2 as additive. Blue: $0.1 \text{ M Mg[BH}_4\text{]}_2$ and $1.5 \text{ M Li[BH}_4\text{]}$ in diglyme + PTHF/THF; red: $0.1 \text{ M Mg[BH}_4\text{]}_2$ and $1.5 \text{ M Li[BH}_4\text{]}$ and $10 \text{ wt}\% \text{ TiO}_2$ in diglyme + PTHF/THF (MLT-GPE).

The overpotentials of the symmetric cells using the GPE with/without TiO_2 nanoparticles were compared at 0.1 mA cm^{-2} (Figure S5). The GPE without TiO_2 nanoparticles shows nearly twice the overpotential than the one with TiO_2 nanoparticles, indicating the comprehensive improvement of the conductive behavior by the introduction of TiO_2 nanoparticles.

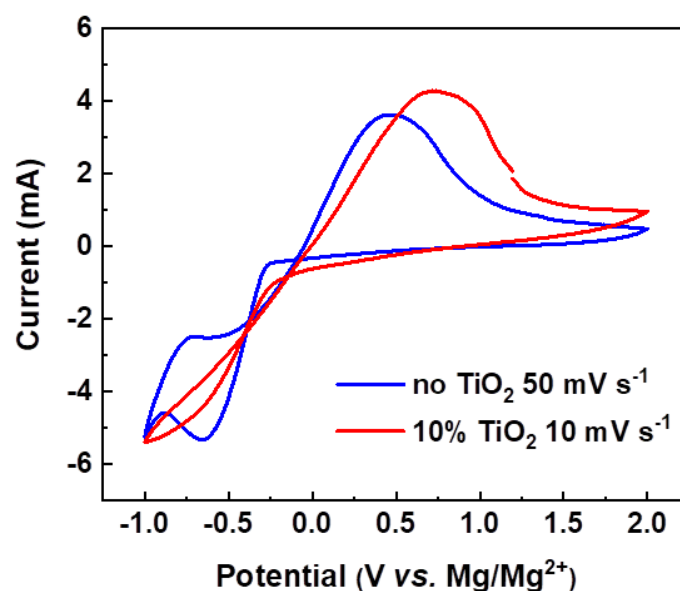


Figure S6. Cyclic voltammetry (CV) of Mg-stainless steel cells using gel polymer electrolytes with and without TiO₂. Red: 0.1 M Mg[BH₄]₂ and 1.5 M Li[BH₄] and 10 wt% TiO₂ in diglyme + PTHF/THF (MLT-GPE); scan rate: 10 mV·s⁻¹; blue: 0.1 M Mg[BH₄]₂ and 1.5 M Li[BH₄] in diglyme + PTHF/THF; scan rate: 50 mV·s⁻¹.

A Mg||SS cell without TiO₂ nanoparticles and a Mg||SS cell with the MLT-GPE was subjected to cyclic voltammetry applying a scan rate of 50 and 10 mV s⁻¹, respectively (Figure S6). The Mg||SS cell with the MLT-GPE shows higher current density even at a slower scan rate, demonstrating the improvements of the cell performance by the TiO₂ nanoparticles.

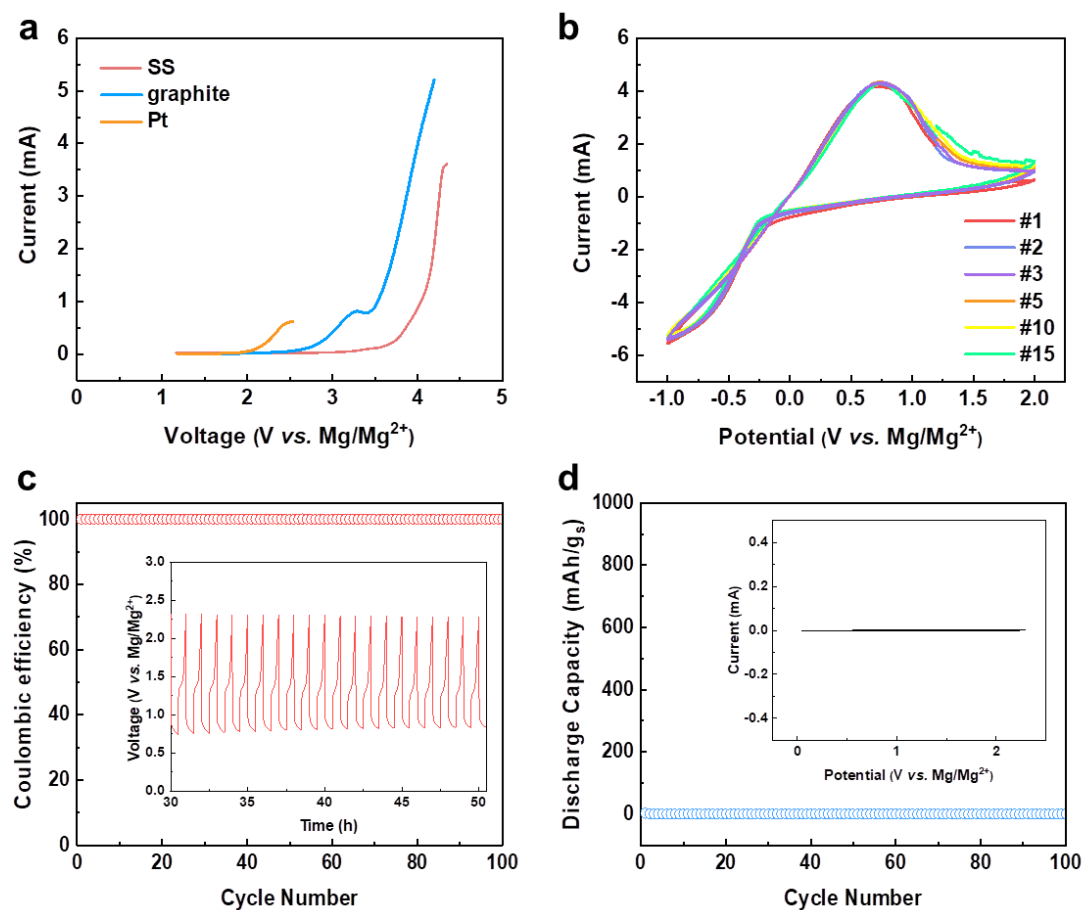


Figure S7. Electrochemical measurements with MLT-GPE as electrolyte: **a)** linear sweep voltammetry (LSV) with Mg foil as counter electrode, stainless steel foil/graphite foil/platinum foil as working electrode; **b)** cyclic voltammetry (CV) of Mg-stainless steel cell; scan rate: $10 \text{ mV}\cdot\text{s}^{-1}$; **c)** coulombic efficiency measurements using a Mg-stainless steel cell; inset: corresponding potential curve; **d)** discharge capacity and CV (inset) of Mg-stainless steel cell, measured in a voltage window of 0.05 V to 2.3 V.

Figure S7a shows the LSV results of the MLT-GPE against three different current collectors: Pt, graphite and stainless steel. Some common current collectors such as Al or carbon coated Al foil were not tested due to the known poor corrosion resistance.[2] According to Figure S7a, the highest oxidative stable voltages of these current collectors (Pt, graphite and stainless steel) are 2 V, 2.6 V and 3.6 V, respectively. The reasons for which the Pt current collector does not show the best corrosion resistance might be due to the solvents existing inside of the gel.[3] Due to the low cost and good corrosion resistance of the stainless steel foil, the stainless steel has been used as current collectors in the following studies.

Figure S7d shows the galvanostatic cycling and CV of a Mg||SS cell to examine whether the stainless steel current collector was inert and the MLT-GPE contributed to the capacity in the voltage window (0.05 V to 2.3 V). Negligible discharge capacity (<1 mAh/g) was detected in the applied voltage window. Also, no signals in CV were detected in this voltage range. Therefore, in the following electrochemical cycling tests, the voltage window was set from 0.05 V to 2.3 V.

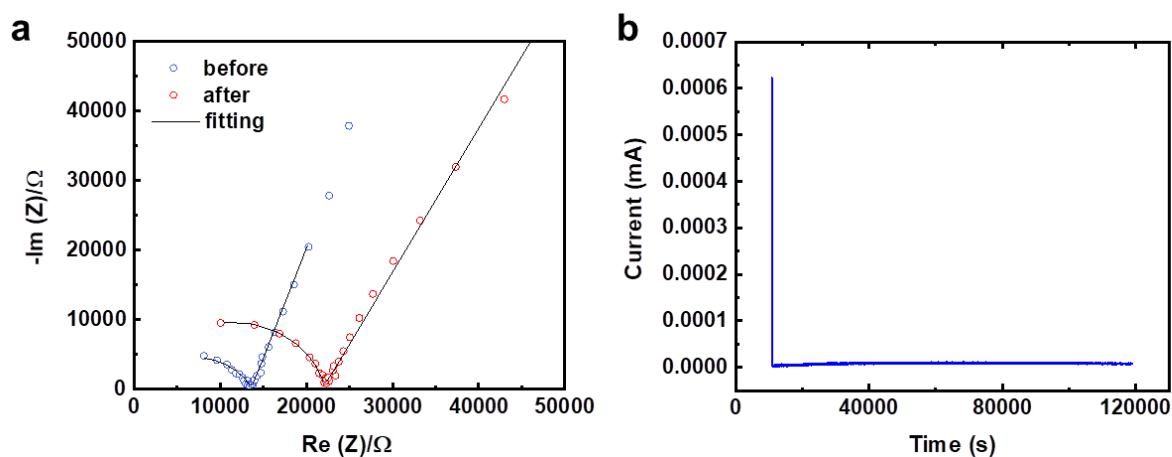


Figure S8. a) Nyquist plots of the Mg^{2+} electrolyte. The red curve shows the impedance spectrum after polarization. The blue curve shows the impedance spectrum before polarization at steady state. The black curves represent the fitting; b) chronoamperogram of a Mg^{2+} electrolyte with an applied voltage of 10 mV.

In order to exclude the influence of Li^+ , the transfer number of Mg^{2+} was measured based on the Bruce and Vincent method (Eq.S1) using a pure Mg^{2+} electrolyte, 0.1 M $\text{Mg}[\text{BH}_4]_2$, 10 wt% TiO_2 in diglyme, with the addition of PTHF/THF (Figure S8). A small constant potential (10 mV) was applied to the electrolyte between two magnesium electrodes, leading to a decrease of the initial current value (0.623 mA) until steady state (8.9 μA) after 2000 minutes (Figure S8b). Since the anions are not involved in the redox reaction, the anion current vanishes after reaching the steady state and the total current is only caused by the Mg^{2+} cations. The contact resistance was measured before and after polarization. Figure S8a shows the chronoamperometric and impedance measurement using the Mg^{2+} electrolyte. The fitted resistance values are listed in Table S3. The transfer number of the Mg^{2+} was further determined by Eq. S1:

$$t_{\text{Mg}^{2+}} = \frac{I_{SS}(\Delta V - I_0 R_{P,0})}{I_0(\Delta V - I_{SS} R_{P,SS})} = \frac{8.938 \mu\text{A} \times (10 \text{ mV} - 623 \mu\text{A} \times 4.4 \text{ k}\Omega)}{623 \mu\text{A} \times (10 \text{ mV} - 8.938 \mu\text{A} \times 10.34 \text{ k}\Omega)} = 0.5 \quad (\text{S1})$$

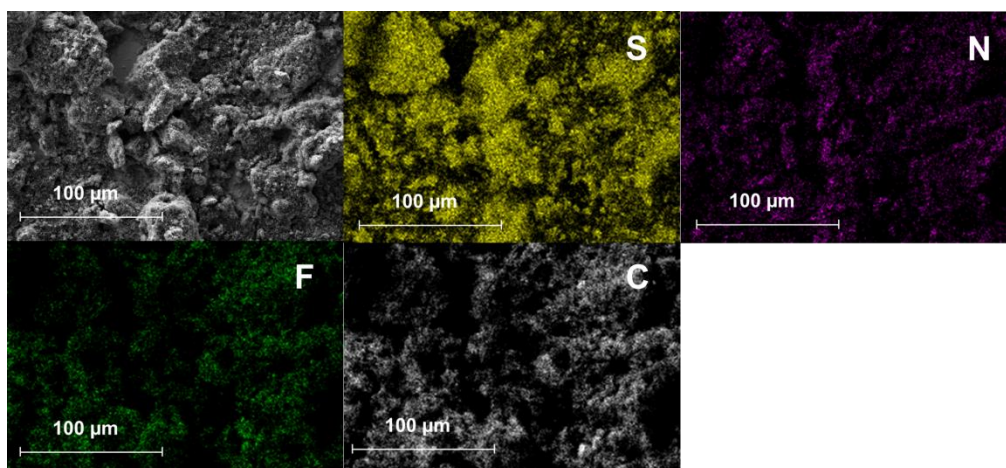


Figure S9. SEM image and elemental mapping of the SPAN cathode.

The elemental mapping of the SPAN cathode shows good homogeneity (Figure S9). Signals for S and N stem from the SPAN structure. Signals for F stem from the binder (PVDF). The C signals stem from conducting super carbon 65, PVDF and SPAN.

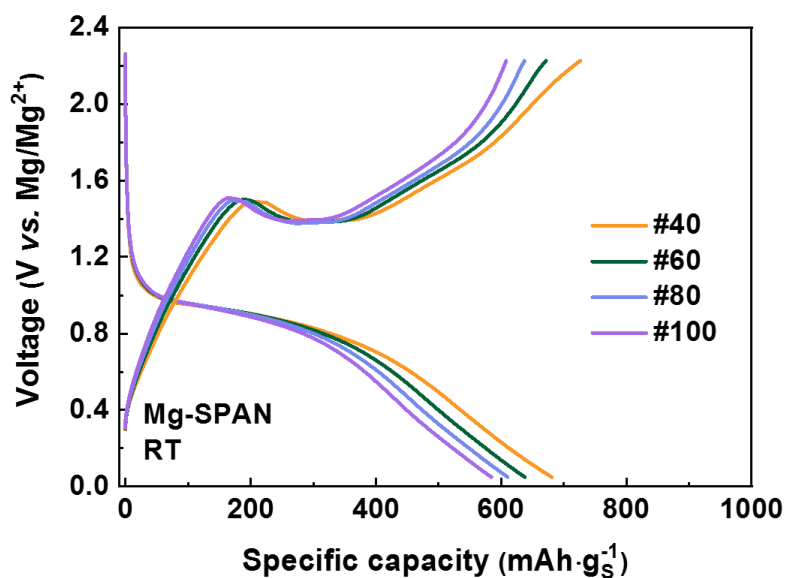


Figure S10. Voltage curves of the Mg||MLT-GPE||SPAN cell shown in Figure 3a.

The voltage curves show the characteristics SPAN features. In the discharge curve, a plateau at around 1 V represents the formation of short chain polysulfides MgS_x ($x < 4$).

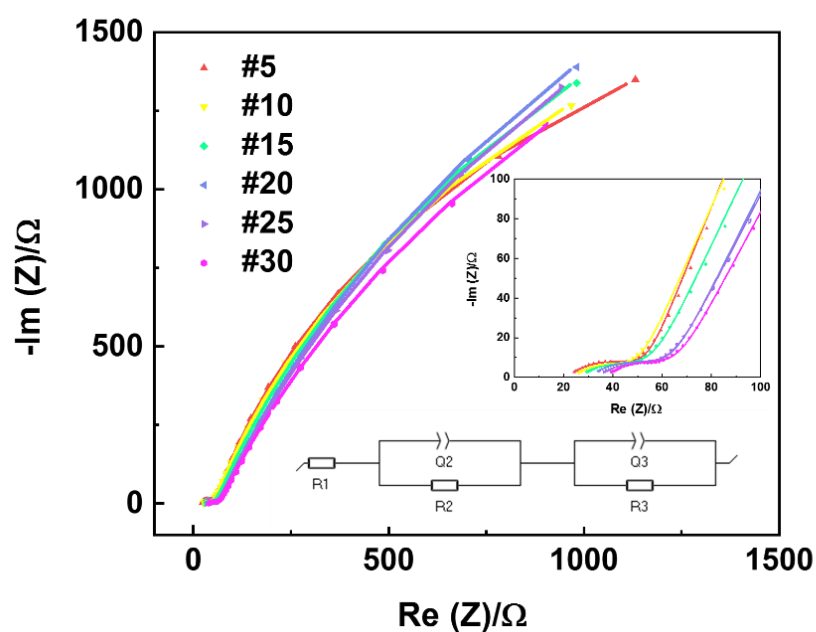


Figure S11. Nyquist plot of a Mg-SPAN cell after 5, 10, 15, 20, 25 and 30 cycles. Dots: experimental data; line: fitted data (by the inset equivalent circuit model); where R_1 is the bulk resistance, R_2 represents the resistance of the solid electrolyte interphase (SEI) layer on the Mg anode; R_3 is the charge transfer resistance between the active material (SPAN) and the electrolyte.[4]

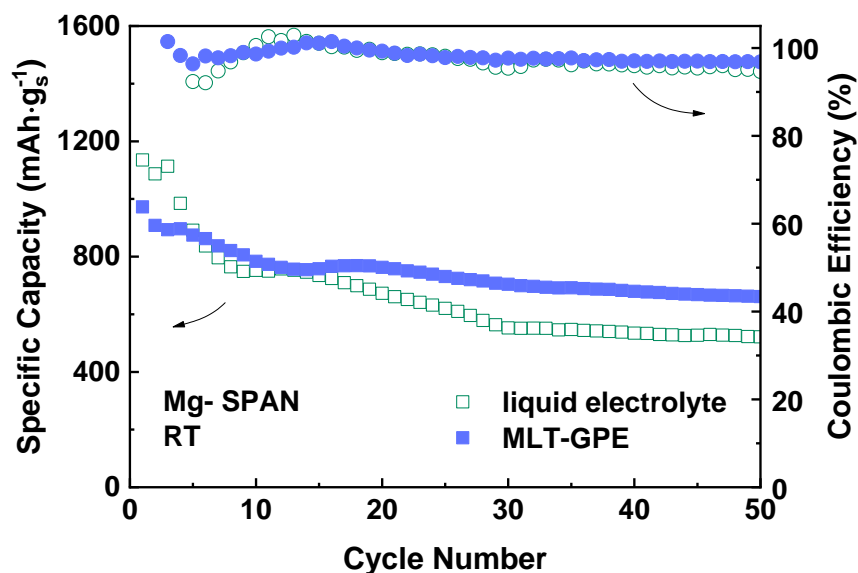


Figure S12. Performance comparison of Mg-SPAN cells cycled with the liquid electrolyte (green, 0.1 M $\text{Mg}[\text{BH}_4]_2$, 1.5 M $\text{Li}[\text{BH}_4]$, 10 wt% TiO_2 in diglyme) and the MLT-GPE (blue) at 0.2 C at room temperature.

The Mg||MLT-GPE||SPAN cell shows better capacity retention than the Mg||liquid electrolyte||SPAN cell, indicating successful suppression of the polysulfide shuttle in the MLT-GPE. Nonetheless, the Mg||liquid electrolyte||SPAN cell still shows acceptable cycle performance compared to other reported systems (Table S4), attributable to an effective retaining of sulfur by covalently bound sulfur in the SPAN structure.

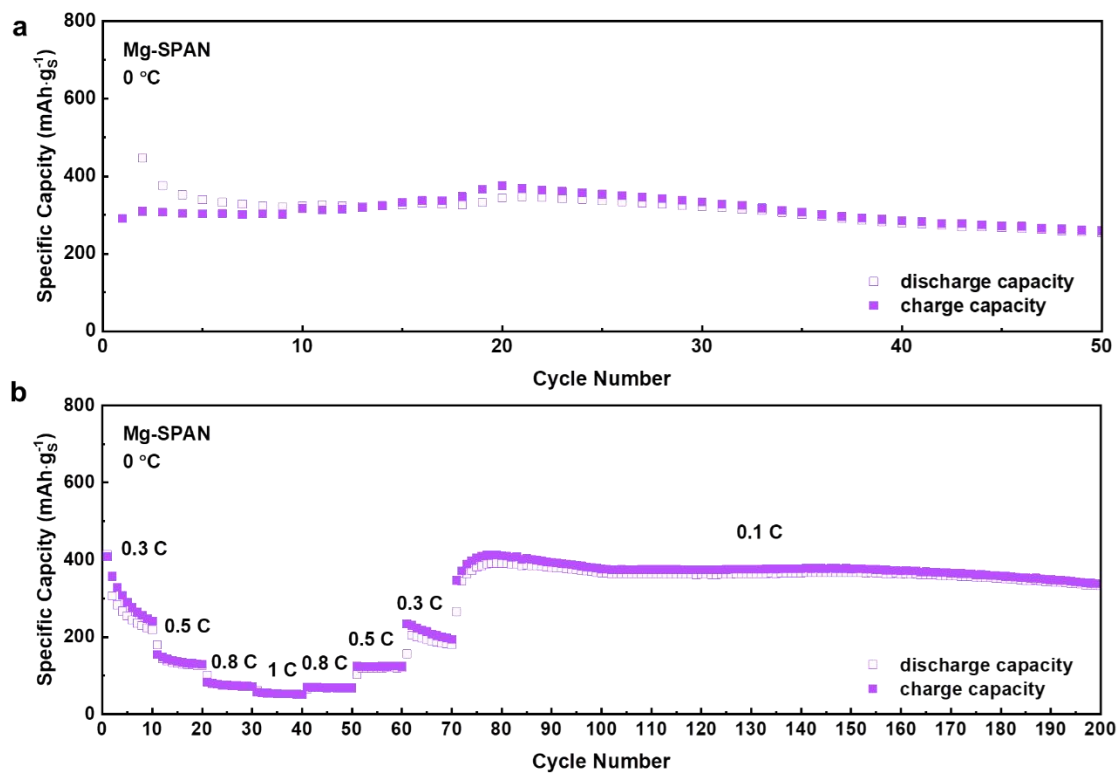


Figure S13. a) Long-term cycling data at 0.2 C and 0 °C; b) rate capability results of the Mg||MLT-GPE||SPAN cell cycled at 0 °C.

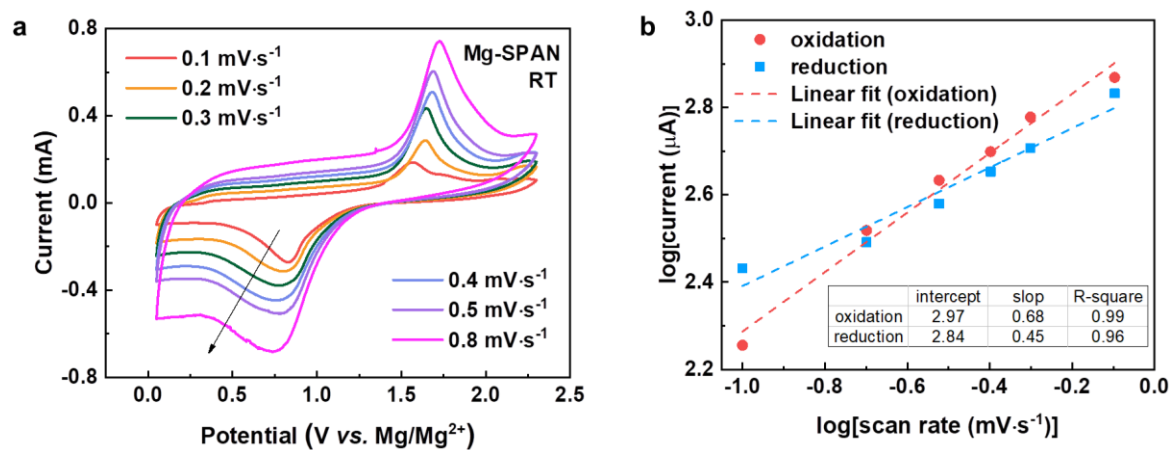


Figure S14. a) Cyclic voltammetry (CV) curves of the Mg||MLT-GPE||SPAN cell at different scan rates (0.1 mV·s⁻¹ to 0.8 mV·s⁻¹); b) logarithm of the anodic and cathodic peak currents versus the logarithm of the scan rate.

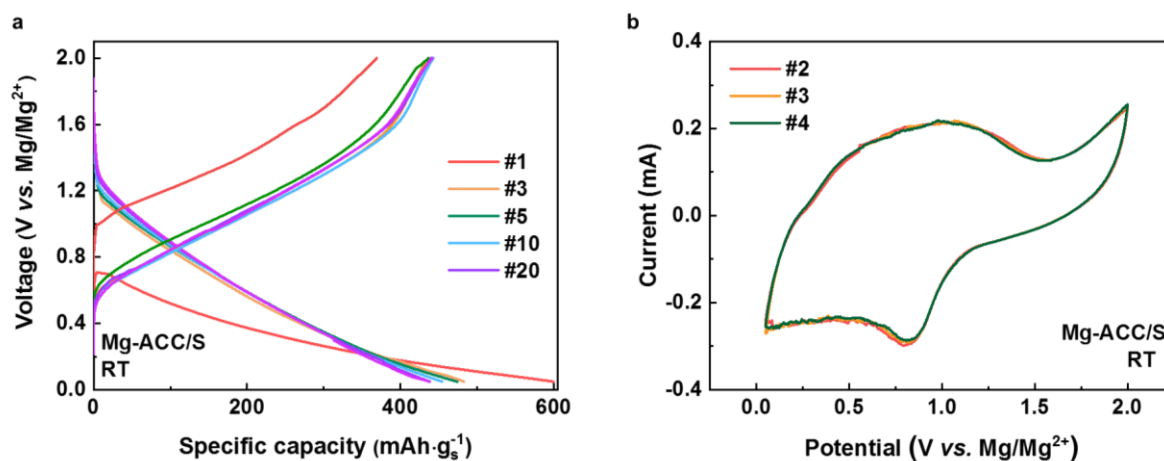


Figure S15. a) Voltage curves of the Mg||MLT-GPE||ACC/S cell charged/discharged at 0.2 C at room temperature; b) typical CV curves of the Mg||MLT-GPE||ACC/S cell, scan rate: 0.2 mV·s⁻¹; c) electrochemical performance of the Mg||liquid electrolyte||ACC/S cell.

After the initial cycle, the voltage curves of the Mg||MLT-GPE||ACC/S cell in Figure S15a shows sloped regions during discharging and charging starting from 1.2 V and 0.5 V respectively, which is in accordance with the typical CV curves in Figure S15b.

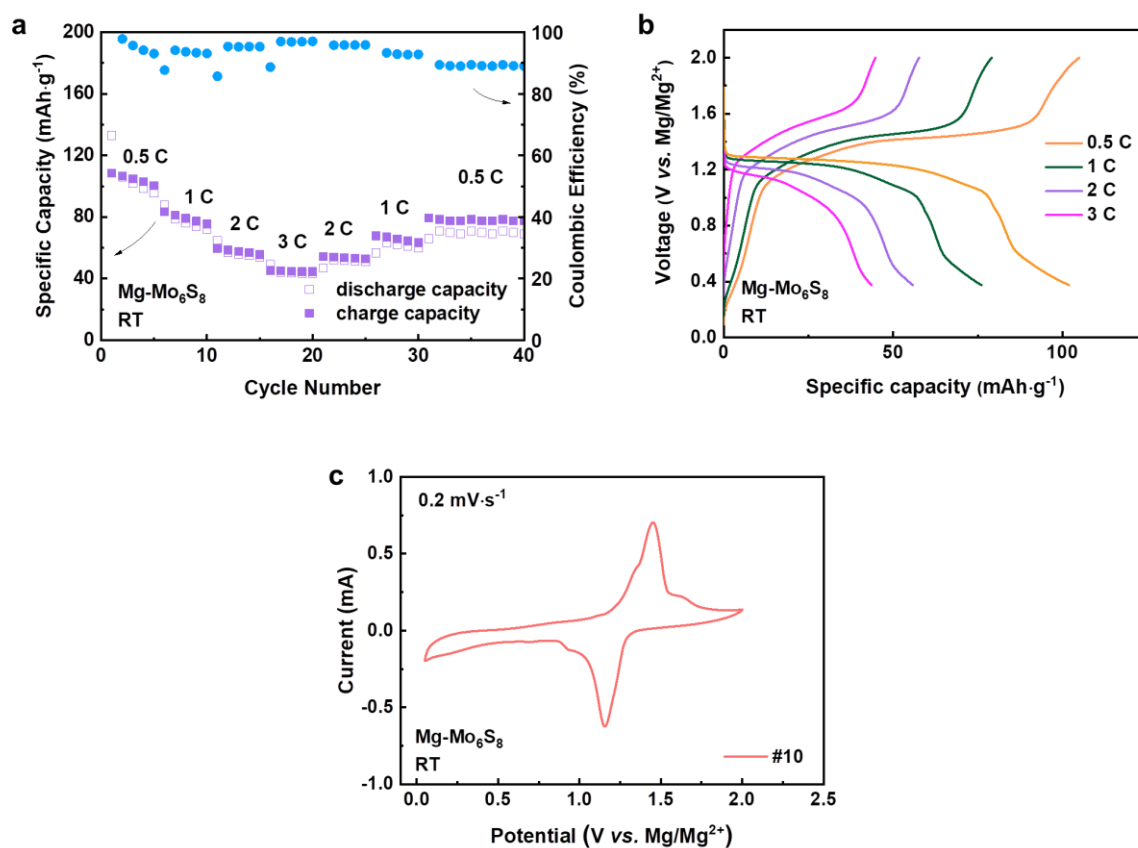


Figure S16. Mg||MLT-GPE||Mo₆S₈ cells: **a)** rate capability test (0.5 C, 1 C, 2 C, 3 C); **b)** voltage curves from S16a; **c)** CV curves at a scan rate of 0.2 mV·s⁻¹.

A Chevrel phase Mo₆S₈ cathode was tested together with a Mg foil and the MLT-GPE (Figure S16). The Mg||MLT-GPE||Mo₆S₈ cell showed good rate capability when cycling the cell from 0.5 C to 3 C (Figure S16 a). A relatively high discharge capacity of *ca.* 80 mAh·g⁻¹ was delivered at 0.5 C. The voltage curves and the CV shown in Figure S16b and c shows plateaus and featured redox peaks, indicating the successful cation insertion and extraction.

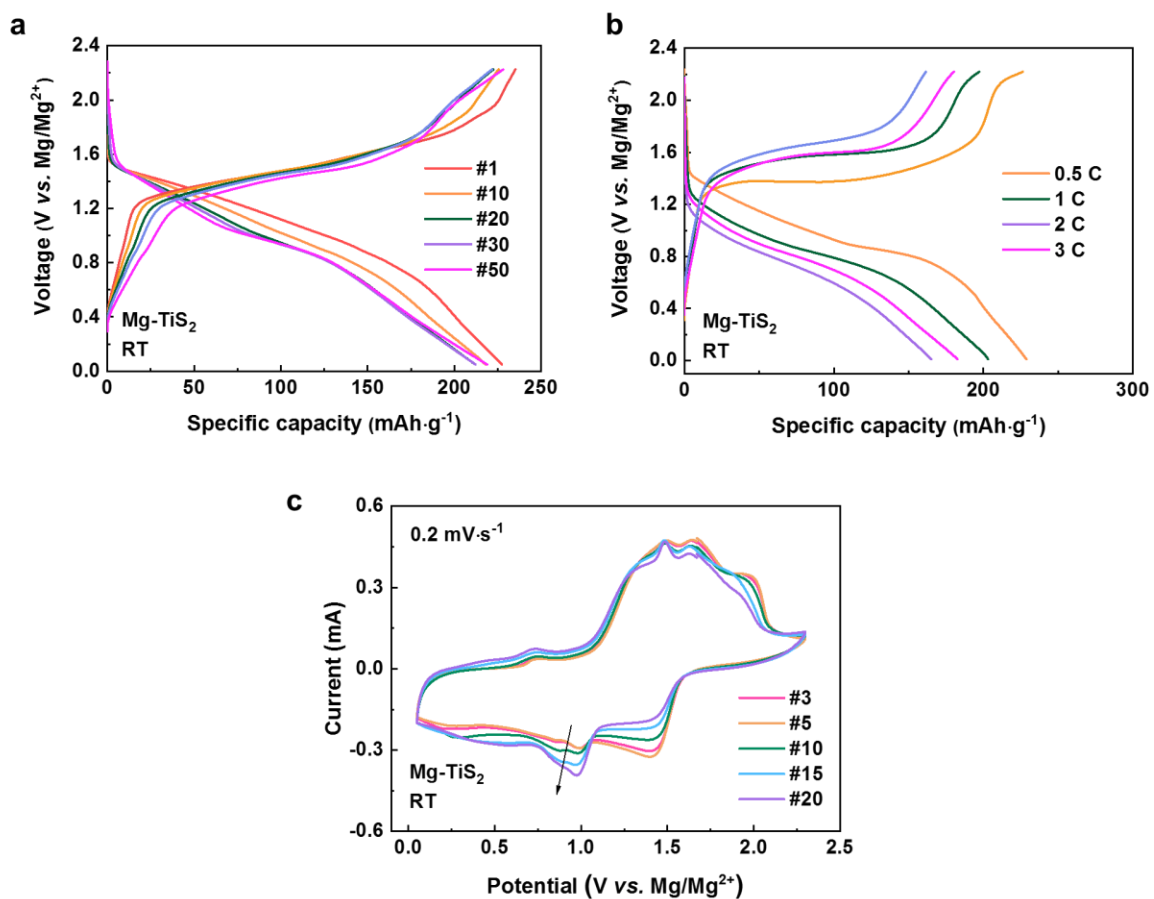


Figure S17. Mg||MLT-GPE||TiS₂ cells: **a)** voltage curves from Figure 5a; **b)** voltage curves from Figure 5b; **c)** CV curves at a scan rate of 0.2 mV·s⁻¹.

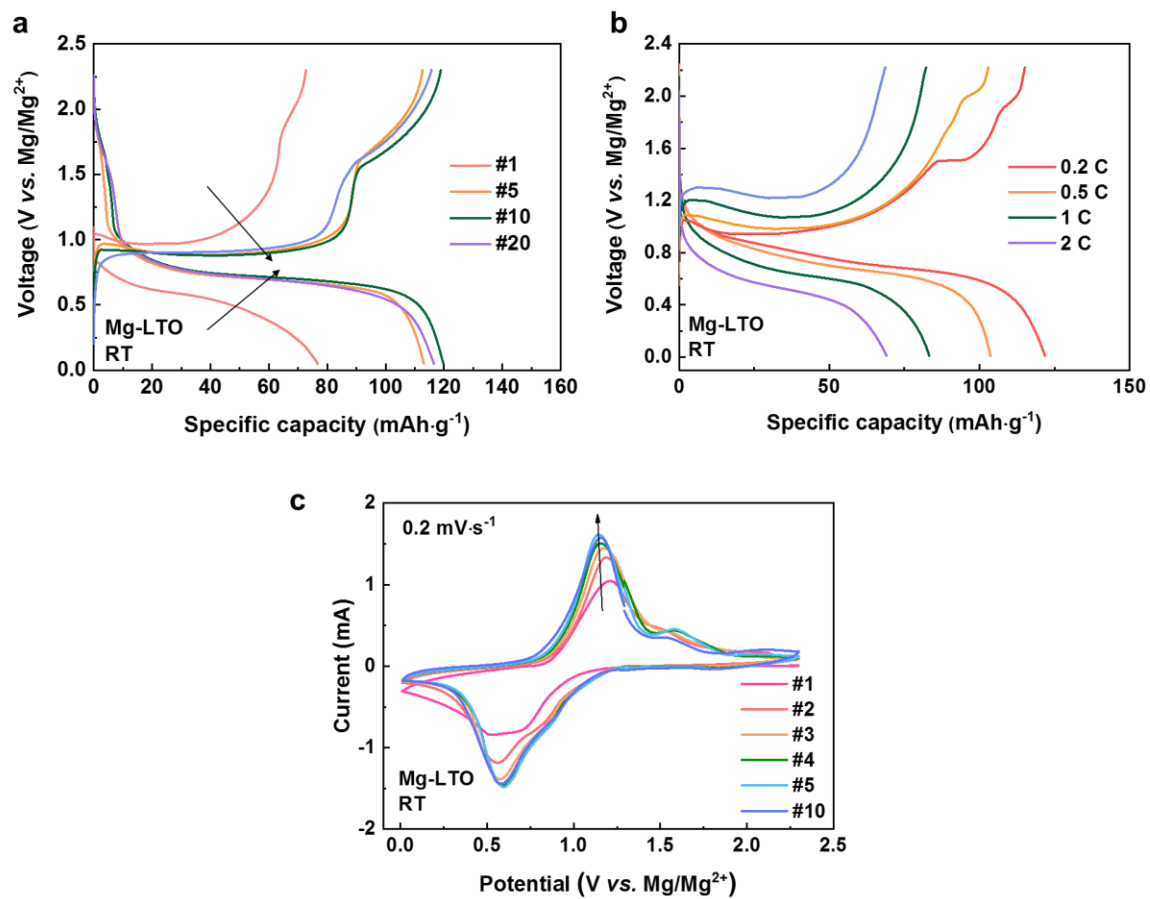


Figure S18. Mg||MLT-GPE||LTO cell: **a)** voltage curves from Figure 5c; **b)** voltage curves from Figure 5d; **c)** CV curves at a scan rate of 0.2 mV·s⁻¹.

Section 2. Supporting Tables

Table S1. Calculated resistance and ionic conductivity of MLT-GPE at different temperatures from Figure 2a.

Temperature (° C)	R1 (Ω)	Ionic conductivity ($S \cdot cm^{-1}$)
0	105.7	1.46×10^{-4}
10	98.9	1.56×10^{-4}
20	89.9	1.72×10^{-4}
30	79.4	1.94×10^{-4}
40	69.3	2.23×10^{-4}

Table S2. Calculated resistance and ionic conductivity of the GPE without TiO₂ additive at different temperatures from Figure S4.

Temperature (° C)	R1 (Ω)	Ionic conductivity ($S \cdot cm^{-1}$)
0	263.7	5.87×10^{-5}
10	257.5	6.01×10^{-5}
20	227.2	6.81×10^{-5}
30	198.7	7.79×10^{-5}
40	173.1	8.94×10^{-5}

Table S3. Fitted resistance values before and after polarization.

	R1 (electrolyte resistance, Ω)	R2 + R3 (electrode resistance, Ω)
Before polarization	4352	$8826/2 = 4413$
Steady state	1223	$20680/2 = 10340$

Table S4. Comparison of Mg-S cell performance with published work.

Cathode	Electrolyte	Current density	Cycle number	Capacity	Ref.
<i>SPAN</i>	<i>MLT-GPE (solid)</i>	<i>0.2 C</i>	<i>140</i>	<i>580 mAh·g_s⁻¹</i>	<i>This work</i>
<i>ACC/S</i>		<i>0.2 C</i>	<i>50</i>	<i>510 mAh·g_s⁻¹</i>	<i>work</i>
CC@PANI+ MgS _x catholyte	MACC (Liquid)	0.01 C	25	428 mAh·g _s ⁻¹	[5]
S ₈ -MXene/carbon nanotube	Mg[B(hfip) ₄] ₂ (liquid)	0.03 C	25	400 mAh·g _s ⁻¹	[6]
SPAN	MBA (liquid)	0.1 C	90	450 mAh·g _s ⁻¹	[7]
VN/60S	MTB (liquid)	0.3 C	100	420 mAh·g _s ⁻¹	[8]
S/NC	Mg[B(hfip) ₄] ₂ +I ₂ (liquid)	0.05 C	100	210 mAh·g _s ⁻¹	[9]
S ₈	THFPB (Liquid, 50°C)	0.06 C	25	915 mAh·g _s ⁻¹	[10]
S/MC	MBA (liquid)	0.04 C	100	400 mAh·g _s ⁻¹	[11]
S/MC	MTB (liquid)	0.05 C	55	390 mAh·g _s ⁻¹	[12]
S/NC	Mg[B(hfip) ₄] ₂ (liquid)	0.02 C	50	200 mAh·g _s ⁻¹	[13]
ACC/S	Mg[B(hfip) ₄] ₂ (liquid)	0.1 C	100	200 mAh·g _s ⁻¹	[14]
S/rGO@PCC	Mg[HMDS] ₂ (liquid)	0.01 C	40	400 mAh·g _s ⁻¹	[15]

Table S5. Fitted resistance values from Figure S11.

Cycle number	R₁ (Ω)	R₂ (Ω)	R₃ (Ω)
5	20.59	35.53	4218
10	22.65	31.06	4673
15	25.02	34.84	5646
20	29.11	37.67	6698
25	32.67	34.12	6423
30	35.92	32.54	5743

Section 3. Supporting References

- [1] A.B. Du, H.R. Zhang, Z.H. Zhang, J.W. Zhao, Z.L. Cui, Y.M. Zhao, S.M. Dong, L.L. Wang, X.H. Zhou, G.L. Cui, *Adv. Mater.*, 31 (2019) 1805930.
- [2] P. Wang, J. Trück, S. Niesen, J. Kappler, K. Küster, U. Starke, F. Ziegler, A. Hintennach, M.R. Buchmeiser, *Batter. Supercaps*, 3 (2020) 1239-1247.
- [3] Z. Zhao-Karger, M.E.G. Bardaji, O. Fuhr, M. Fichtner, *J. Mater. Chem. A*, 5 (2017) 10815-10820.
- [4] S. Waluś, C. Barchasz, R. Bouchet, F. Alloin, *Electrochim. Acta*, 359 (2020) 136944.
- [5] D. Muthuraj, M. Pandey, M. Krishna, A. Ghosh, R. Sen, P. Johari, S. Mitra, *J. Power Sources*, 486 (2021) 229326.
- [6] H. Kaland, F. Haskjold Fagerli, J. Hadler-Jacobsen, Z. Zhao-Karger, M. Fichtner, K. Wiik, N.P. Wagner, *ChemSusChem*, (2021).
- [7] S. Zhang, Y. Huang, Y. NuLi, B. Wang, J. Yang, J. Wang, *J. Phys. Chem. C*, 124 (2020) 20712-20721.
- [8] D. Huang, S. Tan, M. Li, D. Wang, C. Han, Q. An, L. Mai, *ACS Appl. Mater. Interfaces*, 12 (2020) 17474-17480.
- [9] V. Bhaghavathi Parambath, Z. Zhao-Karger, T. Diemant, M. Jäckle, Z. Li, T. Scherer, A. Gross, R.J. Behm, M. Fichtner, *J. Mater. Chem. A*, (2020).
- [10] Z. Zhou, B. Chen, T. Fang, Y. Li, Z. Zhou, Q. Wang, J. Zhang, Y. Zhao, *Adv. Energy Mater.*, 10 (2019) 1902023.
- [11] X. Zhao, Y. Yang, Y. NuLi, D. Li, Y. Wang, X. Xiang, *Chem. Commun.*, 55 (2019) 6086-6089.
- [12] Y. Yang, W. Wang, Y. Nuli, J. Yang, J. Wang, *ACS Appl. Mater. Interfaces*, 11 (2019) 9062-9072.
- [13] B.P. Vinayan, H. Euchner, Z. Zhao-Karger, M.A. Cambaz, Z. Li, T. Diemant, R.J. Behm, A. Gross, M. Fichtner, *J. Mater. Chem. A*, 7 (2019) 25490-25502.

[14] Z. Zhao-Karger, R. Liu, W. Dai, Z. Li, T. Diemant, B.P. Vinayan, C. Bonatto Minella, X. Yu, A. Manthiram, R.J. Behm, M. Ruben, M. Fichtner, *ACS Energy Lett.*, 3 (2018) 2005-2013.

[15] D. Muthuraj, A. Ghosh, A. Kumar, S. Mitra, *ChemElectroChem*, 6 (2018) 684-689.

Chapter 8

Conclusions

In conclusion, four different electrolyte systems have been conceptualized and investigated for Mg-SPAN cells in this thesis. In the first sub-project, Mg-SPAN cells using $\text{Mg}[\text{B}(\text{hfp})_4]_2$ as the conductive salt in the electrolyte and a Mg foil anode reversibly delivered *ca.* 300 mAh g_s^{-1} at C/30. Replacing the Mg foil by a Mg pressed pellet, the discharge capacity increased to *ca.* 550 mAh g_s^{-1} at C/30. In summary, this study showed the possibility of the reversible cycling of Mg-SPAN batteries.

In order to further improve the electrochemical performance of Mg-SPAN cells, a $\text{Mg}^{2+}/\text{Li}^+$ hybrid electrolyte ($\text{Li}[\text{BH}_4]$ and $\text{Mg}[\text{BH}_4]_2$ in diglyme) has been developed to replace the electrolyte containing a pure magnesium salt. The Mg-SPAN cell using the $\text{Mg}^{2+}/\text{Li}^+$ hybrid electrolyte showed improved electrochemical performance. Cells stably delivered *ca.* 800 mAh g_s^{-1} at C/10 with > 99% Coulombic efficiency for 100 cycles, which was among the best performing Mg-S cells. In summary, the addition of a lithium salt into the electrolyte of Mg-SPAN cells greatly improved the cell performance. The detailed functions of the lithium salt in this system could not be investigated due to the low solubility of $\text{Mg}[\text{BH}_4]_2$ in the ether-based solvents.

In order to further understand the role of a lithium salt in Mg-SPAN batteries, an electrolyte, which can dissolve both magnesium and lithium salts has been found. Mg-SPAN cells with a $\text{Mg}^{2+}/\text{Li}^+$ hybrid electrolyte composed of $\text{Mg}[\text{CF}_3\text{SO}_3]_2$, $\text{Li}[\text{CF}_3\text{SO}_3]$, MgCl_2 and AlCl_3 in DME successfully delivered *ca.* 1100 mAh g_s^{-1} at 1 C with > 99.9% Coulombic efficiency for 100 cycles. In contrast, Mg-SPAN cells with a pure Mg^{2+} electrolyte ($\text{Mg}[\text{CF}_3\text{SO}_3]_2$, MgCl_2 and AlCl_3 in DME) delivered lower and unstable capacities. Based on the electrochemical measurements and *post-mortem* analysis, the magnesium (poly)sulfides proved to be harmful since they tended to passivate the magnesium anodes. The addition of a lithium salt to the electrolyte greatly suppressed the passivation of Mg

anodes and polysulfide shuttle. At the same time, the cell resistance and overpotential were greatly reduced *via* the potential formation of MgLiS_x species.

Apart from the addition of a lithium salt, the development of a GPE has also been proved to be capable of suppressing the polysulfide shuttle. A novel high-performance GPE, prepared by an *in-situ* crosslinking reaction between $\text{Li}[\text{BH}_4]/\text{Mg}[\text{BH}_4]_2$ solution and poly(tetrahydrofuran) solution, has been developed for the use of Mg-S/ion batteries. This GPE displayed outstanding ionic conductivities in a wide temperature range, superior polarization behavior, remarkable reversibility and compatibility with different sulfur containing and intercalation cathodes. Specifically, Mg-SPAN and Mg-ACC/S cells delivered discharge capacities of around 600 and 420 $\text{mAh}\cdot\text{g}_s^{-1}$ at 0.2 C after 140 and 50 cycles with almost 100% Coulombic efficiency, respectively. Remarkably, the Mg-SPAN pouch cells also showed excellent flexibility and safety characteristics, which could potentially bridge the gap between the lab cells and the practical applications.

Chapter 9

Future work

Research on Mg-S batteries has made substantial progress during the last decade. However, more investigations still must be carried out in this area in the future. Regarding the electrolyte systems, the development of all-solid-state electrolytes for Mg-S batteries should definitely be investigated, since there are no reports yet in this field. Despite the common issues in all-solid-state electrolyte such as low ionic conductivity and poor interaction between the electrolyte and the electrodes, all-solid-state electrolytes can greatly suppress the polysulfide shuttle and improve the energy density of the cell system, which are attractive in Mg-S batteries.

On the other hand, the development of advanced liquid electrolytes for Mg-S batteries is still an important research direction. Novel electrolyte systems that can successfully suppress the polysulfide shuttle and allow for a stable cell cycling with high energy densities are still highly demanded. The cycle life of the state-of-the-art Mg-S batteries is only around 100 ~200 cycles; however, in the practical applications, a longer cycle life is definitely needed.

Further on, high-performance sulfur cathodes are also highly demanded for Mg-S batteries. The majority of the current applied cathodes are still sulfur-carbon composites, which have shown limitations in cycle performances. Therefore, cathodes with covalently bound sulfur are of great interest for Mg-S batteries. Although SPAN cathodes have shown high compatibility with Mg batteries, low sulfur loading of the SPAN material is a drawback. High sulfur-loading cathode materials need to be developed in the future work.

Also, the development of electrolyte systems that are compatible with high-voltage cathode materials should be further investigated. Due to the intrinsic properties of magnesium anodes and sulfur cathodes, the voltage plateaus of the redox reactions are relatively low, which further limit the energy density of the system. Hence, novel high-voltage cathode

materials with high energy densities together with the corresponding electrolyte systems with high oxidative stability need to be further developed.

Chapter 10

References

- [1] M. Armand, J.-M. Tarascon, *Nature* **2008**, *451*, 652-657.
- [2] D. Linden, *Handbook of Batteries*, McGraw-Hill, **1995**.
- [3] C. Daniel, J. O. Besenhard, *Handbook of Battery Materials*, Wiley, **2012**.
- [4] H. A. Kiehne, *Battery Technology Handbook*, Expert Verlag, Renningen-Malsheim, Gemany, **2003**.
- [5] C. G. Zoski, *Handbook of Electrochemistry*, Elsevier, **2007**.
- [6] R. Korthauer, *Lithium-Ion Batteries: Basics and Applications*, Springer Berlin Heidelberg, **2018**.
- [7] I. Buchmann, *Batteries In A Portable Wold: A Handbook on Rechargeable Batteries for Non-engineers.*, Cadex Electronics Incorporated, **2011**.
- [8] J. Xiao, Li, Q., Bi, Y. et al., *Nat. Energy* **2020**, *5*, 561-568.
- [9] M. Park, K. Y. Kim, H. Seo, Y. E. Cheon, J. H. Koh, H. Sun, T. J. Kim, *J. Electrochem. Sci. Technol* **2014**, *5*, 1-18.
- [10] Y. Zhao, O. Pohl, A. I. Bhatt, G. E. Collis, P. J. Mahon, T. R  ther, A. F. Hollenkamp, *Sustain. Chem.* **2021**, *2*, 167-205.
- [11] S. Dhar, S. R. Ovshinsky, P. R. Gifford, D. A. Corrigan, M. A. Fetcenko, S. Venkatesan, *J. Power Sources* **1997**, *65*, 1-7.
- [12] B. Pinnangudi, M. Kuykendal, S. Bhadra, *The Power Grid*, Joe Hayton, **2017**.
- [13] A. Manthiram, *Nat. Commun* **2020**, *11*, 1550.

-
- [14] A. Manthiram, Y. Fu, S. H. Chung, C. Zu, Y. S. Su, *Chem. Rev.* **2014**, *114*, 11751-11787.
- [15] K. Mizushima, P. C. Jones, P. J. Wiseman, J. B. Goodenough, *Mater. Res. Bull.* **1980**, *15*, 783-789.
- [16] R. Yazami, P. Touzain, *J. Power Sources* **1983**, *9*, 365-371.
- [17] A. Yoshino, *Angew. Chem.* **2012**, *124*, 5898-5900; *Angew. Chem. Int. Ed.* **2012**, *51*, 5798-5800.
- [18] N. Nitta, F. Wu, J. T. Lee, G. Yushin, *Mater. Today* **2015**, *18*, 252-264.
- [19] M. Li, J. Lu, Z. Chen, K. Amine, *Adv. Mater.* **2018**, e1800561.
- [20] Y. Chen, Y. Kang, Y. Zhao, L. Wang, J. Liu, Y. Li, Z. Liang, X. He, X. Li, N. Tavajohi, B. Li, *J. Energy Chem.* **2021**, *59*, 83-99.
- [21] A. Adam, J. Wandt, E. Knobbe, G. Bauer, A. Kwade, *J. Electrochem. Soc.* **2020**, *167*, 130503.
- [22] M. Weiss, R. Ruess, J. Kasnatscheew, Y. Levartovsky, N. R. Levy, P. Minnmann, L. Stolz, T. Waldmann, M. Wohlfahrt-Mehrens, D. Aurbach, M. Winter, Y. Ein-Eli, J. Janek, *Adv. Energy Mater.* **2021**, *11*, 2101126.
- [23] C. T. Love, C. Buesser, M. D. Johannes, K. E. Swider-Lyons, *J. Electrochem. Energy* **2018**, *15*.
- [24] D. P. Finegan, E. Darcy, M. Keyser, B. Tjaden, T. M. M. Heenan, R. Jarvis, J. J. Bailey, N. T. Vo, O. V. Magdysyuk, M. Drakopoulos, M. D. Michiel, A. Rack, G. Hinds, D. J. L. Brett, P. R. Shearing, *Adv. Sci.* **2018**, *5*, 1700369.
- [25] F. Schipper, E. M. Erickson, C. Erk, J.-Y. Shin, F. F. Chesneau, D. Aurbach, *J. Electrochem. Soc.* **2016**, *164*, A6220-A6228.
- [26] X. Feng, M. Ouyang, X. Liu, L. Lu, Y. Xia, X. He, *Energy Storage Mater.* **2018**, *10*, 246-267.
- [27] Z. Chen, R. Xiong, J. Lu, X. Li, *Appl. Energy* **2018**, *213*, 375-383.

References

- [28] P. Huang, Q. Wang, K. Li, P. Ping, J. Sun, *Sci Rep* **2015**, *5*, 7788.
- [29] S. Koch, A. Fill, K. P. Birke, *J. Power Sources* **2018**, *398*, 106-112.
- [30] F. Larsson, P. Andersson, P. Blomqvist, B. E. Mellander, *Sci Rep* **2017**, *7*, 10018.
- [31] F. Larsson, S. Bertilsson, M. Furlani, I. Albinsson, B.-E. Mellander, *J. Power Sources* **2018**, *373*, 220-231.
- [32] J. Xu, S. Dou, H. Liu, L. Dai, *Nano Energy* **2013**, *2*, 439-442.
- [33] Z. Chen, W. Zhang, Z. Yang, *Nanotechnology* **2020**, *31*, 012001.
- [34] J. W. Fergus, *J. Power Sources* **2010**, *195*, 939-954.
- [35] Y. Mekonnen, A. Sundararajan, A. I. Sarwat, *SoutheastCon* **2016**, 1-6.
- [36] W. Tang, Z. Chen, F. Xiong, F. Chen, C. Huang, Q. Gao, T. Wang, Z. Yang, W. Zhang, *J. Power Sources* **2019**, *412*, 246-254.
- [37] W. Liu, P. Oh, X. Liu, M. J. Lee, W. Cho, S. Chae, Y. Kim, J. Cho, *Angew. Chem.* **2015**, *127*, 4518-4536; *Angew. Chem. Int. Ed.* **2015**, *54*, 4440-4457.
- [38] N. Tolganbek, Y. Yerkinbekova, S. Kalybekkyzy, Z. Bakenov, A. Mentbayeva, *J. Alloys Compd.* **2021**, *882*, 160774.
- [39] J. Li, Z.-F. Ma, *Chem.* **2019**, *5*, 3-6.
- [40] K. Zaghib, A. Guerfi, P. Hovington, A. Vijn, M. Trudeau, A. Mauger, J. B. Goodenough, C. M. Julien, *J. Power Sources* **2013**, *232*, 357-369.
- [41] M. J. Lee, S. Lee, P. Oh, Y. Kim, J. Cho, *Nano Lett.* **2014**, *14*, 993-999.
- [42] B. Dunn, H. Kamath, J. M. Tarascon, *Science* **2011**, *334*, 928-935.
- [43] H. W. Lee, P. Muralidharan, R. Ruffo, C. M. Mari, Y. Cui, D. K. Kim, *Nano Lett.* **2010**, *10*, 3852-3856.
- [44] S. B. Park, H. C. Shin, W.-G. Lee, W. I. Cho, H. Jang, *J. Power Sources* **2008**, *180*, 597-601.

-
- [45] Q. Zhao, Z. Yan, C. Chen, J. Chen, *Chem. Rev.* **2017**, *117*, 10121-10211.
- [46] D. Liu, Z. He, X. Liu, *Mater. Lett.* **2007**, *61*, 4703-4706.
- [47] B. Xu, D. Qian, Z. Wang, Y. S. Meng, *Mater. Sci. Eng* **2012**, *73*, 51-65.
- [48] U. H. Kim, D. W. Jun, K. J. Park, Q. Zhang, P. Kaghazchi, D. Aurbach, D. T. Major, G. Goobes, M. Dixit, N. Leifer, C. M. Wang, P. Yan, D. Ahn, K. H. Kim, C. S. Yoon, Y. K. Sun, *Energy Environ. Sci.* **2018**, *11*, 1271-1279.
- [49] Z. Liu, A. Yu, J. Y. Lee, *J. Power Sources* **1999**, *81-82*, 416-419.
- [50] A. K. Stephan, *Joule* **2020**, *4*, 1632-1633.
- [51] J. Lu, Z. Chen, F. Pan, Y. Cui, K. Amine, *EER* **2018**, *1*, 35-53.
- [52] A. Ambrosi, C. K. Chua, A. Bonanni, M. Pumera, *Chem. Rev.* **2014**, *114*, 7150-7188.
- [53] F.-Y. Su, Y.-B. He, B. Li, X.-C. Chen, C.-H. You, W. Wei, W. Lv, Q.-H. Yang, F. Kang, *Nano Energy* **2012**, *1*, 429-439.
- [54] B. J. Landi, M. J. Ganter, C. D. Cress, R. A. DiLeo, R. P. Raffaele, *Energy Environ. Sci.* **2009**, *2*, 638.
- [55] L. Qie, W. M. Chen, Z. H. Wang, Q. G. Shao, X. Li, L. X. Yuan, X. L. Hu, W. X. Zhang, Y. H. Huang, *Adv. Mater.* **2012**, *24*, 2047-2050.
- [56] X. Zuo, J. Zhu, P. Müller-Buschbaum, Y.-J. Cheng, *Nano Energy* **2017**, *31*, 113-143.
- [57] D. Aurbach, Y. Talyosef, B. Markovsky, E. Markevich, E. Zinigrad, L. Asraf, J. S. Gnanaraj, H.-J. Kim, *Electrochim. Acta* **2004**, *50*, 247-254.
- [58] S. S. Zhang, *J. Power Sources* **2006**, *162*, 1379-1394.
- [59] P. Fan, H. Liu, V. Marosz, N. T. Samuels, S. L. Suib, L. Sun, L. Liao, *Adv. Funct. Mater.* **2021**, *31*, 2101380.
- [60] W. H. Meyer, *Adv. Mater.* **1998**, *10*, 439-448.

- [61] D. Baril, *Solid State Ion.* **1997**, *94*, 35-47.
- [62] M. Armand, P. Axmann, D. Bresser, M. Copley, K. Edström, C. Ekberg, D. Guyomard, B. Lestriez, P. Novák, M. Petranikova, W. Porcher, S. Trabesinger, M. Wohlfahrt-Mehrens, H. Zhang, *J. Power Sources* **2020**, *479*, 228708.
- [63] E. Quartarone, P. Mustarelli, *J. Electrochem. Soc* **2020**, *167*, 050508.
- [64] K. Xu, M. S. Ding, S. Zhang, J. L. Allen, T. R. Jow, *J. Electrochem. Soc* **2002**, *149*, A622.
- [65] K. Xu, S. Zhang, J. L. Allen, T. R. Jow, *J. Electrochem. Soc* **2002**, *149*, A1079.
- [66] K. Xu, S. Zhang, J. L. Allen, T. R. Jow, *J. Electrochem. Soc* **2003**, *150*, A170.
- [67] M. S. Ding, K. Xu, T. R. Jow, *J. Electrochem. Soc* **2002**, *149*, A1489.
- [68] Y. E. Hyung, D. R. Vissers, K. Amine, *J. Power Sources* **2003**, *119-121*, 383-387.
- [69] H. Ota, A. Kominato, W.-J. Chun, E. Yasukawa, S. Kasuya, *J. Power Sources* **2003**, *119-121*, 393-398.
- [70] Q. Wang, J. Sun, X. Yao, C. Chen, *Electrochem. Solid-State Lett.* **2005**, *8*, A467.
- [71] T. Famprakis, P. Canepa, J. A. Dawson, M. S. Islam, C. Masquelier, *Nat. Mater.* **2019**, *18*, 1278-1291.
- [72] L. Long, S. Wang, M. Xiao, Y. Meng, *J. Mater. Chem. A* **2016**, *4*, 10038-10069.
- [73] L. Yue, J. Ma, J. Zhang, J. Zhao, S. Dong, Z. Liu, G. Cui, L. Chen, *Energy Storage Mater.* **2016**, *5*, 139-164.
- [74] P. Knauth, *Solid State Ion.* **2009**, *180*, 911-916.
- [75] T. Minami, M. Tatsumisago, K. Takada, S. Kondo, *Lithium ion conductive solid electrolyte and process for synthesizing the same* **1994**,
- [76] L. Porz, T. Swamy, B. W. Sheldon, D. Rettenwander, T. Frömling, H. L. Thaman, S. Berendts, R. Uecker, W. C. Carter, Y. M. Chiang, *Adv. Energy Mater.* **2017**, *7*, 1701003.

-
- [77] K. Takada, *Acta Mater.* **2013**, *61*, 759-770.
- [78] B. Zhang, R. Tan, L. Yang, J. Zheng, K. Zhang, S. Mo, Z. Lin, F. Pan, *Energy Storage Mater.* **2018**, *10*, 139-159.
- [79] R. Khurana, J. L. Schaefer, L. A. Archer, G. W. Coates, *J. Am. Chem. Soc.* **2014**, *136*, 7395-7402.
- [80] J. C. Bachman, S. Muy, A. Grimaud, H.-H. Chang, N. Pour, S. F. Lux, O. Paschos, F. Maglia, S. Lupart, P. Lamp, L. Giordano, Y. Shao-Horn, *Chem. Rev.* **2015**, *116*, 140-162.
- [81] A. Manuel Stephan, K. S. Nahm, *Polymer* **2006**, *47*, 5952-5964.
- [82] D. E. Fenton, J. M. Parker, P. V. Wright, *Polymer* **1973**, *14*, 589.
- [83] S. Ibrahim, M. M. Yassin, R. Ahmad, M. R. Johan, *Ionics* **2011**, *17*, 399-405.
- [84] W. Wiczorek, *Solid State Ion.* **1989**, *36*, 255-257.
- [85] S. S. Zhang, *J. Power Sources* **2013**, *231*, 153-162.
- [86] H.-J. Peng, J.-Q. Huang, X.-B. Cheng, Q. Zhang, *Adv. Energy Mater.* **2017**, *7*, 1700260.
- [87] X. Fan, W. Sun, F. Meng, A. Xing, J. Liu, *Green Energy Environ.* **2018**, *3*, 2-19.
- [88] Z. Zhao-Karger, M. Fichtner, *MRS Commun.* **2017**, *7*, 770-784.
- [89] H. Kim, T. S. Arthur, G. D. Allred, J. Zajicek, J. G. Newman, A. E. Rodnyansky, A. G. Oliver, W. C. Boggess, J. Muldoon, *Nat. Commun.* **2011**, *427*, 1-6.
- [90] X. Xu, S. Wang, H. Wang, B. Xu, *J. Energy Storage* **2017**, *13*, 387-400.
- [91] L. Wang, Y. Ye, N. Chen, Y. Huang, L. Li, F. Wu, R. Chen, *Adv. Funct. Mater.* **2018**, *28*, 1800919.
- [92] M. Huang, M. Li, C. Niu, Q. Li, L. Mai, *Adv. Funct. Mater.* **2019**, *29*, 1807847.

References

- [93] X. Hong, J. Mei, L. Wen, Y. Tong, A. J. Vasileff, L. Wang, J. Liang, Z. Sun, S. X. Dou, *Adv. Mater.* **2018**, e1802822.
- [94] J. Zheng, M. Gu, H. Chen, P. Meduri, M. H. Engelhard, J. Zhang, J. Liu, J. Xiao, *J. Mater. Chem.* **2013**, *1*, 8464-8470.
- [95] T. Li, X. Bai, U. Gulzar, Y. J. Bai, C. Capiglia, W. Deng, X. Zhou, Z. Liu, Z. Feng, R. Proietti Zaccaria, *Adv. Funct. Mater.* **2019**, *29*, 1901730.
- [96] A. Manthiram, Y. Fu, Y.-S. Su, *Acc. Chem. Res.* **2012**, *46*, 1125-1134.
- [97] P. G. Bruce, S. A. Freunberger, L. J. Hardwick, J.-M. Tarascon, *Nat. Mater.* **2011**, *11*, 19-29.
- [98] M. Zhao, B.-Q. Li, X.-Q. Zhang, J.-Q. Huang, Q. Zhang, *ACS Cent. Sci.* **2020**, *6*, 1095-1104.
- [99] G. Li, Z. Li, B. Zhang, Z. Lin, *Front. Energ. Res.* **2015**, *3*, 1-12.
- [100] S. Zhang, K. Ueno, K. Dokko, M. Watanabe, *Adv. Energy Mater.* **2015**, *5*, 1500117.
- [101] G. Xu, B. Ding, J. Pan, P. Nie, L. Shen, X. Zhang, *J. Mater. Chem. A* **2014**, *2*, 12662-12676.
- [102] J. Gao, M. A. Lowe, Y. Kiya, H. D. Abruña, *J. Phys. Chem. C* **2011**, *115*, 25132-25137.
- [103] D. Aurbach, O. Youngman, P. Dan, *Electrochim. Acta* **1990**, *35*, 639-655.
- [104] W. Wang, Y. Wang, Y. Huang, C. Huang, Z. Yu, H. Zhang, A. Wang, K. Yuan, *J. Appl. Electrochem.* **2009**, *40*, 321-325.
- [105] C. Barchasz, J.-C. Leprêtre, S. Patoux, F. Alloin, *Electrochim. Acta* **2013**, *89*, 737-743.
- [106] D. Aurbach, E. Pollak, R. Elazari, G. Salitra, C. S. Kelley, J. Affinito, *J. Electrochem. Soc* **2009**, *156*, A694.

- [107] Y. V. Mikhaylik, I. Kovalev, R. Schock, K. Kumaresan, J. Xu, J. Affinito, *ECS Trans.* **2010**, 25, 23-34.
- [108] S. Xin, L. Gu, N.-H. Zhao, Y.-X. Yin, L.-J. Zhou, Y.-G. Guo, L.-J. Wan, *J. Am. Chem. Soc.* **2012**, 134, 18510-18513.
- [109] Y. Z. Zhang, S. Liu, G. C. Li, G. R. Li, X. P. Gao, *J. Mater. Chem.* **2014**, 2, 4652-4659.
- [110] J. Wang, J. Yang, J. Xie, N. Xu, *Adv. Mater.* **2002**, 14, 13-14.
- [111] L. Wang, X. M. He, J. J. Li, M. Chen, J. Gao, C. Y. Jiang, *Electrochim. Acta* **2012**, 72, 114-119.
- [112] J. Fanous, M. Wegner, M. B. M. Spera, M. R. Buchmeiser, *J. Electrochem. Soc.* **2013**, 160, A1169-A1170.
- [113] J. Fanous, M. Wegner, J. Grimminger, M. Rolff, M. B. M. Spera, M. Tenzerb, M. R. Buchmeiser, *J. Mater. Chem.* **2012**, 22, 23240-23245.
- [114] J. Fanous, M. Wegner, J. Grimminger, A. Andresen, M. R. Buchmeiser, *Chem. Mater.* **2011**, 23, 5024-5028.
- [115] J. Scheers, S. Fantini, P. Johansson, *J. Power Sources* **2014**, 255, 204-218.
- [116] Y. Wang, E. Sahadeo, G. Rubloff, C.-F. Lin, S. B. Lee, *J. Mater. Sci.* **2018**, 54, 3671-3693.
- [117] L. Yang, Q. Li, Y. Wang, Y. Chen, X. Guo, Z. Wu, G. Chen, B. Zhong, W. Xiang, Y. Zhong, *Ionics* **2020**, 26, 5299-5318.
- [118] Y. Li, J. G. Shapter, H. Cheng, G. Xu, G. Gao, *Particuology* **2021**, 58, 1-15.
- [119] A. Eftekhari, D.-W. Kim, *J. Mater. Chem. A* **2017**, 5, 17734-17776.
- [120] X. Ji, K. T. Lee, L. F. Nazar, *Nat. Mater.* **2009**, 8, 500-506.
- [121] B. Zhang, X. Qin, G. R. Li, X. P. Gao, *Energy Environ. Sci.* **2010**, 3, 1531.

References

- [122] L. Ji, M. Rao, S. Aloni, L. Wang, E. J. Cairns, Y. Zhang, *Energ. Environ. Sci.* **2011**, *4*, 5053.
- [123] L. Ji, M. Rao, H. Zheng, L. Zhang, Y. Li, W. Duan, J. Guo, E. J. Cairns, Y. Zhang, *J. Am. Chem. Soc.* **2011**, *133*, 18522-18525.
- [124] G. Zheng, Y. Yang, J. J. Cha, S. S. Hong, Y. Cui, *Nano Lett.* **2011**, *11*, 4462-4467.
- [125] R. Elazari, G. Salitra, A. Garsuch, A. Panchenko, D. Aurbach, *Adv. Mater.* **2011**, *23*, 5641-5644.
- [126] S. Dorfler, M. Hagen, H. Althues, J. Tubke, S. Kaskel, M. J. Hoffmann, *Chem. Commun.* **2012**, *48*, 4097-4099.
- [127] Z. Wu, Z. Chen, X. Du, J. M. Logan, J. Sippel, M. Nikolou, K. Kamaras, J. R. Reynolds, D. B. Tanner, A. F. Hebard, A. G. Rinzler, *Science* **2004**, *305*, 1273-1276.
- [128] S. H. Ng, J. Wang, Z. P. Guo, J. Chen, G. X. Wang, H. K. Liu, *Electrochim. Acta* **2005**, *51*, 23-28.
- [129] M. Frey, R. K. Zenn, S. Warneke, K. Müller, A. Hintennach, R. E. Dinnebier, M. R. Buchmeiser, *ACS Energy Lett.* **2017**, *2*, 595-604.
- [130] S. Warneke, M. Eusterholz, R. K. Zenn, A. Hintennach, R. Dinnebier, M. R. Buchmeiser, *J. Electrochem. Soc.* **2018**, *165*, A6017-A6020
- [131] S. Warneke, R. K. Zenn, T. Leberherz, K. Müller, A. Hintennach, U. Starke, R. E. Dinnebier, M. R. Buchmeiser, *Adv. Sustain. Syst.* **2018**, *2*, 1700144-1700149.
- [132] A. Mayer, M. R. Buchmeiser, *J. Electrochem. Soc.* **2018**, *165*, A3943-A3945.
- [133] T. Kojima, H. Ando, N. Takeichi, H. Senoh, *ECS Trans.* **2017**, *75*, 201-206.
- [134] Z. Shi chao, Z. Lan, Y. Jinhua, *J. Power Sources* **2011**, *196*, 10263-10266.
- [135] L. Xiao, Y. Cao, J. Xiao, B. Schwenzer, M. H. Engelhard, L. V. Saraf, Z. Nie, G. J. Exarhos, J. Liu, *Adv. Mater.* **2012**, *24*, 1176-1181.

- [136] Q. Zhang, Q. Huang, S. M. Hao, S. Deng, Q. He, Z. Lin, Y. Yang, *Adv. Sci.* **2022**, *9*, e2103798.
- [137] S. Wei, L. Ma, K. E. Hendrickson, Z. Tu, L. A. Archer, *J. Am. Chem. Soc.* **2015**, *137*, 12143-12152.
- [138] S. Niesen, J. Kappler, J. Trück, L. Veith, T. Weil, T. Soczka-Guth, M. R. Buchmeiser, *J. Electrochem. Soc.* **2021**, *168*, 050510.
- [139] Z. Wu, S. M. Bak, Z. Shadiké, S. Yu, E. Hu, X. Xing, Y. Du, X. Q. Yang, H. Liu, P. Liu, *Appl. Mater. Interfaces* **2021**, *13*, 31733-31740.
- [140] W. Wang, Z. Cao, G. A. Elia, Y. Wu, W. Wahyudi, E. Abou-Hamad, A.-H. Emwas, L. Cavallo, L.-J. Li, J. Ming, *ACS Energy Lett.* **2018**, *3*, 2899-2907.
- [141] S. Zhang, *Energy* **2014**, *7*, 4588-4600.
- [142] R. Shah, V. Mittal, E. Matsil, A. Rosenkranz, *Adv. Mech. Eng.* **2021**, *13*, 168781402110033.
- [143] P. Wang, M. R. Buchmeiser, *Adv. Funct. Mater.* **2019**, *29*, 1905248-1905275.
- [144] Z. Zhao-Karger, X. Zhao, D. Wang, T. Diemant, R. J. Behm, M. Fichtner, *Adv. Energy Mater.* **2014**, *5*, 1401155-1401164.
- [145] R. Davidson, A. Verma, D. Santos, F. Hao, C. Fincher, S. Xiang, J. Van Buskirk, K. Xie, M. Pharr, P. P. Mukherjee, S. Banerjee, *ACS Energy Lett.* **2018**, *4*, 375-376.
- [146] G. Bieker, V. Küpers, M. Kolek, M. Winter, *Commun. Mater* **2021**, *2*.
- [147] L. Kong, C. Yan, J.-Q. Huang, M.-Q. Zhao, M.-M. Titirici, R. Xiang, Q. Zhang, *Energ. Environ. Mater.* **2018**, *1*, 100-112.
- [148] A. Robba, A. Vizintin, J. Bitenc, G. Mali, I. Arčon, M. Kavčič, M. Žitnik, K. Bučar, G. Aquilanti, C. Martineau-Corcos, A. Randon-Vitanova, R. Dominko, *Chem. Mater.* **2017**, *29*, 9555-9564.
- [149] H. D. Yoo, I. Shterenberg, Y. Gofer, G. Gershinsky, N. Pour, D. Aurbach, *Energ. Environ. Sci.* **2013**, *6*, 2265-2279.

References

- [150] H. Tian, T. Gao, X. Li, X. Wang, C. Luo, X. Fan, C. Yang, L. Suo, Z. Ma, W. Han, C. Wang, *Nat. Commun.* **2017**, *8*, 14083.
- [151] W. Li, S. Cheng, J. Wang, Y. Qiu, Z. Zheng, H. Lin, S. Nanda, Q. Ma, Y. Xu, F. Ye, M. Liu, L. Zhou, Y. Zhang, *Angew. Chem.* **2016**, *128*, 6516-6520; *Angew. Chem. Int. Ed.* **2016**, *55*, 6406–6410.
- [152] Z. Zhang, B. Chen, H. Xu, Z. Cui, S. Dong, A. Du, J. Ma, Q. Wang, X. Zhou, G. Cui, *Adv. Funct. Mater.* **2018**, *28*, 1701718.
- [153] Z. Zhao-Karger, X. Zhao, O. Fuhr, M. Fichtner, *RSC Adv.* **2013**, *3*, 16330.
- [154] T. Gao, M. Noked, A. J. Pearse, E. Gillette, X. Fan, Y. Zhu, C. Luo, L. Suo, M. A. Schroeder, K. Xu, S. B. Lee, G. W. Rubloff, C. Wang, *J. Am. Chem. Soc.* **2015**, *137*, 12388-12393.
- [155] X. Yu, M. Arumugam, *ACS Energy Lett.* **2016**, *1*, 431-437.
- [156] T. Gao, S. Hou, F. Wang, Z. Ma, X. Li, K. Xu, C. Wang, *Angew. Chem.* **2017**, *129*, 13711–13715 *Angew. Chem. Int. Ed.* **2017**, *129*, 13526-13530.
- [157] P. Wang, K. Küster, U. Starke, C. Liang, R. Niewa, M. R. Buchmeiser, *J. Power Sources* **2021**, *515*, 230604.
- [158] P. Wang, J. Trück, S. Niesen, J. Kappler, K. Küster, U. Starke, F. Ziegler, A. Hintennach, M. R. Buchmeiser, *Batter. Supercaps* **2020**, *3*, 1239-1247.
- [159] S. B. Son, T. Gao, S. P. Harvey, K. X. Steirer, A. Stokes, A. Norman, C. Wang, A. Cresce, K. Xu, C. Ban, *Nat. Chem.* **2018**, *10*, 532-539.
- [160] Z. Li, T. Diemant, Z. Meng, Y. Xiu, A. Reupert, L. Wang, M. Fichtner, Z. Zhao-Karger, *ACS Appl. Mater. Interfaces* **2021**, *13*, 33123-33132.
- [161] H. Kaland, F. Haskjold Fagerli, J. Hadler-Jacobsen, Z. Zhao-Karger, M. Fichtner, K. Wiik, N. P. Wagner, *ChemSusChem* **2021**, *14*, 1864-1873.
- [162] S. Zhang, Y. Huang, Y. NuLi, B. Wang, J. Yang, J. Wang, *J. Phys. Chem. C* **2020**, *124*, 20712-20721.

- [163] P. Bonnicks, J. Muldoon, *Adv. Funct. Mater.* **2020**, *30*, 1910510.
- [164] Y. Lu, C. Wang, Q. Liu, X. Li, X. Zhao, Z. Guo, *Small Methods* **2021**, *5*, 2001303.
- [165] Y. Xu, Y. Ye, S. Zhao, J. Feng, J. Li, H. Chen, A. Yang, F. Shi, L. Jia, Y. Wu, X. Yu, P. A. Glans-Suzuki, Y. Cui, J. Guo, Y. Zhang, *Nano Lett.* **2019**, *19*, 2928-2934.
- [166] J. Sun, C. Deng, Y. Bi, K.-H. Wu, S. Zhu, Z. Xie, C. Li, R. Amal, J. Luo, T. Liu, D.-W. Wang, *ACS Appl. Energy Mater.* **2020**, *3*, 2516-2525.
- [167] H. Ye, Y. Li, *InfoMat* **2022**, e12291.
- [168] J. Song, E. Sahadeo, M. Noked, S. B. Lee, *J. Phys. Chem. Lett.* **2016**, *7*, 1736-1749.
- [169] J. Luo, S. He, T. L. Liu, *ACS Energy Lett.* **2017**, *2*, 1197-1202.
- [170] G. Bieker, M. Salama, M. Kolek, Y. Gofer, P. Bieker, D. Aurbach, M. Winter, *ACS Appl. Mater. Interfaces* **2019**, *11*, 24057-24066.
- [171] I. Shterenberg, M. Salama, H. D. Yoo, Y. Gofer, J.-B. Park, Y.-K. Sun, D. Aurbach, *J. Electrochem. Soc.* **2015**, *162*, A7118-A7128.
- [172] L. F. Nazar, M. Cuisinier, Q. Pang, *MRS Bull.* **2014**, *39*, 436-442.
- [173] B. P. Vinayan, Z. Zhao-Karger, T. Diemant, V. S. Chakravadhanula, N. I. Schwarzburger, M. A. Cambaz, R. J. Behm, C. Kubel, M. Fichtner, *Nanoscale* **2016**, *8*, 3296-3306.
- [174] F. Wu, G. Yushin, *Energ. Environ. Sci.* **2017**, *10*, 435-459.
- [175] R. Chen, T. Zhao, F. Wu, *Chem. Commun.* **2015**, *51*, 8-33.
- [176] Y. X. Yin, S. Xin, Y. G. Guo, L. J. Wan, *Angew. Chem.* **2013**, *1258*, 13426-13441; *Angew. Chem. Int. Ed.* **2013**, *52*, 13186.
- [177] L. Yin, J. Wang, J. Yang, Y. Nuli, *J. Mater. Chem.* **2011**, *21*, 6807.
- [178] T. Cleaver, P. Kovacic, M. Marinescu, T. Zhang, G. Offer., *J. Electrochem. Soc.* **2018**, *165*, A6029-A6033.

References

- [179] W. Kang, N. Deng, J. Ju, Q. Li, D. Wu, X. Ma, L. Li, M. Naebe, B. Cheng, *Nanoscale* **2016**, *8*, 16541-16588.
- [180] A. Du, Z. Zhang, H. Qu, Z. Cui, L. Qiao, L. Wang, J. Chai, T. Lu, S. Dong, T. Dong, H. Xu, X. Zhou, G. Cui, *Energ. Environ. Sci.* **2017**, *10*, 2616-2625.
- [181] D.-M. Kim, S. C. Jung, S. Ha, Y. Kim, Y. Park, J. H. Ryu, Y.-K. Han, K. T. Lee, *Chem. Mater.* **2018**, *30*, 3199-3203.
- [182] Y. Li, Y. Zhang, M. Yu, H. Pei, W. Liu, R. Guo, J. Xie, Y. Wang, C. Yang, *Lightweight flexible sulfur electrode and preparation method and application* **2019**,
- [183] S. Y. Ha, Y. W. Lee, S. W. Woo, B. Koo, J. S. Kim, J. Cho, K. T. Lee, N. S. Choi, *ACS Appl. Mater. Interfaces* **2014**, *6*, 4063-4073.
- [184] Z. Zhao-Karger, M. E. G. Bardaji, O. Fuhr, M. Fichtner, *J. Mater. Chem. A* **2017**, *5*, 10815-10820.
- [185] H. Du, Z. Zhang, J. He, Z. Cui, J. Chai, J. Ma, Z. Yang, C. Huang, G. Cui., *Small* **2017**, *13*, 1702277.
- [186] A. C. Kozen, C. F. Lin, A. J. Pearse, M. A. Schroeder, X. Han, L. Hu, S. Lee, G. W. Rubloff, M. Noked, *ACS Nano*. **2015**, *9*, 5884–5892.
- [187] W. Q. Wang, H. C. Yuan, Y. Nuli, J. J. Zhou, J. Yang, J. L. Wang, *J. Phys. Chem. C* **2018**, *122*, 26764-26776.
- [188] X. Zhou, J. Tian, J. Hu, C. Li, *Adv. Mater.* **2018**, *30*, 1704166.
- [189] T. Gao, X. Ji, S. Hou, X. Fan, X. Li, C. Yang, F. Han, F. Wang, J. Jiang, K. Xu, C. Wang, *Adv. Mater.* **2018**, *30*, 1704313.
- [190] D. T. Nguyen, R. Horia, A. Y. S. Eng, S. W. Song, Z. W. Seh, *Mater. Horiz.* **2021**, *8*, 830-853.
- [191] L. Zeng, N. Wang, J. Yang, J. Wang, Y. NuLi, *J. Electrochem. Soc.* **2017**, *164*, A2504-A2512.

- [192] D. Huang, S. Tan, M. Li, D. Wang, C. Han, Q. An, L. Mai, *ACS Appl. Mater. Interfaces* **2020**, *12*, 17474-17480.
- [193] A. Robba, M. Mežnar, A. Vizintin, J. Bitenc, J. Bobnar, I. Arčon, A. Randon-Vitanova, R. Dominko, *J. Power Sources* **2020**, *450*, 227672.
- [194] Z. Zhao-Karger, R. Liu, W. Dai, Z. Li, T. Diemant, B. P. Vinayan, C. Bonatto Minella, X. Yu, A. Manthiram, R. J. Behm, M. Ruben, M. Fichtner, *ACS Energy Lett.* **2018**, *3*, 2005-2013.
- [195] P. Wang, J. Kappler, B. Sievert, J. Häcker, K. Küster, U. Starke, F. Ziegler, M. R. Buchmeiser, *Electrochim. Acta* **2020**, *361*, 137024.
- [196] P. Wang, J. Trück, J. Häcker, A. Schlosser, K. Küster, U. Starke, L. Reinders, M. R. Buchmeiser, *Energy Storage Mater.* **2022**, *49*, 509-517.
- [197] J. Trück, P. Wang, E. Buch, J. Groos, S. Niesen, M. R. Buchmeiser, *J. Electrochem. Soc.* **2022**, *169*, 010505.
- [198] Z. Zhou, B. Chen, T. Fang, Y. Li, Z. Zhou, Q. Wang, J. Zhang, Y. Zhao, *Adv. Energy Mater.* **2019**, *10*, 1902023.
- [199] Y. Cheng, Y. Shao, J. G. Zhang, V. L. Sprenkle, J. Liu, G. Li, *Chem. Commun.* **2014**, *50*, 9644-9646.
- [200] Y. Yang, W. Wang, Y. Nuli, J. Yang, J. Wang, *ACS Appl. Mater. Interfaces* **2019**, *11*, 9062-9072.
- [201] B. Sievert, J. Häcker, F. Bienen, N. Wagner, K. A. Friedrich, *ECS Trans.* **2017**, *77*, 413-424
- [202] R. Mohtadi, F. Mizuno, *Beilstein J. Nanotechnol.* **2014**, *5*, 1291-1311.
- [203] T. J. Carter, R. Mohtadi, T. S. Arthur, F. Mizuno, R. Zhang, S. Shirai, J. W. Kampf, *Angew. Chem.* **2014**, *126*, 3237-3241; *Angew. Chem. Int. Ed.* **2014**, *53*, 3173.
- [204] Y. He, Q. Li, L. Yang, C. Yang, D. Xu, *Angew. Chem.* **2019**, *131*, 7697-7701; *Angew. Chem. Int. Ed.* **2019**, *58*, 7615.

References

- [205] H. Zhao, J. Xu, D. Yin, Y. Du, *Chem.-Eur. J.* **2018**, *24*, 18220-18234.
- [206] Y. Pan, S. Li, M. Yin, J. Li, *Energy Technol.* **2019**, 1900164.
- [207] P. Saha, M. K. Datta, O. I. Velikokhatnyi, A. Manivannan, D. Alman, P. N. Kumta, *Prog. Mater Sci.* **2014**, *66*, 1-86.
- [208] J. Muldoon, C. B. Bucur, T. Gregory, *Angew. Chem.* **2017**, *129*, 12232-12253; *Angew. Chem. Int. Ed.* **2017**, *56*, 12064.
- [209] Y. Xu, W. Li, G. Zhou, Z. Pan, Y. Zhang, *Energy Storage Mater.* **2018**, *14*, 253-257.
- [210] C. Liebenow, Z. Yang, P. Lobitz, *Electrochem. Commun.* **2000**, *2*, 641.
- [211] X. Zhao, Y. Yang, Y. NuLi, D. Li, Y. Wang, X. Xiang, *Chem. Commun.* **2019**, *55*, 6086-6089.
- [212] D. Muthuraj, A. Ghosh, A. Kumar, S. Mitra, *ChemElectroChem* **2018**, *6*, 684-689.
- [213] Y. Nuli, X. Zhao, Y. Yang, J. Yang, J. Wang, *One kind of rechargeable magnesium battery electrolyte and rechargeable magnesium battery* **2019**,
- [214] W. E. Geiger, F. Barrier, *Acc. Chem. Res.* **2010**, *43*, 1030-1039.
- [215] I. Krossing, I. Raabe, *Angew. Chem.* **2004**, *116*, 2116-2142; *Angew. Chem. Int. Ed.* **2004**, *43*, 2066.
- [216] F. Barriere, W. E. Geiger, *J. Am. Chem. Soc.* **2006**, *128*, 3980-3989.
- [217] Z. Zhang, Z. Cui, L. Qiao, J. Guan, H. Xu, X. Wang, P. Hu, H. Du, S. Li, X. Zhou, S. Dong, Z. Liu, G. Cui, L. Chen, *Adv. Energy Mater.* **2017**, *7*, 1602055.
- [218] H. Xu, Z. Zhang, J. Li, L. Qiao, C. Lu, K. Tang, S. Dong, J. Ma, Y. Liu, X. Zhou, G. Cui, *ACS Appl. Mater. Interfaces* **2018**, *10*, 23757-23765.
- [219] Y. Xu, G. Zhou, S. Zhao, W. Li, F. Shi, J. Li, J. Feng, Y. Zhao, Y. Wu, J. Guo, Y. Cui, Y. Zhang, *Adv. Sci.* **2019**, *6*, 1800981-1800987.

- [220] V. Bhaghavathi Parambath, Z. Zhao-Karger, T. Diemant, M. Jäckle, Z. Li, T. Scherer, A. Gross, R. J. Behm, M. Fichtner, *J. Mater. Chem. A* **2020**, *8*, 22998-23010.
- [221] K. Tang, A. Du, S. Dong, Z. Cui, X. Liu, C. Lu, J. Zhao, X. Zhou, G. Cui, *Adv. Mater.* **2019**, *32*, e1904987.
- [222] S. Li, W. Zhang, J. Zheng, M. Lv, H. Song, L. Du, *Adv. Energy Mater.* **2020**, *11*, 2000779.

Chapter 11

Curriculum Vitae

Personal Data

Name: Peiwen Wang
Date of Birth: 20.05.1992
Place of Birth: Shanghai, China
Nationality: Chinese



Education

03/2019 - present	Universität Stuttgart Ph.D Candidate Institute of Polymer Chemistry Prof. Buchmeiser Thesis: Novel Electrolyte Systems for High Performance Magnesium Batteries
03/2018 - 01/2019	Universität Stuttgart Master Thesis & Internship Institute of Polymer Chemistry Prof. Buchmeiser Thesis: Mg-S Batteries Based on SPAN (Grade: 1.0, sehr gut)
04/2017 – 03/2018	Universität Stuttgart Master of Science Materials Science Grade: 1.2, sehr gut
09/2014 – 09/2016	Loughborough University (UK) Exchange Student & Master of Science Polymer Science Grade: 90/100 with Distinction (top 1)
09/2010 – 09/2014	Tongji University (China Top 10) Bachelor of Science Polymer Science Grade: 85/100

Awards

Max Planck Institute Fellowship (Germany)	2017 – 2019
Prof. DR Gabe Prize (UK)	2016, the best Master student
John Goodwin Memorial Prize (UK)	2016, the best Master thesis

Publications

-
1. A Design Concept for Halogen-free Mg²⁺/Li⁺-Dual-Salt-Containing Gel-Polymer-Electrolytes for Rechargeable Magnesium Batteries
P. Wang, J. Trück, J. Häcker, A. Schlosser, K. Küster, U. Starke, L. Reinders, M. R. Buchmeiser, *Energy Storage Mater.* **2022**, *49*, 509-517.
 2. Lithium Titanate as Mg-Ion Insertion Anode for Mg-Ion/Sulfur Batteries Based on Sulfurated Poly(acrylonitrile)
J. Trück, P. Wang, E. Buch, J. Groos, S. Niesen, M. R. Buchmeiser, *J. Electrochem. Soc.* **2022**, *169*, 010505.
 3. Performance Enhancement of Rechargeable Magnesium-Sulfur Batteries Based on a Sulfur Poly(acrylonitrile) Composite and a Lithium Salt
P. Wang, K. Küster, U. Starke, C. Liang, R. Niewa, M. R. Buchmeiser, *J. Power Sources* **2021**, *515*, 230604.
 4. High-Performance Magnesium-Sulfur Batteries Based on a Sulfurated Poly(acrylonitrile) Cathode, a Borohydride Electrolyte and a High-Surface Area Magnesium Anode
P. Wang, J. Trück, S. Niesen, J. Kappler, K. Küster, U. Starke, F. Ziegler, A. Hintennach, M. R. Buchmeiser, *Batter. Supercaps* **2020**, *3*, 1239-1247.
 5. Characteristics of magnesium-sulfur batteries based on a sulfurized poly(acrylonitrile) composite and a fluorinated electrolyte
P. Wang, J. Kappler, B. Sievert, J. Häcker, K. Küster, U. Starke, F. Ziegler, M. R. Buchmeiser, *Electrochim. Acta* **2020**, *361*, 137024.
 6. Rechargeable Magnesium-Sulfur Battery Technology: State of the Art and Key Challenges
P. Wang, M. R. Buchmeiser, *Adv. Funct. Mater.* **2019**, *29*, 1905248-1905275.
 7. Effect of Antibacterial Plant Extracts on the Morphology of Electrospun Poly(Lactic Acid) Fibres
P. Wang, E. Mele, *Materials*, **2018**, *11*, 923.

Patents

1. Borate-based Gel-Polymer Electrolyte for Rechargeable Magnesium Batteries
M. R. Buchmeiser, P. Wang (University of Stuttgart), patent pending (2021)
2. Magnesium sulfur battery with high discharge capacity
P. Wang, M. R. Buchmeiser (University of Stuttgart), EP3826095A1.

Oral Presentation

- 2021 “Electrochemical performance of Mg-S batteries using a dual salt electrolyte.” Online Kolloquium InnovationsCampus Mobilität der Zukunft, Stuttgart, Germany

Conferences

1. A Novel Modelling Approach for Metal-SPAN Batteries
S. Kezia, T. Danner, P. Wang, M. R. Buchmeiser, International Conference on Lithium-Sulfur Batteries (2021)
2. Electrospinning effect on the relaxation molecular dynamics of poly(D,L-lactide) via dielectric relaxation spectroscopy
S. Drakopoulos, G. Psarras, P. Wang, E. Mele, 29th European Conference on Biomaterials

Chapter 11

Review Publication

In the beginning of this PhD work (March 2019), I got the possibility to write a review article in the area of Mg-S batteries. Although the review article does not count into the “accumulative dissertation”, it could give a comprehensive overview and summary regarding the progress and challenges of the Mg-S batteries at that time. Hence, this review article entitled “*Rechargeable Magnesium-Sulfur Battery Technology: State of the Art and Key Challenges*” is also attached as the last chapter of the thesis.

It is not difficult and also exciting to realize that some major progresses or milestones have been accomplished in the field of Mg-S batteries within the three years, although there are still numerous challenges in this field.

Publication

P. Wang, M. R. Buchmeiser, *Adv. Funct. Mater.* **2019**, 29, 1905248-1905275.

Author Contributions: P. Wang: Conceptualization, Writing - original draft, Writing - review & editing; M. R. Buchmeiser: Conceptualization, Supervision, Writing - original draft, Writing - review & editing.

Reprinted with permission from the © 2019 WILEY-VCH Verlag GmbH & Co. KGaA, Weinheim.

Rechargeable Magnesium–Sulfur Battery Technology: State of the Art and Key Challenges

Peiwen Wang and Michael R. Buchmeiser*

Inspired by the first rechargeable Mg battery about 20 years ago, based on a Chevrel phase cathode, a Mg foil anode, and a magnesium organo-aluminate electrolyte, research on rechargeable batteries using sulfur as the cathode together with Mg as the anode has gained substantial and increasing interest. In particular, the safety characteristics of magnesium–sulfur (Mg–S) batteries, the high abundance of both magnesium and sulfur, and the high theoretical volumetric energy density of magnesium render this system specifically interesting for mobile applications that require high volumetric energy densities, i.e., the automotive and aviation sector. While the development of Mg–S batteries is still at a nascent stage, some breakthroughs have already been accomplished. Consequently, it appears necessary to provide a comprehensive up-to-date review about the current achievements to facilitate further improvements in this field. In this review, the state of the art in Mg–S batteries is summarized, focusing on sulfur conversion cathodes, magnesium anode materials, currently employed electrolyte systems, as well as on current collectors and separator design. In addition, the challenges and some possible future work to realize a practically applicable and technically viable Mg–S battery are highlighted.

due to the emerging of LIBs in 1991.^[6] The main advantages of LIBs, including stable electrochemistry and long cycle life, has made LIBs one of the leading technologies of electric energy storage during that time.^[7] They have been commercialized in the areas of portable applications, electric vehicles and mobile robotics.^[7] After the year 2000, the need for high energy density in applications, such as military power supply, led to the resurgent of Li–S batteries, because of their high theoretical energy density (2600 Wh kg⁻¹), which is about four to five times higher than that of LIBs.^[5,8]

Despite its favorable electrochemical characteristics, Li–S batteries suffer from several drawbacks. On the one hand, the formation of a passivation film generated from dissolved corrosive polysulfides as well as continuous lithium erosion is critically limiting the performance of Li–S cells.^[9,10] On the other hand, lithium-based batteries display some safety issues,

such as the uncontrolled formation of lithium dendrites, which bear the potential to pierce the separators and lead to short microcircuits.^[9,11,12] At the same time, lithium dendrites tend to dissolve in the local region and detach from lithium anodes, resulting in delithiation and formation of “dead” lithium. This can further decrease cycle stability and specific capacities.^[9,13–15]

As an alternative to Li–S batteries, rechargeable Mg–S batteries (Figure 1c), first reported by a research group of Toyota Motor Corp. in 2011,^[12] show some attractive advantages and research in this field has recently accelerated (Figure 1a).^[16] The mechanism of Mg–S batteries is based on the redox reactions between Mg and sulfur. During discharge, the Mg anode is oxidized to form Mg²⁺ ions and two electrons. Mg²⁺ migrates to the sulfur cathode through the electrolytes and separators, whereas the electron transfer from the anode to the cathode proceeds via an external electrical circuit. On the cathode side, sulfur is stepwise converted into long chain polysulfides, short chain polysulfides and, finally, MgS. During charging, Mg²⁺ ions are reduced and deposited (plated) onto the anode. The magnesium (poly)sulfides are ideally reoxidized to their original state, i.e., to sulfur.

Mg–S batteries show the following advantages. Magnesium generally does not plate in a dendritic manner, which translates into better safety characteristics of Mg anodes.^[17] Moreover, Mg–S cells possess a higher theoretical volumetric capacity than Li–S batteries (2062 vs 3832 mAh cm⁻³) due to the divalent nature of Mg²⁺^[17] and the higher physical density of magnesium (0.53 vs 1.74 g cm⁻³).^[18] In addition, Mg is the fifth-most

1. Introduction

Since Volta's invention, energy storage technology has shown a great potential in the field of portable and mobile electrical power applications, especially in the automotive industry.^[1,2] In the field of rechargeable batteries, lithium-ion batteries (LIBs) currently represent the dominating cell technology; nonetheless, lithium–sulfur (Li–S) batteries clearly have the potential and a level of readiness to replace LIBs in the near future.^[3,4] In the 1960s, Herbert et al. published a US Patent in the field of Li–S batteries.^[5] However, the research on Li–S batteries was paused

P. Wang, Prof. M. R. Buchmeiser
Institute of Polymer Chemistry
University of Stuttgart
70569 Stuttgart, Germany
E-mail: michael.buchmeiser@ipoc.uni-stuttgart.de

Prof. M. R. Buchmeiser
German Institutes of Textile and Fiber Research (DITF) Denkendorf
73770 Denkendorf, Germany

 The ORCID identification number(s) for the author(s) of this article can be found under <https://doi.org/10.1002/adfm.201905248>.

© 2019 The Authors. Published by WILEY-VCH Verlag GmbH & Co. KGaA, Weinheim. This is an open access article under the terms of the Creative Commons Attribution License, which permits use, distribution and reproduction in any medium, provided the original work is properly cited.

DOI: 10.1002/adfm.201905248

abundant metal on earth.^[19] In view of these merits and the high abundance of sulfur, increasing interest has been raised on post Li–S battery systems, including magnesium–selenium batteries, Mg–S batteries, which display higher energy density, low costs and improved safety in comparison to Li–S batteries.^[11, 20–23]

Despite the advantages of Mg–S batteries, major issues in this field are related to the severe overcharge behavior and low sulfur utilization of the cathode during charging and discharging in general, the formation of magnesium polysulfides and the slow diffusion of Mg²⁺, which all result in poor electrochemical behavior.^[17, 22, 24, 25] Substantial efforts have been made to improve cell performance so far, including the modification of cathode materials, anodes and separators,^[25] the synthesis of novel electrolyte systems,^[24, 26] which all to some extent can improve the cell behavior. Figure 1d gives a timeline of all the novel findings in the area of Mg–S batteries in each year. Figure 1b demonstrates an overview of the topics addressed in the published research articles in Mg–S batteries. According to this survey, the research community developed a strong preference for investigating novel electrolyte systems, modifying sulfur cathode materials and carrying out mechanistic studies. By contrast, only few research groups devoted their work to the other components of a Mg–S battery, such as the anode and the separator. Major improvements related to the latter two will also be thoroughly discussed in the following sections.

Several reviews already discussed the developments in Mg batteries based on intercalation cathode materials.^[1, 15, 27–30] By contrast, accounts on Mg batteries containing a sulfur-based conversion cathode, which benefits from high theoretical energy density, a reasonable potential difference with Mg, nontoxicity and high earth abundance^[11, 31, 32] are rare. This review solely refers to Mg–S batteries that use sulfur-based conversion cathodes.

The purposes of this review are to summarize and highlight the most up-to-date and novel findings for Mg–S batteries, addressing sulfur-based conversion cathodes and Mg anode materials, separator modifications as well as various electrolyte systems. Furthermore, since the research on Mg–S batteries is still at an initial stage, some challenges, including the capacity decay mechanism, a lack of suitable electrolyte systems and the passivation of the Mg anode, which so far impedes any superior electrochemical performance in Mg–S batteries, will also be addressed. In addition, we also listed and discussed some possible future prospects for high energy Mg–S batteries. Finally, the currently reported Mg–S systems have been summarized in a table for easy comparison.

This review on rechargeable Mg–S batteries is arranged in the following sequences. In the first section, currently applied anode materials (various forms of Mg anodes) and prospective anodes are discussed. Next, various sulfur-based conversion cathodes, which mainly focus on sulfur accommodated in micro/meso/nanoporous carbon materials are introduced. This section is followed by the discussion about the performance of different current collectors, especially of concomitantly used Cu current collectors together with a nucleophilic electrolyte. Further on, electrolyte systems are thoroughly explained, in the sequence of nucleophilic electrolytes and nonnucleophilic electrolytes. Specifically, nonnucleophilic electrolytes are outlined in a detailed manner, including hexamethyldisilazide (HMDS), bis(trifluoromethanesulfonyl)imide (TFSI), and boron-based electrolytes. Also, various additives that are beneficial for cell performance, such as Li salts, are explained. Furthermore, recent



Peiwen Wang received her bachelor's degree from Shanghai Tongji University, China. After obtaining her first master's degree in polymer science from Loughborough University (UK), she received a Max Planck Fellowship and obtained her second master's degree in materials science from Stuttgart University, Germany. Since 2019, she is pursuing her Ph.D. studies in Prof. Buchmeiser's group working on high-performance magnesium–sulfur batteries.



Michael R. Buchmeiser received his doctoral degree from the University of Innsbruck, Austria. After a year of postdoctoral research at MIT (Prof. R. R. Schrock), he became first Assistant, and after his “Habilitation” in Macromolecular Chemistry, Associate Professor. During 2000–2001, he was Visiting Professor at the Graz

University of Technology, Austria; from 2004 to 2009, he was Full Professor at the University of Leipzig, Germany. Since 2009, he holds the Chair in Macromolecular Compounds and Fiber Chemistry at the University of Stuttgart, Germany. His current research interests include all aspects of synthetic polymer chemistry and polymerization catalysis and their application to material science including fibers and batteries.

progress in separator design, which can to some extent solve the problem of the reoxidation of MgS, is discussed. Finally, full device design and interface issues of the electrodes are briefly introduced. Conclusions, current challenges and an outlook to future investigation in the area of high-energy Mg–S batteries are provided.

2. Anode Materials

In the field of Mg–S batteries, the Mg anode plays a crucial role in electrochemical performance since the interactions between the Mg metal and electrolyte have a direct influence on the electrochemical performance.^[1, 15, 19, 27–30, 33, 34] It is well known that the blocking layers on the Mg anode formed via electrolyte decomposition or reaction with traces of water and oxygen prevent the diffusion of Mg²⁺ ions; consequently, the reversible Mg deposition and dissolution are impeded.^[19, 33, 34] For instance, polar aprotic solvents including carbonates and nitriles, tend to form an impermeable layer on the metal surface, which limits the variety of the electrolyte.^[34–36] Surprisingly, compared to the

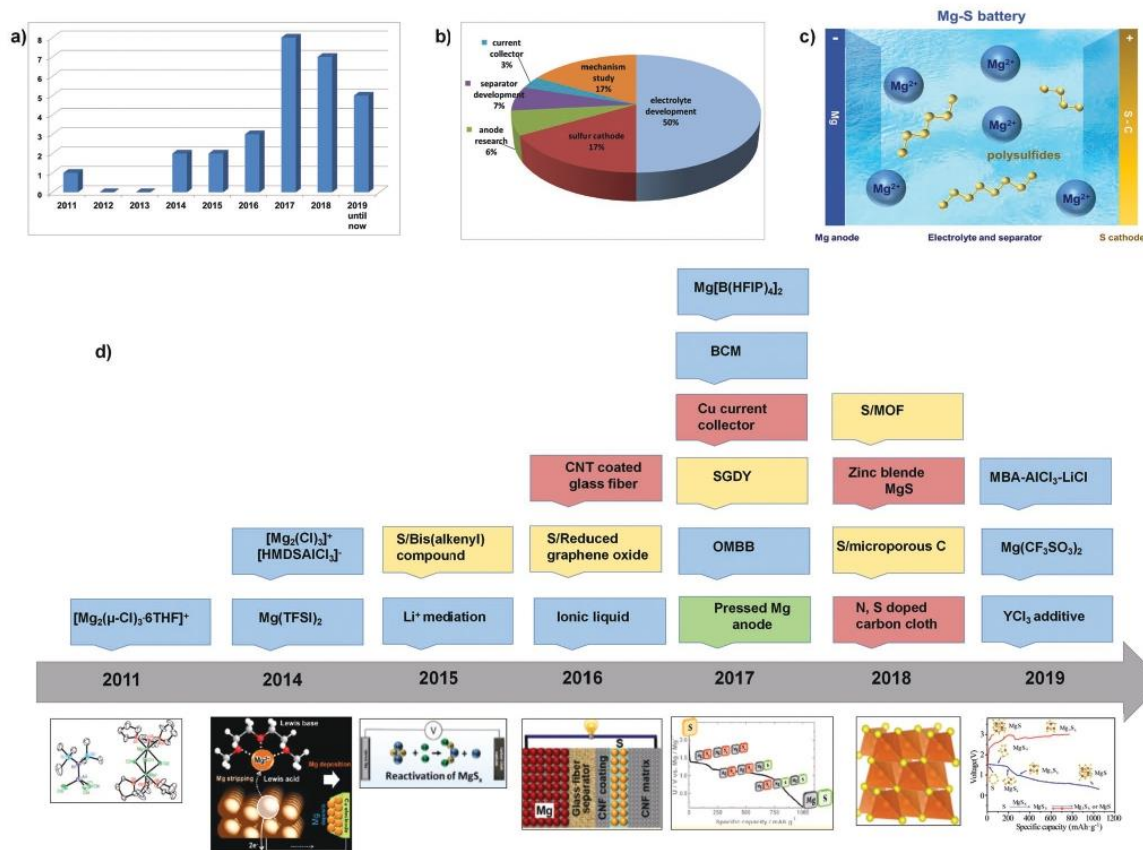


Figure 1. a) The growing trend of research interest in Mg-S batteries, number of published articles on Mg-S batteries since 2011; b) a comparison of topics addressed in all the published research articles about batteries containing a Mg anode and a sulfur-based conversion cathode; c) a schematic illustration of a Mg-S battery with a sulfur-based cathode and a Mg anode, separated by a separator and the electrolyte. Mg²⁺ ions are produced through electrochemical reaction between the Mg anode and the sulfur cathode; d) novel findings in terms of electrolyte (blue), sulfur-based cathode (yellow), anode (green), and current collector and separator (pink). Reproduced with permission.^[12] Copyright 2011, Nature Publishing Group. Reproduced with permission.^[37] Copyright 2014, American Chemical Society. Reproduced with permission.^[24] Copyright 2015, American Chemical Society. Reproduced with permission.^[25] Copyright 2016, American Chemical Society. Reproduced with permission.^[18] Copyright 2017, American Chemical Society. Reproduced with permission.^[96] Copyright 2018, American Chemical Society. Reproduced with permission.^[95] Copyright 2019, American Chemical Society.

number of studies carried out on different electrolyte systems and cathode materials, comparably few research groups dedicated their work to the anode material.

2.1. Forms of Mg Metal Currently Used as Anode Material

Among all reported Mg-S batteries, currently used anode materials are mainly composed of metallic magnesium in form of magnesium discs,^[37,38] plates,^[24] ribbons,^[39] or foils.^[18,24,25,37,40-43] These types of anodes generally have a low surface area. As already outlined, Mg does not form dendrites during charge. While this substantially improves safety and longevity of the anode, it prevents the formation of new and reactive anode surface, which in terms negatively influences cycle behavior.

Friedrich and co-workers^[44] addressed this issue and reported on pressed magnesium powder anodes with an increased

surface area. They compared the electrochemical performance of anodes based on pressed and conventional magnesium foil, respectively. For the preparation of powder-based magnesium anodes, they ball-milled a mixture of magnesium powder and graphite powder in a weight ratio of 4:1 and compressed the ground powder with a hydraulic press and a dye at 75 and 350 MPa, respectively. The resulting anodes were termed pressed anode at low pressure (PALP) and pressed anode at high pressure (PAHP).^[44] The authors stated that the PALP anode showed a dull surface and could soak more electrolyte than the PAHP anode and Mg foil, which both had a shiny surface. In order to compare the electrochemical behavior of cells based on these different anode materials, the authors conducted cycle tests with a cathode material containing 50 wt% elemental sulfur (50S) using an [HMDS]₂Mg-based electrolyte system at 0.1 C (Figure 2).

Clearly, cells containing a pressed anode (Figure 2a,b) showed better Coulombic efficiencies than those based on a

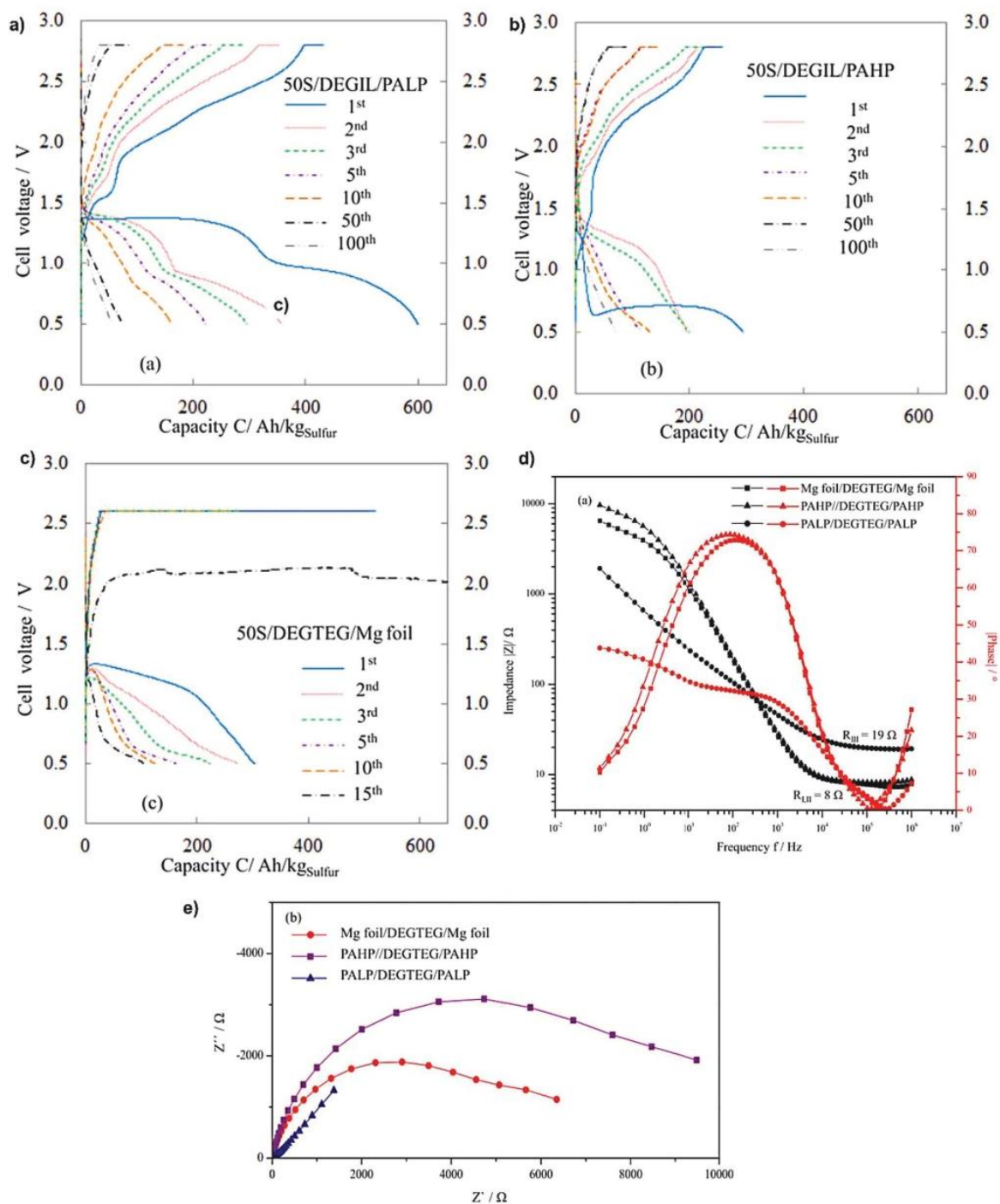


Figure 2. Electrochemical behavior of cells using a) a pressed anode prepared at low pressure with diglyme and an ionic liquid (DEGIL) as electrolyte solvent; b) a pressed anode prepared at high pressure; c) magnesium foil, diglyme and tetraglyme (DEGTEG) as solvent and a cathode material containing 50 wt% elemental sulfur, 0.1 C; and d) Bode and e) Nyquist plots for symmetrical magnesium cells with Mg foil, a PAHP anode and a PALP anode.^[44] Reproduced with permission.^[44] Copyright 2017, ECS Transactions.

Mg foil (Figure 2c) due to a more efficient charging.^[44] Furthermore, cells containing pressed anodes lasted for 100 cycles while those based on Mg foil were reported to fail after only 15 cycles.^[44] Notably, the authors also found that cells containing pressed anodes prepared at low pressure showed better electrochemical behavior and better voltage plateau recovery than those based on PAHP.^[44] According to Figure 2a, a PALP-based cell gave an initial discharge capacity of 600 mAh g⁻¹ sulfur and clearly showed two voltage plateaus at 1.4 and 1.1 V,^[44] respectively, indicating the formation of magnesium polysulfides. The recovered voltage plateaus were also observed in the second and third cycles. However, after ten cycles, the voltage plateau at 1.4 V vanished.^[44] By comparison, a cell (Figure 2b) showed only one plateau at 0.7 V in the initial cycle. In the second and third cycles, the voltage plateau increased to 1.3 V. In the following cycles, the plateaus were hardly visible.^[44] Figure 2d shows the Ohmic resistance, which is in general a result of the contact resistance of the current collector, the cell configuration, the inner electrode resistance and the electrolyte resistance.^[44] These three symmetric Mg–Mg cell setups, for which the same electrolyte but three different forms of anodes were used (PALP, PAHP, and foil), clearly revealed the origin of the Ohmic resistance, which is related to the different physical forms of the anodes. According to Figure 2d, the Ohmic resistance of a cell based on Mg foil or PAHP was 8 Ω; whereas the Ohmic resistance of a PALP anode was 19 Ω. The much higher Ohmic resistance of the PALP anodes was attributed to the electrolyte soaked into the electrode. The Nyquist plots in Figure 2e also prove the higher porosity of the PALP anodes, since the phase angle with PALP anodes (–45°) is lower than that of anodes based on Mg foil or PAHP (–90°). In summary, pressed Mg anodes, PALP, at least to some extent, improve the whole cell performance.

2.2. Prospective Anodes

Carbonate-based solvents are known to be noncorrosive and more stable versus anodic oxidation compared to ether-based solvents.^[45] However, the reaction between the Mg metal and carbonate solvents tends to form an impermeable layer on top of the Mg anode, which in turn prevents Mg deposition during charging.^[33,46,47] Therefore, to compensate for that, the design of an appropriate conductive and protective artificial interphase on Mg anodes presents a potentially feasible approach.^[46,48–50] Further on, a physically deposited atomic layer, which is thin and conductive, might also be an attractive approach to protect the metal surface from corrosion by tracers of oxygen or water, sulfur and the electrolyte.^[51] Due to the special application in battery technology, the traditional technologies such as chemical vapor deposition and physical vapor deposition were found unsuitable, since these methods did not deliver protective layers with the necessary appropriate thickness and high uniformity.^[51] Thus, the protective layer should uniformly cover the surface and be a few nanometers thick to maintain high ionic conductivity without increasing cell impedance in the battery.^[51] Therefore, the concept of atomic layer deposition which was first applied in Li batteries using a Al₂O₃ layer, is currently considered more suitable for Mg anodes.^[51–53]

3. Cathode Materials

A high energy density Mg battery should contain a well-performing cathode material, which is able to deliver reversibly high capacities, show low capacity fading upon charging/discharging, possess a high electrochemical potential against Mg/Mg²⁺ and which is earth abundant.^[54] In the field of Mg batteries, intercalation cathodes,^[55–59] e.g., transition metal sulfides such as TiS₂ and Mo₆S₈,^[23,38,60–62] as well as transition metal oxides such as V₂O₅,^[63,64] or MnO₂,^[65,66] MoO₃,^[67] conversion cathodes such as sulfur and oxygen, organic cathodes such as 2,5-dimethoxy-1,4-benzoquinone^[68–72] and carbon-based cathodes such as fullerenes^[73] have been studied and reported so far.^[19,31,58,68,74,75] Here, we solely focus on sulfur-based conversion cathodes, since the other types of cathode materials have already been summarized in several reviews.^[1,14,27,59,64,68,75,76]

3.1. Active Cathodes Materials

In sulfur-based conversion cathodes, unlike in intercalation cathodes, the discharge and charge processes reduce and oxidize elemental sulfur.^[77] Table 1 lists some examples for conversion cathodes, including sulfur- and oxygen-based ones. The main drawback of oxygen as cathode material is the formation of the discharge product, MgO, which forms irreversibly and is electrochemically inactive.^[54] Also, the disadvantages of metal halide as cathodes (e.g., CuF₂ and AgCl) are the irreversibility and poor solubility of the discharge products.^[54] In view of these drawbacks, a sulfur-based cathode is considered an attractive candidate for rechargeable Mg batteries. Sulfur is earth abundant, nontoxic and, most important, has a relatively high theoretical energy density (1675 mAh g⁻¹).^[19] Therefore, in this section, Mg batteries containing sulfur-based conversion cathodes will be thoroughly discussed.

Similar to Li–S technology,^[5,8,78–81] the reported cathode materials in Mg–S batteries so far mainly focus on carbonaceous materials containing elemental sulfur (α- or β-S₈).^[40] Different groups utilized various porous, conductive, high surface area carbon additives for the accommodation of S₈ in the cathode to improve the utilization of active material and to reduce the diffusion of polysulfides, which should further improve cell performance. A carbon-based matrix material should possess high electrical conductivity and a good interaction with both the sulfur and the polysulfides.^[82] At the same time, it should have a high mechanical stability to uphold the volume change caused by the sulfur during cycling.^[82] Further

Table 1. Theoretical properties of typical conversion cathodes for Mg batteries.^[54] Copyright 2017. Wiley-VCH Verlag GmbH & Co. KGaA, Weinheim.

Cathode	Capacity [mAh g ⁻¹]	Voltage [V] vs Mg	Cathode specific energy [Wh kg ⁻¹]
Oxygen	3350	2.95	9880
Sulfur	1675	1.77	2960
CuF ₂	528	3.05	1610
AgCl	187	1.93	361

on, the electrolyte should easily migrate into the cathode material.^[82] The applied carbon materials include carbon black,^[12,83] activated carbon clothes (ACC),^[24,52] and metal organic frameworks (MOFs).^[42]

Active carbon clothes were first applied in Li–S batteries by Aurbach and co-workers.^[84] The binder-free monolithic cathode material was composed of an activated carbon fiber cloth and elemental sulfur. The ACC–S cathode was prepared by overlaying elemental sulfur with active carbon cloth discs in a stainless-steel vessel, maintaining the temperature at 155 °C for 10–15 h, which facilitated the impregnation of S into the ACC. The simple preparation methods and the promising electrochemical results in Li–S batteries allowed for the utilization of this cathode material in Mg–S batteries by Gao et al.^[24,26,85] and Zhao-Karger et al.^[43] In 2018, Gao et al.^[85] studied the fundamental mechanism of Mg-ACC/S batteries using both experimental and computational approaches to verify the step-wise pathway of the formation of the individual magnesium polysulfides from elemental sulfur and the dissolution of long-chain polysulfides in the initial stage. The latter is followed by a solid-state transition from short chain polysulfides to magnesium sulfides.

Generally, the use of elemental sulfur may result to some extent in the so-called “shuttle effect.”^[78,86] This phenomenon was observed by Gao et al.,^[26] using an ACC–S cathode material and 0.25 M Mg(TFSI)₂-based electrolyte. The high-order magnesium polysulfides (MgS_x, 3 < x < 8), which directly form via the reduction of elemental sulfur, can easily dissolve in ether-based solvents, which renders them electrochemically addressable. However, at the same time, they can migrate from the cathode to the anode, resulting in the loss of active material and in capacity fading.

One possible way to avoid the dissolution of polysulfides is the encapsulation of sulfur in carbon-based materials such as microporous,^[87,88] mesoporous,^[89] or hollow carbonaceous materials.^[90–92] The currently applied porous carbon materials in Mg–S batteries include CMK-3,^[37,41,93] nitrogen-doped graphene,^[21] carbon nanotubes (CNTs),^[40] carbon nanofibers,^[25,94] and reduced graphene oxide (rGO).^[82]

In 2009, Nazar and co-workers investigated CMK-3/S composite cathode materials for use as cathode materials in Li–S batteries.^[93] Due to the good performance of the CMK-3/S composite cathode, it was further applied to Mg–S batteries by Ha et al.,^[37] Zhao-Karger et al.,^[17] and Gao et al.^[85] The main advantages of applying CMK-3, the most famous mesoporous carbon framework formed from carbon nanotubes, is that it allows for the creation of highly ordered interwoven composites.^[93] A highly ordered mesoporous carbon framework has a uniform pore diameter (3–4 nm), a very high pore volume, interconnected porous structures that can be filled with sulfur (Figure 3a), leading to an electrical contact between sulfur and carbon, a prerequisite for electrochemically addressing the sulfur.^[93] The authors prepared a CMK-3/S composite following a melt-diffusion strategy (Figure 3b). After the impregnation of the sulfur into the channels of carbon at 160 °C by capillary forces, the Brunauer–Emmett–Teller (BET) surface area decreased from 1976 to 46 m² g^{−1}, indicating the partially filling of the channels. Moreover, the ionic conductivity remained at 0.2 S cm^{−1},

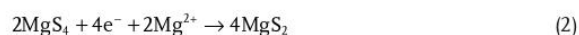
showing that the electrical current transport paths were not blocked.^[93]

By using this type of cathode in a Mg–S battery, a specific discharge capacity of 250 mAh g^{−1} sulfur at a charge and discharge rate of 20 mA g^{−1} was reached for 20 cycles with a modified nonnucleophilic electrolyte, (HMDS)₂Mg–2AlCl₃–MgCl₂/tetraglyme.^[17] The same group used a CMK-3/S cathode to examine the electroactivity of the conductive salt, Mg[B(hfp)₄]₂ in diglyme-tetraglyme. The cell delivered around 200 mAh g^{−1} sulfur at 0.1 C. Based on these results, an electrochemical mechanism was proposed for the CMK-3/S cathode (Figure 3c).

The entire discharge process can be divided into three steps. In the first step, a solid liquid two-phase reduction takes place, i.e., the elemental sulfur in the cathode is transformed into MgS₈, which dissolves in the electrolyte and which is subsequently converted into MgS₄. The discharge process reaches a first voltage plateau around 1.5 V, providing a specific discharge capacity around 370 mAh g^{−1} sulfur, which is close to the theoretical specific discharge capacity for the conversion of S₈ into MgS₄. Accordingly, the reaction of the first step can be written as^[17]



The second step is assigned to a liquid–solid two-phase reduction from MgS₄ to MgS₂, corresponding to the second small voltage plateau around 0.8 to 1.0 V (Figure 3c). The reaction is described in Equation (2)^[17]



The final step entails the reduction of MgS₂ into MgS^[17]



Yu and co-workers^[95] also investigated the capacity degradation mechanism of both the discharge and charge process in Mg–S batteries. A Mg–S₈ cell based on a Mg(HMDS)₂–AlCl₃ electrolyte was applied and a clear discharge plateau around 1.5 V and two slopes (1.5–1.0 and 1.0–0.3 V) were observed (Figure 3e), resulting in ≈1080 mAh g^{−1} sulfur discharge capacity; the charge profile showed undistinguishable plateaus. From the second cycle on, the discharge capacity first dropped to 400 and then to 200 mAh g^{−1} sulfur, without showing any clear plateaus in the discharge profile. Spin-polarized DFT calculations were performed to shed light on the nature of the polysulfides species formed during charge and discharge. Figure 3d shows the stable structure with the lowest formation energies. The stable structures of Mg_xS₈ (x = 1, 2, 3, 8) are amorphous, whereas the most stable structure MgS is crystalline. More importantly, in situ XAS measurement results suggest that Mg₃S₈ is formed irreversibly; consequently, from the second cycle on the discharge capacity solely originates from the oxidation of low-order Mg₃S₈ to MgS. Notably, MgS was found to be electrochemically virtually inactive in the chosen electrolyte. Recently, Nakayama et al.^[96] elucidated the nature of the phase of the formed MgS after discharge, which is metastable zinc blende MgS rather than the rock salt phase. The high stability of both Mg₃S₈ and MgS was made responsible for the high polarization and the unclear charge plateaus.^[95]

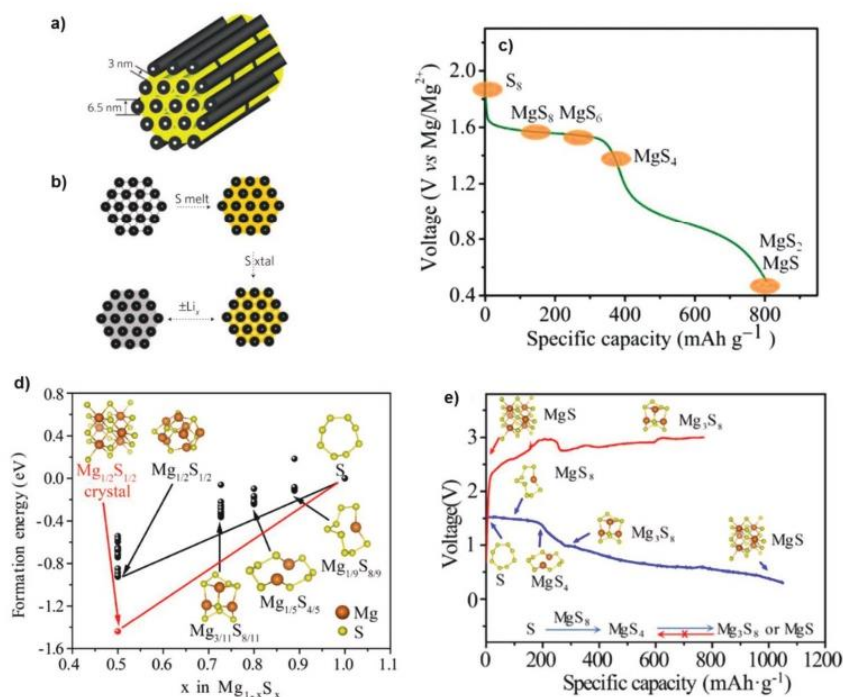


Figure 3. a) Illustration of sulfur (yellow) in intercalated CMK-3 (grey); b) illustration of the synthesis of CMK-3/S composites: incorporation of molten sulfur into the mesoporous carbon (160 °C), followed by densification using a crystallization process (Reproduced with permission.^[93] Copyright 2009, Springer Nature); c) proposed electrochemical reaction mechanism of Mg–S batteries with a CMK-3/S composite cathode.^[17] Reproduced with permission.^[17] Copyright 2015, Wiley-VCH Verlag GmbH & Co. KGaA, Weinheim; d) density functional theory (DFT) calculated structures of different forms of magnesium polysulfides and their formation energy; black dots: the possible amorphous structures of polysulfides, red dot: the formation energy of crystalline MgS; e) charge/discharge profile of the redox reactions of a Mg–S battery. Reproduced by permission.^[95] Copyright 2019, American Chemical Society.

Overall, the opening circuit voltage in the Mg–S batteries lies around 1.8 V. During its entire discharge reaction, Mg–S batteries based on an S_8 cathode can be operated between 0.4 and 1.8 V, where the discharge plateaus are at 1.6 and 1.0 V, respectively, resulting in a specific discharge capacity of 800 $\text{mAh g}^{-1}_{\text{sulfur}}$. In comparison, the initial discharge process in rechargeable Li–S batteries can take place between 1.0 and 3.0 V, with two discharge plateaus at 2.4–2.1 and 2.1–1.5 V, respectively, resulting in a higher theoretical gravimetric energy density around 1000 $\text{mAh g}^{-1}_{\text{sulfur}}$ ^[81,97] but a lower volumetric energy density of 2062 mAh cm^{-3} compared to the one of Mg–S batteries (3832 mAh cm^{-3} , vide supra). In addition, unlike in the Li–S system, where the lithium polysulfides have similar stability and are all redox-active,^[98] the discharge products from Mg–S batteries, Mg_3S_8 and MgS, were found to be highly stable, which significantly impedes and often stops recharging of the batteries.^[95]

Apart from the mesoporous CMK-3/S cathode, another porous cathode material, e.g., graphdiyne, was utilized. In 2017, Du et al.^[86] successfully synthesized a sulfur-containing cathode based on sulfur graphdiyne (SGDY) via a thermal reaction. The authors stated that the SGDY cathode was compatible with the nucleophilic APC electrolyte in the presence of LiCl, which was attributed to the reduced electrophilicity of the SGDY

cathode. Graphdiyne (GDY), a conductive carbon allotrope, has a layered structure, which is formed by benzene rings, linked by butadiyne linkages (Figure 4a).^[86] Due to the unique structure, GDY has uniformly distributed pores with a diameter of 5.42 Å and large interlayer distances of 0.365 nm. The synthesis of SGDY is accomplished by the thermally induced cleavage of elemental sulfur into shorter sulfur chains (S_x , $1 \leq x \leq 4$) at 350 °C, which further react with the available carbon–carbon triple bonds in GDY and anchor in the triangle pores of GDY.^[86] XPS, XRD, and FTIR results all indicated the presence of C–S bonds and S–S bonds instead of S_8 in the SGDY structure. Together with the size of the carbon skeleton GDY, only short-sulfide units (S_x , $1 < x < 5$) are accommodated in the structure, which are electrochemically reactive sites.^[86] Also, the conjugated linkages in the carbon matrix provide high electrical conductivity of the cathode material. All these results are beneficial for the proposed structure of SGDY in Figure 4a.^[86]

Overall, sulfur is confined within the nanopores, which prevents its dissolution and consecutive shuttle effects.^[86] Using a SGDY cathode, they observed an initial discharge capacity of 1125 $\text{mAh g}^{-1}_{\text{sulfur}}$ and a charge capacity of 540 $\text{mAh g}^{-1}_{\text{sulfur}}$ for 35 cycles at a charge/discharge rate of C/30 (Figure 4b). Figure 4c shows the charge/discharge profiles for two cycles, the following cycles are overlapping, indicating the good

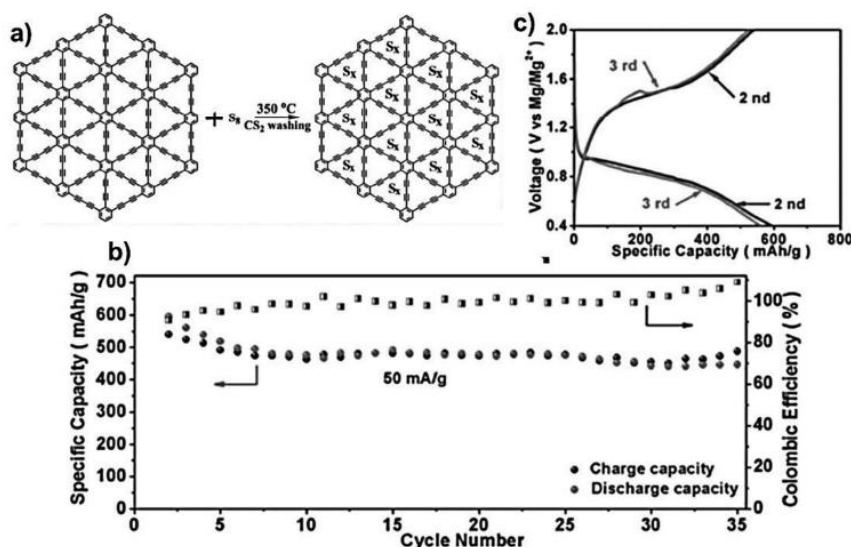


Figure 4. a) Illustration of sulfur graphdiyne prepared by thermal synthesis, during which only short-chain polysulfides are confined in the structure, $1 < x < 5$; b) cycle stability test; and c) charge/discharge profiles of Mg-SGDY cathode with APC electrolyte using LiCl as an additive at 50 mA g⁻¹. Reproduced with permission.^[86] Copyright 2017, Wiley-VCH Verlag GmbH & Co. KGaA, Weinheim.

reversibility of the cell. However, from the 36th cycle on, severe overcharging was observed, which was attributed to the reduction of the electrolytes or the corrosion of the cell.^[86]

Wang et al.^[88] used a similar setup, i.e., microporous carbon working as the carbon host for the adsorption of small S₂₋₄ inside its microporous structure and of S₈ molecules on the outside wall of the carbon and prepared a sulfur at microporous carbon composite (S@MC) as the electrochemical active material. This setup allowed for a fast transport of ions into the microporous carbon, a better adsorption of polysulfides and higher ionic conductivity. The composite material had a sulfur content of 64.7% and was coated onto a Cu current collector as the cathode. Apart from high conductivity, the major benefit of a Cu current collector is that it allows for the formation of copper sulfides via reaction with the free sulfur that exists outside the carbonaceous matrix during the cathode drying process at 50 °C. The strong interaction between Cu and S protects the sulfur from reacting with the nucleophilic electrolyte: This increases cycle stability and suppresses the dissolution of polysulfides.^[88,99] This novel concept for the stabilization of the cathode material by copper has also been used by Zeng et al.^[99] In a similar approach, Cui et al.^[100] filed a patent about the cathode based on sulfur, a metal sulfide and a ternary copper composite. The metal sulfides comprised FeS₂, SnS₂, MoS₂, Co₃S₄, and Ni₂S₃. The authors claimed that these cathode materials could successfully suppress the shuttle effect on the cathode side when used in Mg-S batteries. For example, the dissolution of copper was made responsible for the formation of an intermediate Cu_xS phase, which was identified to promote the electrochemical conversion of MgS and consequently improve both cell capacity and cycle stability.

While mostly carbonaceous materials are used for the accommodation of sulfur, cathode materials for Mg-S batteries are not entirely limited to these materials. Until now, the majority of cathode materials applied in Mg-S batteries originally stem

from Li-S battery technology and are mainly based on elemental sulfur or accommodation sulfur in microporous or mesoporous carbon material. However, the same issues observed with Li-S batteries still exist, particularly the shuttle effect. An alternative approach that can reduce the shuttle effect is by covalently binding sulfur to a conductive carbon matrix, which has successfully been applied in the field of Li-S batteries.^[101-108] Moreover, a protective coating on the active material in the cathodes could also be an alternative approach to prevent the dissolution and loss of sulfur from the cathode material.^[109]

3.2. Current Collectors

In Mg-S batteries, the choice of the current collector has also a great impact on the electrochemical behavior particularly in the case of halogen-containing corrosive electrolytes, the nature of the electroactive cathode materials and the dissolution of polysulfides during cycling.^[110] The currently reported commercial metal-based current collectors include aluminum foil,^[18,21,37,40] stainless-steel (SS) foil,^[41,43,85,99,111] carbon-coated aluminum foil,^[44] copper,^[39,40,88,99,112] and the anticorrosion alloy Inconel 625.^[17,82,99] While Cu is generally considered unstable against chloride-containing electrolytes,^[113] Zeng et al.^[99] recently reported that a sulfur cathode is compatible with the traditional APC electrolyte using copper as current collector below 1.7 V versus Mg/Mg²⁺. The electrochemical behavior of the cell was even better than the one with a stainless-steel current collector. They also observed that the electric conductivity of the cathode using a Cu current collector was higher after drying at 50 °C (926 μS cm⁻¹) than without drying (769 μS cm⁻¹). Formation of copper sulfides at the interface between S and Cu, which could to some extent protect the free sulfur in the cathode from reacting with APC electrolytes (vide supra), was indeed confirmed by XRD measurements. In

comparison, the diffraction peaks of copper sulfides were not observed on cathodes based on stainless-steel current collectors dried at 50 °C.^[99] Also, the TGA results of the cathode with a stainless-steel current collector suggest a reaction of sulfur with the nucleophilic electrolyte as evidenced of the large weight loss of sulfur in the cathode after cycling. Due to the unique advantages of the Cu current collector,^[88,99] it was also applied in combination with other halogenated electrolytes including the organic magnesium boron-based (OMBB) electrolyte,^[40] the boron-centered base magnesium (BCM) electrolyte,^[114] the magnesium bis(diisopropylamide) (MBA) electrolyte^[112] and a trifluoromethanesulfonate-based electrolyte.^[39]

Apart from the commercial current collectors, Muthuraj et al.^[115] developed an effective current collector, which is stable against corrosive electrolytes and can also catch polysulfides. Very recently, they presented a N-, S-dually doped carbon cloth (DCC) as current collector, which possesses a 3D interconnected porous structure that provides superior cycle stability and high conductivity.^[116] Notably, due to the hydrophobic property of the carbon cloth, the formed magnesium polysulfides can barely be trapped inside the porous structure, leading to the dissolution of polysulfides in the electrolytes. To overcome this issue, the authors N- and S-doped the carbon cloth to increase the hydrophilicity of the surface, which successfully suppressed the dissolution of polysulfides and improved cycle performance. Their results showed that using S/rGo as the electroactive material and an HMDS-based electrolyte, the cell with a DCC current collector was capable of delivering around 388 mAh g⁻¹_{sulfur} for 40 cycles at 0.01 C with Coulombic efficiencies >90%. By contrast, the cell with a undoped carbon cloth as current collector could only be cycled over 18 cycles, and severe overcharging was observed, underlining the advantages of the DCC current collector.

4. Electrolyte Systems

Mg–S batteries still suffer from limitations in terms of the electrolyte systems.^[35,67–70] The general requirements for a suitable electrolyte include high ionic conductivity, good electrochemical and chemical stability toward the electrodes, good thermal stability and sufficiently low toxicity and flammability.^[1,17] In addition, an appropriate electrolyte system should allow for a reversible Mg deposition and dissolution and also provide a wide voltage window.^[117–120] Therefore, the design of novel electrolyte systems that are fully compatible with Mg–S batteries and the underlying chemistry is of great importance. It is worth to mention that a large group of the traditional electrolytes in Mg batteries have nucleophilic properties, which are generally incompatible with sulfur cathodes. Therefore, the modification of the cathode for compatibility with the nucleophilic electrolytes is under investigation.^[86,88,99] At the same time, new non-nucleophilic electrolyte systems that are compatible with sulfur cathodes are intensely synthesized and investigated.

4.1. Nucleophilic Electrolytes

The Grignard-based nucleophilic all-phenyl complex (APC) electrolyte, which can be synthesized by the reaction between

PhMgCl and AlCl₃, is generally considered incompatible with S-based conversion cathodes, due to the nucleophilicity of the organomagnesium compounds, although this electrolyte shows high oxidative stability against Mg (3.2 V) and high cycle efficiency (around 100%).^[11,54] Therefore, the APC electrolyte was initially not considered for application in Mg–S batteries. However, in 2017, the selection of an appropriate current collector^[99] and the development of new cathode materials^[86] have brought the APC electrolyte back for use in Mg–S batteries.

As has already been discussed in Section 3.2, the utilization of a Cu-based current collector rather than a stainless-steel current collector allows for the successful cycling of a cell based on an S₈ cathode and an APC electrolyte.^[99] The cell was able to cycle for 20 cycles, indicating the principle possibility of combining an APC electrolyte with a sulfur cathode. However, the cell could only deliver around 100 mAh g⁻¹_{sulfur} at the 20th cycle at 0.005 C. The authors explained this unsatisfactory cycle performance with the formation of irreversible discharge products. Addition of LiCl into the nucleophilic electrolyte successfully improved cycle performance, which was ≈300 mAh g⁻¹_{sulfur} after the 40th cycle at a discharge rate of 0.005 C.^[99] The same research group further improved the electrochemical behavior of the cell by developing a novel cathode active material, S@microporous carbon,^[88] in combination with a Cu current collector and a nucleophilic APC electrolyte containing LiCl as additive. Using this system, the Mg–S cell was capable of delivering 368 mAh g⁻¹_{sulfur} at 200th cycle at 0.1 C.^[88]

As mentioned in Section 3.1, the SGDY cathode was also reported to be compatible with the nucleophilic APC electrolyte.^[86] The reduced electrophilicity of short-chain sulfides in SGDY compared to the long-chain sulfides formed from S₈ was made responsible for the compatibility with the APC electrolyte, even though the current collector was Al instead of Cu.^[86]

4.2. Nonnucleophilic Electrolytes

Due to the electrophilic nature of the sulfur cathode, nonnucleophilic electrolytes are of great importance and have consequently been applied in the majority of Mg–S batteries.^[28,121] In this section, the less/nonnucleophilic electrolyte systems in Mg–S batteries are divided into chloride-containing and chloride-free, noncorrosive electrolytes.

4.2.1. Chloride-Containing, Non/Less Nucleophilic Electrolytes

A common approach to the synthesis of Mg salts for the electrolyte is the combination a Mg complex containing a nonnucleophilic base, such as [HMDS]₂Mg,^[23,122] HMDSMgCl,^[123] bis(diisopropyl)amide,^[112] with a boron- or aluminum-containing Lewis acid.^[21] Liebenow et al.^[123] reported that the Hauser base-derived magnesium hexamethyldisilazide chloride (HMDSMgCl) electrolyte supported magnesium stripping and plating in rechargeable Mg batteries. Muldoon and co-workers^[12] reported on a performance improvement of the HMDSMgCl electrolyte by forming a molecular species possessing a [Mg₂(μ-Cl)₃][HMDSAAlCl₃] species (Figure 5a) upon

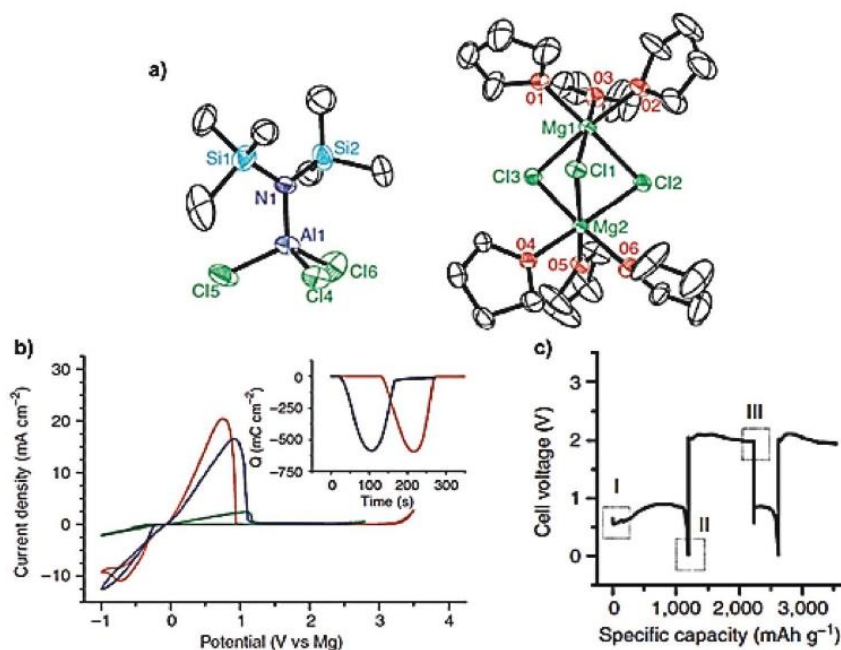


Figure 5. a) Single crystal X-ray structure of $[\text{Mg}_2(\mu\text{-Cl})_3][\text{HMDSAAlCl}_3]$; b) cyclic voltammograms of HMDSMgCl (green), in situ prepared product from the reaction of HMDSMgCl with AlCl_3 (3:1) (blue) and of crystalline $[\text{Mg}_2(\mu\text{-Cl})_3][\text{HMDSAAlCl}_3]$ (red) applying a scan rate of 25 mV s^{-1} ; c) cycle performance of a Mg–S coin cell, using a S/C composite as cathode and Mg foil as anode. Reproduced with permission.^[12] Copyright 2011, Nature Publishing Group.

addition of a Lewis acid (AlCl_3). While voltage stability was not improved using an in situ formed $[\text{Mg}_2(\mu\text{-Cl})_3][\text{HMDSAAlCl}_3]$ species (Figure 5b), the use of purified stoichiometric $[\text{Mg}_2(\mu\text{-Cl})_3][\text{HMDSAAlCl}_3]$ increased stability to 3.3 V. This substantial increase in voltage stability was explained by the removal of unreacted HMDSMgCl in the electrolyte, which starts to decompose at 2.5 V. In addition, they stated that this electrolyte was also compatible with sulfur cathodes.^[12] Using purified $[\text{Mg}_2(\mu\text{-Cl})_3][\text{HMDSAAlCl}_3]$ in THF as the electrolyte, Muldoon and co-workers prepared a cell using an elemental sulfur/carbon black composite as cathode material and Mg foil as the anode. The open-circuit voltage (OCV) was 0.55 V (Figure 5c), which was only about one half of the theoretical cell voltage (1.77 V). Also, the discharge voltage started from 0.89 V. Fracturing of the resistive surface layer on the Mg anode was considered one reason of the slightly increasing initial voltage.^[12] Notably, the initial discharge capacity was $1200 \text{ mAh g}^{-1}_{\text{sulfur}}$. However, substantial capacity fading was observed in the second cycle, with a specific discharge capacity of only $394 \text{ mAh g}^{-1}_{\text{sulfur}}$, which was attributed to the polysulfide shuttle effect. In addition, the active compound $[\text{Mg}_2(\mu\text{-Cl})_3, 6\text{THF}]^+[\text{HMDSAAlCl}_3]^-$ could only be obtained from flammable and volatile THF.^[11]

Since single crystals of the bisamide-based, nonnucleophilic electrolyte based on $[\text{Mg}_2(\mu\text{-Cl})_3, 6\text{THF}]^+[\text{HMDSAAlCl}_3]^-$ can only be obtained from THF, which limits the solvent selection, Fichtner and co-workers^[17] successfully modified the electrolyte by a one-step reaction between magnesium bis(hexamethyldisilazide), $[(\text{HMDS})_2\text{Mg}]$, and AlCl_3 in different

ethers (diglyme, tetraglyme). This simple reaction led to an electrochemically active compound, $[\text{Mg}_2\text{Cl}_3][\text{HMDSAAlCl}_3]$, which dissolved in diglyme and tetraglyme. Importantly, according to the cyclic voltammograms of the electrolyte (Figure 6a), Mg plating and stripping was successful, and the stability of the electrolyte was maintained up to 3.2 V. Moreover, Mg plating and stripping was found to take place when the ionic liquid (IL) *N*-methyl-*N*-butyl-piperidinium TFSI (PP14TFSI) was added to the electrolyte (Figure 6b).

The authors also stated that the corresponding electrochemical behavior of Mg–S cells, shown in Figure 6b,c, was better than the previously described electrolytes prepared from THF investigated by Muldoon and co-workers.^[12] As can be seen from Figure 6c, a cell containing a tetraglyme (TEG)-based electrolyte had an OCV of about 2 V.^[17] The discharge curve showed two voltage plateaus, indicating the formation of high- and low-order polysulfides.^[17] It delivered an initial discharge capacity of $550 \text{ mAh g}^{-1}_{\text{sulfur}}$ at 0.01 C (C/100), dropping to $250 \text{ mAh g}^{-1}_{\text{sulfur}}$ after 20 cycles (Figure 6d). In addition, the authors also investigated the influence of the IL PP14TFSI as a cosolvent in the electrolyte.^[17] The results showed that after the addition of IL to the electrolyte the initial capacity and the capacity at the 20th cycle increased to $800 \text{ mAh g}^{-1}_{\text{sulfur}}$ and $280 \text{ mAh g}^{-1}_{\text{sulfur}}$, respectively.^[17] Due to the attractive electrochemical properties and the simplicity in synthesis, this type of electrolytes was also utilized by Vinayan et al.,^[82] Yu and Arumugam,^[25] Friedrich and co-workers,^[44] and Muthuraj et al.,^[115] though with combinations of different cathodes, anodes and current collectors.

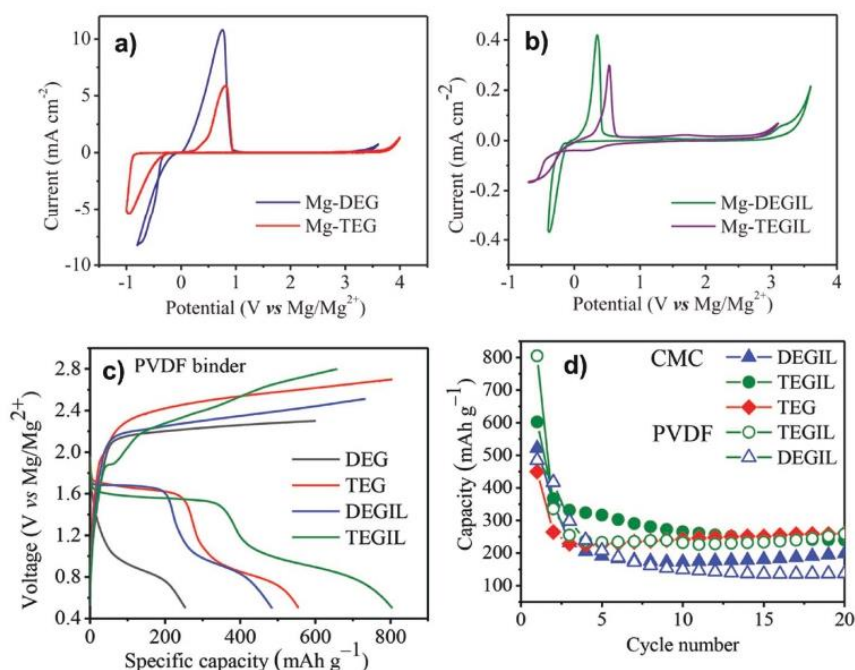


Figure 6. Cyclic voltammograms of (HMDS)₂Mg-2AlCl₃ in a) diglyme (DEG), tetraglyme (TEG); b) diglyme and ionic liquid (DEGIL), tetraglyme and ionic liquid (TEGIL); electrochemical performance of Mg-S batteries (cathode: CMK3-S composite; anode: pressed Mg); c) initial charge-discharge curves using PVDF binders; d) cycle stability.^[17] Reproduced with permission.^[17] Copyright 2015, Wiley-VCH Verlag GmbH & Co. KGaA, Weinheim.

Gao et al.^[24] reported improved electrochemical data using the previously published electrolyte, i.e., 0.1 M (HMDS)₂Mg-2AlCl₃-MgCl₂ in the presence of lithium bis(trifluoromethanesulfonyl)imide (LiTFSI). According to their cyclic voltammograms, Mg plating and stripping successfully took place in the LiTFSI-containing electrolyte and the voltage was stable up to 2.8 V (vs Mg). Also, increasing amounts of LiTFSI were found to increase both the plating and stripping current density, which was explained by an increasing ionic conductivity. In order to study the compatibility of the electrolyte with the sulfur cathode, they carried out galvanostatic tests using active carbon cloth/elemental sulfur as the cathode and Mg foil as the anode. The corresponding cycle behavior is illustrated in Figure 7. The discharge curves (Figure 7a) clearly show two voltage plateaus at 1.75 and 1.0. Also, an increase in discharge capacity during cycling was observed and attributed to a slow infiltration of the cathode material with electrolyte. Notably, the discharge capacity of the cells containing LiTFSI remained at 1000 mAh g⁻¹_{sulfur} at 0.03 C up to 30 cycles (Figure 7b); whereas cells without LiTFSI delivered only 10 mAh g⁻¹_{sulfur}. The higher discharge capacity was attributed to a lower kinetic barrier of reoxidation for MgS_x (4 < x < 8), either by reacting Li⁺ with MgS_x (4 < x < 8), thereby forming soluble, higher-order MgLi polysulfides, as well as to an ion exchange reaction between Li⁺ and MgS and MgS₂, forming electrochemically active Li₂S and Li₂S₂.

In terms of morphology of the deposits on Mg foil, SEM investigations revealed that after LiTFSI addition spherical Mg deposits about 2 μm in diameter formed without any

observable dendrite formation (Figure 7c,d). In view of these findings, LiTFSI is considered a promising additive for Mg-S batteries as also outlined by Zhou et al.^[42]

In a similar approach, Li⁺ was added to the electrolyte. Zuo et al.^[124] added an excess of metallic Li into an, e.g. [HMDS]₂Mg-based electrolyte to improve the electrochemical performance of a Mg-S battery at high current rates. They indeed observed that cell capacity did not decay even at high current rates. Stress test results showed that the cell capacity remained around 1100 mAh g⁻¹ at current rates of 0.3 C, 0.5 C, 1 C, and 2 C. Even at 5 C, the discharge capacity was still around 1000 mAh g⁻¹.

In 2019, Nuli et al.^[112,125] reported on a novel electrolyte for rechargeable Mg-S batteries consisting of MBA and AlCl₃ dissolved in THF. The authors pointed out that the electron-rich amide in MBA limits the anodic stability of the salt, since electrons can be easily withdrawn from it at high voltages. By contrast, introduction of the Lewis acid AlCl₃ stabilizes the Mg-N bond in MBA even at high potentials since the high electron affinity of AlCl₃ could suppress the withdrawal of electrons from the Mg-N bond.^[112] Consequently, the molar ratio of MBA and AlCl₃ was adjusted from 2:1 to 1:2. According to their Mg plating/stripping test results (Figure 8a), the higher the amount of AlCl₃ was, the higher both cycle efficiency and stability were. The authors also compared the oxidation stability of the 0.25 M MBA-AlCl₃/THF electrolyte with the traditional nucleophilic 0.4 M APC electrolyte, (PhMgCl)₂-AlCl₃/THF. Results suggest that the stability of the MBA-2AlCl₃/THF electrolyte (2.35 V/Al, 2.65 V/SS) was better than the one of the APC electrolyte

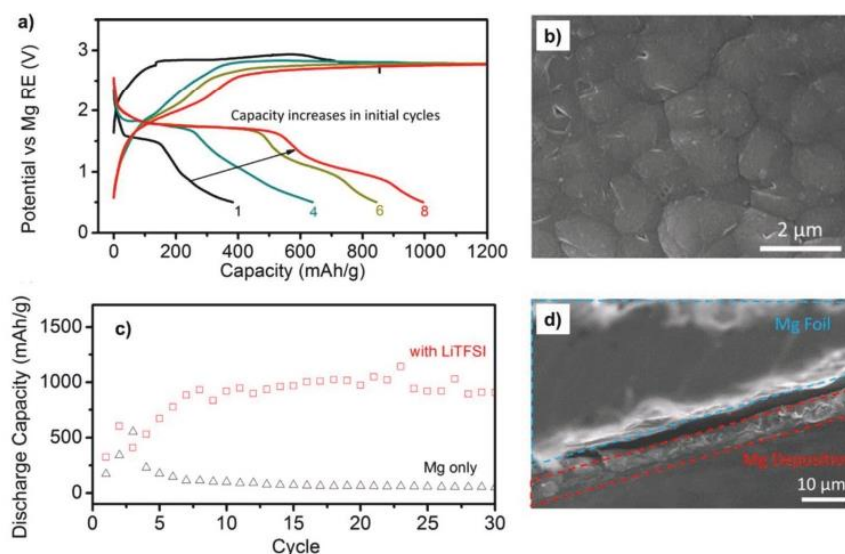


Figure 7. Electrochemical data of Mg-S batteries (cathode: ACC/S; anode: Mg foil) with 0.1 M $(\text{HMDS})_2\text{Mg}-2\text{AlCl}_3$ and 1.0 M LiTFSI as additive at 0.03 C and room temperature; a) charge-discharge curves; b) cycle stability with and without LiTFSI; c) top view of Mg deposits on Mg foil; and d) cross-section of Mg deposits on Mg foil.^[24] Reproduced with permission.^[24] Copyright 2015, American Chemical Society.

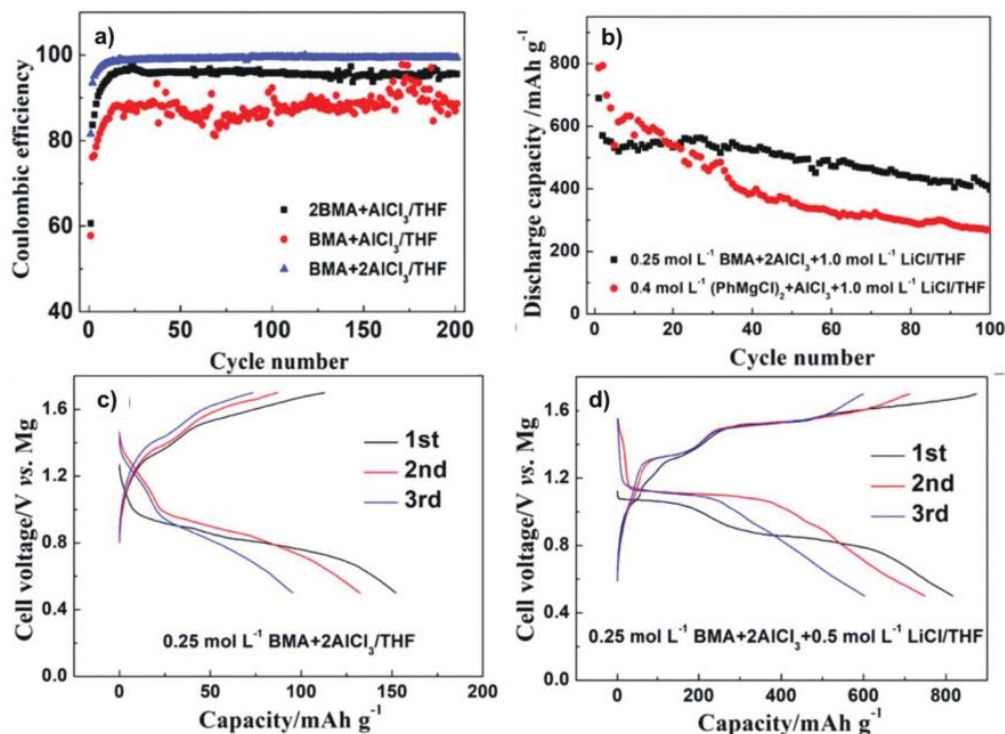


Figure 8. a) Cycle efficiency with an MBA- AlCl_3 /THF electrolyte at molar ratios of MBA:Al of 2:1, 1:1 and 1:2 (working electrode: stainless steel); b) cycle stability of a Mg-S@MC cell with 0.25 mol L^{-1} BMA/ AlCl_3 (molar ratio = 1:2) and 1 mol L^{-1} LiCl in THF at 0.04 C; discharge and charge profiles of Mg-S@MC cell with c) 0.25 mol L^{-1} BMA/ AlCl_3 (molar ratio = 1:2) in THF; and d) 0.25 mol L^{-1} BMA/ AlCl_3 (molar ratio = 1:2) and 1 mol L^{-1} LiCl in THF.^[112] Reproduced with permission.^[112] Copyright 2019, Royal Society of Chemistry.

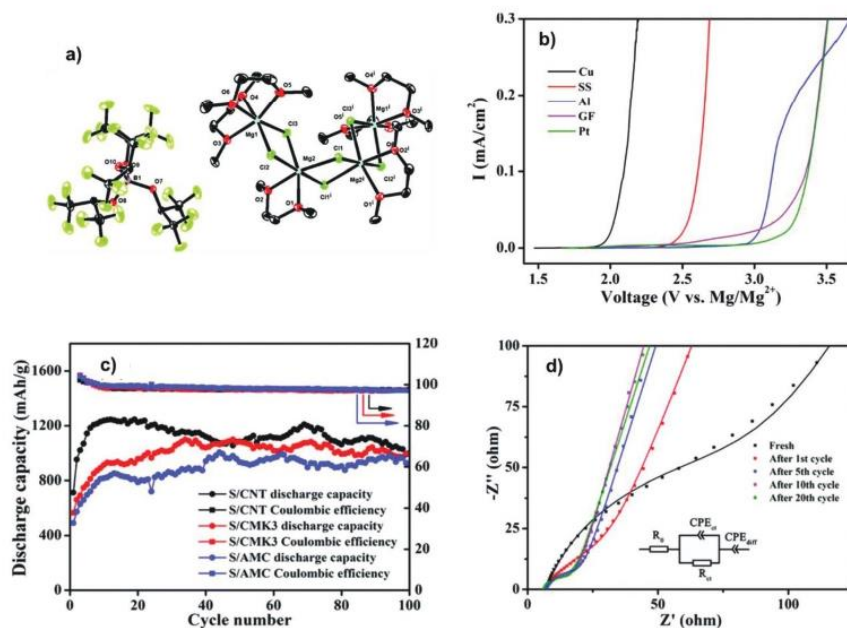


Figure 9. a) ORTEP plot of $[\text{Mg}_4\text{Cl}_6(\text{DME})_6][\text{B}(\text{hfip})_4]_2$; b) LSV curves 0.5 M OMBB electrolyte on various working electrodes (Cu, SS, Al, GF, and Pt), with Mg as counter and reference electrode; c) cycle stability test of 0.5 M OMBB electrolyte with various cathode materials, S/CNT, S/CMK-3 and S/AMC at 0.1 C; d) EIS measurements of different cycles, with fitting lines; in the equivalent circuit, R_0 is the bulk resistance, R_{ct} is charge transfer resistance, CPE_{ct} is the constant phase element of the double layer capacitance. Reproduced with permission.^[40] Copyright 2017, Royal Society of Chemistry.

(1.3 V/Al, 2.2 V/SS) when using an Al or stainless-steel working electrode.^[112] Based on single-crystal X-ray analysis, the formula of the electroactive species is $[\text{Mg}_2(\mu\text{-Cl})_3 \cdot (\text{THF})_6][\text{AlCl}_4]$. Using this electrolyte, the discharge capacity of the Mg-S@microporous carbon (MC) at a discharge capacity of 0.04 C was only around 100 mAh g^{-1} in the third cycle (Figure 8c).

In order to further improve the electrochemical performance by introducing Li ions into the electrolyte, Nuli and co-workers^[112] additionally dissolved 1 mol L^{-1} of LiCl into 0.25 mol L^{-1} MBA/ 0.5 mol L^{-1} of AlCl_3 in THF. As illustrated in Figure 8c,d, a higher retentivity of the major capacity contribution at 1.1 V was successfully established by the addition of LiCl. The discharge capacity was retained at 537 mAh g^{-1} after the 30th cycle with a Coulombic efficiency of 94%. Clearly, the addition of LiCl successfully reduced the amount of magnesium polysulfides in the electrolyte. The authors claimed that this electrolyte system outperformed other reported ones due to the simple preparation method and the commercial availability of the starting materials.

By using different combinations of the anion and cation in the magnesium salt, one can tailor its stability and conductivity. In 2017, Du et al.^[40] reported on an OMBB electrolyte, which contained bulky tetranuclear Mg-containing species $[\text{Mg}_4\text{Cl}_6(\text{DME})_6]^{2+}$, and a bulky $[\text{B}(\text{hfip})_4]^-$ anion (Figure 9a) by a simple reaction between tris(hexafluoroisopropyl) borate $\text{B}[\text{HFP}]_3$, MgCl_2 and excessive Mg powder in DME. They optimized the MgCl_2 : $\text{B}[\text{HFP}]_3$ ratio to 1:2 in order to obtain the lowest plating overpotential ($-0.11 \text{ V vs Mg/Mg}^{2+}$), the highest oxidative peak current (25.3 mA) and the highest Coulombic

efficiency (98.67%). The obtained electroactive cation $[\text{Mg}_4\text{Cl}_6(\text{DME})_6]^{2+}$ distinguished itself from the well-known $[\text{Mg}_2(\mu\text{-Cl})_3 \cdot 6\text{THF}]^+$ by utilization of donor ligands of different etheral solvents and the large and bulky $[\text{B}(\text{hfip})_4]^-$ counter anions. Furthermore, the use of tetranuclear $[\text{Mg}_4\text{Cl}_6(\text{DME})_6]^{2+}$ instead of mononuclear $[\text{Mg}(\text{DME})_3]^{2+}$ was reported to lower the energy needed for Mg deposition, which results in high Mg plating/stripping reversibility.^[126]

Examination of the oxidative stability of the 0.5 M OMBB electrolyte (Figure 9b) indicated that the electrolyte was stable up to 3.3 V versus Mg/Mg^{2+} on a Pt electrode, up to 3 V versus Mg/Mg^{2+} on an Al electrode, up to 2.5 V versus Mg/Mg^{2+} on a stainless-steel electrode, and up to 2 V versus Mg/Mg^{2+} on a Cu electrode.^[40] The comparably low stability against nonnoble metals was attributed to the chloride ions in the electrolyte. The OMBB electrolyte showed good cycle performance in combination with an S-CNT cathode (Figure 9c). The Mg-S/CNT cell with a 0.5 M OMBB electrolyte delivered around $1000 \text{ mAh g}^{-1}_{\text{sulfur}}$ at 0.1 C for 100 cycles.^[40] Interestingly, the capacity increased during the first few cycles. Impedance measurements (Figure 9d) revealed that the charge transfer resistance R_{ct} decreased dramatically during the first few cycles, which served as explanation for the increasing discharge capacity.^[40]

Another simple salt, $\text{Mg}[\text{TFSI}]_2$, was considered as an attractive alternative because of its high anodic stability, ionic conductivity and high solubility in ethers.^[39] However, its use lead to poor electrochemical performance. Ha et al.^[37] introduced 0.3 M $\text{Mg}(\text{TFSI})_2$ in glyme/diglyme and tested its compatibility

with a sulfur-based cathode. They applied C/200 for the initial discharge to initiate Mg stripping. At this discharge rate the Mg-CMK/S cell delivered an initial discharge capacity of 500 mAh g⁻¹. The current rate was then increased to C/100, which lead to a fast deterioration over the next four cycles. Similarly, Itaoka et al.^[111] studied the electrochemical behavior of Mg-S batteries using elemental sulfur and a bis(alkenyl) compound with a crown ether unit and a linear ether unit as cathode material together with a Mg(TFSI)₂-based electrolyte. The cell showed an initial discharge capacity of 500 mAh g⁻¹_{sulfur}; however, after ten cycles, the battery delivered no further capacity, suggesting an incompatibility of the Mg(TFSI)₂ salt with Mg-S batteries. The incompatibility between glyme-based solvent and Mg(TFSI)₂ was reported to result in dendrite growth on the Mg anode and, finally, in short circuits.^[127,128] Interestingly, mixtures of diglyme and Mg(TFSI)₂ were found to be chemically unstable even before applying any voltage due to water impurities, which are unavoidable in commercially available salts.^[129] Diglyme can easily chelate Mg²⁺ ions, which introduces strain into the structure of the diglyme and expose a proton for the nucleophilic attack. The hydroxyl groups present on the Mg surface can then deprotonate the diglyme molecule, resulting in diglyme cleavage and further formation of water.^[127] Consequently, the purity level of Mg(TFSI)₂ directly governs the electrochemical performance of the cell. One possible way to chemically purify Mg(TFSI)₂ is the addition of dibutylmagnesium, which can react with traces of water, oxygen and free trifluoromethanesulfonic acid (HTFSI) to form butane, magnesium hydroxide, magnesium oxide and Mg(TFSI)₂. Another explanation for the poor electrochemical performance was related to the reduced stability of the TFSI-anion upon reduction of Mg²⁺ to Mg⁺, which resulted in the deposition of the TFSI⁻ anion on the Mg surface and a passivation of the Mg anode.^[85,127,129]

One breakthrough in Mg(TFSI)₂-based electrolytes was the addition of MgCl₂ to the electrolyte as reported by Gao et al. in 2017.^[26] The Mg-S/ACC cell delivered around 600 mAh g_{sulfur}⁻¹ using 1 M Mg(TFSI)₂/MgCl₂/DME at 0.01 C. Introduction of MgCl₂ into the electrolyte was believed to form the electroactive species, [Mg₂(μ-Cl)₃]⁺.^[130,131] The role of the chloride ions is to stabilize the Mg²⁺ cation and to remove the passivation layer, thereby facilitating Mg plating.^[64,131]

The identification of suitable nonnucleophilic magnesium salts is still one important aspect to improve cell performance. In 2019, Yang et al.^[39] reported a new electrolyte based on magnesium trifluoromethanesulfonate (Mg(CF₃SO₃)₂)–AlCl₃–MgCl₂–anthracene–LiCl dissolved in THF and tetraglyme. First, only Mg(CF₃SO₃)₂ was dissolved in the electrolyte to examine Mg plating and stripping. Mg(CF₃SO₃)₂ was used instead of Mg(TFSI)₂ because of its better commercial availability, its low price, high purity and low moisture content. As reported, Mg(CF₃SO₃)₂ is only soluble in THF. The corresponding solutions possessed low viscosities for concentrations up to 0.5 M; therefore, they selected tetraglyme as the cosolvent since the high dielectric constant of tetraglyme (7.7) was expected to promote the dissolution of Mg(CF₃SO₃)₂. However, Mg deposition/dissolution proved to be hard as indicated by a high overpotential, for which an inherent oxide layer on the Mg anode was made responsible. Since Cl⁻ was found to be able to stabilize

the Mg²⁺ ions and inhibit the passivation of the Mg surface by an inherent oxide layer,^[132] MgCl₂ was added to the electrolyte system, which at least to some extent improved Mg plating/stripping performance. However, a satisfying Mg plating and stripping was still not achieved, especially in the first few cycles. To overcome this, AlCl₃ as Lewis acid was added to facilitate Mg(CF₃SO₃)₂ dissociation and to form the electroactive species, [Mg₂(μ-Cl)₃(THF)₆][(CF₃SO₃)AlCl₃], which resulted in an efficient Mg plating and stripping performance, indicating the inherent oxide layer on the Mg anode had been removed upon cycling.^[133,134] Next, anthracene, a π-rich molecule, which can further decrease the large overpotentials by accelerating the reaction of Mg(CF₃SO₃)₂ with AlCl₃, was added as a coordinating ligand. At last, a Mg-S@microporous carbon cell containing 0.125 M Mg(CF₃SO₃)₂ + 0.25 M AlCl₃ + 0.25 M MgCl₂ + 0.025 M anthracene/THF and tetraglyme (1:1, v:v) electrolyte was cycled at 0.05 C (Figure 10a,b).^[39] Nearly 100% Coulombic efficiency was reached after few cycles; however, the discharge capacity dropped dramatically after two cycles to only 50 mAh g_{sulfur}⁻¹ after the 50th cycle, which was attributed to large amounts of unreacted sulfur in the cathode and a poor Mg-ion dissociation.^[39]

Finally, addition of Li⁺ into the electrolyte to promote the dissolution of Mg²⁺ was attempted in order to decrease the kinetic barrier and increase the solubility of the low-order polysulfides and consequently improve the electrochemical performance.^[24] The authors added LiCl (Figure 10c,d) and LiCF₃SO₃ (Figure 10e,f), respectively, to a 0.125 M Mg(CF₃SO₃)₂ + 0.25 M AlCl₃ + 0.25 M MgCl₂ + 0.025 M anthracene/THF and tetraglyme (1:1, v:v) solution. Figure 10c,d shows that the plateau at 1.05 V of the discharge curve persists longer, leading to a higher discharge capacity and reversibility in the presence of LiCl, indicating that Li⁺ successfully promotes Mg dissolution. Interestingly, the use of 0.5 M LiCF₃SO₃ as the additive improved the cell performance even more. The cell was able to deliver around 400 mAh g_{sulfur}⁻¹ at 0.05 C for 50 cycles, indicating that the addition of CF₃SO₃Li also reduces the destructive effect on Mg plating.^[39]

4.2.2. Non/Less Corrosive, Nonnucleophilic Electrolytes

Muldoon et al.^[113] stated that chlorides in the electroactive species [Mg₂(μ-Cl)₃·6THF] are a main factor for corrosion. In addition, the bulky nature of the cation, i.e., the two octahedrally coordinated Mg atoms connected by three chlorides, is not beneficial for Mg ion transport. Consequently, research on the synthesis of novel, chloride-free salts for Mg-S batteries is of growing importance. Li et al.^[21] synthesized a chloride-free electroactive salt, [Mg(THF)₆][AlCl₄]₂ (Figure 11a), by reacting MgCl₂ with two equivalents of AlCl₃ in THF and an IL, i.e., N-methyl-N-butyl pyrrolidinium bis(trifluoromethanesulfonyl) imide (PYR14TFSI) at 95 °C.^[21] At elevated temperature, AlCl₃ completely replaced the chloride ions in MgCl₂.^[21] The obtained salt was reported to have high ionic conductivity (8.5 mS cm⁻¹) and good ionic stability (2.5 V vs Mg). Furthermore, according to cyclic voltammography (CV; Figure 11b), a stable and reversible Mg plating and stripping was demonstrated. To further understand the stability of the interface between the electrolyte and the Mg surface, electronic impedance spectroscopy (EIS) measurements on a symmetrical Mg-Mg cell

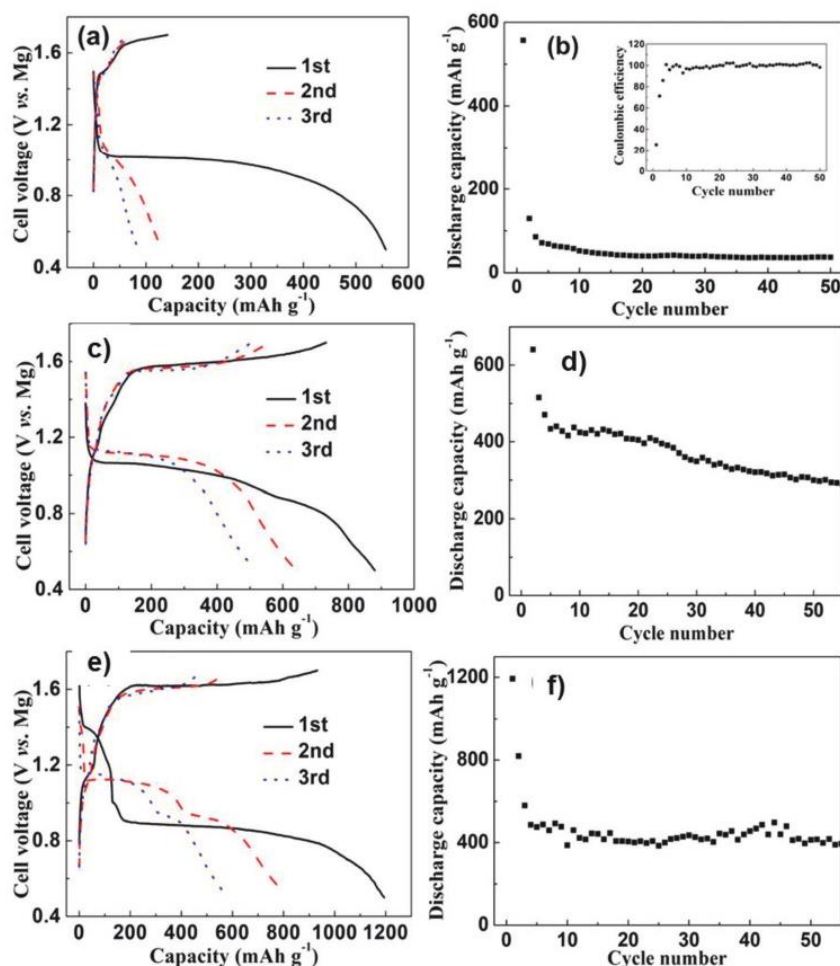


Figure 10. a) Charge and discharge curves; b) cycle performance of a Mg-S@MC coin cell with 0.125 M Mg(CF₃SO₃)₂ + 0.25 M AlCl₃ + 0.25 M MgCl₂ + 0.025 M anthracene/THF and tetraglyme (1:1, v:v) electrolyte @0.05 C; c) charge and discharge curves; d) cycle performance of Mg-S@MC coin cell with 0.125 M Mg(CF₃SO₃)₂ + 0.25 M AlCl₃ + 0.25 M MgCl₂ + 0.025 M anthracene/THF and tetraglyme (1:1, v:v) electrolyte in the presence of 0.5 M LiCl @0.05 C; e) charge and discharge curves; f) cycle performance of Mg-S@MC coin cell with 0.125 M Mg(CF₃SO₃)₂ + 0.25 M AlCl₃ + 0.25 M MgCl₂ + 0.025 M anthracene/THF and tetraglyme (1:1, v:v) electrolyte adding LiCF₃SO₃ @0.05 C. Reproduced with permission.^[39] Copyright 2019, American Chemical Society.

containing [Mg(THF)₆][AlCl₄]₂ in PYR14TFSI/THF were conducted (Figure 11c). Results revealed that the bulk resistance of the electrolyte remained constant upon cycling while the semi-circle, which represents the interfacial resistance, decreased after 60 cycles and stayed stable afterward, indicating the interface between Mg surface and electrolyte was not stable in the initial cycles, but slowly stabilizes within the first 60 cycles.^[21] Li et al. also investigated the cycle performance of a Mg-S battery using the as-prepared electrolyte (Figure 11d).^[21] The cell delivered around 700 mAh g⁻¹ at 0.01 C for the initial cycle; however, the discharge capacity dropped sharply in the following 19 cycles to only 130 mAh g⁻¹. They observed capacity fading was explained by the poor electric conductivity during cycling and a shuttle effect of the cathode material.^[21]

Research on novel Lewis acid is also ongoing. Xu et al.^[135] synthesized a Y-based electrolyte by substituting AlCl₃ by YCl₃. They reacted MgCl₂ and two equivalents of YCl₃ with the IL PYR14TFSI and diglyme at 120 °C. They stated that YCl₃ outperformed AlCl₃ for the following reasons. First, the higher standard electrode potential of the Y ion (-2.372 V vs SHE) compared to the Al ion (-1.66 V vs SHE) prevents the codeposition of Al on Mg. Second, YCl₃ is known to be a good water scavenger, which can remove traces of water in the electrolyte.^[135] They compared the cell performance of the newly synthesized Y-based electrolyte with the one of a conventional Al-based electrolyte using a magnesium polysulfide cathode material. Figure 12a shows that the cell with the Y-based electrolyte was stably cycled for 50 cycles with a discharge capacity

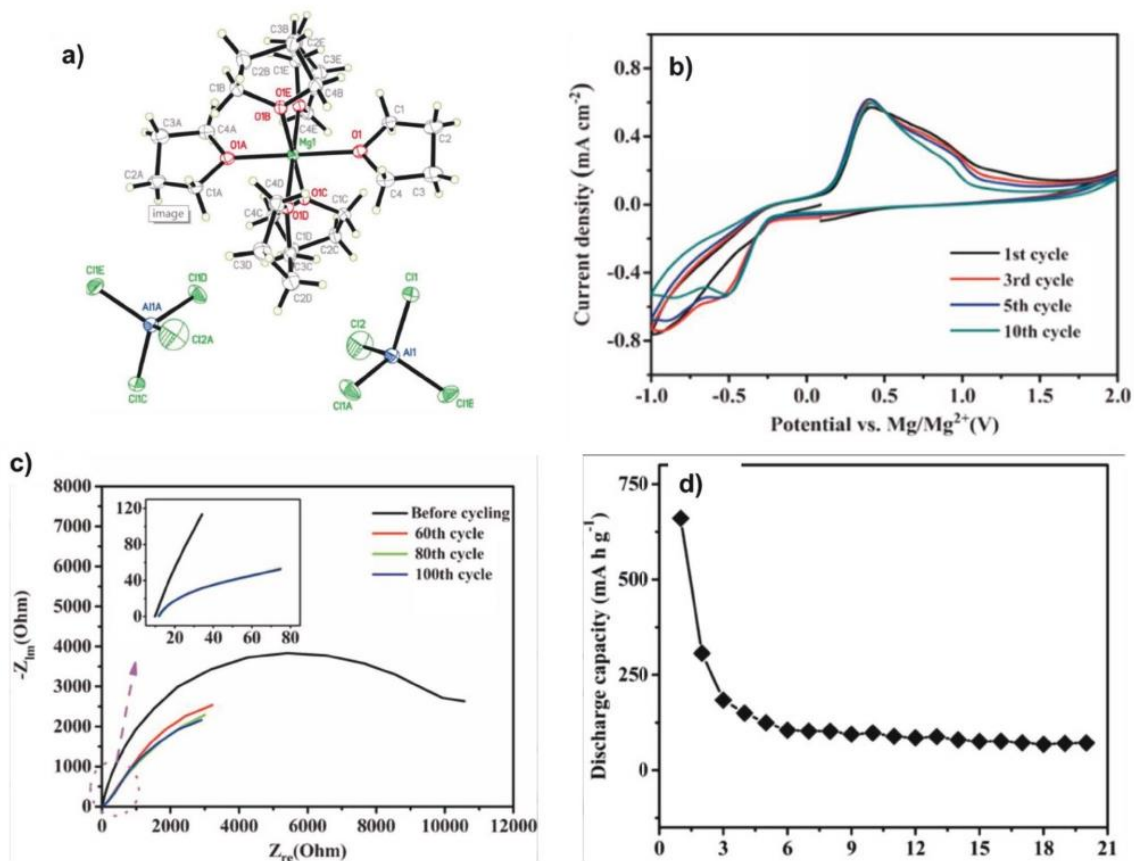


Figure 11. a) Single crystal X-ray structure of $[\text{Mg}(\text{THF})_6][\text{AlCl}_4]_2$; b) cyclic voltammogram using the as-prepared electrolyte (Pt disc as working electrode; Mg plate as counterelectrode and reference electrode; scan rate: 25 mV s^{-1}); c) Nyquist plot of a symmetrical Mg–Mg cell using $[\text{Mg}(\text{THF})_6][\text{AlCl}_4]_2$ in $\text{PYR14TFSI}/\text{THF}$ as electrolyte at different cycles; d) cycle performance of Mg/S cell at 0.01 C (cathode: N-doped graphene-S-carbon black; anode: Mg disc). Reproduced with permission.^[21] Copyright 2016, Wiley-VCH Verlag GmbH & Co. KGaA, Weinheim.

around 900 mAh g^{-1} . In contrast, the cell with the Al-based electrolyte cycled for only 20 cycles with a sharp capacity decay. Further, EIS data (Figure 12b) revealed a lower impedance of the Y-based electrolyte.^[135]

Recently, Zuo et al.^[136] filed a patent on a novel electrolyte for Mg–S batteries. They dissolved $0.2\text{--}0.8 \text{ mol L}^{-1}$ of AlCl_3 and $0.006\text{--}0.024 \text{ mol L}^{-1}$ of TiCl_4 in an ether-based solvent. Then, excess of Mg was added to the solution, and stirred for 3–5 h.

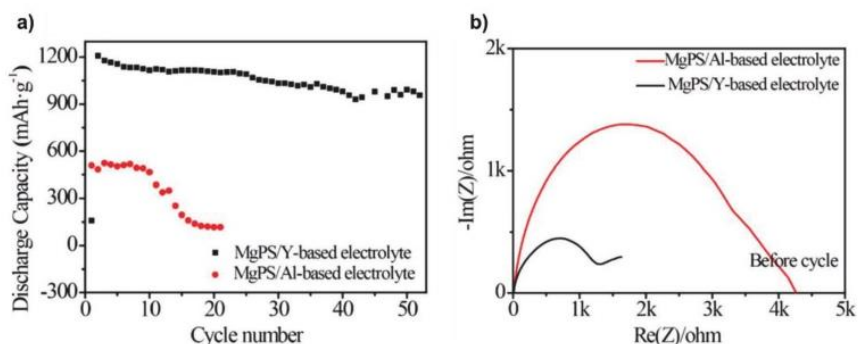


Figure 12. a) Cycle performance and b) EIS data of Mg–S battery containing a Y-based and an Al-based electrolyte, respectively (cathode: magnesium polysulfide cathode; anode: Mg foil; current rate: 0.04 C).^[135] Reproduced with permission.^[135] Copyright 2019, Wiley-VCH Verlag GmbH & Co. KGaA, Weinheim.

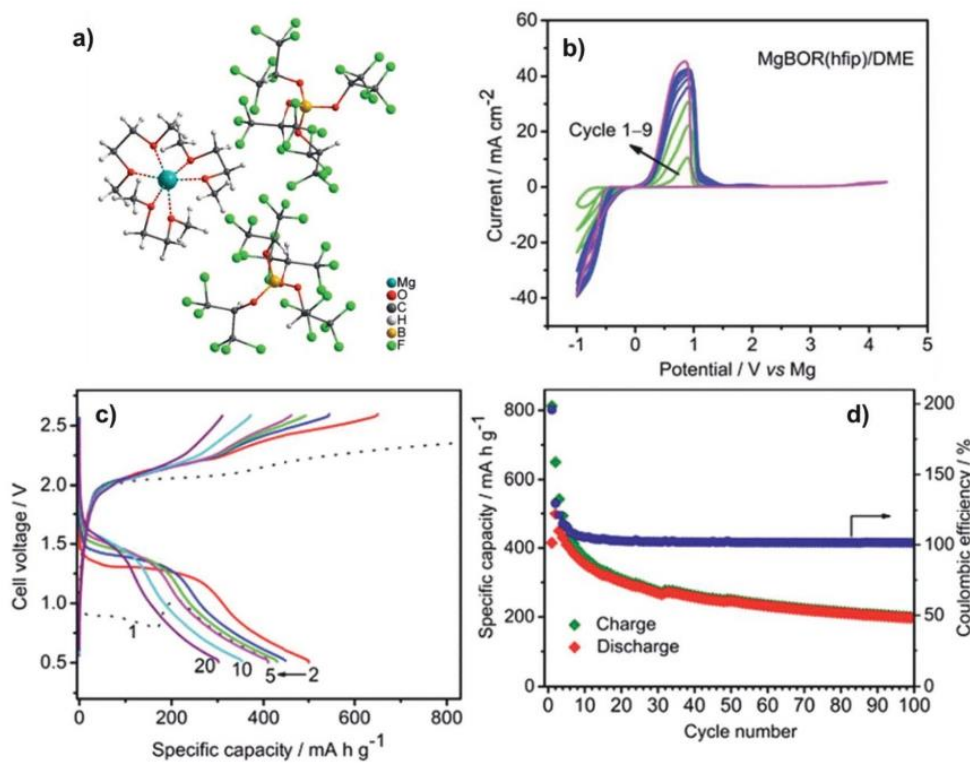


Figure 13. a) Ball-and-stick illustration of $\text{Mg}[\text{B}(\text{hfip})_4]_2 \cdot 3 \text{ DME}$; b) cyclic voltammogram (working electrode: Pt; counter and reference electrodes: Mg; scan rate: 25 mV s^{-1}); electrochemical performance of a Mg–S (CMK-3) cell containing $\text{Mg}[\text{B}(\text{hfip})_4]_2 \cdot 3 \text{ DME}$ in DME at 0.1 C ; c) charge–discharge curves; d) cycle stability.^[41] Reproduced with permission.^[41] Copyright 2017, Royal Society of Chemistry.

The weight ratio between Mg and the solution was maintained between 3:10 and 12:10. Finally, the solution was filtered and ready for use in Mg–S batteries. They claimed that the electrolyte was cheaper than all reported ones while at the same time showing both high stability and Coulombic efficiency (99.6%).

One group of noncorrosive electrolytes are those on weakly coordinating anions (WCAs). WCAs are known to possess some unique properties, including a low nucleophilicity and high solubility of their salts in some low polarity solvents.^[137] Owing to these superior properties, WCAs have been considered as attractive candidates for the synthesis of new salts for electrolytes used in Mg–S batteries.^[138,139] Recently, Zhao-Karger et al.^[41] have synthesized a fluorinated magnesium alkoxyborate-based electrolyte for Mg–S batteries. They prepared the conductive salts by the reaction of $\text{Mg}[\text{BH}_4]_2$ with fluorinated alcohols ($\text{R}^{\text{F}}\text{-OH}$) in ethereal solvents (such as DME), as shown in Equation (4).^[41] By using hexafluoro-2-propanol (hfip), the conductive salt, $\text{Mg}[\text{B}(\text{hfip})_4]_2 \cdot 3 \text{ DME}$ was obtained after removal of the solvent^[41]



Zhao-Karger et al. also studied the crystal structure of this compound by single-crystal X-ray crystallography (Figure 13a).^[41] The crystal unit consists of Mg^{2+} ions solvated

by three dimethyl ether (DME) molecules, leading to a slightly distorted octahedral coordination geometry.^[41] In the anion, the boron center is bound to four hexafluoroisopropoxy groups resulting in a tetrahedral structure. The authors also stated that the obtained magnesium salt turned out to be water and air insensitive as evidenced by NMR analysis.^[41]

Zhao-Karger et al. examined a 0.6 M $\text{Mg}[\text{B}(\text{hfip})_4]_2 \cdot 3 \text{ DME}/\text{DME}$ electrolyte by CV for its propensity to support reversible Mg deposition and dissolution (Figure 13b).^[41] Based on the CV results, successful Mg plating and stripping was confirmed. Moreover, the current density gradually increased upon scanning, indicating enhanced Mg plating. This finding was explained by a facilitated nucleation of Mg crystals triggered by the Mg deposition during the first cycle.^[41] The same authors applied 0.8 M $\text{Mg}[\text{B}(\text{hfip})_4]_2$ in diglyme/tetraglyme as electrolyte for Mg–S batteries (cathode: S-CMK-3; anode: Mg plate).^[41] They charged and discharged the cell at 0.1 C at room temperature (Figure 13c,d).^[41] Charge and discharge profiles of the initial to the 5th cycle as well as of the 10th and the 20th cycle are given in Figure 13c. The initial cycle possessed a discharge capacity around $400 \text{ mAh g}^{-1}_{\text{sulfur}}$, which increased to $500 \text{ mAh g}^{-1}_{\text{sulfur}}$ in the second cycle, due to the activation of Mg anode during cycling.^[41] After the second cycle, the discharge capacity decreased but remained around $200 \text{ mAh g}^{-1}_{\text{sulfur}}$ up to the 100th cycle (Figure 13d). Based on these results, the authors

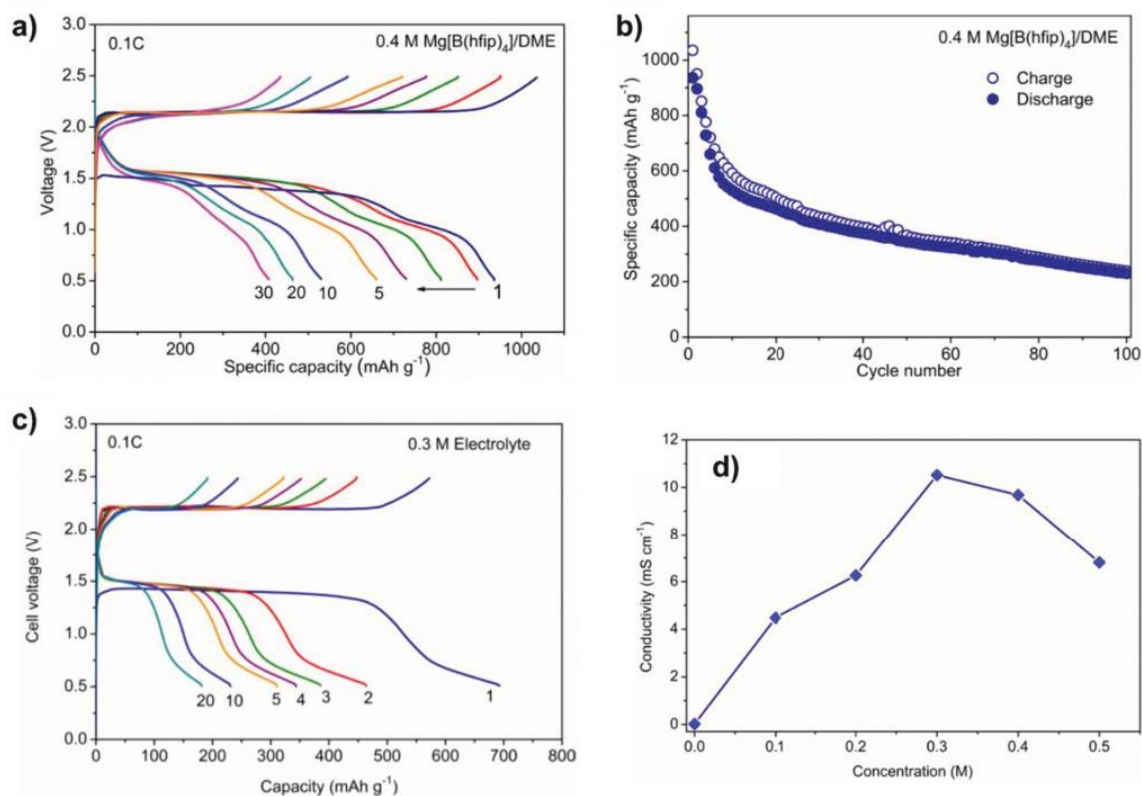
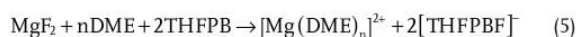


Figure 14. Electrochemical behavior of a Mg–S cell (cathode: ACC-based sulfur composites; anode: Mg foil; electrolyte: Mg[B(hfip)₄]₂ · 3 DME in DME); a) charge–discharge profiles at 0.1 C (0.4 M Mg[B(hfip)₄]₂ · 3 DME in DME); b) cycle stability (0.4 M Mg[B(hfip)₄]₂ · 3 DME in DME); c) charge–discharge profiles at 0.1 C (0.3 M Mg[B(hfip)₄]₂ · 3 DME in DME); d) influence of electrolyte concentration (Mg[B(hfip)₄]₂ in DME) on ionic conductivity at 23 °C.^[43] Reproduced with permission.^[43] Copyright 2018, American Chemical Society.

stated that the fluorinated alkoxyborate-based electrolytes are promising candidates for Mg–S batteries.^[41]

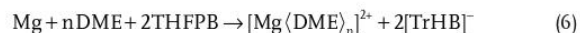
The same research group also investigated the influence of the concentration of the conductive salt in the electrolyte, Mg[B(hfip)₄]₂ · 3 DME on battery behavior by using ACC-based sulfur composites as cathode materials.^[43] Since ionic conductivity is a key parameter in the quantification of ion mobility in the electrolyte, which also influences the rate capability of batteries, they evaluated the ionic conductivity of the electrolyte solutions at room temperature.^[43] Measurements revealed (Figure 14d) that the ionic conductivity increased linearly when the concentration was increased from 0.1 to 0.3 M. At a higher concentration, the ionic conductivity decreased again (Figure 14d). The better performance of the cell containing the 0.3 M electrolyte was explained by the suppression of the solubility and the diffusion of magnesium polysulfides by increasing the concentration of the magnesium conductive salt, which could further avoid a fast capacity decay.^[43]

Zhang et al.^[114] also synthesized a so-called boron-centered base magnesium (BCM) electrolyte by reacting tris(2*H*-hexafluoroisopropyl) borate (THFPB) with MgF₂ in DME (Equation (5))



In a freshly prepared BCM electrolyte, the fluoro-tris(hexafluoro-2-propoxy) borate (FTHPB[−]) anion (Figure 15c) is formed due to the strong affinity between the boron center and the F[−] in MgF₂. After cycling, according to mass spectroscopy, the electroactive species in the electrolyte comprise [Mg(DME)_n]²⁺ (Figure 15d) and the tetra(hexafluoroisopropyl) borate anion ([TrHB][−]; Figure 15e).

For the formation, the authors proposed the following chemical reaction^[114]



Notably, both the effective anion [TrHB][−] and the cation formed upon cycling had a similar, if not the same structure than Mg[B(hfip)₄]₂ reported by Zhao-Karger et al.^[41,43] Zhang et al.^[114] also examined the electrochemical compatibility of the BCM electrolyte with a Mg anode by CV (Figure 15a). They noticed that current density increased upon cycling, indicating improved electrochemical properties. Their explanation was that MgF₂ has a low solubility and the electroactive species was only gradually generated over several cycles.^[114] In addition, they investigated the cycle stability of the Mg–S cell using the BCM electrolyte (Figure 15b).

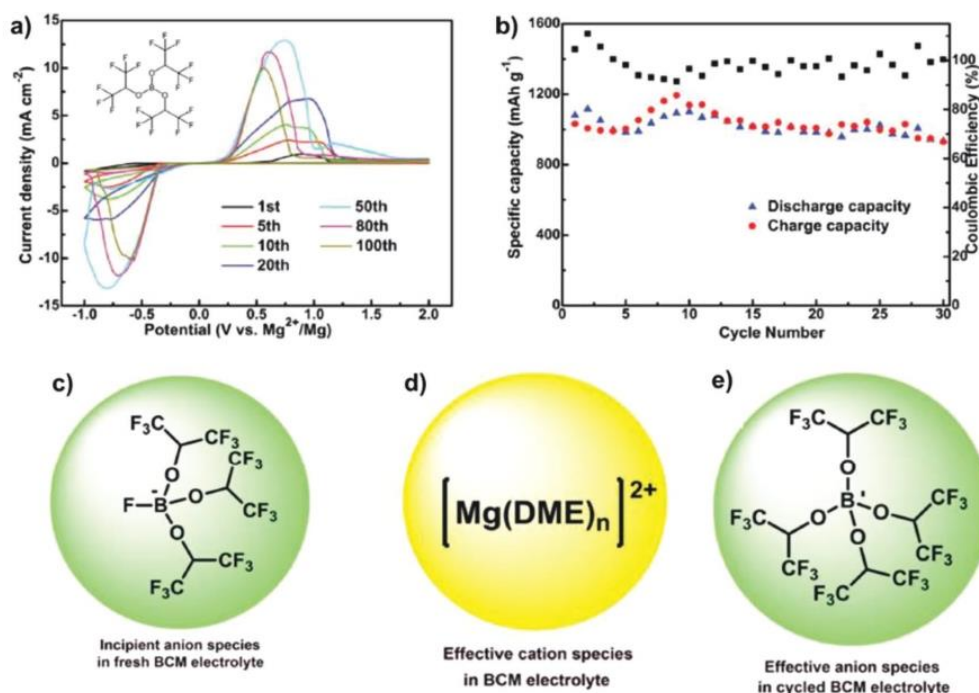


Figure 15. a) CV results using a BCM electrolyte; b) cycle stability results of a Mg–S/C cell using a BCM electrolyte at C/30; c) incipient anion species in a BCM electrolyte; d) effective cationic species in the BCM electrolyte; e) effective anion species in a cycled BCM electrolyte.^[114] Reproduced with permission.^[114] Copyright 2017, Wiley-VCH Verlag GmbH & Co. KGaA, Weinheim.

The cell delivered a discharge capacity around 1000 mAh g^{-1} , indicating that the BCM electrolyte might be a promising model electrolyte for Mg–S batteries.^[114]

In addition, on the basis of this electrolyte, Hintennach filed a patent related to additives in an electrolyte.^[140] He pointed out that the addition of a mixture of two thiobarbituric acids derivatives such as thiobarbital and 2-thiobarbituric acid, at a concentration between 0.01 and 1.9 wt%, respectively, was beneficial for both Mg–S and Mg ion batteries.

4.3. Summary and Prospective Electrolyte Systems for Mg–S Batteries

Research on electrolyte systems suitable for Mg–S batteries is still ongoing; nonetheless, some achievements have already been accomplished. Table 2 summarizes all clearly identified electroactive species in the electrolytes investigated so far. The development of novel electrolyte systems that are compatible with a sulfur cathode clearly depends on the successful realization of noncorrosive magnesium salts, utilization of various solvents and additives. Apart from that, an in-depth understanding of the underlying chemistry at the surface of the electrodes and in the electrolytes is of great importance for the future development too. For the prospective magnesium salts, boron- or aluminum-centered weakly coordinating anions are promising candidates. In addition, a polymer-based electrolyte may also


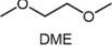
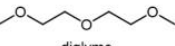
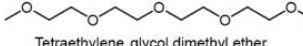
be worth to be studied for the following reasons: i) no internal short circuits and ii) no leakage and easy fabrication.^[62] However, the problems in polymer electrolytes, such as the incompatibility with the Mg anode and a low Mg ion transfer number need to be solved for a successful application in cells.

5. Separator Design

Separators play a crucial role in liquid electrolyte batteries. They are placed between the cathode and anode to prevent any physical contact but allow for free ion transportation.^[141,142] Currently used separators in Mg–S batteries are mainly based on commercial glass fiber sheets^[17,18,24,40–44,85,86,114] and microporous polymer membranes;^[21,39,82,88,99,111,112] a brief comparison between these two types of separators is illustrated in Figure 16a. Generally, glass fiber separators outperform others in terms of thermal dimensional stability, porosity, permeability and ionic conductivity; but they are more costly and require more electrolyte.^[141,142]

Due to the low solubility and irreversibility of the low-order magnesium polysulfides (MgS , Mg_3S_8), the surface modification of separators is also feasible in the field of Mg–S batteries to enhance the cell performance.^[25,95] Yu and Arumugam^[25] recently presented an activated carbon nanofiber (CNF)-coated glass fiber separator, which was prepared by a vacuum-filtration process (Figure 16b). The purpose of the CNF coating was to

Table 2. Summary of available electrolyte systems in terms of cations, anions, solvents, and additives for use in Mg-S batteries.

Type	salt cation	salt anion	additives	solvents
Nucleophilic	$\left[\begin{array}{c} \text{THF} \quad \text{Cl} \quad \text{THF} \\ \quad \quad \\ \text{THF}-\text{Mg}-\text{Cl}-\text{Mg}-\text{THF} \\ \quad \quad \\ \text{THF} \quad \text{Cl} \quad \text{THF} \end{array} \right]^+$ $\left[\begin{array}{c} \text{Cl} \quad \text{THF} \\ \quad \\ \text{Mg} \\ \\ \text{THF} \end{array} \right]^+$	$\left[\begin{array}{c} \text{Ph} \quad \text{Ph} \\ \quad \\ \text{Al} \\ \\ \text{Ph} \end{array} \right]^-$ $\left[\begin{array}{c} \text{Cl} \quad \text{Cl} \\ \quad \\ \text{Al} \\ \\ \text{Cl} \quad \text{Cl} \end{array} \right]^-$	LiCl	 THF
Non-nucleophilic	$\left[\begin{array}{c} \text{THF} \quad \text{Cl} \quad \text{THF} \\ \quad \quad \\ \text{THF}-\text{Mg}-\text{Cl}-\text{Mg}-\text{THF} \\ \quad \quad \\ \text{THF} \quad \text{Cl} \quad \text{THF} \end{array} \right]^+$ $\left[\text{MgCl} \right]^+$ $\left[\text{Mg}_2\text{Cl}_3 \right]^+$	$\left[\begin{array}{c} \text{O} \quad \text{O} \\ \quad \\ \text{F}_3\text{C}-\text{S}-\text{N}-\text{S}-\text{CF}_3 \\ \quad \\ \text{O} \quad \text{O} \end{array} \right]^-$ $\left[\begin{array}{c} \text{H}_3\text{C} \quad \text{CH}_3 \\ \quad \\ \text{H}_3\text{C}-\text{Si}-\text{N}-\text{Si}-\text{CH}_3 \\ \quad \\ \text{H}_3\text{C} \quad \text{CH}_3 \\ \quad \\ \text{Cl} \quad \text{Cl} \end{array} \right]^-$ $\left[\begin{array}{c} \text{H}_3\text{C} \quad \text{CH}_3 \\ \quad \\ \text{H}_3\text{C}-\text{Si}-\text{N}-\text{Si}-\text{CH}_3 \\ \quad \\ \text{H}_3\text{C} \quad \text{CH}_3 \\ \quad \\ \text{Cl} \quad \text{Cl} \end{array} \right]^-$	$\text{Li}^+ \left[\begin{array}{c} \text{O} \quad \text{O} \\ \quad \\ \text{F}_3\text{C}-\text{S}-\text{N}-\text{S}-\text{CF}_3 \\ \quad \\ \text{O} \quad \text{O} \end{array} \right]^-$ $\text{Li}^+ \left[\begin{array}{c} \text{Cl} \quad \text{Cl} \quad \text{O} \quad \text{O} \quad \text{CF}_3 \\ \quad \quad \\ \text{Cl} \quad \text{Cl} \quad \text{S} \end{array} \right]^-$ LiCl	 DME  diglyme  Tetraethylene glycol dimethyl ether
	$\left[\begin{array}{c} \text{THF} \quad \text{Cl} \quad \text{THF} \\ \quad \quad \\ \text{THF}-\text{Mg}-\text{Cl}-\text{Mg}-\text{THF} \\ \quad \quad \\ \text{THF} \quad \text{Cl} \quad \text{THF} \end{array} \right]^{2+}$ $\left[\begin{array}{c} \text{THF} \quad \text{THF} \quad \text{THF} \\ \quad \quad \\ \text{Mg} \\ \\ \text{THF} \quad \text{THF} \end{array} \right]^{2+}$	$\left[\begin{array}{c} \text{Cl} \quad \text{O} \quad \text{O} \quad \text{CF}_3 \\ \quad \\ \text{Cl} \quad \text{S} \end{array} \right]^-$ $\left[\begin{array}{c} \text{Cl} \quad \text{Cl} \\ \quad \\ \text{Al} \\ \\ \text{Cl} \quad \text{Cl} \end{array} \right]^-$		
	$\left[\begin{array}{c} \text{O} \quad \text{O} \\ \quad \\ \text{Mg} \\ \quad \\ \text{O} \quad \text{O} \end{array} \right]^{2+}$	$\left[\begin{array}{c} \text{F}_3\text{C} \quad \text{CF}_3 \\ \quad \\ \text{O} \quad \text{O} \\ \quad \\ \text{F}_3\text{C} \quad \text{CF}_3 \end{array} \right]^-$		
	$\left[\begin{array}{c} \text{O} \quad \text{O} \\ \quad \\ \text{Mg} \\ \quad \\ \text{O} \quad \text{O} \end{array} \right]^{2+}$	$\left[\begin{array}{c} \text{F}_3\text{C} \quad \text{CF}_3 \\ \quad \\ \text{O} \quad \text{O} \\ \quad \\ \text{F}_3\text{C} \quad \text{CF}_3 \end{array} \right]^-$		
	$\left[\begin{array}{c} \text{O} \quad \text{O} \\ \quad \\ \text{Mg} \\ \quad \\ \text{O} \quad \text{O} \end{array} \right]^{2+}$	$\left[\begin{array}{c} \text{F}_3\text{C} \quad \text{CF}_3 \\ \quad \\ \text{O} \quad \text{O} \\ \quad \\ \text{F}_3\text{C} \quad \text{CF}_3 \end{array} \right]^-$		

act as a current collector to increase sulfur utilization and at the same time to trap the polysulfides intermediates. The coating layer on the separator plays an important role to reactivate and reuse the sulfur species that diffuse out of the active material upon cycling. The cell with a coated separator delivered around

950 mAh g⁻¹ for the first cycle; the capacity remained around 800 mAh g⁻¹ at C/50 at the 20th cycle. By comparison, a cell with an uncoated separator was capable of delivering about 1000 mAh g⁻¹ for the first cycle; however, the capacity dropped dramatically to only 200 mAh g⁻¹ after the 20th cycle at C/50,

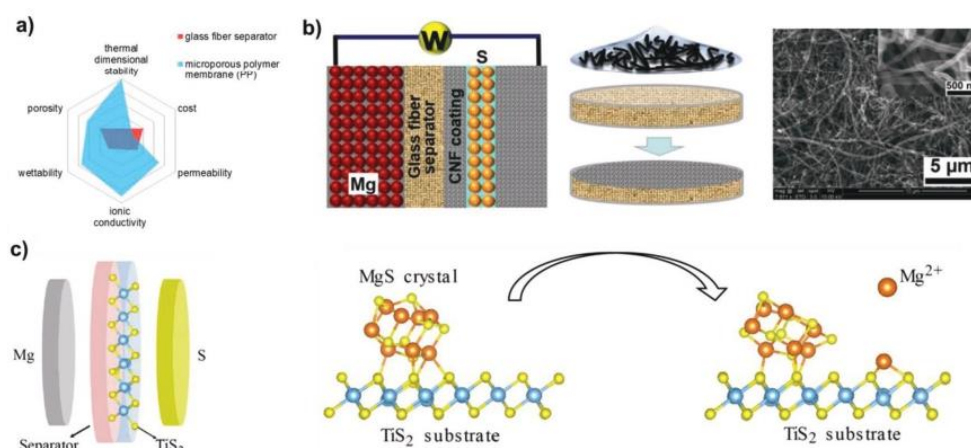


Figure 16. a) Comparison between a glass fiber separator and a microporous polymer membrane.^[141,142] b) schematic illustration of a cell containing a CNF-coated glass fiber separator, the vacuum filtration process to make the CNF-coated glass fiber, an SEM image of the surface modification of a glass fiber separator with an activated CNF coating. Reproduced with permission.^[25] Copyright 2016, American Chemical Society. c) Illustration of the catalytic effect of TiS₂ in a Mg-S battery and the MgS decomposition on the TiS₂ surface. Reproduced with permission.^[95] Copyright 2016, American Chemical Society.

clearly indicating the performance enhancement brought by the CNF-coated separator.

Finally, an approach that utilizes a catalyst to reactivate electrochemically inert MgS and Mg₃S₈ to reform high-order polysulfides or S is another approach to improve the discharge capacity and cycling life. It has been reported that TiS₂ has a catalytic effect on the activation of low-order magnesium polysulfides.^[143–145] In 2019, Xu et al.^[95] presented a TiS₂-coated separator prepared by a vacuum-filtration process. The Mg-S cell with the coated separator (for the configuration refer to Figure 16c) delivered around 800 mAh g⁻¹ for 30 cycles at 0.05 C, while a cell without any TiS₂ could only deliver around 200 mAh g⁻¹ for 20 cycles. XPS measurements confirmed that both the S and the polysulfide peak showed up at the fully charged state, indicating that TiS₂ successfully reoxidized both MgS and Mg₃S₈ back to higher-order polysulfides and S and that the Mg-S bond in MgS can be broken by TiS₂ (Figure 16c).^[95]

6. Electrode–Electrolyte Interfaces and Full Device Design

Interface issues concerning the electrodes in Mg-S batteries and those in their analogous Li-S batteries are quite different.^[146] In Li-S batteries, the lithium polysulfides are formed and dissolved in the electrolyte solution and then further reduced to insoluble Li₂S at the Li anode, where a so-called solid electrolyte interphase (SEI) forms, whose composition is crucial for cell performance. Ideally, the formed SEI allows for the permeation and transportation of Li⁺ ions; hence Li dissolution and deposition are still possible. By contrast, in Mg-S batteries, the SEI layer is more a blocking layer. The reduction of the sulfur at the cathode leads to a general formation of soluble MgS₈. MgS₈ is then further reduced to MgS, which leads to the blocking of the

Mg anode and a high impedance of the cell.^[147] In addition to this blocking of the Mg surface from polysulfides, thereby preventing any further reduction of sulfur, the deposition of electrolytes also destroys the Mg surfaces. Ding et al.^[127] observed some dendrite growth on a Mg anode when using Mg(TFSI)₂/diglyme as electrolyte, leading to a so-called “soft short-circuit” phenomenon, since the cells were not purely resistive. Due to the native oxide layer on the Mg surface, only parts of the surface are electrochemically active if the electrolyte cannot remove the blocking layer on the Mg anode. Consequently, current density is not homogeneous over the entire surface, leading to the observed dendrite formation.^[127] Typical components on the surface of a cycled anode include Mg metal, MgF₂, Mg(TFSI)₂ and MgO, where magnesium fluoride and oxide originate from the decomposition of Mg(TFSI)₂ dissolved in diglyme.^[129] Further on, using in situ AFM and optical microscopy, Hu et al.^[128] observed that the use of Mg(HMDS)₂-AlCl₃ dissolved in different ethers (diglyme and tetraglyme) influences the Mg anode surface due to different dynamic processes. Due to the differences in the chemical structure between diglyme and tetraglyme, the dynamic stripping processes of the two solvents are different, too. Diglyme has three oxygen atoms, which allows, together with three chloride atoms, for the formation of anionic hexacoordinated Mg²⁺ complexes. By comparison, tetraglyme, having five oxygen atoms, can form cationic monochloride complexes, which benefit from the chelating effect of the oxygens and thus experience better solvation. Consequently, the stripping process with tetraglyme as solvent is slow and homogeneous. Therefore, the use of tetraglyme improves the reversibility of a cell.

When selecting the cathodes, anodes, electrolytes, etc., for the construction of a full Mg-S battery, it is necessary to consider the compatibility of the individual components. Table 3 summarizes published data of Mg-S batteries. To date, solvents for the electrolytes are limited to ethers, such as THF, DME,

Table 3. A summary of currently reported Mg–S batteries (in chronological order).

Author/Year	Cell type	Cathode	Sulfur loading [wt%]	Anode	Separator	Electrolyte	Anodic stability [V vs Mg/Mg ²⁺]	Coulombic efficiency [%]	Capacity [mAh g ⁻¹ sulfur] / current rate / cycle number
Muldoon and co-workers 2011 ^[12]	Coin cell	S@carbon black on porous carbon substrate	61	Mg foil	No data	[Mg ₂ (μ-Cl) ₃ ·6THF] [HMDSAICl ₃]/THF (nonnucleophilic)	3.3/Pt	95–100	394/no data/2nd
Ha et al. 2014 ^[37]	Coin cell	70% CMK3/S–20% Super P–10% PVDF on Al	69.3	Mg disc	No data	0.3 M Mg(TFSI) ₂ /DME-diglyme (nonnucleophilic)	4.2/Al 4.8/SS	No data	100 @C/30 /4th
Zhao-Karger et al. 2014 ^[7]	Swagelok type cell	75% S/CMK–15% Super P–10% PVDF in NMP or CMC in water on Inconel 625	55%	Pressed Mg powder and carbon black (4:1 wt.) Pellet	Borosilicate glass fiber sheet	1.2 M (HMDS) ₂ Mg–2AlCl ₃ –MgCl ₂ in tetraglyme or diglyme; 1.2 M (HMDS) ₂ Mg–2AlCl ₃ –MgCl ₂ in diglyme or tetraglyme/PP14TFSI (nonnucleophilic)	No data	≈100	≈150 @0.01 C/20th (PVDF, diglyme) ≈200 @0.01 C/20th (CMC, diglyme) ≈250 @0.01 C/20th (PVDF, tetraglyme) ≈260 @0.01 C/20th (CMC, tetraglyme)
Gao et al. 2015 ^[24]	Swagelok type cell	ACC-S	15 wt% 0.5 mg cm ⁻²	Mg foil	Whatmann glass fiber	0.1 M (HMDS) ₂ Mg–2AlCl ₃ + 1 M LiTFSI (nonnucleophilic)	2.7/Pt	≈92	1000 @0.03 C/30th
Itaoka et al. 2015 ^[11]	Coin cell	Sulfur/bis (undec-10-enyloxy-methylbenzo)-18-crown-6-ether (BUMB18C6); sulfur-oxybis (2,1-ethanedioxy-2,1-ethanedioxy) ester (UOEE); on SS	No data	Mg plate	Celgard 2500	0.5 M Mg(TFSA) ₂ in triglyme or acetonitrile (nonnucleophilic)	No data	No data	23 @0.01 C/10th (acetonitrile) 68.1 @0.01 C/10th (triglyme)
Li et al. 2016 ^[21]	Coin cell	S–N-doped graphene–carbon black–PVDF in NMP; on Al foil	50 wt%	Mg disc	Celgard 2400	[Mg(THF) ₆][AlCl ₄] ₂ /PYR14(TFSI) in THF (salt) (nonnucleophilic)	2.4/Al–C 2.5/Al 2.1/Cu 2.3/ss	No data	40 @0.01 C/20th
Vinayan et al. 2016 ^[8]	Swagelok type cell	Reduced graphene oxide–S (rGo–S) 75% rGo–S–15% Super P–10% PVDF on Inconel 625	49 wt%	Pressed Mg powder and carbon black (4:1 wt) composite pellet	Celgard 2500	(HMDS) ₂ Mg–2AlCl ₃ –MgCl ₂ in tetraglyme (nonnucleophilic)	No data	≈100	236 @0.01 C/50th
Yu and Arumugam 2016 ^[23]	Coin cell	CNF–S	50 wt%	Mg foil	Carbon nanofiber-coated glass fiber	3.6 M (HMDS) ₂ Mg–2AlCl ₃ –MgCl ₂ in tetraglyme (nonnucleophilic)	No data	≈85	800 @0.01 C/20th
Sievert et al. 2017 ^[4]	Swagelok type cell	70% elemental S–20% carbon black–10% PVDF; on Al/C	1 mg cm ⁻²	Pressed Mg/graphite anode	Glass fiber (Whatman GF/A)	HMDSMgCl (nonnucleophilic)	No data	≈100	30 @0.1 C/100th
Du et al. 2017 ^[40]	Coin cell	S–CNT 80% S–CNT–10% Super P–10% PVDF in NMP; on Cu;	1	Mg foil	Glass fiber	OMBB 0.5 M [Mg ₄ Cl ₆ (DME) ₆] ₂ ⁺ [B(HFP) ₄] ⁻ 2 B(HFP) ₃ –MgCl ₂ (nonnucleophilic)	3/Al 3.2/Pt 2.0/Cu 2.5/ss	100	1000 @0.1 C/100th
Gao et al. 2017 ^[26]	Swagelok type cell	ACC–S	1	Mg disc	Glass fiber	1 M Mg(TFSI) ₂ –MgCl ₂ in DME (nonnucleophilic)	No data	93	600 @0.01 C/100th

Table 3. Continued.

Author/Year	Cell type	Cathode	Sulfur loading [wt%]	Anode	Separator	Electrolyte	Anodic stability [V vs Mg/Mg ²⁺]	Coulombic efficiency [%]	Capacity [mAh g ⁻¹ _{sulfur}] / current rate / cycle number
Du et al. 2017 ^[86]	Coin cell	70% SGDY–20% Super P–10% PVDF; on Al	1	Mg disc	Glass fiber	All-phenyl complex (PhMgCl) ₂ –AlCl ₃ + LiCl in THF (nucleophilic)	No data	100	800 @0.1 C/100th
Zeng et al. 2017 ^[99]	Coin cell	70% S–20% Super P–10% PVDF in NMP; on SS/Cu	No data	Mg ribbon	Entek PE membrane	APC 0.4 M (PhMgCl) ₂ –AlCl ₃ + LiCl in THF (nucleophilic)	1.7/Cu	100	300 @0.005 C/40th
Robba et al. 2017 ^[18]	Pouch cell	Graphite/S–multiwalled CNT; on Al	No data	Mg foil	Glass fiber (Whatman GF/A)	0.4 M Mg(TFSI) ₂ –MgCl ₂ (1:1) in tetraglyme:1,3-dioxolane (DOL) (1:1) (nonnucleophilic)	2.5/Al	No data	400 @C/60/4th
Zhang et al. 2017 ^[114]	Coin cell	80% S/C composite–10% acetylene black–10% PVDF in NMP on Cu	85 wt%	Mg foil	Glass fiber	BCM (0.5 M THFPB + 0.05 M MgF ₂ in DME) (nonnucleophilic)	2/Cu	≈100	900 @0.03 C/30th
Zhao-Karger et al. 2017 ^[41]	Swagelok type cell	75% S/CMK-3–15% carbon black–10% CMC on SS	1 mg cm ⁻²	Mg foil	Borosilicate glass fiber sheet GF/C	0.8 M Mg(B(hfp) ₄) ₂ in diglyme:tetraglyme (1:1) (nonnucleophilic)	3/Al 3.2/Pt 4.5/ss 2/graphite 2.5/Cu	≈100	≈200 @0.1 C/100th
Gao et al. 2018 ^[85]	Swagelok type cell	S-ACC on SS; S/CMK-3 on SS	1 mg cm ⁻²	Mg disc	Glass fiber	Mg(TFSI) ₂ in DME (nonnucleophilic)	3.0/ss	100	668 @0.01 C /20th 400 @0.01 C /3th
Aurbach and co-workers 2018 ^[147]	–	Carbon cloth/S	–	Mg foil	–	Mg(TFSI) ₂ –MgCl ₂ in DME (nonnucleophilic)	–	–	–
Muthuraj et al. 2018 ^[115]	–	70% S/rGO–20% Super P–10% PVDF in NMP; on N, S dual doped carbon cloth current collector	1 mg cm ⁻²	Mg disc	Activated CNF-coated glass fiber	(HMDS) ₂ Mg–2AlCl ₃ –MgCl ₂ in tetraglyme (nonnucleophilic)	–	≈93	388 @0.01 C/40th
Wang et al. ^[88] 2018	Coin cell	70% S@MC–20% Super P–10% PVDF in NMP 20 μm; on Cu	64.7 wt%	Mg	PE membrane	APC: 0.4 M (PhMgCl) ₂ –AlCl ₃ + 1 M LiCl/THF (nucleophilic)	1.7/Cu	≈100	368.8 @0.1 C/200th
Zhou et al. 2018 ^[42]	Coin cell	MOF-S	1 mg cm ⁻²	Mg foil	Glass fiber (Whatman GF/A)	(HMDS) ₂ Mg–2AlCl ₃ with LiTFSI additive (nonnucleophilic)	No data	No data	400 @0.1 C/200th
Zhao-Karger et al. 2018 ^[43]	Swagelok type cell	S-ACC on SS	1.2 mg cm ⁻²	Mg foil	Glass fiber	Mg[B(hfp) ₄] ₂ in DME (nonnucleophilic)	4.5/Pt 3.0/SS 2.9/Al 3.0/C–Al 2.6/Cu	≈100	200 @0.1 C/100th
Xu et al. 2019 ^[135]	Coin cell	MgS ₈ @G-CNT	0.7–1 mg cm ⁻²	Mg metal	No data	YCl ₃ –MgCl ₂ in <i>N</i> -methyl-(<i>N</i> -butyl)pyrrolidinium bis(trifluoromethanesulfonyl) imide/diglyme (1/1, v/v) (nonnucleophilic)	3.0/Pt	98.7	900 @0.04 C/50th

Table 3. Continued.

Author/Year	Cell type	Cathode	Sulfur loading [wt%]	Anode	Separator	Electrolyte	Anodic stability [V vs Mg/Mg ²⁺]	Coulombic efficiency [%]	Capacity [mAh g ⁻¹ sulfur] / current rate / cycle number
Yang et al. 2019 ^[39]	Coin cell	80% S@ microporous carbon-10% Super P-10% PVDF in NMP; on Cu	55 wt%	Mg Ribbon	PE separator	Mg(CF ₃ SO ₃) ₂ -AlCl ₃ in THF and tetraglyme (nonnucleophilic)	3.25/Pt, 2.5/SS, 2.0/Cu, 1.85/Al	≈90	400 @0.05 C/50th
Zhao et al. 2019 ^[172]	Coin cell	80% S@ microporous carbon-10% Super P-10% PVDF in NMP; on Cu	55.8 wt%	Mg metal	PE separator	Magnesium bis(diisopropyl) amide MBA-AlCl ₃ -LiCl in THF (nonnucleophilic)	1.85/Cu, 2.35/Al, 2.65/SS	≈94	400 @0.04 C/100th

diglyme, triglyme, and tetraglyme. This is a result of the finding that carbonate-based solvents react with Mg anodes, resulting in blocked, carbonate-containing anode surfaces. In addition, due to the nucleophilic character of the polysulfides, the electrolyte may not be electrophilic, unless both the cathode and the separators are specifically modified.^[147,148]

7. Summary and Outlook

Over the last ten years, increasing attention has been devoted to novel rechargeable Mg-S batteries due to their safety characteristics, high energy density and earth abundance of both magnesium and sulfur. However, some major issues still exist in this field, which impede the development of reliable Mg-S batteries. One major challenge is related to the formation of magnesium polysulfides. The intermediary polysulfides dissolve in the electrolyte, leading to severe overcharging, loss of active material and low sulfur utilization of the cathode during charge and discharge. This results in a shuttle effect, capacity decay and irreversible reactions, which will in turn lead to short cycle life and capacity fading. The final products, MgS and MgS₂, are also electrochemically inactive, since they lack solubility and are hard to reoxidize during charging. With regards to these issues, novel cathode materials for Mg-S batteries, which are able to suppress the shuttle effect and which possess a high sulfur content need to be synthesized and further studied. To date, cathode systems are generally based on elemental sulfur or sulfur species confined in microporous carbon materials, which can to some extent immobilize sulfur and magnesium polysulfides, too. Since the design principles of cathode materials for Mg-S batteries are at least similar to those of Li-S batteries in terms of high sulfur loading, high conductivity and good surface chemisorptivity, polymers containing covalently bound sulfur as cathode material might present a future research direction. Also, it is important to study the fundamental electrochemistry behind the individual redox reactions in order to understand the capacity decay phenomenon and to further improve cell performance. In that regards, Cu-based current collectors as well as modified separators have been reported to be beneficial to increase reversibility and maintain capacity.

With regards to Mg anodes, research in this area is far less active as compared to electrolytes and cathode materials. Unlike Li metal, which deposits in a dendritic manner and creates high surface area upon cycling, Mg generally does not plate in a dendritic manner. This is beneficial for safety reasons; however, it reduces the active surface area, which in turn results in a poor electrochemical performance of the cell. In view of this challenge, pressed Mg anodes out of Mg powder or nanoparticles that possess a high surface area are under investigation. Another major challenge is related to the manipulation of the Mg anode surface with the electrolyte system. Thus, commonly used carbonate-based electrolytes in Li batteries are unsuitable for Mg batteries, due to the formation of an impermeable layer on the Mg surface, which hinders Mg deposition and dissolution. The generation of an artificial conductive layer on Mg anodes, which could protect the Mg anodes from reacting with the electrolytes, might be a new direction for novel anodes. Also, the utilization of magnesium ion insertion anodes, which can host Mg²⁺ ions, is another possible solution for the use of magnesium salts in polar aprotic solvents used in the electrolytes. For example, Bi nanotubes, which can be formed in situ, can effectively accommodate the volume change of the anodes, decrease the diffusion length of Mg²⁺ and retain the electronic contact. However, the compatibility of magnesium ion insertion anodes with sulfur-based cathode has not yet been addressed, but might also present a novel route to prevent reaction of the electrolyte and especially of the polar solvents with the Mg metal.

In terms of electrolyte development for Mg-S batteries, major challenges are related to the divalent nature of the Mg²⁺ ions, which possess a higher energy barrier between electrolyte and Mg anodes than monovalent Li ions, resulting in sluggish Mg plating and stripping. Also, sufficient transport properties and anodic stability are crucial for the cycle performance. For example, a suitable viscosity of the electrolyte that can allow for the fast migration of Mg ions, and at the same time, reduce the Mg polysulfide shuttle effect, is important. In addition, corrosion-free electrolytes with a large potential window are desirable for practical Mg-S batteries. Up to now, nucleophilic electrolytes, which are known to react with the sulfur cathode,

were applied, together with modified cathode materials, but are increasingly replaced by nonnucleophilic electrolytes for which variations both in the Mg salt and the Lewis acid have been carried out to obtain new electroactive species. Specifically, cationic, chloride-containing electrolytes have been found to be corrosive to the cell body. Consequently, the development of chloride-free noncorrosive Mg compounds is an ongoing research. So far, nonnucleophilic fluorinated alkoxyborate-based magnesium electrolytes seem to be the most promising systems; both in terms of anodic stability, capability of Mg plating and stripping, and compatibility with the sulfur-based cathode. Perspective, alternative conductive salts containing boron- and aluminum-based weakly coordinating anions, together with the addition of lithium salts and ionic liquids might be another future research direction. Further on, polymer-based electrolytes that benefit from low leakage and practical use are also interesting.

In summary, rechargeable Mg–S batteries are currently still in a nascent stage. Fortunately, growing interest is devoted for obtaining a high energy-density system that outperforms Li batteries. A practical and reliable Mg–S cell might be soon realized.

Acknowledgements

Financial support by the German Federal Ministry of Education and Research (project number 03XP0208J) and by the German Federal Ministry of Economic Affairs and Energy (project number 03ETE003E) is gratefully acknowledged.

Conflict of Interest

The authors declare no conflict of interest.

Keywords

magnesium anode, magnesium battery electrolytes, magnesium–sulfur batteries, post lithium–sulfur batteries, sulfur-based cathodes

Received: July 1, 2019

Revised: August 12, 2019

Published online: September 6, 2019

- [1] P. Saha, M. K. Datta, O. I. Velikokhatnyi, A. Manivannan, D. Alman, P. N. Kumta, *Prog. Mater. Sci.* **2014**, *66*, 1.
- [2] H. Budde-Meiwes, J. Drillkens, B. Lunz, J. Muennix, S. Rothgang, J. Kowal, D. Sauer, *Proc. Inst. Mech. Eng., Part D* **2013**, *227*, 761.
- [3] L. Medenbach, P. Adelhelm, *Top. Curr. Chem.* **2017**, *375*, 81.
- [4] C. Wadia, P. Albertus, V. Srinivasan, *J. Power Sources* **2011**, *196*, 1593.
- [5] Y. X. Yin, S. Xin, Y. G. Guo, L. J. Wan, *Angew. Chem.* **2013**, *1258*, 13426; *Angew. Chem., Int. Ed.* **2013**, *52*, 13186.
- [6] H. Tian, T. Gao, X. Li, X. Wang, C. Luo, X. Fan, C. Yang, L. Suo, Z. Ma, W. Han, C. Wang, *Nat. Mater.* **2016**, *11*, 19.
- [7] J. Dewulf, K. Denturck, H. Van Langenhove, W. Ghyoot, J. Tytgat, *Resour., Conserv. Recycl.* **2010**, *54*, 229.
- [8] T. Cleaver, P. Kovacic, M. Marinescu, T. Zhang, G. Offer, *J. Electrochem. Soc.* **2018**, *165*, A6029.
- [9] X. Xu, S. Wang, H. Wang, B. Xu, *J. Energy Storage* **2017**, *13*, 387.
- [10] J. Zheng, M. Gu, H. Chen, P. Meduri, M. H. Engelhard, J. Zhang, J. Liu, J. Xiao, *J. Mater. Chem. A* **2013**, *1*, 8464.
- [11] Z. Zhao-Karger, M. Fichtner, *MRS Commun.* **2017**, *7*, 770.
- [12] H. Kim, T. S. Arthur, G. D. Allred, J. Zajicek, J. G. Newman, A. E. Rodnyansky, A. G. Oliver, W. C. Boggess, J. Muldoon, *Nat. Commun.* **2011**, *427*, 1.
- [13] L. Wang, Y. Ye, N. Chen, Y. Huang, L. Li, F. Wu, R. Chen, *Adv. Funct. Mater.* **2018**, *28*, 1800919.
- [14] M. Huang, M. Li, C. Niu, Q. Li, L. Mai, *Adv. Funct. Mater.* **2019**, *29*, 1807847.
- [15] X. Hong, J. Mei, L. Wen, Y. Tong, A. J. Vasileff, L. Wang, J. Liang, Z. Sun, S. X. Dou, *Adv. Mater.* **2018**, e1802822.
- [16] J. Muldoon, (Toyota Motor Engineering & Manufacturing), *US20110244338*, **2011**.
- [17] Z. Zhao-Karger, X. Zhao, D. Wang, T. Diemant, R. J. Behm, M. Fichtner, *Adv. Energy Mater.* **2015**, *5*, 1401155.
- [18] A. Robba, A. Vizintin, J. Bitenc, G. Mali, I. Arčon, M. Kavčič, M. Žitnik, K. Bučar, G. Aquilanti, C. Martineau-Corcos, A. Randon-Vitanova, R. Dominko, *Chem. Mater.* **2017**, *29*, 9555.
- [19] H. D. Yoo, I. Shterenberg, Y. Gofer, G. Gershinsky, N. Pour, D. Aurbach, *Energy Environ. Sci.* **2013**, *6*, 2265.
- [20] H. Tian, T. Gao, X. Li, X. Wang, C. Luo, X. Fan, C. Yang, L. Suo, Z. Ma, W. Han, C. Wang, *Nat. Commun.* **2017**, *8*, 14083.
- [21] W. Li, S. Cheng, J. Wang, Y. Qiu, Z. Zheng, H. Lin, S. Nanda, Q. Ma, Y. Xu, F. Ye, M. Liu, L. Zhou, Y. Zhang, *Angew. Chem.* **2016**, *128*, 6516; *Angew. Chem., Int. Ed.* **2016**, *55*, 6406.
- [22] Z. Zhang, B. Chen, H. Xu, Z. Cui, S. Dong, A. Du, J. Ma, Q. Wang, X. Zhou, G. Cui, *Adv. Funct. Mater.* **2018**, *28*, 1701718.
- [23] Z. Zhao-Karger, X. Zhao, O. Fuhr, M. Fichtner, *RSC Adv.* **2013**, *3*, 16330.
- [24] T. Gao, M. Noked, A. J. Pearse, E. Gillette, X. Fan, Y. Zhu, C. Luo, L. Suo, M. A. Schroeder, K. Xu, S. B. Lee, G. W. Rubloff, C. Wang, *J. Am. Chem. Soc.* **2015**, *137*, 12388.
- [25] X. Yu, M. Arumugam, *ACS Energy Lett.* **2016**, *1*, 431.
- [26] T. Gao, S. Hou, F. Wang, Z. Ma, X. Li, K. Xu, C. Wang, *Angew. Chem.* **2017**, *129*, 13711; *Angew. Chem., Int. Ed.* **2017**, *56*, 13526.
- [27] D. Aurbach, G. S. Suresh, E. Levi, A. Mitelman, O. Mizrahi, O. Chusid, M. Brunelli, *Adv. Mater.* **2007**, *19*, 4260.
- [28] J. Muldoon, C. B. Bucur, A. G. Oliver, T. Sugimoto, M. Matsui, H. S. Kim, G. D. Allred, J. Zajicek, Y. Kotani, *Energy Environ. Sci.* **2012**, *5*, 5941.
- [29] J. Song, E. Sahadeo, M. Noked, S. B. Lee, *J. Phys. Chem. Lett.* **2016**, *7*, 1736.
- [30] C. B. Bucur, *Challenges of a Rechargeable Magnesium Battery*, Springer, Switzerland **2018**.
- [31] Z. Zhao-Karger, M. Fichtner, *Front. Chem.* **2018**, *6*, 656.
- [32] L. Kong, C. Yan, J.-Q. Huang, M.-Q. Zhao, M.-M. Titirici, R. Xiang, Q. Zhang, *Energy Environ. Mater.* **2018**, *1*, 100.
- [33] D. Aurbach, I. Weissman, Y. Gofer, E. Levi, *Chem. Rec.* **2003**, *3*, 61.
- [34] Z. Lu, A. Schechter, M. Moshkovich, D. Aurbach, *J. Electroanal. Chem.* **1999**, *466*, 203.
- [35] R. Mohtadi, F. Mizuno, *Beilstein J. Nanotechnol.* **2014**, *5*, 1291.
- [36] L. C. Merrill, J. L. Schaefer, *Front. Chem.* **2019**, *7*, 194.
- [37] S. Y. Ha, Y. W. Lee, S. W. Woo, B. Koo, J. S. Kim, J. Cho, K. T. Lee, N. S. Choi, *ACS Appl. Mater. Interfaces* **2014**, *6*, 4063.
- [38] Y. Cheng, Y. Shao, J. G. Zhang, V. L. Sprenkle, J. Liu, G. Li, *Chem. Commun.* **2014**, *50*, 9644.
- [39] Y. Yang, W. Wang, Y. Nuli, J. Yang, J. Wang, *ACS Appl. Mater. Interfaces* **2019**, *11*, 9062.
- [40] A. Du, Z. Zhang, H. Qu, Z. Cui, L. Qiao, L. Wang, J. Chai, T. Lu, S. Dong, T. Dong, H. Xu, X. Zhou, G. Cui, *Energy Environ. Sci.* **2017**, *10*, 2616.
- [41] Z. Zhao-Karger, M. E. Gil Bardaji, O. Fuhr, M. Fichtner, *J. Mater. Chem. A* **2017**, *5*, 10815.

- [42] X. Zhou, J. Tian, J. Hu, C. Li, *Adv. Mater.* **2018**, *30*, 1704166.
- [43] Z. Zhao-Karger, R. Liu, W. Dai, Z. Li, T. Diemant, B. P. Vinayan, C. Bonatto Minella, X. Yu, A. Manthiram, R. J. Behm, M. Ruben, M. Fichtner, *ACS Energy Lett.* **2018**, *3*, 2005.
- [44] B. Sievert, J. Häcker, F. Bienen, N. Wagner, K. A. Friedrich, *ECS Trans.* **2017**, *77*, 413.
- [45] K. Xu, *Chem. Rev.* **2004**, *104*, 4303.
- [46] S. B. Son, T. Gao, S. P. Harvey, K. X. Steirer, A. Stokes, A. Norman, C. Wang, A. Cresce, K. Xu, C. Ban, *Nat. Chem.* **2018**, *10*, 532.
- [47] Y. Wang, E. Sahadeo, G. Rubloff, C.-F. Lin, S. B. Lee, *J. Mater. Sci.* **2019**, *54*, 3671.
- [48] P. Canepa, G. Sai Gautam, D. Broberg, S.-H. Bo, G. Ceder, *Chem. Mater.* **2017**, *29*, 9657.
- [49] P. Canepa, S. H. Bo, G. Sai Gautam, B. Key, W. D. Richards, T. Shi, Y. Tian, Y. Wang, J. Li, G. Ceder, *Nat. Commun.* **2017**, *8*, 1759.
- [50] M. B. Pinson, M. Z. Bazant, *J. Electrochem. Soc.* **2013**, *160*, A243.
- [51] E. Marin, A. Lanzutti, F. Andreatta, M. Lekka, L. Guzman, L. Fedrizzi, *Corros. Rev.* **2011**, *29*, 191.
- [52] A. C. Kozen, C. F. Lin, A. J. Pearce, M. A. Schroeder, X. Han, L. Hu, S. Lee, G. W. Rubloff, M. Noked, *ACS Nano*. **2015**, *9*, 5884.
- [53] P. C. Wang, Y. T. Shih, M. C. Lin, H. C. Lin, M. J. Chen, K. M. Lin, *Thin Solid Films* **2010**, *518*, 7501.
- [54] J. Muldoon, C. B. Bucur, T. Gregory, *Angew. Chem.* **2017**, *129*, 12232; *Angew. Chem., Int. Ed.* **2017**, *56*, 12064.
- [55] T. D. Gregory, R. J. Hoffman, R. C. Winterton, *J. Electrochem. Soc.* **1990**, *137*, 775.
- [56] W. Kaveevitvachai, A. J. Jacobson, *Chem. Mater.* **2016**, *28*, 4593.
- [57] M. Levi, E. Lancri, E. Levi, H. Gizbar, Y. Gofer, D. Aurbach, *Solid State Ionics* **2005**, *176*, 1695.
- [58] Z. Ma, D. R. MacFarlane, M. Kar, *Batteries Supercaps* **2019**, *2*, 115.
- [59] D. Aurbach, Z. Lu, A. Schechter, Y. Gofer, H. Gizbar, R. Turgeman, Y. Cohen, M. Moshkovich, E. Levi, *Nature* **2000**, *407*, 724.
- [60] R. E. Doe, R. Han, J. Hwang, A. J. Gmitter, I. Shterenberg, H. D. Yoo, N. Pour, D. Aurbach, *Chem. Commun.* **2014**, *50*, 243.
- [61] Y. Li, H. Ye (Suzhou University), *CN106898750A*, **2017**.
- [62] A. Du, H. Zhang, Z. Zhang, J. Zhao, Z. Cui, Y. Zhao, S. Dong, L. Wang, X. Zhou, G. Cui, *Adv. Mater.* **2019**, *31*, 1805930.
- [63] L. Yu, X. Zhang, *J. Colloid Interface Sci.* **2004**, *278*, 160.
- [64] I. Shterenberg, M. Salama, Y. Gofer, E. Levi, D. Aurbach, *MRS Bull.* **2014**, *39*, 453.
- [65] S. Rasul, S. Suzuki, S. Yamaguchi, M. Miyayama, *Electrochim. Acta* **2012**, *82*, 243.
- [66] R. Zhang, X. Yu, K.-W. Nam, C. Ling, T. S. Arthur, W. Song, A. M. Knapp, S. N. Ehrlich, X.-Q. Yang, M. Matsui, *Electrochem. Commun.* **2012**, *23*, 110.
- [67] G. Gershinsky, H. D. Yoo, Y. Gofer, D. Aurbach, *Langmuir* **2013**, *29*, 10964.
- [68] M. Mao, T. Gao, S. Hou, C. Wang, *Chem. Soc. Rev.* **2018**, *47*, 8804.
- [69] J. Muldoon, C. B. Bucur, T. Gregory, *Chem. Rev.* **2014**, *114*, 11683.
- [70] H. Sano, H. Senoh, M. Yao, H. Sakaebe, T. Kiyobayashi, *Chem. Lett.* **2012**, *41*, 1594.
- [71] Y. NuLi, Z. Guo, H. Liu, J. Yang, *Electrochem. Commun.* **2007**, *9*, 1913.
- [72] B. Pan, J. Huang, Z. Feng, L. Zeng, M. He, L. Zhang, J. T. Vaughey, M. J. Bedzyk, P. Fenter, Z. Zhang, A. K. Burrell, C. Liao, *Adv. Energy Mater.* **2016**, *6*, 1600140.
- [73] R. Zhang, F. Mizuno, C. Ling, *Chem. Commun.* **2015**, *51*, 1108.
- [74] E. Levi, Y. Gofer, Y. Vestfried, E. Lancry, D. Aurbach, *Chem. Mater.* **2002**, *14*, 2767.
- [75] M. M. Huie, D. C. Bock, E. S. Takeuchi, A. C. Marschilok, K. J. Takeuchi, *Coord. Chem. Rev.* **2015**, *287*, 15.
- [76] C. B. Bucur, T. Gregory, A. G. Oliver, J. Muldoon, *J. Phys. Chem. Lett.* **2015**, *6*, 3578.
- [77] F. Wu, G. Yushin, *Energy Environ. Sci.* **2017**, *10*, 435.
- [78] R. Chen, T. Zhao, F. Wu, *Chem. Commun.* **2015**, *51*, 8.
- [79] L. Yin, J. Wang, J. Yang, Y. Nuli, *J. Mater. Chem.* **2011**, *21*, 6807.
- [80] W. Kang, N. Deng, J. Ju, Q. Li, D. Wu, X. Ma, L. Li, M. Naebe, B. Cheng, *Nanoscale* **2016**, *8*, 16541.
- [81] A. Manthiram, Y. Fu, S. H. Chung, C. Zu, Y. S. Su, *Chem. Rev.* **2014**, *114*, 11751.
- [82] B. P. Vinayan, Z. Zhao-Karger, T. Diemant, V. S. Chakravadhanula, N. I. Schwarzburger, M. A. Cambaz, R. J. Behm, C. Kubel, M. Fichtner, *Nanoscale* **2016**, *8*, 3296.
- [83] Y. Li, Y. Zhang, M. Yu, H. Pei, W. Liu, R. Guo, J. Xie, Y. Wang, C. Yang, (Shanghai Space Dianyuan Institute), *CN201811478988*, **2019**.
- [84] R. Elazari, G. Salitra, A. Garsuch, A. Panchenko, D. Aurbach, *Adv. Mater.* **2011**, *23*, 5641.
- [85] T. Gao, X. Ji, S. Hou, X. Fan, X. Li, C. Yang, F. Han, F. Wang, J. Jiang, K. Xu, C. Wang, *Adv. Mater.* **2018**, *30*, 1704313.
- [86] H. Du, Z. Zhang, J. He, Z. Cui, J. Ma, Z. Yang, C. Huang, G. Cui, *Small* **2017**, *13*, 1702277.
- [87] H. B. Wu, S. Wei, L. Zhang, R. Xu, H. H. Huang, X. W. Lou, *Chem. – Eur. J.* **2013**, *19*, 10804.
- [88] W. Q. Wang, H. C. Yuan, Y. Nuli, J. J. Zhou, J. Yang, J. L. Wang, *J. Phys. Chem. C* **2018**, *122*, 26764.
- [89] M. Oschatz, S. Thieme, L. Borchardt, M. R. Lohe, T. Biemelt, J. Bruckner, H. Althues, S. Kaskel, *Chem. Commun.* **2013**, *49*, 5832.
- [90] S. Chen, X. Huang, H. Liu, B. Sun, W. Yeoh, K. Li, J. Zhang, G. Wang, *Adv. Energy Mater.* **2014**, *4*, 1401761.
- [91] N. Jayaprakash, J. Shen, S. S. Moganty, A. Corona, L. A. Archer, *Angew. Chem.* **2011**, *123*, 6026; *Angew. Chem., Int. Ed.* **2011**, *50*, 5904.
- [92] G. He, S. Evers, X. Liang, M. Cuisinier, A. Garsuch, L. F. Nazar, *ACS Nano*. **2013**, *7*, 10920.
- [93] X. Ji, K. T. Lee, L. F. Nazar, *Nat. Mater.* **2009**, *8*, 500.
- [94] P. Zuo, Y. Li, M. He, R. Li, Y. Ma, C. Du, Y. Gao, G. Yin, (Harbin Institute of Technology), *CN107910535A*, **2018**.
- [95] Y. Xu, Y. Ye, S. Zhao, J. Feng, J. Li, H. Chen, A. Yang, F. Shi, L. Jia, Y. Nu, X. Yu, P. A. Glans-Suzuki, Y. Cui, J. Guo, Y. Zhang, *Nano Lett.* **2019**, *19*, 2928.
- [96] Y. Nakayama, R. Matsumoto, K. Kumagai, D. Mori, Y. Mizuno, S. Hosoi, K. Kamiguchi, N. Koshitani, Y. Inaba, Y. Kudo, H. Kawasaki, E. C. Miller, J. N. Weker, M. F. Toney, *Chem. Mater.* **2018**, *30*, 6318.
- [97] G. Li, Z. Li, B. Zhang, Z. Lin, *Front. Energy Res.* **2015**, *3*, 1.
- [98] R. Dominko, M. U. M. Patel, V. Lapornik, A. Vizintin, M. Koželj, N. N. Tušar, I. Arčon, L. Stievano, G. Aquilanti, *J. Phys. Chem. C* **2015**, *119*, 19001.
- [99] L. Zeng, N. Wang, J. Yang, J. Wang, Y. NuLi, *J. Electrochem. Soc.* **2017**, *164*, A2504.
- [100] G. Cui, L. Fu, X. Huimin, Z. Zhonghua, H. Xu, X. Wang, (Qingdao Institute Of Bioenergy & Bioprocess Technology Chinese Academy Of Science), *CN 106935796 A*, **2017**.
- [101] M. Frey, R. K. Zenn, S. Warneke, K. Müller, A. Hintennach, R. E. Dinnebier, M. R. Buchmeiser, *ACS Energy Lett.* **2017**, *2*, 595.
- [102] S. Warneke, M. Eusterholz, R. K. Zenn, A. Hintennach, R. Dinnebier, M. R. Buchmeiser, *J. Electrochem. Soc.* **2018**, *165*, A6017.
- [103] J. Wang, J. Yang, J. Xie, N. Xu, *Adv. Mater.* **2002**, *14*, 13.
- [104] S. Warneke, R. K. Zenn, T. Leberz, K. Müller, A. Hintennach, U. Starke, R. E. Dinnebier, M. R. Buchmeiser, *Adv. Sustainable Syst.* **2018**, *2*, 1700144.
- [105] J. Fanous, M. Wegner, M. B. M. Spera, M. R. Buchmeiser, *J. Electrochem. Soc.* **2013**, *160*, A1169.
- [106] J. Fanous, M. Wegner, J. Grimminger, M. Rolf, M. B. M. Spera, M. Tenzer, M. R. Buchmeiser, *J. Mater. Chem.* **2012**, *22*, 23240.
- [107] J. Fanous, M. Wegner, J. Grimminger, Å. Andresen, M. R. Buchmeiser, *Chem. Mater.* **2011**, *23*, 5024.
- [108] A. Mayer, M. R. Buchmeiser, *J. Electrochem. Soc.* **2018**, *165*, A3943.

- [109] A. Hintennach, (Daimler AG), *DE102016014148A1*, **2017**.
- [110] D. P. Lv, T. Xu, P. Saha, M. K. Datta, M. L. Gordin, A. Manivannan, P. N. Kumta, D. H. Wang, *J. Electrochem. Soc.* **2013**, *160*, A351.
- [111] K. Itaoka, I. Kim, K. Yamabuki, N. Yoshimoto, H. Tsutsumi, *J. Power Sources* **2015**, *297*, 323.
- [112] X. Zhao, Y. Yang, Y. NuLi, D. Li, Y. Wang, X. Xiang, *Chem. Commun.* **2019**, *55*, 6086.
- [113] J. Muldoon, C. B. Bucur, A. G. Oliver, J. Zajicek, G. D. Allred, W. C. Boggess, *Energy Environ. Sci.* **2013**, *6*, 482.
- [114] Z. Zhang, Z. Cui, L. Qiao, J. Guan, H. Xu, X. Wang, P. Hu, H. Du, S. Li, X. Zhou, S. Dong, Z. Liu, G. Cui, L. Chen, *Adv. Energy Mater.* **2017**, *7*, 1602055.
- [115] D. Muthuraj, A. Ghosh, A. Kumar, S. Mitra, *ChemElectroChem* **2019**, *6*, 684.
- [116] Y. Zhang, Z. Bakenov, Y. Zhao, A. Konarov, Q. Wang, P. Chen, *Ionics* **2014**, *20*, 803.
- [117] T. J. Carter, R. Mohtadi, T. S. Arthur, F. Mizuno, R. Zhang, S. Shirai, J. W. Kampf, *Angew. Chem.* **2014**, *126*, 3237; *Angew. Chem., Int. Ed.* **2014**, *53*, 3173.
- [118] Y. He, Q. Li, L. Yang, C. Yang, D. Xu, *Angew. Chem.* **2019**, *131*, 7697; *Angew. Chem., Int. Ed.* **2019**, *58*, 7615.
- [119] H. Zhao, J. Xu, D. Yin, Y. Du, *Chem. – Eur. J.* **2018**, *24*, 18220.
- [120] Y. Pan, S. Li, M. Yin, J. Li, *Energy Technol.* **2019**, 1900164, <https://doi.org/10.1002/ente.201900164>.
- [121] C. Wall, Z. Zhao-Karger, M. Fichtner, *ECS Electrochem. Lett.* **2014**, *4*, C8.
- [122] Y. Xu, W. Li, G. Zhou, Z. Pan, Y. Zhang, *Energy Storage Mater.* **2018**, *14*, 253.
- [123] C. Liebenow, Z. Yang, P. Lobitz, *Electrochem. Commun.* **2000**, *2*, 641.
- [124] P. Zuo, Y. Li, G. Yin, R. Li, Y. Ma, C. Du, Y. Gao (Harbin Institute of Technology), *CN 109244544 A*, **2019**.
- [125] Y. Nuli, X. Zhao, Y. Yang, J. Yang, J. Wang (Shanghai Jiao Tong University), *CN1096870727A*, **2019**.
- [126] N. N. Rajput, X. Qu, N. Sa, A. K. Burrell, K. A. Persson, *J. Am. Chem. Soc.* **2015**, *137*, 3411.
- [127] M. S. Ding, T. Diemant, R. J. Behm, S. Passerini, G. A. Giffin, *J. Electrochem. Soc.* **2018**, *165*, A1983.
- [128] X.-C. Hu, Y. Shi, S.-Y. Lang, X. Zhang, L. Gu, Y.-G. Guo, R. Wen, L.-J. Wan, *Nano Energy* **2018**, *49*, 453.
- [129] Y. Yu, A. Baskin, C. Valero-Vidal, N. T. Hahn, Q. Liu, K. R. Zavadil, B. W. Eichhorn, D. Prendergast, E. J. Crumlin, *Chem. Mater.* **2017**, *29*, 8504.
- [130] Y. Cheng, R. M. Stolley, K. S. Han, Y. Shao, B. W. Arey, N. M. Washton, K. T. Mueller, M. L. Helm, V. L. Sprenkle, J. Liu, G. Li, *Phys. Chem. Chem. Phys.* **2015**, *17*, 13307.
- [131] I. Shterenberg, M. Salama, H. D. Yoo, Y. Gofer, J.-B. Park, Y.-K. Sun, D. Aurbach, *J. Electrochem. Soc.* **2015**, *162*, A7118.
- [132] J. G. Connell, B. Genorio, P. P. Lopes, D. Strmcnik, V. R. Stamenkovic, N. M. Markovic, *Chem. Mater.* **2016**, *28*, 8268.
- [133] T. Liu, Y. Shao, G. Li, M. Gu, J. Hu, S. Xu, Z. Nie, X. Chen, C. Wang, J. Liu, *J. Mater. Chem. A* **2014**, *2*, 3430.
- [134] G. Vardar, A. E. Sleightholme, J. Naruse, H. Hiramatsu, D. J. Siegel, C. W. Monroe, *ACS Appl. Mater. Interfaces* **2014**, *6*, 18033.
- [135] Y. Xu, G. Zhou, S. Zhao, W. Li, F. Shi, J. Li, J. Feng, Y. Zhao, Y. Wu, J. Guo, Y. Cui, Y. Zhang, *Adv. Sci.* **2019**, *6*, 1800981.
- [136] P. Zuo, Y. Li, G. Yin, R. Li, Y. Ma, C. Du, Y. Gao (Harbin Institute of Technology), *CN 109473714 A*, **2019**.
- [137] W. E. Geiger, F. Barrier, *Acc. Chem. Res.* **2010**, *43*, 1030.
- [138] I. Krossing, I. Raabe, *Angew. Chem.* **2004**, *116*, 2116; *Angew. Chem., Int. Ed.* **2004**, *43*, 2066.
- [139] F. Barriere, W. E. Geiger, *J. Am. Chem. Soc.* **2006**, *128*, 3980.
- [140] A. Hintennach, (Daimler AG), *DE102017007426A1*, **2018**.
- [141] S. S. Zhang, *J. Power Sources* **2007**, *164*, 351.
- [142] J. Zhu, M. Yanilmaz, K. Fu, C. Chen, Y. Lu, Y. Ge, D. Kim, X. Zhang, *J. Membr. Sci.* **2016**, *504*, 89.
- [143] G. Zhou, H. Tian, Y. Jin, X. Tao, B. Liu, R. Zhang, Z. W. Seh, D. Zhuo, Y. Liu, J. Sun, J. Zhao, C. Zu, D. S. Wu, Q. Zhang, Y. Cui, *Proc. Natl. Acad. Sci. USA* **2017**, *114*, 840.
- [144] X. Sun, P. Bonnicks, V. Duffort, M. Liu, Z. Rong, K. A. Persson, G. Ceder, L. F. Nazar, *Energy Environ. Sci.* **2016**, *9*, 2273.
- [145] X. Sun, P. Bonnicks, L. F. Nazar, *ACS Energy Lett.* **2016**, *1*, 297.
- [146] R. Attias, M. Salama, B. Hirsch, Y. Goffer, D. Aurbach, *Joule* **2019**, *3*, 27.
- [147] M. Salama, R. Attias, B. Hirsch, R. Yemini, Y. Gofer, M. Noked, D. Aurbach, *ACS Appl. Mater. Interfaces* **2018**, *10*, 36910.
- [148] H. Xu, Z. Zhang, J. Li, L. Qiao, C. Lu, K. Tang, S. Dong, J. Ma, Y. Liu, X. Zhou, G. Cui, *ACS Appl. Mater. Interfaces* **2018**, *10*, 23757.